Jan Streffing

Modelling the atmosphere-ocean interface with improved energetic consistency

PhD Thesis
June 2023

Dept. of Mathematics & Logistics

Committee: Dr. Stephan Juricke, Prof. Dr. Marcel Oliver, Prof. Dr. Sergey Danilov, Prof. Dr. Joakim Kjellsson, Prof. Dr. Marc Hütt

Acknowledgements

I would like to thank my PhD supervisor, Dr. Stephan Juricke, for giving me the freedom to develop my work in the directions I found most interesting, and for his unwavering confidence in my progress. Under him I had the opportunity to work on my degree in a way that has become increasingly rare. I would like to acknowledge the valuable guidance of my thesis committee members, Prof. Dr. Marcel Oliver, Prof. Dr. Sergey Danilov, Prof. Dr. Joakim Kjellsson and Prof. Dr. Marc Hütt, in shaping this work and giving me the chance to pursue my interests in this area.

I want to thank Dr. Yangyang Liu for her support in difficult times, when a shoulder to lean on is most needed. I thank my parents for supporting me on my long journey through education the system and for instilling in me the foundations of curiosity and playfulness around computers and physics. I would like to thank Dr. Miguel Andres Martinez, Dr. Paul Gierz and Dr. Evan Gowan for many a drink with fruitful discussions about all things climate and computing, and Dr. Christian Stepanek and Dr. Tido Semmler for giving me the chance to start in this most interesting of scientific fields.

My thanks also go to Prof. Dr. Thomas Jung and Prof. Dr. Gerrit Lohmann for welcoming me as a guest at the Alfred Wegener Institute Climate Dynamics and Paleoclimate Dynamics sections for the duration of my PhD. The working environment I found there was a great motivation throughout the years. I would like to thank the FESOM2, OpenIFS, OASIS3MCT, and esm-tools development teams, for pouring countless hours into tools I was able to combine into AWI-CM3.

Publications

Peer-reviewed

Streffing, J., Sidorenko, D., Semmler, T., Zampieri, L., Scholz, P., Andres-Martinez, M., Koldunov, N., Rackow, T., Kjellsson, J., Goessling, H., Athanase, M., Wang, Q., Hegewald, J., Sein, D. V., Mu, L., Fladrich, U., Barbi, D., Gierz, P., Danilov, S., Juricke, S., Lohmann, G., and Jung, T. (2022). AWI-CM3 coupled climate model: description and evaluation experiments for a prototype post-CMIP6 model. Geoscientific Model Development, 15(16):6399–6427.

Pithan, F., Athanase, M., Dahlke, S., Sanchez-Benitez, A., Shupe, M. D., Sledd, A., **Streffing, J.**, Svensson, G., and Jung, T. (2023). Nudging allows direct evaluation of coupled climate models with in situ observations: a case study from the mosaic expedition. Geoscientific Model Development, 16(7):1857–1873.

Shi, J., Stepanek, C., Sein, D., **Streffing, J.**, and Lohmann, G. East asian summer precipitation in awi-cm3: Comparison with observations and cmip6 models. International Journal of Climatology, n/a(n/a)

Smith, D. M., Eade, R., Andrews, M. B., Ayres, H., Clark, A., Chripko, S., Deser, C., Dunstone, N. J., Garcia-Serrano, J., Gastineau, G., Graff, L. S., Hardiman, S. C., He, B., Hermanson, L., Jung, T., Knight, J., Levine, X., Magnusdottir, G., Manzini, E., Matei, D., Mori, M., Msadek, R., Ortega, P., Peings, Y., Scaife, A. A., Screen, J. A., Seabrook, M., Semmler, T., Sigmond, M., **Streffing, J.**, Sun, L., and Walsh, A. (2022). Robust but weak winter atmospheric circulation response to future arctic sea ice loss. Nature Communications, 13(1):727.

Mu, L., Nerger, L., **Streffing, J.**, Tang, Q., Niraula, B., Zampieri, L., Loza, S. N., and Goessling, H. F. (2022). Sea-ice forecasts with an upgraded awi coupled prediction system. Journal of Advances in Modeling Earth Systems, 14(12):e2022MS003176. e2022MS003176 2022MS003176.

Sidorenko, D., Danilov, S., **Streffing, J.**, Fofonova, V., Goessling, H. F., Scholz, P., Wang, Q., Androsov, A., Cabos, W., Juricke, S., Koldunov, N., Rackow, T., Sein, D. V., and Jung, T. (2021). Amoc variability and watermass transforma-

tions in the awi climate model. Journal of Advances in Modeling Earth Systems, 13(10):e2021MS002582. e2021MS002582 2021MS002582.

Wang, S., Gong, X., Qiao, F., Gowan, E. J., **Streffing, J.**, and Lohmann, G. (2021). The impact of non-breaking surface waves in upper-ocean temperature simulations of the last glacial maximum. Environmental Research Letters, 16(3):034008

Submitted

Streffing, J., Semmler, T. (2023).Climate Model Performance Index (CMPI) toolbox. Journal of Open Research Software.

In Preparation

Streffing, J., Juricke, S. (2024). Stochastic coupling at characteristic atmospheric boundary layer timescales.

Conference Contributions

Streffing, J., Semmler, T., Sidorenko, D., Pithan, F., Juricke, S. (2023). A set of deterministic and stochastic model improvements for the AWI-CM3 climate model, EGU General assembly 2023.

Streffing, J. (2023) High resolution coupling with OpenIFS-FESOM2, 6th Workshop on Coupling Technologies for Earth System Models (CW2023).

Abstract

Our unintentional large-scale geoengineering project, characterized by a rapid increase in greenhouse gas concentrations, poses significant challenges in predicting and mitigating global and regional consequences. Climate researchers worldwide are constructing and refining climate models to understand and navigate the complex Earth system state and evolution. This thesis focuses on my contributions to this endeavor, specifically the construction, evaluation, and application of the AWI-CM3 coupled climate model.

Additionally, I address the importance of improving the energetic consistency across the critical interface between the atmosphere and ocean. This research was conducted as part of the DFG collaborative Research Center Transregio (TRR) 181 "Energy Transfers in Atmosphere and Ocean", which aims to develop mathematically rigorous tools for climate analysis and modelling. By focusing on the interactions between the atmosphere and ocean, I strive to enhance our understanding of the exchange of heat, momentum, and mass, while incorporating model components for sea ice and river runoff.

I review the selection and method of computation for physical interface fluxes, introduce of stochastic remapping to conserve information across the coupling interface, and adapt vertical ocean mixing parameterizations to enhance the realism of the AWI-CM3 model. Through these efforts, I aim to contribute to the development of a comprehensive Earth System Model and advance our understanding of climate change and its societal implications.

Contents

Chapter 1

Introduction

"Everything in the world is a story,
and the stories are all connected"
-Australian Aboriginal worldview

1.1 Motivation

The development of breakthroughs in the natural sciences is founded on advances in theory and tools applying those theories. Nowhere are such breakthroughs more needed than in the research field of climate sciences, where, as a species, we have collectively and inadvertently performed a geoengineering project unprecedented in scale within the lifetime of our civilization. We introduced sharp upward ticks into thus far gradually evolving greenhouse gas concentration curves, and we are left to predict, avoid, and mitigate a myriad of global and regional knock on effects for decades and centuries to come. Yet the precise nature and quantity of those effects remains only partially explored, with many parts left unknown on our maps for the 21st century. Climate researchers from around the globe are building, refining, and employing climate models, numerical representations of parts of the complex earth system, in an effort to understand and navigate through the consequences of our grand climate experiment. In this thesis, I will present my own small contributions to this effort. I will present the construction, evaluation, and application of the AWI-CM3 coupled climate model, as well as efforts to improve the energetic consistency across its most important interface, between atmosphere and ocean.

Centuries ago it was possible for a dedicated reader to learn nearly all that was known across a wide range of fields, in just a few years of intensive reading. The polymath Ibn Sina (980 - 1037 CE) advanced the fields of medicine, mathematics, logic, ethics, astronomy, geology, geography, early chemistry, and theology, all the while being a governor and poet. Figures like Gottfried Wilhelm Leibniz and Leonardo da Vinci have made similarly wide ranging contributions in the 15th to 18th century. Given the tenfold increase in the number of people alive (Roser et al., 2013) and the ten fold increase in literacy rate (Roser and Ortiz-Ospina, 2016), we would expect dozens of Ibn Sinas and Da Vincis alive today. Yet polymaths do not seem as omnipresent as might be expected (Ross, 2011). Connecting different research at the forefront of different disciplines is harder than ever before, as the body of scientific knowledge grows in all directions. The natural sciences have thus become the victims of their own success. No longer is it sufficient to read a half dozen books to reach the terra incognita of mathematics, atmospheric physics or physical oceanography. In the year 2021 alone nearly 10 million scientific documents were published across all fields (SCImago, 2022) and their sheer information load defeats any attempt to be as wide ranging as the polymaths of old.

Yet even in the prolific and highly specialized world of higher education of natural sciences today, building a comprehensive Earth System Model requires interfacing. The development, evaluation, and application of one such interface, between atmosphere, ocean, sea ice, and river runoff is described in this thesis. Indeed, the breakdown of large scale problems into ever smaller sections has made connecting the individual solutions back into a larger model a scientific endeavor in and of itself.

My interest in creating coupled climate models and advancing the capabilities of modern Earth System Model development stems from three sources. Firstly there is the need to further research the very practical problem of investigating the impacts of climate change onto our society and onto our very own lives. The zero and first order effects, Global Warming and Arctic Amplification are qualitatively explored and established beyond reasonable doubt (Lynas et al., 2021; Cohen et al., 2020). Thanks to a global model development effort the likely range for Global Warming by doubling of CO_2 (so called climate sensitivity) has been narrowed from 1.5 to 4.5°C to 2.0 to 4.5°C between the two latest Assessment Reports AR5 and AR6 of the Intergovernmental Panel on Climate Change (IPCC) (Pörtner et al., 2022). Progress is being made by both revisiting of model assumptions and increasing level of detail included in the simulation of the included model spheres, as well as in the number of included processes. This reflects positively onto the potential for respresenting non-linear model feedbacks that were previously unexplored. The work I present here is the beginning of the next generation AWI Earth System Model (ESM), and aims at pushing the envelope of comprehensiveness and complexity (compare figure 2.1).

The second motivation is that the model that I started to develop can bridge the gap between coarse zero and first order term investigation with global models and second order term investigation with regional models. It is able to do so by being built on highly optimized and scalable components, and has been used to produce simulations down to 9km atmosphere and 2km ocean resolution. Models at this scale can be used to drive impact models of for example extreme event cost, which in turn can guide local policies and climate adaptation strategy. Previously, such links would have required impact models driven by regional models, driven by global models, complicating research.

Finally, the comprehensive ESM is our best effort to describe the world around us, the spaceship Earth on which we reside. While the model developed and presented here is still quite a ways off from this goal, the first steps have been made. Our need to understand, to describe, predict and ultimately take charge of the world around us, for better or worse, is perhaps the most uniquely human characteristic. As such, I find building a model of the geosphere a basic research pursuit and an intrinsically worthwhile goal.

In my work, I focus chiefly on one particular step in the long journey from first principles to a comprehensive ESM: the coupling of the atmosphere and ocean models at their interface. Building on existing and well proven models of atmosphere and ocean, this is the next important piece of the puzzle. For exchanges on timescales of seconds to centuries the world oceans are the largest reservoir of heat, water, and carbon in the climate system, by orders of magnitude. The fluxes in and out of this gigantic reservoir have thus significant impact on the levels of heat, water, and carbon in the remaining spheres. The ocean itself is a mechanical engine driven by atmospheric winds at the top. The direction and strength of those winds in conjunction with ocean internal density gradients governs the oceans' circulation patters. These circulation patterns in turn modify the ability of the ocean to take up heat by breaking the stratification in key regions, connecting the voluminous deep ocean with the surface. In the other direction the ocean surface provides about 2/3 of the total lower boundary conditions for the atmosphere.

Simulating the exchange of heat, momentum, and mass as accurately as possible is thus imperative for a climate model that is to have a chance at making reliable and faithful climate predictions. It is under this premise that I first develop an interface based on previous AWI coupled climate models, and then reevaluate and refine it.

1.2 Objectives and Structure

The research presented in this thesis was conducted as part of the Deutsche Forschungsgemeinschaft (DFG) collaborative Research Center Transregio (TRR) 181 "Energy Transfers in Atmosphere and Ocean“. The overarching goals of this project are the development of energetically consistent mathematical tools for climate analysis and modelling. Within the TRR181 there exist several focus areas working on different scales, from millimeters to thousands of kilometers, and dealing with two domains, ocean and atmosphere. My personal contribution can be found at the large end of the scales and right at the interface between the two central climate model domains, atmosphere and ocean. Other model components included in the system I work on are those for the domains of sea ice and river runoff.

In chapter 2 of the thesis I will present the theories upon which the implementation of the coupled model and its core component rests. I outline the basic principles behind the numerical implementation of the interconnected components in the coupled climate model. I particularly focus on the implications for energy transfers and energy sources and sinks, which are investigated in neighbouring topics under the TRR 181 umbrella. The second section of the theories chapter is on the coupling itself, considerations of information conservation, spatial remapping, and the time averaging.

Chapter 3 mainly consists of a previously published scientific article entitled "AWI-CM3 coupled climate model: description and evaluation experiments for a prototype post-CMIP6 model". The chapter contains the bulk of the implementation work. Some details of the work that went into this first published version of the model were, for brevity sake, left out of the scientific article. They concern the implementation of the new sea ice surface thermodynamics scheme, and are presented in the later section 5.1 instead.

Chapter 4 contains considerations on the condensation of complex information into easy to grasp and interpret forms to evaluate and further improve climate models. With the development and application of a system as complex as a

Coupled Climate or Earth System Model, the number degrees of freedom is too large, and non-linear interactions are too plentiful for any one researcher to have a comprehensive overview based on raw model data. The chapter contains a short manuscript on one tool for information condensation which I submitted to the Journal of Open Research Software under the title "Climate Model Performance Index (CMPI) toolbox".

As mentioned before chapter 5 starts with the implementation of new sea ice thermodynamics, which was prompted by errors found in an ensemble Kalman filer data assimilation variant of AWI-CM3. What follows is a description and evaluation of collection of improvements to the physical fluxes send between the atmosphere, ocean, and sea ice. The fluxes in question are the enthalpy of snow falling into the open ocean, a heat flux from precipitation temperature, a heat flux from snow falling on glaciers simulated as quasi-icebergs, and ocean current feedback to the atmosphere. The chapter ends with the introduction of stochastic coupling processes, developed to better represent the real model uncertainties and limitations.

I close this thesis in chapter 6 with a summary and a discussion of questions that appeared and still remain open for exploration, as well as giving an overview over planned developments to turn AWI-CM3 into the more comprehensive AWI-ESM3.

Chapter 2

Theory

"Nothing is particularly hard,
if you divide it into small jobs."
-Henry Ford

2.1 Fundamentals of Earth System Modelling

In its Platonic form, earth system modelling places a system boundary between earth and space; today we typically mean between the mesosphere and thermosphere, at about 85km above sea level. Everything found inside the system we call the geosphere, which shall ideally be simulated by the model. Everything outside is considered forcing and thus prescribed. Separation of concerns has sensibly led to the Earth System being subdivided before any discretisation is attempted. There are numerous conventions for the decision regarding which parts of the geosphere deserve their own model. A none exhaustive list includes atmosphere, hydrosphere, cryosphere, biosphere and lithosphere. These spheres can then be further subdivided into atmospheric dynamics and atmospheric chemistry, physical oceanography and river modelling, land and sea ice, ocean biogeochemistry and vegetation modelling, and last but not least the anthroposphere. Many more subdivisions are possible and their implementation is left to the digression of the individual researcher or research group.

2.1.1 Thermodynamic Models

Although the final goal may be the creation of a comprehensive model of the entire geosphere, such a model has a large number of degrees of freedom. The model would be able to predict all sorts of states, but it can also make all sorts of errors. Instead of addressing the whole breadth of processes right away, earth system modellers start with simpler models, and consider parts of the earth system as outside of the system boundaries. Figure 2.1 provides an overview of commonly used climate model types, their comprehensiveness and complexity. Historically, the first part of the earth system that researchers created high complexity models for was the atmospheric dynamics, as these noticeably affect our day to day lives in ways that other spheres generally do not. For such a model, the system boundaries lie at the mesosphere at the top, where long and shortwave radiation are exchanged with outer space, and at the boundary between gaseous air and liquid water or solid ground at the bottom. Furthermore, there are massive internal simplifications, such as modelling an atmosphere that contains only an ideal gas and water, rather than the thousands of trace gases and aerosols that are present in the real atmosphere.

In the following I will introduce atmospheric models of increasing complexity, until I arrive at GCMs used throughout the rest of this study. The separation of different types of atmospheric models can be made along a variety of axis. I can divide, for example, into diagnostic (analysis of state t_n) or prognostic (prediction of state t_{n+1}) models. Other possible distinctions are thermodynamic or dynamic models as well as by number of simulated physical dimensions.

Figure 2.1: **Chart of model complexity against comprehensiveness adapted from Houghton et al. (1997). The simplest models are Energy Balance Models (EBM), that are highly idealized representations of one climate sphere. Connecting multiple such EBMs we can build Box Models. With quasi-geostrophic models 3D dynamics nearly reduced to the (geostrophic) balance of pressure gradient and Coriolis force can be included. Connecting quasi-geostrophic balance models with equally simple ice sheet, dynamic vegetation, and chemistry models leads to a class of comprehensive Earth system Models of Intermediate Complexity (EMIC). Even full Earth System Models (ESM) typically have to make some compromise in reducing complexity of the included Atmospheric General Circulation (AGCM) and Ocean General Circulation (OGCM) Models, because the inclusion of ocean biogeochemistry and atmospheric chemistry increases the computational costs of running GCMs manifold. Atmospheric Oceanic General Circulation Models (AOGCM) are frequently used as a trade-off between complexity and comprehensiveness. All of these model types have their place in addressing different research questions.**

0D EBM Having simplified from the full geosphere to the atmosphere, we can start to find mathematical expressions for its behaviour. The most basic model we can construct is a zero dimensional one, where the atmosphere and its upper and lower boundary are all represented by a single dot. From the ratio of the unidirectional incoming shortwave (solar) radiation over the shadow area of Earth

$$Q_{swi} = \pi R^2 S \tag{2.1}$$

to the reflected shortwave radiation

$$Q_{swr} = \pi R^2 S \alpha \tag{2.2}$$

plus the omnidirectional outgoing longwave radiation

$$Q_{lwo} = 4\pi R^2 \epsilon \sigma T_s^4 \tag{2.3}$$

we can obtain the planetary energy balance for Earth from $Q_{swi} - Q_{swr} - Q_{lwo} = 0$:

$$\epsilon \sigma T_s^4 = \frac{S(1-\alpha)}{4} \tag{2.4}$$

In the energy balance equation 2.4, the Earths radius R has cancelled out, leaving the balance dependent only on the emissivity ϵ, a measure of how effective of a black body the Earth is over the range of wavelengths in which it is emitting radiation, the Stefan-Boltzmann constant $\sigma = 5.67 \cdot 10^8 \frac{W}{m^2 K^4}$, the mean surface temperature T_s, the solar constant $S \approx 1361 \frac{W}{m^2}$ (Prša et al., 2016), and the planetary albedo α as the average reflectivity of Earth's surface looking down from space. For this model one makes the implicit assumption of a single temperature representing the whole planet, which in turn neglects the meridional and diurnal gradients (Lohmann, 2020). Using the observed mean surface temperature ($T_s \approx 287\,K$) and the planetary albedo of Earth $\alpha \approx 0.3$ (Stephens et al., 2015), we can solve for the emissivity and obtain $\epsilon = 0.8$. One can now in turn solve the model for T_s, and observe how it reacts to changes in emissivity, for example through shifts in greenhouse gas concentrations, or to changes in the planetary albedo, for example through increase in stratospheric sulfur dioxide after a major volcanic eruption.

1D EBM For the next step up in model complexity one can create multiple linked energy balance models, for example one for the atmosphere and one for the ocean, or one for every 10° latitude band, as done by Arrhenius (1896) in his seminal paper, for the first time quantifying the greenhouse gas effect on surface temperature. Connecting the heat content within each latitude band using a diffusive flux with shape:

$$Q_d = -K_d \frac{dT}{dx} \tag{2.5}$$

where the heat flux Q_d depends on the diffusivity of the climate system K_d and is downgradient with respect to temperature. With increasing complexity of the model, there is no longer the one correct way to create a climate model. It is up to the model developer to decide whether, for example, a 1D EBM is good enough with constant albedo over the latitude bands, or if the natural variation of albedo observed in the real world should be included in the model itself. One step further and the albedo could be made to depend on the simulated surface temperature in a latitude band and the diffusion be made dependent on the size of said band. Another adaptation might be the stochastic inclusion of clouds and their interaction with radiative processes.

The degree of choice over which processes to resolve, to parameterize, to use as forcing, and which to ignore only grows as the models become more complex.

2.1.2 Dynamic Models

While the earth system is fundamentally driven by radiation, dynamic energy transports play a large role in determining global and local climate and heat storage. Models targeting the full three dimensions of space typically represent the fluid dynamics not just with diffusive terms but with some form of the momentum equations for fluid flow.

3D momentum equations Following Holton (1973) we can write Newtons second law for motion such that the acceleration depends on the Coriolis force, the pressure gradient force, gravity, and friction while dividing out mass as:

$$\frac{D\mathbf{U}}{Dt} = -2\mathbf{\Omega} \times \mathbf{U} - \frac{1}{\rho}\nabla p + \mathbf{g} + \mathbf{F}_r \tag{2.6}$$

With the spherical assumption we can split equation 2.6 into the zonal (u,x), meridional (v,y) and vertical (w,z) momentum equations and obtain:

$$\frac{Du}{Dt} - \frac{uv\,tan\phi}{a} + \frac{uw}{a} = -\frac{1}{\rho}\frac{\partial p}{\partial x} + \Omega v\,sin\phi - \Omega w\,cos\phi + F_{rx} \tag{2.7}$$

$$\frac{Dv}{Dt} + \frac{u^2\,tan\phi}{a} + \frac{vw}{a} = -\frac{1}{\rho}\frac{\partial p}{\partial y} + \Omega u\,sin\phi + F_{ry} \tag{2.8}$$

$$\frac{Dw}{Dt} - \frac{u^2 + v^2}{a} = -\frac{1}{\rho}\frac{\partial p}{\partial z} - g + \Omega u\,cos\phi + F_{rz} \tag{2.9}$$

where ϕ is the latitude angle, a the Rossby number, $\Omega = 7.2921 \times 10^{-5}\frac{rad}{s}$ the rotation rate of the Earth, the gravitational force is g, the pressure p, and the density ρ. Naturally, every summand in these momentum equations has the same unit ($\frac{m}{s^2}$). Given observed characteristic lengths of typical fluid flow patterns as well as the associated fluid velocities we can obtain the approximate scale of each term. Note that for the horizontal equations 2.7 and 2.8 the scale flow patterns is not generally uniform throughout the atmosphere. One example for a scale analysis for mid latitude synoptic systems is given by Holton (1973):

Eq. 2.7	$\frac{Du}{Dt}$	$-2\Omega v \sin\phi$	$+2\Omega w \cos\phi$	$+\frac{uw}{a}$	$-\frac{uv\tan\phi}{a}$	$= -\frac{1}{\rho}\frac{\partial p}{\partial x}$	$+F_{rx}$
Eq. 2.8	$\frac{Dv}{Dt}$	$+2\Omega u \sin\phi$		$+\frac{vw}{a}$	$+\frac{u^2\tan\phi}{a}$	$= -\frac{1}{\rho}\frac{\partial p}{\partial y}$	$+F_{ry}$
$\frac{m}{s^2}$	10^{-4}	10^{-3}	10^{-6}	10^{-8}	10^{-5}	10^{-3}	10^{-12}

The balance of Coriolis force and horizontal pressure gradient force in two orders of magnitude larger than the next term, meaning that at large scales the horizontal momentum equations are dominated by this equilibrium. This so called geostrophic balance does not contain any time derivatives, meaning that geostrophic balance is a purely prognostic model.

In the same vein a scale analysis of the vertical momentum equation can be analysed, and again a dominant balance is revealed, this time between vertical pressure gradient force and gravity:

Eq. 2.9	$\frac{Dw}{Dt}$	$-2\Omega u \cos\phi$	$-\frac{u^2+v^2}{a}$	$= -\frac{1}{\rho}\frac{\partial p}{\partial z}$	$-g$	$+F_{rz}$
$\frac{m}{s^2}$	10^{-7}	10^{-3}	10^{-5}	10^{1}	10^{1}	10^{-15}

This particular balance is called the hydrostatic balance, and is much more dominant than geostrophic balance, at a prominence of four orders of magnitude of the next largest term.

Geostrohpic balance From here on out a variety of dynamical core formulations can be made, with the simplest one being the diagnostic geostrophic balance models. Planet Earths' surface experiences strong differences in absorbed surface solar shortwave radiation between equator and polar regions. This is partially due to differences in downward shortwave radiative flux and partially caused by different surface and cloud albedo. The outgoing longwave radiation is also higher at the equator than at the poles, but the difference is not as large as for the absorbed shortwave radiation. The sum of surface longwave plus shortwave radiation is on average positive at the equator and negative at the poles. The difference is balanced by atmospheric and oceanic meridional heat transports.

As air parcels near the surface at the equators are warmed up, they are becoming buoyant and rise up. Air parcels in the polar regions on the other hand cool down and sink. The sinking motion at the poles causes high surface pressure and low pressure at the top of the tropopause. Meanwhile the rising air masses at the equator cause lower surface air pressure and high pressure at height. The resulting horizontal restoring force towards equal pressures is called pressure gradient force.

If earth was an non-rotating system, the circulation resulting from absorption imbalances and pressure gradient force would form a single global convection cell wherein mean surface winds flow equators-wards at right angle to the equator, while winds at the top of the troposphere point in the opposite direction.

Earth of course is a rotating system, and thus air parcels flowing polewards from the equator at height start with an eastward velocity equal to the earths circumference divided by the length of a day $\frac{40{,}075km}{24h} \approx 1670\frac{km}{h}$. On its polarward track, the wind flows over a surface that has the same angular momentum as at the equator but with an eastward velocity of just $cos(\phi) \cdot 1670\frac{km}{h}$. The polarward flowing winds thus build up an eastwards velocity component relative to the surface.

Eventually, the eastward component is dominant and the wind direction is dominated by a balance between pressure gradient force and Coriolis force. The same happens in reverse to equatorward flow from the poles, which is deflected westwards. The poleward and eastward deflected air masses travel in zonal direction for so long, that they begin to cool down and sink. As shown in figure 2.2

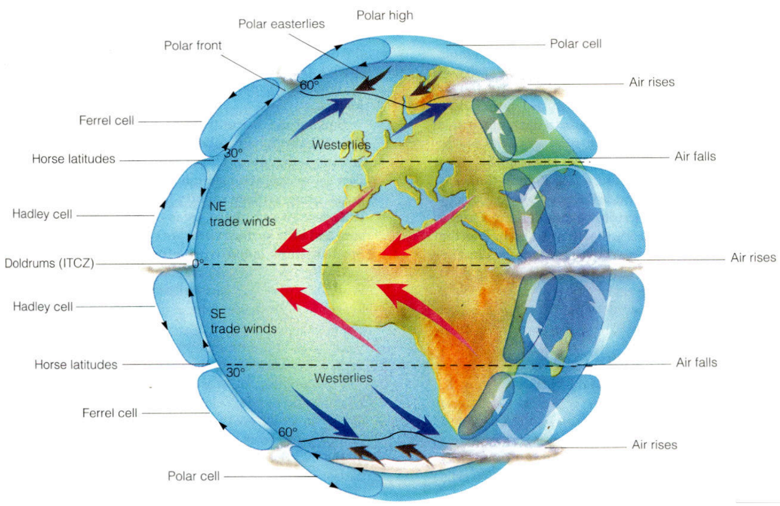

Figure 2.2: Atmospheric circulation cells resulting from the geostrophic balance of pressure gradient and Coriolis force. Graphic from Garrison (2012).

the now disconnected polar and equator (Hadley) cells flow in the same direction, spawning at least one counter rotating (Ferrell) cell in the mid latitudes. If Earth was larger or spinning faster, it could support a larger but always uneven number of cells in between, as for example the gas giants Saturn and Jupiter do.

Geostrophic models can also be constructed for the ocean, albeit with one additional term. For the ocean the Coriolis force is balanced by the sum of horizontal pressure gradient force and gravitational force acting upon density surfaces. While this makes the momentum flux equation more complex, geostrophic models are still important tools for research and understanding, the main body of work presented here deals with the coupling of two models with more complex dynamical cores.

Quasi-geostrophic models Quasi-geostrophic models are the next step up in sophistication of dynamics models and were the first type of predictive models solved with pen and paper by Exner (1908) and on the earliest electronic computers by Charney et al. (1950). For this class of models the causes of fluid parcel movement are reduced to small deviations from the geostrophic flow, caused by inertial terms in the Coriolis force. In modern research, quasi-geostrophic models can be found in EMICS such as LOVECLIM (Goosse et al., 2010) where the strong reduction in complexity of the governing equations combined with some predictive power strikes a good balance between computing cost and accuracy.

The scale analysis shows that if the research area is focused on large scale mid latitude dynamics the geostrophic assumption is reasonable, while polar dynamics, where Coriolis force direction changes, are not well captured. At the equator the Coriolis force, given by the sine of latitude becomes zero, which would imply infinite wind speeds, invalidating the assumption there. Subsequently, quasi-geostrophic models are not will suited to answer research questions that focus on these regions.

Primitive Equation Models For the most detailed description of the dynamics of ocean and atmosphere we use General Circulation Models (GCMs). GCMs, like quasi-geostrophic models, are based on the momentum equations, but are simplified to the primitive equations instead. In contrast to quasi-geostrophic models, the governing equations also allow for gravity waves, turbulence and frictional effects (Wallace and Hobbs, 2006).

The scale analysis by Holton (1973) shows that the hydrostatic assumption is valid globally when the horizontal model resolution is coarser than about 1km. While most atmospheric GCMs still use the hydrostatic approximation, some are starting to enter the realm of kilometer scale horizontal resolutions that put its continued use in question. AWI-CM3 however is foreseen to be used at 4.5 - 100 km in the atmosphere, where the hydrostatic approximation is acceptable. The full sets of primitive equations as solved in FESOM2 and OpenIFS can be found in Danilov et al. (2017) and ECMWF (2017a), respectively.

The vast majority of oceanic GCMs use the Boussinesq approximation by which density differences affect only gravitational, not inertial forces. As with other approximations, exceptions to the norm exist, with model codes written specifically study the effects that other models exclude (Auclair et al., 2018).

2.1.3 Parameterizations

Aside from the dynamical core of models, a plethora of subgrid-scale physics are implemented in GCMs, some of which are central to the work I show here. Parameterizations, while absolutely vital for approximating the effects of subgrid-scale physics onto resolved physics, are at the same time one of the largest sources of model error. As such, many climate or ESM developers will spend their time working on better parameterizations rather than numerical cores.

In the atmosphere, main examples include the radiation, turbulent transport, and interactions with the surface, subgrid-scale orographic drag, non-orographic gravity wave drag, convection, clouds and large-scale precipitation and more (ECMWF, 2017b). For ocean models main examples are vertical mixing (Scholz et al., 2022), sea ice thermodynamics (Zampieri et al., 2021b), surface wave (Roach et al., 2019) or the Gent-McWilliams parameterization of the impact that eddies have on the mean flow (Gent and Mcwilliams (1990)) in case the model is not eddy resolving. Additional parameterizations for surface flux coupling, river runoff, and icebergs sit right at the coupling interface.

2.2 Fundamentals of Model Domain Coupling

The separation of concerns between model spheres has allowed researches to improve the representation of processes that they are most knowledgeable about, without being impeded by overly complex software that simulates all manner of peripheral effects. Once development in one sphere is sufficiently advanced there is the chance to connect models into a larger system through a process called model coupling. The exact nature of the coupling is an optimization problem further discussed in the next section 2.2.1.

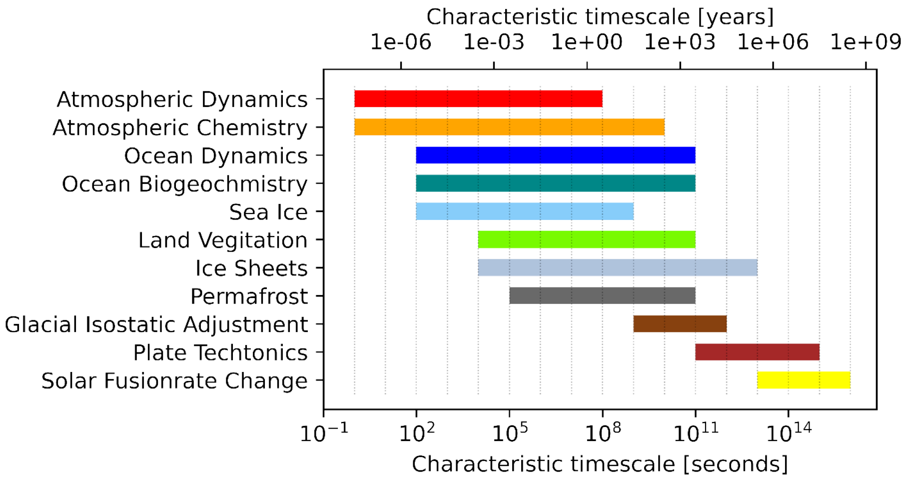

Figure 2.3: The approximate characteristic timescales of spheres typically modelled have wide ranges from seconds for the fastest modes in atmospheric and ocean dynamics, to a million years for the slowest modes of ice sheet accumulation (modified from Holbrook et al. (2019); Meehl et al. (2021); Lemke et al. (2007)). Even slower climate modes are carbon dioxide draw-down via enhanced chemical weathering from infrequent collision of continental tectonic plates (Ruddiman, 2008), or the gradual increase of solar energy from the sun (Gough, 1981). These effects are often omitted as they are not relevant to human or civilizational timescales. The timescales of the included effects play an important role in determining the optimal method of model coupling.

2.2.1 Depth of Integration

Below, I present my personal definition of four distinct levels of integrating model source codes with one another to achieve model coupling. If two components are in direct contact in the real world, then the level of similarity in their characteristic temporal scales, seen in figure 2.3, is a good indicator for the necessary depth of integration. Spheres that are close to (far from) one another in temporal scales benefit from tight (loose) integration.

Level Zero In the simplest case the model of a particular sphere can read from a hard-drive the output from another sphere and make a simulation without feeding back at all. I consider this level zero of model coupling with essentially no integration at all. Such forced model runs are frequently performed when the research focus is placed on the internal processes of the sphere in question, but forcings from another sphere cannot but fully ignored. Examples are plentiful and range from ocean modelling with atmospheric radiation, momentum and water flux forcing, modelling of the impact of precipitation and temperatures on crop yields, or ski tourism, to ice sheets forced by ocean temperature induced basal melting, and glacial isostatic adjustment forced by ice sheet geometry changes.

Level One At the first level integration depth the forcing through files read from disk can now happen both ways. Early coupled atmosphere ocean models would write their respective interface values onto disk, from where the other component would read them, for example once every simulated month. For AOGCMs running both ocean and atmosphere concurrently, such techniques, called offline coupling, are no longer common. They do however still find application for coupled models where components run on fairly different timescales. The method is used for example in AWI-ESM1 (Gierz et al., 2020) where a short period of atmosphere-ocean simulation is followed by a longer ice sheet simulation, on repeat. Coupling through files makes sense in this case, as the coupling happens relatively infrequently (e.g. once a year), and because the simulation speeds and timescales are quite different. As shown in figure 2.3, ice sheets grow and decay on timescales of millennia to millions of years, while atmosphere and oceans operate on timescales of minutes to millennia. The faster ice sheet surface mass balance happens on yearly and daily cycles, but is much quicker to solve than ocean or atmosphere dynamics. The turns the two models are taking can be of different length according to the characteristic timescales, a year for the AOGCM, followed by 100 years for the ice sheets.

Upsides of level one coupling are that it requires no intrusion into the source codes and allows for low idle time by reassigning the computational resources to match the requirements of each model in turn. Downsides are the slow data transfer and thus limited ability to couple at high time frequency. For use cases where frequent coupling is beneficial, the employment of higher coupling levels are advisable.

Level Two The most common level of model coupling is the level two (also called online or in Dynamic Random Access Memory (DRAM)) exchange of data between spheres. Within systems coupled in this fashion all contributing models are running concurrently, and information exchange is realized in DRAM, rather than via writing/reading to/from hard drive. This coupled model architecture allows for more frequent exchange of information, and is therefore well suited for the coupling of spheres with similar characteristic timescales. Typical processes included in an online coupled comprehensive ESM include the first six entries in figure 2.3.

To enable the exchange of information in DRAM, all component models have to be aware of one another while the simulation is ongoing. In modern coupled models this is typically done through the Message Passing Interface (MPI) (Walker and Dongarra, 1996). The use of MPI puts the climate researcher in close contact to the High Performance Computer (HPC) communication hardware. To ease the use of MPI for climate model development, a handful of interface software packages have been developed. The one I use for AWI-CM3, is OASIS (Craig et al., 2017a), earlier versions of which were used for the predecessor models AWI-CM & ESM 1 & 2. Other examples of such climate science specific interfaces on top of MPI include the Earth System Modeling Framework (ESMF) (Hill et al., 2004) and Yet Another Coupler (YAC) (Hanke et al., 2016).

The interface libraries also take care of the calculation of remapping weights for fields that shall be exchanged between the different models and their respective meshes. I will take an in depth look at some of the available options for remapping weight generation, as well as their respective advantages and disadvantages in section 5.6. Once a suitable set of weights for the matrix multiplication from source to target model has been obtained, the interface libraries ensure that every point on the source side of the exchange computes exactly the needed elements of the local target grid.

While it is possible, for any one model coupling, to write a simpler communication interface based on MPI, this is typically not done. Thanks to the more general formulation of libraries such as OASIS, ESMF and YAC, the addition of further climate spheres becomes possible without a major redevelopment of a bespoke coupling interface. Another reason handmade coupling interfaces are rare, is the lack of familiarity in the community. When a new colleague joins a team, onboarding is simpler with an interface already used by many other groups. Finally the major coupling libraries are maintained by experts at significant cost, but provided for free.

The downsides of level two coupling, are the need to implement an additional piece of code that serves as the interface to the coupling library into each model component, as well as the need to balance the runtimes of each component. If one model is slower than the others, the remaining models will idle in an MPI Barrier command waiting for the coupled simulation to be allowed to advance. For similar reasons level two coupling is ill-suited for the most accurate coupling time schemes as I will show in section 2.2.3.

Level Three At the third level of integration a component is included in the parent model as a library. The component is computed on the same numerical grid, evaluated in the same time loop, and coupling is as simple as a pointer onto the required field. Using libraries thus has obvious advantages and finds its use cases. The FESOM2 ocean circulation model includes the Icepack sea ice thermodynamics model as a library (Zampieri et al., 2021a). Curiously, there exists a parallel development at AWI and ECMWF that builds a coupled model based on IFS and FESOM2, wherein FESOM2 is included as a library in IFS. This parallel development is focused on the extreme right in the complexity vs. comprehensiveness chart figure 2.1.

Coupling at level three or above also enables the use of more accurate time-stepping schemes without idling resources, a point I will expand upon in section 2.2.3. Downsides are the loss of sphere optional meshes, or the need to build a coupling interface from scratch. In general the system will have reduced maintainability due to tighter integration. Level three coupling tends to suffer in overall model speed compared to level two, as all components run in sequence. Thus all component models need to scale to the full computational allocation for the entire system. Even if this state is reached, this typically demands higher investment in computational optimization, which under limited resources suggests less effort placed into model physics.

Level Four Finally, a process can be fully integrated within the model, without any ability to separate it out of the host model at all. Examples of such coupling include the wave model WAM hardwired into OpenIFS (Guenther et al., 1992) or the integration of the water isotope tracing model WISO into the atmospheric model ECHAM6 (Cauquoin et al., 2019). Sometimes separation, while possible, is just not envisioned, and direct integration at level four keeps the interface as simple as possible.

The advantages and disadvantages between level two and four are similar to those between level two and three. Additionally such codes are harder to understand, due to the lack of a clearly defined interface. It can, however, be easier to maintain a code base in which all model components are in sync if all of them are stored in the same source code repository.

2.2.2 Fields Exchanged Between Ocean and Atmosphere

After selecting a coupling integration depth, and inserting the necessary infrastructure to make the exchange of fields happen, the next step is an analysis of what information needs to be exchanged. Here I present such an analysis for the coupling between atmosphere and ocean.

In the real world, the relevant time and spatial scales are at the molecular level, were heat and momentum transfer at the interface result from individual particle collisions. The same is true for evaporation, which requires individual molecules to travel fast enough and in the right direction, overcoming vapor pressure, and escaping as a gas (Silberberg, 2006). Obviously an AOGCM cannot resolve every molecule at the air-sea interface, or even just molecular viscosity and diffusion. Instead of individual particle interactions mean flow rates per unit area (fluxes) are computed, using for example Monin-Obukhov similarity theory (Monin and

Obukhov, 1954) in IFS (ECMWF, 2017b), or a simpler bulk formula approach in the case of uncoupled FESOM2 simulations (Timmermann et al., 2009).

Monin-Obukhov theory is based on the assumption of scale invariance of atmospheric boundary layer turbulence, which allows the development of dimensionless similarity functions that relate the statistical properties of turbulence to surface and atmospheric conditions. The simpler bulk formulation meanwhile approximates the atmospheric boundary layer variables as a single value over height, rather than a similarity function.

There are three types of fluxes that need to be computed at the air-sea interface: momentum, heat, and mass. The fields required for the computation of surface fluxes are present partially on the ocean and partially on the atmosphere side. The next decision is thus where the flux computation shall take place: in the atmospheric model, in the ocean model, or in some new intermediate component.

In practice, the simplest, though not the only course of action, is to use the flux computation already implemented in the atmospheric model. This is mainly true because the surface radiative heat fluxes require 3D information about the clouds to be computed. In general, it is good practice to avoid coupling 3D data where possible, as doing so can increase the amount of data to be transferred by orders of magnitude.

Reusing the flux computation already existent in the atmosphere reduces the implementation cost. In the specific case of FESOM2 and OpenIFS, the flux computation in the atmospheric model using MOST is more sophisticated than that available inside FESOM2, further reinforcing the decision. Similar computational and implementation complexity considerations lead many coupled model developers to transfer the required scalar fields from the ocean to the atmospheric model. Consequently fluxes are coupled in the opposite direction, from the atmosphere to the ocean.

Ocean to Atmosphere Scalar Fields

The first order terms implemented for AWI-CM version 3.0 are found in figure 3.1. The main influence of the ocean surface-to-flux computation is encapsulated in just the sea surface temperature. Other first order terms, such as surface roughness, and related wave state would be important coupling fields. However, for AWI-CM3, these are already computed within IFS and do not need to be coupled. The diffuse ocean albedo is a second order coupling term in case the ocean model is run with bio-geochemistry or river sediments. In the AWI-CM3 versions built and documented in this work, neither is the case.

Over sea ice, the surface temperature plays the most important role as well. However, there are additional fields over sea ice that need to be exchanged. The sea ice concentration impacts the surface roughness selection in OpenIFS as well as the mixture of surfaces tile fractions. The sea ice albedo can change dramatically when sea ice meltponds are simulated, which is only parameterized in FESOM2, not in OpenIFS. Furthermore, the thickness of a possible snow layer on top of sea ice impacts both the albedo and surface roughness as well.

Another second order contribution to the flux computations comes from the ocean surface currents. Renault et al. (2016a) recently showed that inclusion of this effect has considerable impact on the simulation of eddy kinetic energy (EKE). It is one of the effects that will be examined further in section 5.2, as it was only implemented in version 3.1 of AWI-CM3.

Once the ocean surface fields are available on the atmospheric side, they are used to overwrite the existing fields that the model is either initialized with or retains from the previous coupling time step. For some fields this integration is seamless, and a simple overwrite is sufficient. In other cases, a degree of adaption to OpenIFS is needed. For example, the albedo values for sea ice coming from FESOM2 are broadband values. In other words, there is only one value per area and coupling time step. OpenIFS on the other hand computes the short wave radiation physics in six spectral bands ranging from infrared to ultraviolet. Sea ice has very different albedo in these bands, ranging from about 0.9 in the infrared to about 0.1 in the ultraviolet (Light et al., 2022). The broadband value thus has to be split into six spectral bands included in OpenIFS while the weighted sum of the spectral albedo equals the broad band value and fulfils physical limitations (0 <albedo< 1). The required implementation was developed within the EC-Earth community and is shown in figure 2.4.

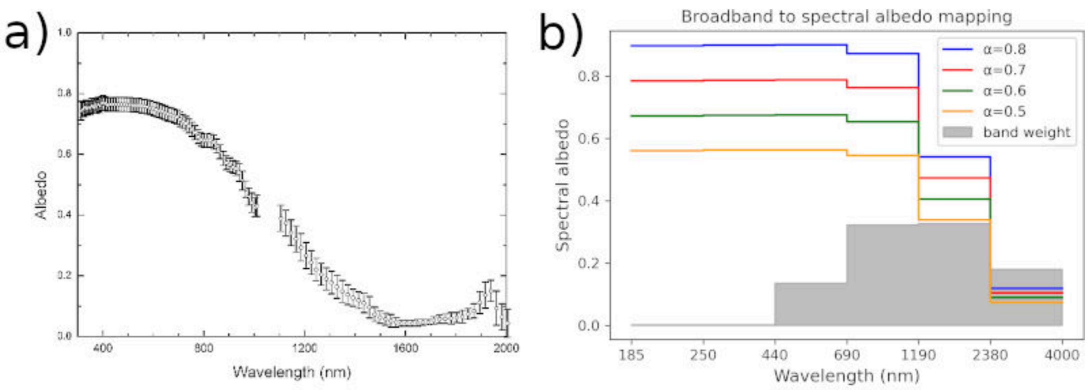

Figure 2.4: a) Dependence of sea ice broad band albedo on shortwave radiation wavelength (Perovich et al., 2002). b) Implementation of dependence originally developed by Klaus Wyser for IFS-NEMO coupling in EC-Earth, and reused for OpenIFS-FESOM. Four example broadband albedo values and their respective mappings are shown. The grey bars show the relative share of each wavelength band as a part of the total solar spectrum. The larger the grey bar, the more impact do albedo values in the band have on the broadband average.

After all the ocean and sea ice surface values have been used to overwrite the existing OpenIFS field values, as shown in appendix C.2, the fluxes can be computed and coupled.

Atmosphere to Ocean Flux Fields

Next, the computed fluxes from the assorted air-sea interface physics are assembled into the form that is required by the ocean model.

Thermal energy For AWI-CM3 v3.0 I send over the open ocean, a non combined non-solar heat flux Q_{ns}, consisting of the sum of the latent heat flux Q_{lat}, sensible heat flux Q_{se}, and longwave radiation Q_{lw}. The shortwave radiation Q_{sw} is sent as a separate field, as it will be allowed to partially penetrate the top most ocean layers and insert energy throughout the euphotic zone. Since the AOGCM AWI-CM3 does neither simulate nor gets forced with turbidity of water-masses it uses a constant thickness of 80 meters for the euphotic zone. The exact composition of Q_{lat} was refined in the process of this study. Section 5.2 provides detailed information on how the enthalpy of fusion is accounted for when snow falls into the open ocean, as well as the handling of rainfall that has a different temperature compared to the ocean surface. Over sea ice, all four thermal energy fluxes are added up and no shortwave penetration is simulated. The flux is multiplied by the sea ice mask, a process to be reversed on the ocean/sea ice side. Mask mismatch between the two models is one component of any residual thermal energy losses in the coupled model, even if conservative remapping is used.

Mechanical energy In contrast to the scalar thermal energy, transfer of momentum flux energy comes in tensor form. As the coupling libraries like OASIS3MCT do not support the remapping of tensors, I split the momentum flux tensor into its zonal M_x and meridional M_y component. The components M_x and M_y can be calculated based on 10 meter wind speeds and surface roughness, approximating ocean surface current velocity to 0. For better accuracy, the momentum flux calculated based on relative winds, including the consideration of ocean surface velocities, as detailed in section 5.2.

Water mass The final set of fluxes contains the water mass exchanges between ocean and atmosphere. First order terms comprise rainfall, snowfall, evaporation, and sublimation. Furthermore, a residual of precipitation - evaporation - soil water content over land needs to be routed from river basins to arrival points at the coast. As a second order term, AWI-CM3 v3.1 introduces a water mass flux of snow that falls onto glaciers. The idea, implementation and results are presented in detail in section 5.2 The assembled fluxes are interpolated to the ocean mesh and sent to the ocean model. In the case of AWI-CM3 with its level three coupling (compare 2.2.1) this communication is performed in memory through MPI, using the Model Coupling Toolkit (MCT) underneath OASIS3MCT.

2.2.3 Coupling Time Schemes

While in the real world coupling physics happen continuously in time, for our simulated coupling we must choose a finite coupling frequency. For model spheres operating on similar time scales, such as atmosphere and ocean boundary layers, the coupling frequency should be close to the model discretisation time step lengths, to avoid gross errors, such as smoothing over the diurnal cycle. Typical frequencies found in modern climate models range from a few seconds for the highest resolution setups up to six hours.

Ideally the coupling physics should be solved as an iterative system where ocean surface conditions, atmosphere lower boundary conditions, and fluxes converge towards a single solution. Such a time scheme has recently been implemented by Marti et al. (2021) and is shown in figure 2.5c). While this time scheme is as close as the system can be to the real world, it requires all equations to be solved many times over for a single time step, resulting in high investment of computational resources. Given finite resources, iterative coupling necessarily results in cutting corners elsewhere, for example by reduced spacial resolution or less complex physics parameterizations. As such, the selection of a suitable time stepping scheme is a cost optimization problem that seeks to minimize the errors caused by limited temporal coupling, spatial resolution as well as limited model complexity.

In consequence, the majority of climate models use what Marti et al. (2021) call parallel coupling (figure 2.5a)), where both atmosphere and ocean solve their respective equations at the current time step t using the interface values from the previous time step. The state vector of the atmosphere A at time step t is calculated using atmospheric contributions from time step t and ocean contributions from time step $t - \Delta t$. However the fluxes f received by the ocean at time t are computed in the atmosphere at time step $t - \Delta t$ based on the ocean surface values from $t - 2\Delta t$. This double time delay leads to larger model errors compared to the iterative and sequential schemes.

Sequential coupling is also frequently found, especially for level three and four coupling. As shown by Marti et al. (2021), sequential coupling is very close in terms of model error to iterative coupling with full convergence. Why then do many climate models use parallel coupling? While coupling level three strikes a great balance between keeping code bases apart and simple on the one hand and coupling frequency high on the other, it is uniquely ill suited for sequential coupling. All models in a level two coupling run at the same time, in the same computational allocation of resources, but on strictly separate cores. Sequential coupling necessitates models waiting for the other spheres. For level three coupling, the computational resources sit idle while doing so. In contrast for level one coupling, separate computational allocations are used allowing for the unused resources to be reused by other jobs. For level three and four coupling the same cores run all model components, again allowing for efficient use of the resources.

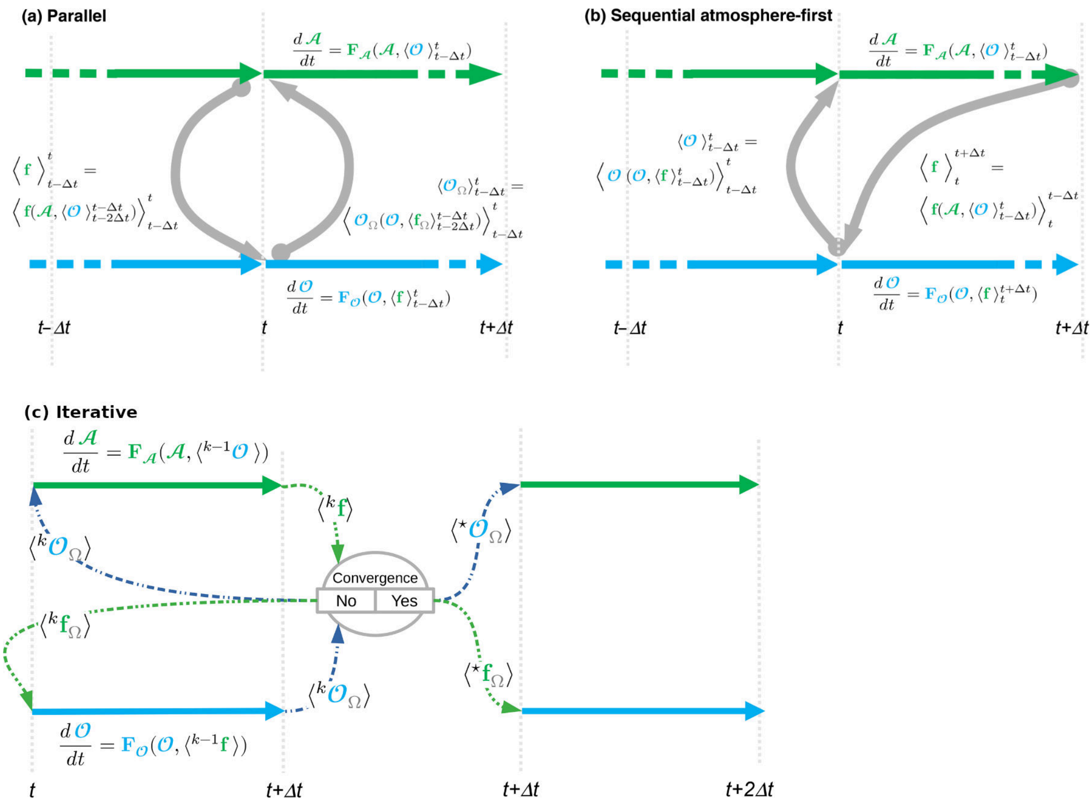

Figure 2.5: a) Parallel coupling: The atmosphere surface state update $\frac{dA}{dt}$ is computed based on ocean values from time step $t - \Delta t$. The ocean surface surface state update $\frac{dO}{dt}$ is based on fluxes f computed in the atmosphere at time step $t - \Delta t$ in turn using the ocean surface values from $t - 2\Delta t$. b) Sequential atmosphere-first coupling: The atmosphere still computes the surface based on values t for its own sphere, and $t - \Delta t$ for the ocean. The ocean meanwhile waits, and only starts computing its surface update for time t once the fluxes computed for t in the atmosphere become available. c) Schwartz iterative where both models start with method b), check for convergence and update both internal and coupled values with each subsequent iteration. Only once convergence is reached does the model integration move forward to the next time step. Graphic from Marti et al. (2021).

Chapter 3

Model Description and Evaluation

"The true test of a model is not how well it fits the data, but how well it predicts the future."

-ChatGPT

The contents of this chapter have been published under peer review as Streffing et al. (2022) in the journal Geoscientific Model Development. Reproduction as part of this thesis is permitted by the publisher under Creative Commons Attribution 4.0 License. Some of the content of the later section 5 was already included in the model presented here, but had but cut from the journal article for brevity sake.

3.1 Introduction

The evolution of coupled climate models between phases of the Coupled Model Intercomparison Project (CMIP) is advancing our ability to simulate the Earth's climate and to quantify humankind's past and future impact.

The Alfred Wegener Institute (AWI) contributed to CMIP6 with the Atmosphere-Ocean General Circulation Model (AOGCM) AWI-CM1.1-MR (Semmler et al., 2020) as well as the Earth System Model (ESM) AWI-ESM1.1-LR (Danek et al., 2020), built upon AWI-CM1 through using an additional dynamic vegetation module. The AOGCM version also contributed to the HighResMIP of CMIP6 (Rackow et al., 2022) with AWI-CM1.1-LR and AWI-CM1.1-HR.

Experience from HighResMIP shows that, with respect to model accuracy, high resolution climate models are about one CMIP generation ahead of their standard resolution counterparts (Bock et al., 2020). Moreover, atmospheric modeling studies indicate that a number of key processes ranging from orographic drag (Pithan et al., 2016) to atmospheric blocking (Schiemann et al., 2017; Davini et al., 2017), storm tracks (Willison et al., 2015; Baker et al., 2019), precipitation (van Haren et al., 2015), as well as mean sea level pressure (Hertwig et al., 2015), can be improved by increased horizontal resolution. In many of these cases the operational resolutions of the current NWP systems (10km) would be sufficient, but are often not reached by climate models running more commonly at 100km resolution, due to computational cost and time-to-solution limitations.

While the scientific evaluation of CMIP6 is still ongoing, we turn our attention to lessons learned and begin the development of our next-generation climate model. Our CMIP6 model, AWI-CM1, has reached the limits of scalability, both in the design of its numerical cores, and in the peripheries, such as data structures, and IO schemes. As a first step forward, AWI embarked on a mission to create a FESOM version 2.0 with a finite volume numerical core instead of finite elements (Danilov et al., 2017; Scholz et al., 2019; Koldunov et al., 2019a). In the vertical dimension the Arbitrary Lagrangian Eulerian (ALE) framework in FESOM2 allows the vertical grids to follow the isopycnals with reduced numerical mixing and to follow bottom topography with improved representation of bottom boundary layers. FESOM2 thus bears resemblance to the MPAS model described by Petersen et al. (2015). Following the development of FESOM2, a new climate model was assembled, coupling this upgraded ocean model with the same atmospheric model as before, ECHAM6 (Sidorenko et al., 2019). This model, dubbed AWI-CM2, is however practically limited to an atmospheric resolution of about

100 km grid spacing, with an absolute upper limit of 50 km.

Highly relevant atmosphere-ocean coupled processes such as local energy transfer, ocean warm layer formation, and diurnal cycles require not only high resolution in the ocean component, but an atmosphere that can adequately react to the ocean in an eddying regime (Ma et al., 2016; Renault et al., 2016a). We therefore couple FESOM2 to the OpenIFS atmospheric model to develop our new AOGCM AWI-CM3. OpenIFS is based on the Integrated Forecasting System (IFS) numerical weather prediction suite. IFS and OpenIFS are highly scalable and have been used in the Centre of Excellence in Simulation of Weather and Climate in Europe (ESiWACE) (Zeman et al., 2021). They constitute the highest atmospheric resolution contribution to HighResMIP (Haarsma et al., 2016), and have a long history of experimental (Jung et al., 2012) and operational (Malardel et al., 2016) high resolution atmospheric modelling.

While it might be tempting to apply the coupled model at the highest possible spatial resolution right from the start, cost and time considerations dictate that initial development and evaluation best be done at lower resolution. Furthermore many future applications of AWI-CM3, especially as the basis for a paleoclimate-capable full Earth System Model (ESM), will likely not employ particularly high resolutions, due to long simulation periods and/or a large number of tracers. Finally, conducting this first model development phase at relatively low resolutions enables a fair comparison between this model and the old AWI-CM1.1, as well as other well-established climate models. We therefore present in detail the capabilities and scientific applicability of the lower-resolution AWI-CM3 here, with a glance at its higher-resolution performance. What we consider low resolution for the OpenIFS atmosphere TCo159L91 (61km) is already beyond the practical limits of our previous AWI-CM1 and AWI-CM2 models with ECHAM6 (100 km). The higher resolution simulation that we briefly touch on features a TCo319L137 (31km) atmosphere as well as a 5-27km ocean, making the simulation more finely resolved than the HighResMIP contribution with AWI-CM1.1 HR.

3.2 Model Components

The AWI-CM3 coupled system encompasses two major components with the atmosphere (OpenIFS) and ocean (FESOM2), as well as an auxiliary component, the runoff mapper. The fourth component (XIOS), running in parallel, handles the output from the atmospheric model.

3.2.1 OpenIFS 43R3 Atmosphere

For its atmospheric component AWI-CM3 uses OpenIFS, which is based on ECMWF's Integrated Forecast System (IFS) (ECMWF, 2017a,b,c). With the readily available OpenIFS, ECMWF aims to provide cutting-edge performance from the world of operational numerical weather forecasting to the research community, while

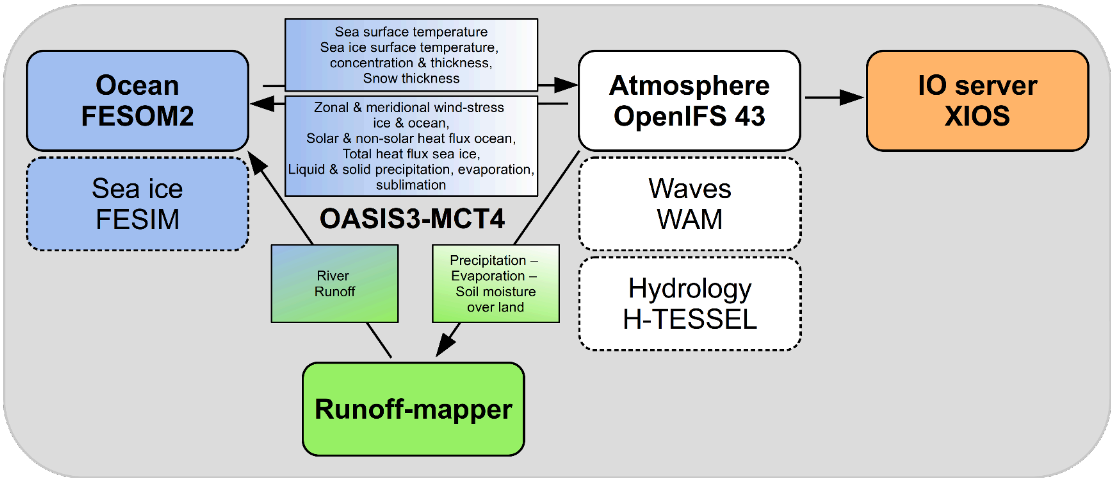

Figure 3.1: Schematic of the coupling between AWI-CM3 model components. Two hourly parallel communication in AWI-CM3 is implemented via the OASIS3-MCT 4.0 library. Heat, mass and momentum fluxes are sent from OpenIFS to FESOM2, while ocean and ice surface state variables are sent back. The precipitation minus evaporation over land is handled with a runoff mapper that generates river runoff at basin discharge points. OpenIFS output is written in parallel with optional online postprocessing via XIOS.

in turn presenting a testbed for developments that can feed back into weather forecasting.

As such, OpenIFS contains the hydrostatic dynamical core, the physical parameterizations, as well as the H-TESSEL hydrology model (Balsamo et al., 2009) and the WAM wave model (Komen et al., 1996) from the ECMWF IFS suite. The two-way OpenIFS-WAM coupling makes the surface roughness calculation dependent on the wave state, which in turn influences the calculation of momentum and sensible heat fluxes. WAM wave fields are currently not directly coupled to FESOM2 for e.g. wave induced vertical mixing calculations. H-TESSEL provides column model type soil moisture computations, while horizontal water transport on land is simulated using a separate runoff-mapper, as shown in figure 3.1. In contrast to the operational IFS NWP system, the 4D-var data assimilation, the non-hydrostatic core, the adjoint/tangent-linear versions, the Meteo France IO server, and the subroutine level implementation of the NEMO ocean model have been removed from OpenIFS.

The defining feature of the OpenIFS numerical core is its semi-Lagrangian (Ritchie et al., 1995) semi-implicit (Robert et al., 1972) advection scheme (Ritchie, 1987; Ritchie et al., 1995), which allows for advection distances in excess of the Courant–Friedrichs–Lewy (CFL) condition. At the same grid resolution and with the same characteristic fluid velocities this permits OpenIFS simulations to be numerically stable at much longer time steps than equivalent Eulerian integrations. What the model saves in terms of computing resources can be invested instead into higher model resolution, larger ensembles or longer simulations. We use the cycle

43R3V1 version of OpenIFS released in September 2020, that is based on IFS CY43R3, which constituted the operational NWP system at ECMWF between July 2017 and June 2018. In contrast to ECHAM6, OpenIFS allows for the use of both full and reduced Gaussian grids (Hortal and Simmons, 1991), thus reducing grid cell shape distortion near the poles.

OpenIFS is available at a wide variety of horizontal resolutions, ranging from a TQ21 (626km) toy model to the TCo1279 (9km) operational NWP. Even higher experimental horizontal resolutions require only minor source code changes. Three options exist for the representation of highest (truncation) resolution spherical harmonics in grid point space. The linear truncation TL grids with two gridpoints for the smallest spherical harmonics, the quadratic TQ with three and the cubic octahedral TCo with four grid points (Malardel et al., 2016). Of these, the TCo grids are the most accurate and applicable to coupled climate simulations, as the coupling takes place in grid point space. The vertical resolution choice is much more limited than the horizontal one, as each horizontal resolution is typically paired with one optimal vertical resolution, for which the model parameterizations have been tuned.

The main experiments we present were performed at a resolution of TCo159 (61km) with 91 vertical layers (TCo159L91), with some experiments at TCo319L137 (31km). Further resolutions we successfully tested computationally are TCo95L91 (100km) and TCo639L137 (16km). All grids have a ceiling pressure level of 0.01 hPa, with the L137 grids resolving the vertical space in between more finely than the L91 grids.

3.2.2 FESOM2 Ocean

The ocean dynamics of AWI-CM3 are simulated by the Finite volumE Sea ice Ocean Model (FESOM2), the second version of the global unstructured-mesh ocean model developed at AWI (Danilov et al., 2017).

FESOM2 is formulated with a finite volume dynamical core using ALE vertical coordinates. FESOM2 is a global unstructured-mesh ocean model that has computational performance comparable to structured-mesh models. Unstructured meshes allow for local mesh refinements without sharp resolution boundaries, as encountered by classical nesting models. In practice, the mesh can be designed to follow the patterns of local sea surface height variability or to scale corresponding to the local Rossby radius of deformation (Sein et al., 2017). FESOM2 contains the embedded FESIM sea ice model (Danilov et al., 2015). For the coupled model presented here, FESIM was modified such that it calculates prognostically the sea ice surface temperature, while in the previous AOGCMs AWI-CM1 and AWI-CM2 this computation was performed in the atmospheric component.

For the experiments presented here we employ a mesh called CORE2, which has about 127k surface nodes, as shown in Koldunov et al. (2019a). The mesh has 47 vertical layers and horizontal resolution varying from 25 to 125 km depending on latitude and distance to coastlines. We tested a second mesh called DART with shorter simulations. The DART mesh has 3.1 million surface nodes with 80 vertical layers and horizontal resolution of 5 to 27km. We show the spacial distribution of horizontal resolution for both meshes in Figure 3.2. In the vertical, for the first two layers of both meshes have 5 meters resolution, and subsequent layers are in 10 meter intervals till 100 meters depth. Below 100 meters depth the CORE2 vertical resolution decreases downwards more rapidly than the DART resolution.

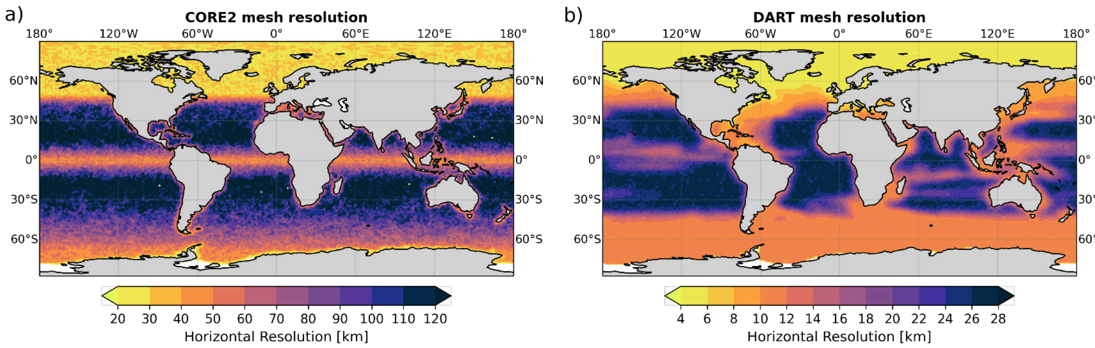

Figure 3.2: a) Horizontal resolution of the CORE2 mesh used for the main simulations presented in this work. b) As a) but for the DART mesh with higher resolution, which is based on a mix of local Rossby radius of deformation and local sea surface height variability. The DART mesh is used in Section 3.5.1 for an outlook of high resolution applications.

The low-resolution CORE2 mesh for FESOM2 is not eddy-resolving, and we employ the Gent-McWilliams (GM) parameterization to include the effect of mesoscale eddies on temperature, salinity and tracers (Gent and Mcwilliams, 1990). For all runs presented here, FESOM2 was configured with the ”zstar” vertical coordinate, where the total change in sea surface height is distributed over all layers in the vertical, except the partial cell layer at the bottom (Scholz et al., 2019). Such a vertical setup reduces erroneous numerical mixing in the vertical (Adcroft and Campin, 2004). Parameterization of physical vertical mixing is achieved via the K-Profile Parameterization (KPP) scheme after Large et al. (1994). In the Southern Ocean we additionally apply vertical mixing within the Monin–Obukhov length scale calculated based on heat flux, freshwater flux, wind stress, sea ice concentration and sea ice velocity, as developed by Timmermann and Beckmann (2004a) based on Lemke (1987). For the horizontal viscosity, FESOM2 applies the kinematic backscatter scheme of Juricke et al. (2020) with a backscatter coefficient of 1.5. This scheme dissipates kinetic energy on small scales, but reinjects kinetic energy on large scales, resulting in an overall reduced dissipation. Detailed information on the available mixing scheme options in FESOM2 can be found in Scholz et al. (2022). For the experiments shown below, the net evaporation - precipitation - runoff (E-P-R) integrated over the global ocean is forced to 0 at each time step by subtracting the residual.

The FESIM sea ice model is integrated directly in FESOM2 source code on a module level. The sea ice computations are done on the ocean surface grid and the dynamics use an adaptive elastic-viscous-plastic solver (Kimmritz et al., 2016; Koldunov et al., 2019b). For the thermodynamics FESIM implements a 0-layer scheme after Parkinson and Washington (1979). The standalone ocean model FESOM2 allows for the optional use of the Icepack sea ice thermodynamics module (Hunke et al., 2020; Zampieri et al., 2021b), representing a potential future upgrade for AWI-CM3.

Bodies of water that are cut off by land from the world oceans, such as the Caspian Sea and the Great Lakes are not simulated via FESOM2, but are included as lakes via the OpenIFS lake module.

For the low-resolution CORE2 mesh in particular, several ocean basins with narrow outflow channels are not included. These are: the White Sea, Persian Gulf, Black Sea, and the Gulf of Ob. Such narrow inlets on a coarse mesh would reduce the smallest horizontal grid spacing, and thus incur a smaller time step in order to still fulfill the CFL condition globally. The higher resolution DART mesh does not omit these basins.

3.2.3 Runoff-mapper

In addition to the two major components, AWI-CM3 includes a river routing scheme. It receives from OpenIFS the difference between precipitation, evaporation and soil moisture over land (P-E-S), and uses a map of river basins to deliver the water to discharge points along the coastline. The current river routing component has no water storage and thus acts instantaneously. Separation of the routing component from the atmosphere and ocean is a design decision shared with EC-Earth, where the flexibility and ease of modification are core ideas. This design keeps open the option of swiftly replacing the basic runoff mapper with a more sophisticated hydrological model, such as mHM (Samaniego et al., 2010) or CaMa Flood (Yamazaki et al., 2011) in the future.

3.2.4 XIOS parallel IO server

The fourth model component of AWI-CM3 is a technical helper. ECMWF removes the parallel IO server developed by Meteo France for IFS when generating a new release of OpenIFS. This leaves OpenIFS with only the possibility to provide sequentially written GRIB file output.

While this sequential IO scheme has been used, for example, by Döscher et al. (2021), it can often reach data-throughput limits in practical applications. Furthermore, while GRIB files are common in the NWP community, the climate modelling community often uses NetCDF files. Thus, the sequential output has to be converted for most analysis tools after each simulation.

With increasing model resolution and improved use of MPI/OMP hybrid parallelization, the sequential IO overhead constitutes an ever-growing fraction of the computational cost of running OpenIFS. Recently Yepes-Arbós et al. (2021) implemented the parallel XML Input/Output Server (XIOS) 2.5 into OpenIFS for this reason, and we make use of it for AWI-CM3 to reduce the computational cost and increase the integration speed.

While XIOS takes the file writing out of the critical path of the simulation, the overhead cost of XIOS is non-zero. The main reason is that XIOS works only in grid point space, and therefore requires spectral fields to be transformed inside OpenIFS before they can be sent to XIOS for writing. Nevertheless it provides a significant reduction of computing cost, as shown in table 3.1. Furthermore, XIOS enables online data postprocessing, such as vertical and horizontal interpolation, as well as temporal operators for maximum, minimum, mean etc. In doing so, XIOS reduces the number of times that files have to be written and read from disk, saving storage space, and reducing the number of job steps in the work flow. Finally XIOS allows for output directly in NetCDF, facilitating the use of AWI-CM3 model output.

FESOM2 contains its own bespoke parallel IO routines and the integration of an external dedicated IO Library is currently not envisioned.

3.3 Coupled Model Description

The coupled climate model is constructed by combining and building on the approaches of Hazeleger et al. (2010) and Sidorenko et al. (2015). The OpenIFS version 43R3 is common between a number of AOGCMs and ESMs with regular ocean grids currently under development, including EC-Earth4 of the EC-Earth consortium and GEOMAR's FOCI-OpenIFS (Kjellsson et al., 2020). Indeed the basic functionality of the coupling interface, as well as the future ESM component integration will be shared between EC-Earth4 and AWI-CM3. Nevertheless, some differences in the coupling strategy exist, and the setup developed for AWI-CM3 shall be detailed further here.

The ESM-Tools (version 3) infrastructure software (Barbi et al., 2021) was used to manage the configuration, compiling, and runtime-scripts of the coupled model, as well as to ensure simulation reproducibility.

3.3.1 Coupling strategy

The surface heat, mass and momentum fluxes are calculated within OpenIFS and supplied to FESOM2. Here the state variables for ocean and sea ice surface are updated accordingly. The runoff-mapper calculates its river routing after the atmosphere component computes and provides the P - E over land for a given coupling time step.

We employ so called concurrent coupling, with surface condition updates that are considered to be numerically independent between ocean and atmosphere. The temporal exchange of the ocean and atmosphere surface conditions is taking place at the least common multiple of the ocean and atmosphere time steps. For the TCo159L91-CORE2 simulations the time steps for coupling, the atmospheric model and the oceanic model are 120, 60 and 40 minutes respectively, while for the TCo319L137-DART simulation they are 60, 15 and 4 minutes. In the production mode both the atmosphere and ocean components compute their own surface update at time t_n based on time lagged information at t_{n-1} of the other component. The physical inconsistencies resulting from this double-sided-lag method are small compared to those stemming from e.g. spatial and temporal truncation and are generally accepted in the climate modelling community, as they allow for parallel execution of model components (Lemarié et al., 2015; Marti et al., 2021).

AWI-CM3 can also be run in a sequential atmosphere-first mode, updating the ocean at time step t_n with atmospheric fluxes from t_n. In this mode climate models can get very close to what would be a converged solution of an iterative coupling at the atmosphere-ocean interface (Marti et al., 2021). Integration of a Schwarz iterative method for fully converged surface coupling is not planned, due to the high computational cost compared to small reduction in model error.

On the technical side all three components of the coupled model are compiled into their own respective executables and a parallel communication library, OASIS3-MCT 4.0 (Craig et al., 2017b), is integrated into each one. The realized AOGCM setup is sketched in Figure 3.1. Since FESOM2 has previously been coupled to the atmospheric model ECHAM6 (Sidorenko et al., 2019), an interface for the data exchange already existed, and the grouping of fluxes in OpenIFS has been modeled after the grouping in ECHAM6. OpenIFS CY43R3 had not been coupled via OASIS before, but an older related model OpenIFS CY40R1 was coupled via OASIS as a test case in EC-Earth 3. The coupling of interface for OpenIFS CY43R3 is inspired by this predecessor. Future releases of OpenIFS will be published with this coupling interface already included.

3.4 Climatological Performance

In this section we will outline the ability of the new coupled system to reach a stable equilibrium with constant greenhouse gas and solar forcing from the year 1850. Thereafter we test to what degree the model can simulate the climate as observed over the period 1850 to 2014, with a particular focus on the last 25 years, when the observational coverage is most dense and reliable. Finally this is followed by a characterization of the response to two idealized future CO_2 emission scenarios, one with a sudden 4x increase of CO_2, and the other with a constant increase of 1% per year, starting from 1850 values.

3.4.1 Spinup drift (SPIN)

A 700-year long spinup of AWICM3 was carried out under constant greenhouse gas and solar forcing from the year 1850, starting from winter Polar Science Center Hydrographic Climatology (PHC3) (Steele et al., 2001). The forcing fields were collected from the input4MIPs data server (https://esgf-node.llnl.gov/search/input4mips/, last access: 6 November 2019). Aerosol fields were kept at present day levels, as the integration of the emissions-based aerosols into OpenIFS CY43R3 through the EC-Earth Consortium with tracing via the M7 model (Vignati et al., 2004) is still ongoing. This implies a somewhat colder pre-industrial state in particular in regions of the northern hemisphere, that are cooled in present day observations due to industrial aerosol emissions.

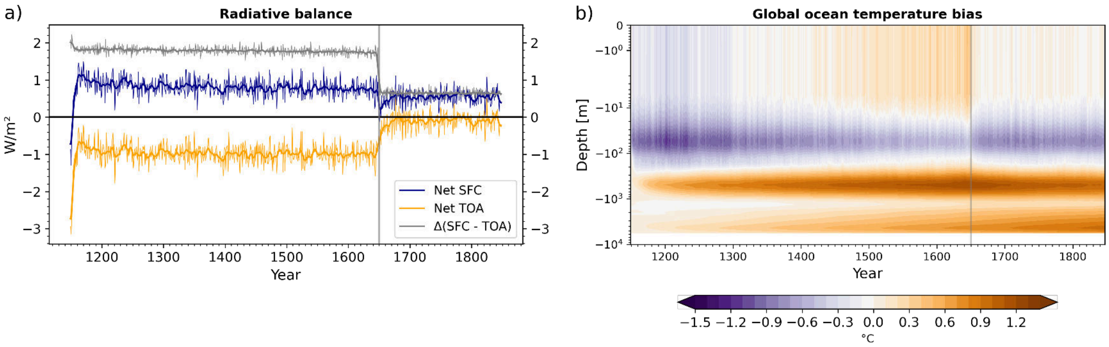

Figure 3.3: a) Net radiative imbalance at the top of atmosphere (TOA) and at the surface (SFC) in the spinup simulation. Positive (negative) values indicate downwards (upwards) net heat flux. The difference results from spurious energy production in the atmosphere. b) Semi-logarithmic depth Hovmöller diagram of the evolution of the global mean ocean temperature bias over the spinup period with respect to PHC3 climatological values (Steele et al., 2001). Switching from dry to total mass fixer after 500 years reduced spurious heat production in the atmosphere and halted the ocean warming trend in the upper 1000 meters. Warming at depth continued.

During the first 500 years of the spinup simulation we noted positive global ocean temperature trends throughout nearly the entire water column, as can be seen in the Hovmöller diagram of Figure 3.3b. Evaluation of the top of atmosphere (TOA) and surface (SFC) net heat fluxes in the atmospheric model revealed a near constant radiative imbalance of $2\,W/m^2$, depicted in Figure 3.3a. A partial solution is to switch the OpenIFS mass fixer from dry mass to total mass conservation (Malardel et al., 2019) with the McGregor scheme (McGregor, 2005). We implemented this solution starting from year 1651. Subsequently the radiative imbalance reduced to $+0.7\,W/m^2$, which is within the range of imbalance of CMIP6 models (Wild, 2020).

Further experiments showed that decreasing the OpenIFS time step from 60 minutes to 30 minutes reduced the imbalance to $+0.4\,W/m^2$. An additional reduction to 15 minutes time steps showed no more improvements. We surmise that the time step-dependent component of the error implicates the semi-lagrangian trajectory algorithm operating close to the stability limit for the given atmospheric resolution of TCo159. For our analysis we judged this additional error an acceptable price for a doubling in model integration speed, and we thus keep the 60 min time step. The time step independent flux imbalance of $+0.4\,W/m^2$ will be targeted in future model development and tuning efforts.

In the global mean ocean temperature Hovmöller diagram (Figure 3.3) we can see that after switching to total mass conservation the reduction of spurious heat production in the atmosphere led to a stabilization of the ocean temperatures in the upper 1000 meters. The trend in the deep ocean, strongest at 4500 meters depth, on the other hand has hardly slowed down and, thus, likely has a different origin. One candidate currently under investigation is the topography-influenced equilibrium depth of the Gibraltar Straight overflow. Alternatively we speculate that overestimated mixing from the KPP mixing scheme (Large et al., 1994) might be the reason. The bias pattern is very similar to that of the previous FESOM2-ECHAM6 (AWI-CM2) coupled model (Sidorenko et al., 2019).

Another potential contributor to the accumulation of heat at depth is a consistent positive shortwave radiation bias of OpenIFS in the Southern Hemisphere. Some of the spuriously heated Southern Ocean surface water gets entrained into the Antarctic Intermediate Water (AAIW). In recent years, the Southern Ocean shortwave radiation bias has been the subject of research which led to its reduction by $5 - 10\,W/m^2$ (Forbes et al., 2016). We have already back-ported these improvements originally developed for the operational IFS CY45 model into OpenIFS CY43R3 prior to our spinup simulation. Even with the improvements, a positive shortwave downward radiation bias of up to $5-10\,W/m^2$ between 45-60°S remains, and can be seen in Figure 3.7 e). Idealized experiments have shown that removal of the remaining shortwave radiation bias would cool the Southern Ocean by roughly $1\,K$ within a decade, with potentially larger improvements on longer timescales (not shown).

3.4.2 Pre-industrial control (PICT)

As evident from the Hovmöller diagram (Figure 3.3b), the spinup run is not yet in equilibrium at depths greater than 1000 meters. A small residual drift can also be found at the ocean surface and in the atmosphere, which can be seen as a consequence of the still-drifting deep ocean. Based on experience with other ocean models we can estimate that a 3000-5000 year long simulation would be needed for the model to reach full equilibrium (Rackow et al., 2018). Instead, we run a pre-industrial control experiment which serves as a reference for correcting the historical-period simulation with respect to the remaining trends. The pre-industrial control run thus extends the spinup run by 165 years with the same year 1850 greenhouse gas and solar forcing. We construct a simple linear regression model for the remaining drifts in PICT and subtract these when we analyze the response to historical forcing in the historical simulation.

3.4.3 Climatological performance for the historical period (HIST)

In the following we first characterize the most prominent bias patterns of the last 25 years of the historical simulation with regards to reanalysis and satellite data products. We then take a look at the climate response to the historical forcing in comparison to the pre-industrial control.

For a succinct overview of the model performance we calculated climate model performance indices, based on Reichler and Kim (2008) and shown in Table 3.4. For the four seasons, seven regions and twelve key variables, the fraction of absolute error of climatology of the last 25 years in AWI-CM3 historic simulation to the absolute error averaged over 30 CMIP6 contributing models can be seen. A complete list of the CMIP6 models serving as the evaluation set is given in Appendix 3.7. The list of observational datasets used to calculate all mean absolute errors is also given in Appendix 3.7. For all model and observational datasets, where available, the time period from December 1989 until November 2014 is considered. As the performance of AWI-CM3 is expressed as a fraction of the errors of the CMIP6 average performance, values below 1 indicate better performance, values above 1 point to larger model errors.

For the majority of variables, seasons and regions our post-CMIP6 prototype model is already performing better than the average CMIP6 model. The lead is especially large for cloud cover (clt) and 500 hPa geopotential height (zg). For surface meridional wind (vas), surface zonal winds (uas), 300 hPa zonal wind (ua), TOA outgoing longwave radiation (rlut), and precipitation (pr) the bias to observations is mostly below average. The very important near surface (2m) air temperature (tas) is simulated well in the Arctic (60°-90°N) and reasonably well in the northern mid-latitudes (30°-60°N) and tropics (30°S-30°N). In the southern mid-latitudes (30°-60°S) and Antarctic (60°-90°S) the air temperature bias is relatively high. A look at the sea ice concentration (siconc) reveals that the respective errors are far above average in the Antarctic. The problem is particularly severe in the austral winter season. This bias is in co-occurrence with a large mixed layer depth bias in the Antarctic. We note that the mixed layer depth from reanalysis we used here as the reference could be associated with uncertainties too, as it is based on the implementation of mixing parameterizations in the reanalysis model. The standard deviation of sea surface height (zos) shows reasonable variability of the ocean currents in the mid and high latitudes, with problems found in the Nino34 region (5°S-5°N, 170°W-120°W). On the other hand, the standard deviation of temperature is best represented here, with deficiencies in the Antarctic cold season and northern mid latitude summer.

A simple average over all individual performance indices gives AWI-CM3 a score of 0.931, with 15 out of the 30 considered CMIP6 models performing better. The overall index of the AWI-CM3 prototype simulation is improved compared to its CMIP6 predecessor with similar resolution and computational cost (AWI-

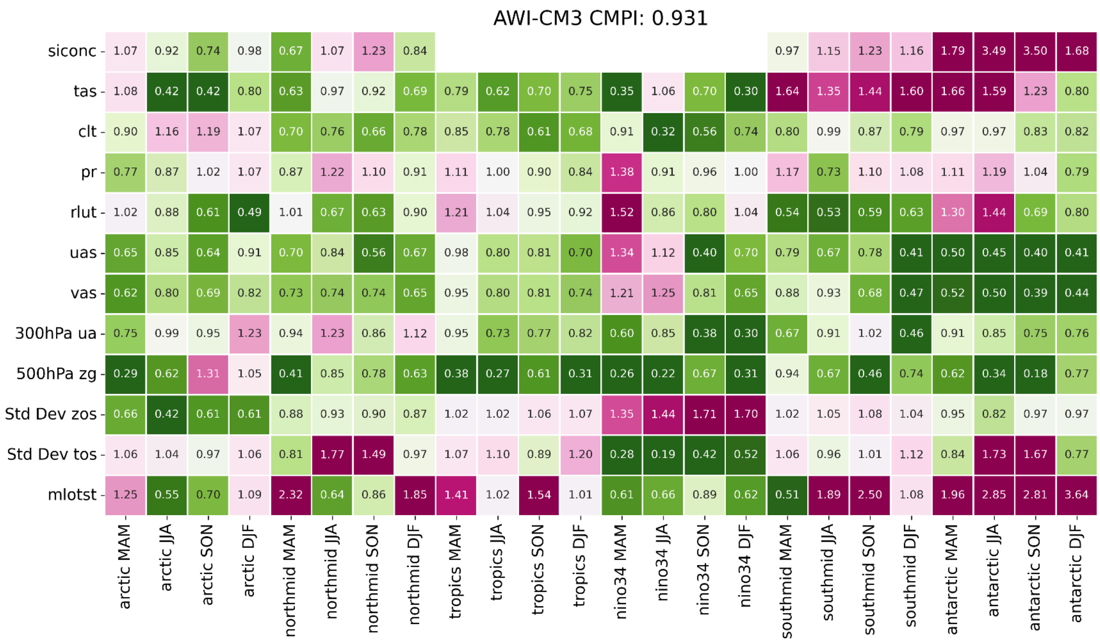

Figure 3.4: Performance indices after Reichler and Kim (2008) that give the fraction of absolute error of climatology of the last 25 years in AWI-CM3 historic simulation to the absolute error averaged over CMIP6 models. Values below (above) one correspond to below (above) CMIP6 average biases. The underlying observations against which all models were evaluated are OSISAF OSI-450 (Lavergne et al., 2019): sea ice concentration (siconc); MODIS Atmosphere L2 Cloud Product (Platnick et al., 2015): cloud cover (clt); Global Precipitation Climatology Project (GPCP) Monthly Analysis (Adler et al., 2018b): precipitation (pr); Clouds and the Earth's Radiant Energy System (CERES) (Wielicki et al., 1996): TOA outgoing longwave radiation (rlut); ECMWF re-analysis ERA5 Hersbach et al. (2020a): near-surface air temperature (tas), eastward near-surface wind (uas), northward near-surface wind (vas), 300 hPa eastward wind (ua), 500 hPa geopotential height; NOAA JASON-1, JASON-2, CryoSat-2 combined: Sea surface height (zos); HadISST2 (Titchner and Rayner, 2014a): Sea surface temperature (tos); C-GLORSv7 (Storto et al., 2016b): Mixed layer depth (mlotst). A full list of the considered CMIP6 models is given in Appendix 3.7.

ESM1.1-LR, 1.044). The performance of our medium-resolution AWI-CM1.1-MR CMIP6 contribution (Semmler et al., 2020) is better (0.894), but this model configuration is 20 times more expensive to run than the simulations presented here. Preliminary tests with higher resolution at equal computational cost indicate that AWI-CM3 can achieve better climatological performance than AWI-CM1.1-MR, as we will show in Section 3.5.1. A major contributing factor are the faster dynamic cores and better computational scalability of the model components, allowing for higher resolutions at equal computational cost.

With this overview in mind we will limit our model bias analysis to problematic areas, knowing that for the variables we do not focus on we achieved good model performance.

Sea ice and mixed layer depth The sea ice thickness in the Arctic contains realistic values for both end of summer (EOS) and winter (EOW), PICT and HIST runs (Figure 3.5). In the central Arctic, PICT sea ice thickness ranges from 3.5m at the EOW to 2.5m at the EOS. The mean over the last 25 years of the HIST simulation reveals a reduction of sea ice thicknesses to 2.5m and 1.5m in these two seasons. In both simulations, the maxima of EOW ice thickness can be found in the East Siberian Sea and along the coastline of northern Greenland. Although, in some years, a local maximum of sea ice thickness was observed along the East Siberian Sea coast, in the multi-year-mean field it should not be as large as presented by the model. Similar issues are common in many CMIP6 models and exist even in the PIOMAS reanalysis (Watts et al., 2021). One clear bias in comparison to observations is a too wide tongue of sea ice extending eastward in the Greenland Sea during the winter months. A similar feature can be seen in our previous model versions. The annual cycle of sea ice extent is represented well with 16 to 7 million square kilometers in the last 25 years, compared to observational values of 15 to 6 million square kilometers by Walsh et al. (2019).

The Antarctic sea ice biases require the most improvement as follows from the metrics presented in Table 3.4. In both the PICT and HIST simulations the sea ice covered area is strongly underestimated during austral winter (Figure 3.5c&g). Notable are two spots of low sea ice thickness in the Weddell Sea and in the eastern Ross Sea. Both areas feature low EOW mean sea ice thickness of less than 20cm during the PICT run, and are partially ice free during the last 25 years of HIST. These locations feature persistent large scale polynyas. In reality, polynyas were observed in the Weddell Sea (e.g., during the winters 1974 to 1976), however, the frequency of their occurrence (not presented in this paper) is clearly overestimated in our model.

In order to gain an understanding towards the reasons for the persisting polynya, we investigate the mean mixed layer depth (MLD), defined as the depth at which the potential density differs by 0.125 $\frac{kg}{m^3}$ from the surface density (Monterey and Levitus, 1997). The MLD shown in Figure 3.6 a) features large values in the Weddell and increased values in the Ross seas that are co-located with low sea ice concentration values seen in figure 3.6 b). We therefore speculate that the large MLD could be one of the reasons for the underestimated wintertime sea ice, as the ocean heat from the warmer Circumpolar Deep Water (CDW) can be mixed up to reach sea ice from below. The salinity profile over the highlighted region confirms that the surface layer is more saline in our model than the PHC3 climatology. The exact reason for the overestimated MLD is not clear and understanding whether the salinity bias is the main cause is among our planned future research.

We hypothesize that in the subsequent austral summer the reduced sea ice cover results in a strong positive sea ice albedo feedback, further heating up the surface ocean. We examine this feedback in the following section.

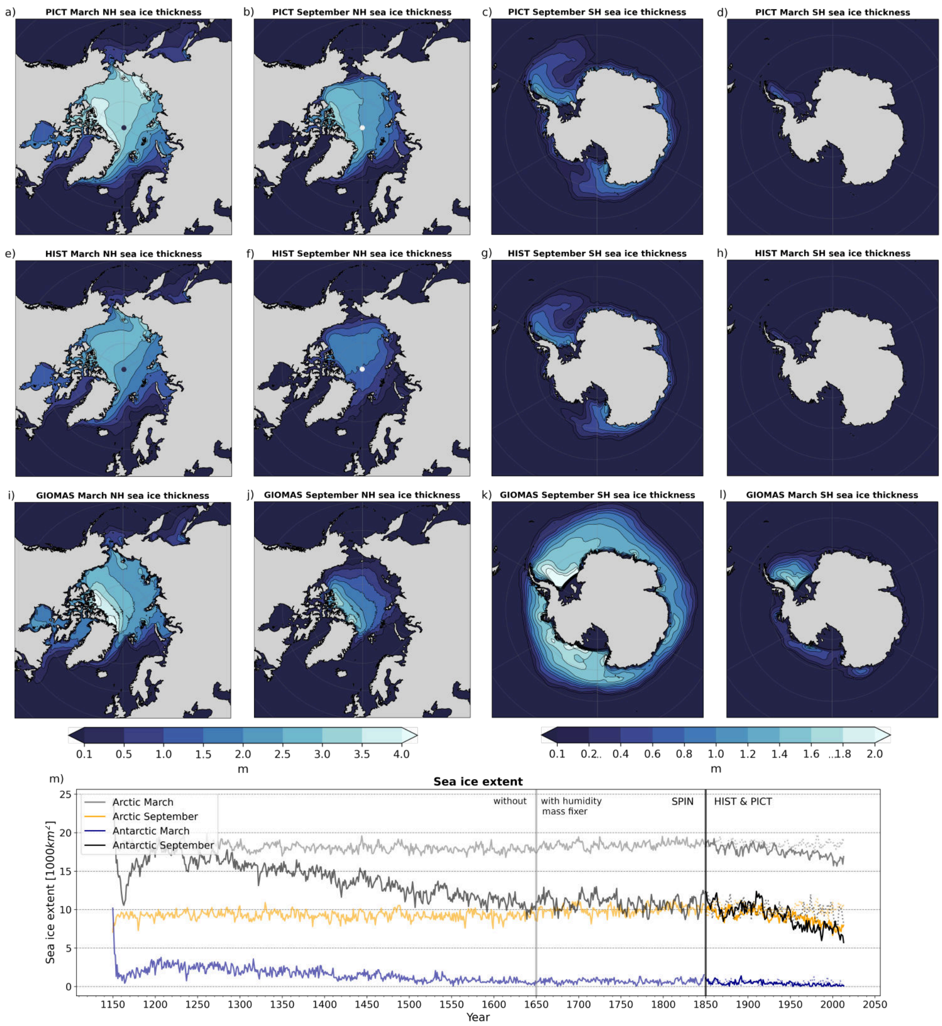

Figure 3.5: a-d) Mean sea ice volume per unit area over last 25 years of PICT simulation. e-h): Same as top row but for the HIST simulation. i-l): Same as top row but for GIOMAS sea ice thickness reanalysis product. (Zhang and Rothrock, 2003). m): Evolution of sea ice extent over SPIN, as well as HIST and PICT simulations. Mass fixer switched from dry to total in years 1650. HIST and PICT forcing applied from 1850 onwards.

Surface temperature and fluxes The near surface (2m) air temperature bias in comparison to ERA5 largely shows a pattern similar in sign (Figure 3.7a), and at somewhat higher amplitude compared to the CMIP6 multi-model mean bias shown in Bock et al. (2020). In the tropical Pacific we find a slight cold bias located at the equator, flanked by equally sized warm biases, which is typical of a too-strong double-ITCZ found in many coupled models and associated with characteristic percipitation and short-wave radiation biases (see below). The upwelling regions off the west coasts of southern Africa and South America feature well known warm biases of up to 4°C resulting from insufficient upwelling, too little stratocumulus cloud cover and thus too much downwelling short-waver radiation with our low

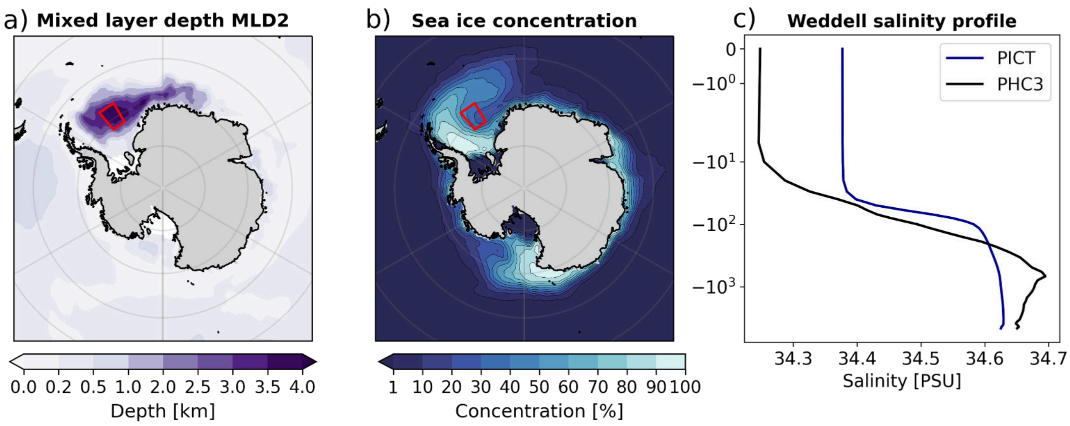

Figure 3.6: a) Austral winter mean mixed layer depth (MLD) where the potential density over depth differs by 0.125 $\frac{kg}{m^3}$ from the surface density (Monterey and Levitus, 1997) averaged over the last 25 years of the PICT simulation. b) High MLD values in the Weddell and Ross seas contribute to the persistent polynyas visible in the mean austral winter sea ice concentration over the same time period. c) Salinity profile over the region marked in red in comparison to PHC3 climatology (Steele et al., 2001).

resolution ocean model. Further north and south the subtropical gyres feature cold biases on the order of -1 to -2°C.

In the mid-latitudes, the most prominent bias is the misplacement of the Gulf Stream which fails to represent the correct North West Corner detachment (Figure 3.7a). This is a well known bias in OGCMs of coarser than 10 km resolution in the North Atlantic. For the FESOM2 model, a study by Sein et al. (2017) shows that this problem can be mitigated by increasing the ocean model resolution in the region.

At high latitudes we find a strong warm bias of more than +8°C over areas of the Southern Ocean (SO) adjacent to Antarctica and a moderate one over Antarctica of +3 to +4°C, as well as a cold bias of around -2°C in the Arctic. The cold bias in the Arctic likely stems from the ERA5 reanalysis, which misses snow cover on sea ice (Batrak and Müller, 2019a), rather than from AWI-CM3. We thus focus on the southern warm biases in our analysis, some of which are well known for IFS based climate models and can also be seen in Döscher et al. (2021) and Roberts et al. (2018). We hypothesize that these biases are caused by the direct effect of heat released from a spuriously deep mixed layer (as noted in Section 3.4.3), a positive ice albedo feedback to the resulting reduced sea ice cover, and a remaining positive net shortwave downward heat flux bias between 45-60°S.

Nearly all of the near surface temperature biases (Figure 3.7a) can be associated with co-located net surface shortwave radiation biases (Figure 3.7c). These can be largely explained by surface downward radiation biases (Figure 3.7e), which in turn result from total cloud cover fraction biases (Figure 3.7f). This linkage pattern is well known in the modelling community (Satoh et al., 2019) and will

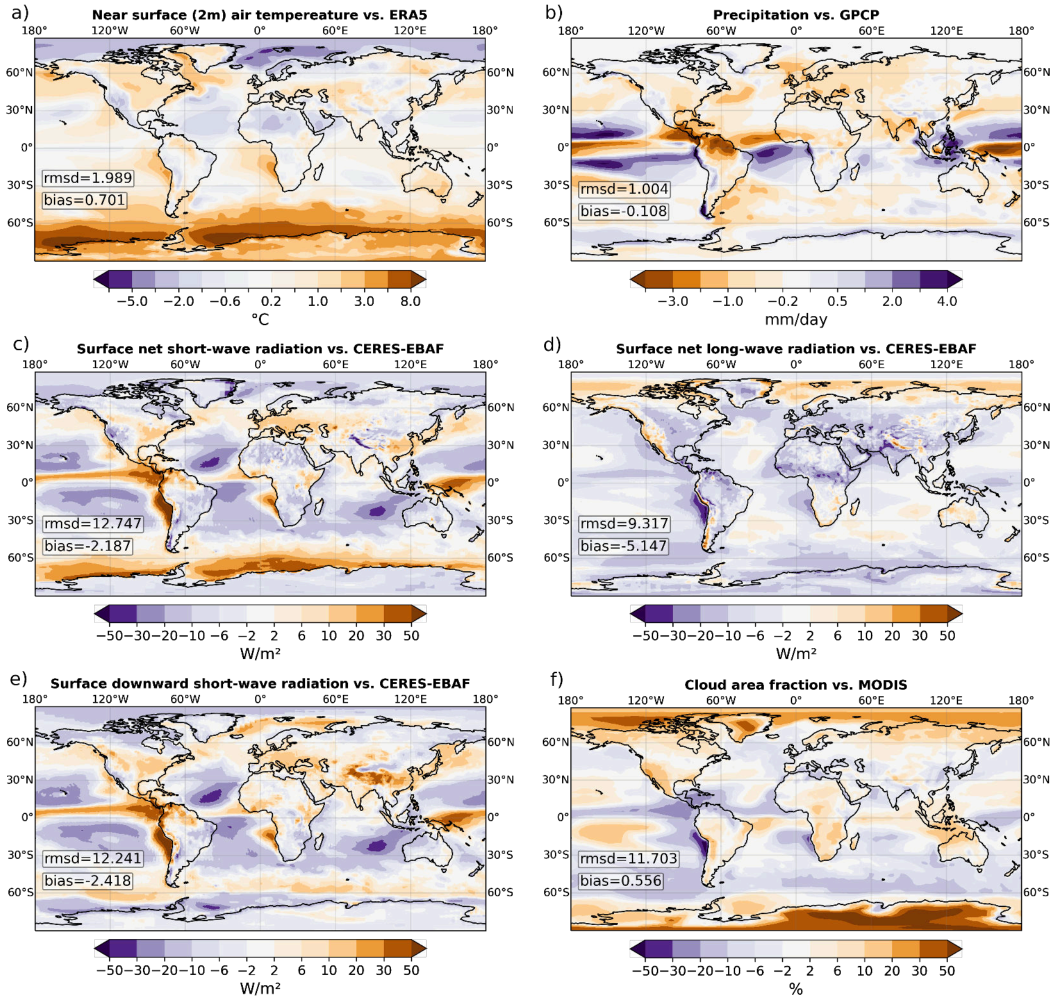

Figure 3.7: Annual mean a) Near surface (2m) air temperature bias with respect to ERA5. b) Precipitation bias with respect to GPCP. c) Surface net shortwave radiation bias with respect to CERES (2001-2014). d) Surface net longwave radiation bias with respect to CERES (2001-2014). e) Surface downward shortwave radiation bias with respect to CERES (2001-2014). f) Total cloud cover fraction bias with respect to MODIS. For each variable rmsd gives the area weighted root mean square distance between observations and model data, and bias gives the area weighted mean distance.

likely remain a dominant source for surface temperature biases until deep convection resolving atmospheric models become readily available for multidecadal to centennial climate simulations.

There are two notable exceptions to this causal chain in our simulations. Firstly, we found a cold bias over the Greenland sea where the surface downward shortwave radiation bias is positive. The cold bias in the region is the result of a lobe of sea ice drifting into the area from the Greenland coast during winter. This results in an overestimation of surface albedo and a reduction of the net surface shortwave radiation.

The second and similar exception is the previously mentioned warm bias south of 60°S in the SO. While the model overestimates the cloud and thus underestimates surface downward shortwave radiation in the region, the sea ice fraction in this area is too low. The surface net shortwave radiation and the near surface temperature biases are therefore positive. As the SO surface net shortwave radiation bias is negative the low sea ice concentrations cannot originally be caused by shortwave biases. Indeed, the near-surface (2m) air temperature and sea ice concentration biases south of 60°S peak during the austral winter season, while the biases in the southern mid-latitudes peak during austral summer (Table 3.4). Correcting the largest biases south of 60°S in our model will probably necessitate work on non-solar heat fluxes and mixed layer depths at high-latitudes.

The precipitation biases shown in Figure 3.7b feature the canonical double ITCZ bias in the Tropics. Notably the mid-latitudes receive too little precipitation, especially over western boundary currents, Europe and North America east of the Rocky Mountains.

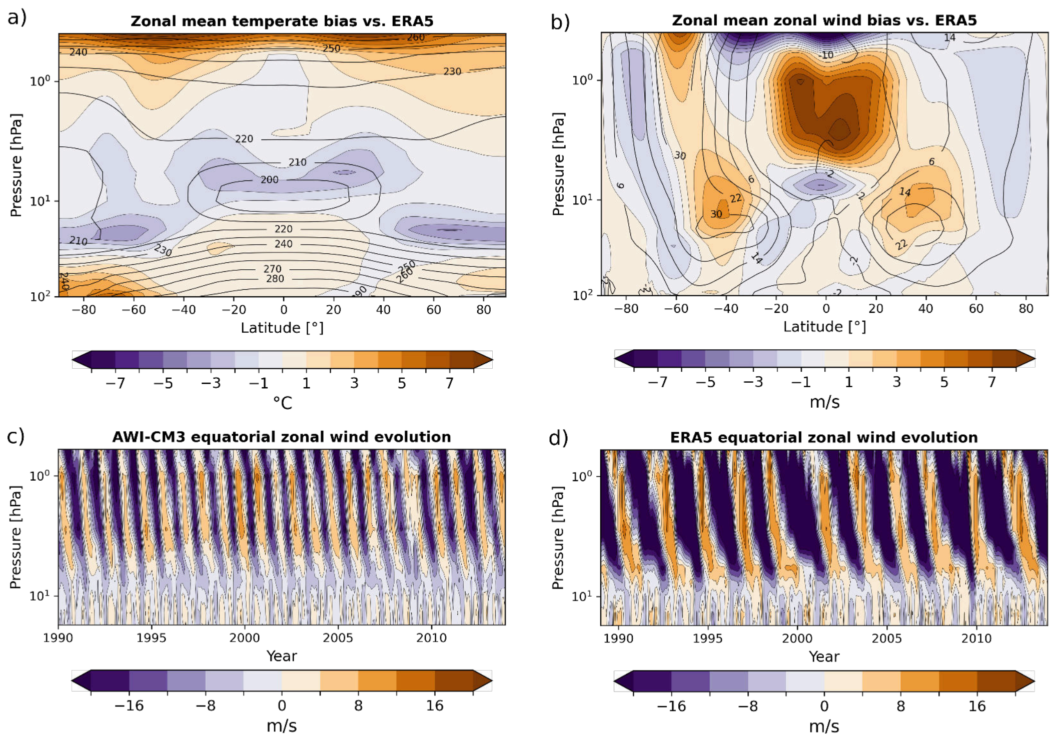

Figure 3.8: AWI-CM3 HIST a) Zonal mean air temperature bias with respect to ERA5 averaged over the last 25 years. b) Zonal mean zonal wind bias with respect to ERA5 averaged over the last 25 years. c) Near equator zonal wind over time and height for AWI-CM3 HIST simulation. d) Same as c) but for ERA5 reanalysis, showing Quasi-Biennial Oscillation.

Figure 3.8 a) depicts the zonal mean temperature bias averaged over the last 25 years of the HIST simulation with respect to ERA5 for the same period. The previously seen Southern Ocean surface warm bias is well visible up to 500 hPa.

Around the tropopause height the model exhibits a prominent cold bias of up to -4°C. In the high stratosphere meanwhile we find a large warm bias of up to 8°C. The stratospheric bias will be reduced with ECMWF's next minor release of OpenIFS, cy43r3v2, which enables the use of spectral solar insolation instead of total solar irradiance (not shown).

The zonal mean zonal wind in figure 3.8 b) broadly shows overestimation of the subtropical jet strength and height, as well as underestimation of the polar jet streams. The most notable feature though is the miss-representation of equatorial stratospheric winds.

A closer look at the near equator (10°N-10°S) zonal and meridional mean wind-speeds over height and time in figure 3.8 c) reveals that the Quasi-Biennial Oscillation (QBO) is in fact an annual oscillation in the last 25 years of the HIST simulation. Contrasted with the same winds in the ERA5 reanalysis of the equivalent time period the QBO frequency error is apparent. The main reason for this behavior is a lack of tuning for the gravity wave flux parameterization, as was confirmed by tests conducted with OpenIFS at GEOMAR (not shown). Tuning of the gravitational wave flux parameterization will be addressed in future model releases.

Ocean temperature On the ocean side of the coupling interface, we find mean sea surface temperature biases with respect to PHC3 that are nearly identical to the aforementioned near surface air temperature biases (Figure 3.9). At a depth of 100 meters the bias looks similar to that at the surface in high-latitudes where mixed layer depths are large. In the Tropics and Subtropics this depth range is dominated by cold biases, which could be partially due to missing vertical mixing associated with Langmuir circulation in the current version of FESOM2. It is known that including a parameterization for this mixing can effectively alleviate the cold bias in the near-surface ocean in the mid-latitudes and tropics (Wang et al., 2019; Ali et al., 2019), and the integration of a Langmuir circulation parameterization in vertical mixing schemes is planned.

At a depth of 1000 meters the Atlantic shows a strong warm bias, which we speculate results partially from spuriously warm SO surface water entrained into the AAIW. Ultimately the whole bias probably stems from multiple yet to be identified sources in both hemispheres. The cold bias found in the Indian Ocean at this depth is likely the result of insufficient warm outflow from the Persian Gulf because the narrow strait is not well resolved on the FESOM2 CORE2 mesh.

AWI-CM3 shows a pronounced warm bias of 3-5K in the Atlantic subpolar gyre. Sidorenko et al. (2015) noted a similar bias when analyzing AWI-CM1 simulations. This bias is shared between many climate models which contributed to CMIP. Hence, a similar drift in ocean hydrography is also described in Sterl et al. (2012); Delworth et al. (2006, 2012); Jungclaus et al. (2013). These authors discuss different factors that may be responsible for the bias. Sterl et al. (2012) show that overestimation of the Mediterranean outflow can significantly increase the deep-

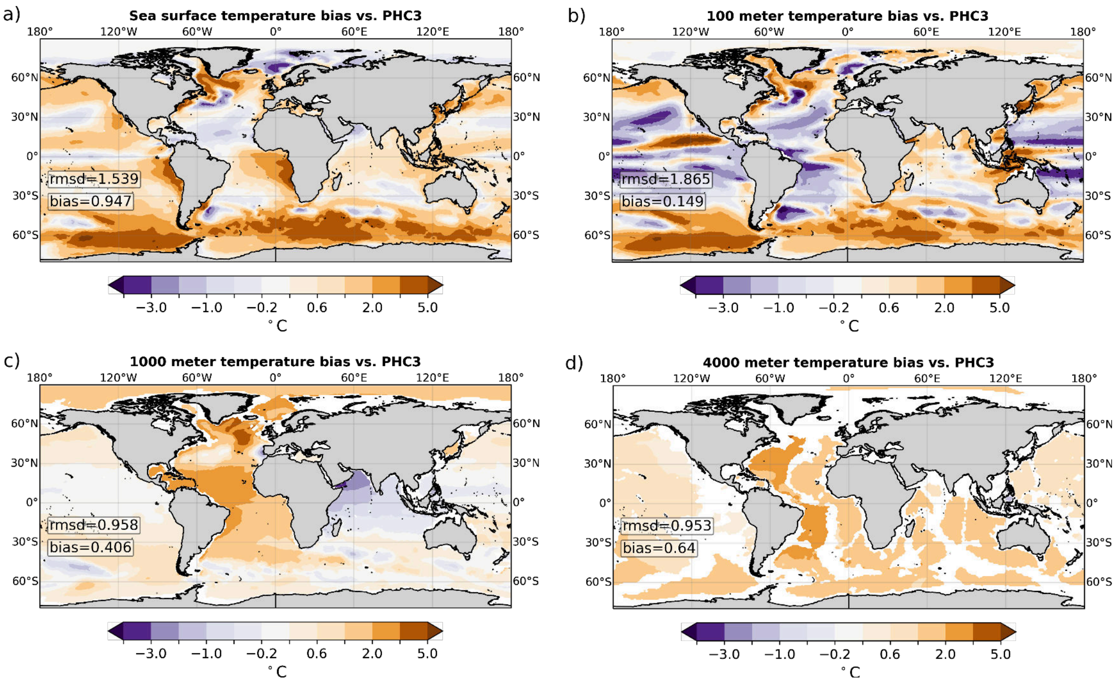

Figure 3.9: Mean ocean temperature bias of the last 25 years of the historical simulation with respect to PHC3 at a) 0, b) 100, c) 1000 and d) 4000 meters depth. For each depth rmsd gives the area weighted root mean square distance between observations and model data, and bias gives the area weighted mean distance. At the surface the ocean-resolution-specific warm biases in upwelling regions and western boundary currents can be seen, in addition to a pronounced Southern Ocean warm bias. At depth, a warm bias is dominating in the Atlantic.

ocean salinity bias. Delworth et al. (2012) attribute this anomaly to the insufficient eddy transport required to compensate for the wind-driven subduction in the subtropical gyres. They show that moving towards an eddy-resolving setting or a parameterization of the eddy stirring reduces the temperature biases significantly. Jungclaus et al. (2013) suggest that part of the problem arises from the improper interbasin exchange between the Indian and South Atlantic oceans.

At 4000 meters depth we observe the warm biased Atlantic water mass spreading into the whole global ocean. As the meridional circulation at this depth is northward in the Antarctic Bottom Water (AABW) cell, the origin of the warm bias is presumably insufficient cold AABW formation in the Southern Ocean on this coarse mesh. The slowness of the AABW circulation in the Atlantic coincides with the slow but continued global-mean warming trends at great depths seen in Figure 3.3. Biases presented in Figure 3.9 explain the Hovmöller diagram in Fig 3.3 which we addressed in Section 3.4.1. The three sets of anomalies in the Hovmöller diagram at depths 100m, 1000m and 4000m stem from the biases in the mid latitudes, the North Atlantic and in the entire ocean, respectively.

El Niño-Southern Oscillation To assess the model capabilities in representing climate variability, we investigate the representation of the El Nino Southern Oscillation (ENSO). Using the entire HIST simulation and the EOFs toolsbox (Dawson, 2016) Figure 3.10a) depicts the spatial extent of the correlation between the first principle component and the input data set at each point in space. Also depicted is the Nino3.4 box (5°N to 5°S, 120°W to 170°W) upon which we based our further analysis.

We calculated the area mean SST within the box, applied a linear detrending, subtracted the mean seasonal cycle, and finally computed a three month running mean. The resulting Nino3.4 index time series is shown in Figure 3.10c. Comparison with the Nino3.4 index based on the HadISST observational estimates (Figure 3.10d) reveals that our simulated amplitude of ENSO, with a range of +1.9 to -1.6°C, is lower than the observed. Indeed, the histograms in Figures 3.10e and 3.10f reveal missing tails of the distribution in the simulation.

While the overall strength of ENSO is underestimated by AWI-CM3, the normalized power spectrum density (PSD) in Figure 3.10b shows that the frequencies of the observed HadISST ENSO are well reproduced. We find several peaks concentrated between periods of 2.8 and 12 years. Further analysis (not shown) indicated that ENSO phase locking is rather weak in the model version presented, and that both ENSO amplitude and phase locking can be improved through reduction of equatorial Pacific precipitation and temperature biases. Understanding how to do so without negatively impacting model performance in other regions is work in progress.

Future improvements for the ENSO amplitude could also potentially be achieved by activating the OpenIFS internal stochastic parameterization schemes, as shown by Yang et al. (2019). Indeed, HighResMIP simulations performed by Roberts et al. (2018) with IFS CY43 that employed the Stochastically Perturbated Parametrisation Tendencies (SPPT) scheme (Buizza et al., 1999) had an ENSO amplitude more in line with observational estimates. Since these studies used the SPPT scheme, they required additional humidity mass fixers for climate-length integrations.

Alternatively, in order to use the new - and from a mass conservation perspective more favorable - Stochastically Perturbed Parametrisations (SPP) scheme (Ollinaho et al., 2017), the full version of SPP has to either be backported from IFS CY47 to OpenIFS CY43R3, or the new version OpenIFS CY47 has to be released. Noteworthy is also that CMIP6 simulations done with CNRM-CM6-1, featuring the IFS atmosphere with the ARPEGE physics package (not in use AWI-CM3, as we employ ECMWF physics) and no stochastic parameterizations, also had a high ENSO amplitude. However the frequency of ENSO was too focused with a sharp single peak in the 3-4 year band (Voldoire et al., 2019).

Finally, experiments with stochastic coupling at the atmosphere ocean interface conducted with AWI-CM1 yielded improved ENSO phase locking (Rackow and Juricke, 2020), providing another potential development avenue.

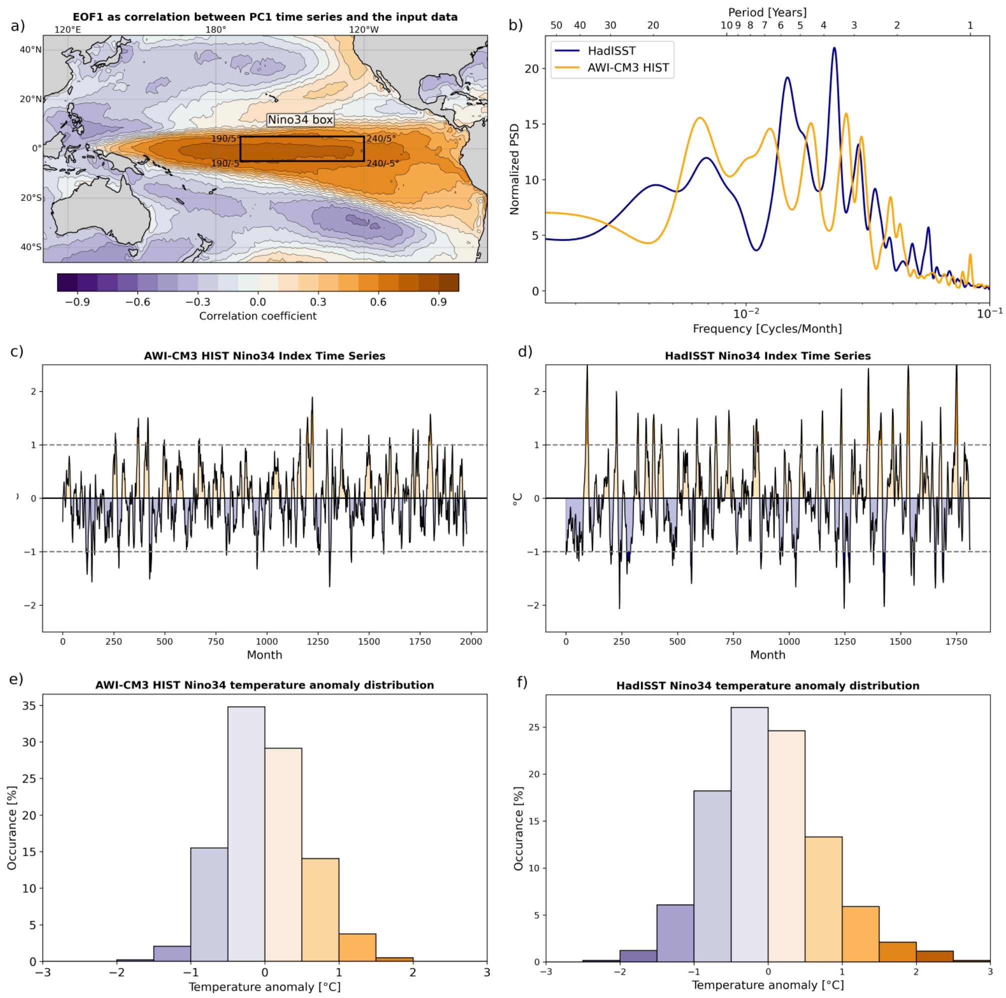

Figure 3.10: **a) Extent of the Nino3.4 box, as well as the first empirical orthogonal function expressed as the correlation between the first principal component and the input data set at each point in space. Calculated from the entire HIST simulation using the EOFs toolsbox (Dawson, 2016). b) Normalized power spectrum density of simulated ENSO within the Nino3.4 box in comparison to HadISST observational estimates for the years 1850 to 2014. c) & d) Nino3.4 SST index defined as the detrended, seasonal cycle removed and 3-months running mean time series of SST averaged over the Nino3.4 box. The results from AWI-CM3 HIST and HadISST observational estimates are shown, respectively. e) & f) As c) & d) but depicting occurrence of temperature anomalies in bins with a width of $0.5°C$.**

3.4.4 Impact of Historical Forcing

Air temperature After we have established that AWI-CM3 behaves reasonably for much of the globe and many important climate parameters, we will now characterize the impact of historical greenhouse gas and solar forcing on the evolution of several of these variables.

The global mean near surface (2m) air temperature increases under HIST forcing, as seen in Figure 3.11a. Since our SPIN experiment did not establish a full equilibrium in the deep ocean, we analyze the air temperature change in our pre-industrial control experiment PICT, and obtain the residual drift of $0.00091^\circ C$/Year via linear regression. Over the 165-year-long simulation this amounts to a drift of 0.15°C in the PICT run.

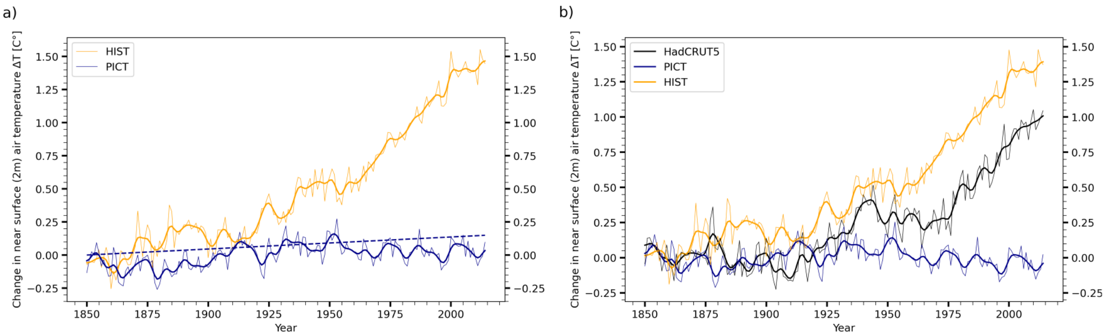

Figure 3.11: a) Near surface (2m) air temperature changes over the historic period and in the pre-industrial control simulation. Thick lines show the 10 year running means. The pre-industrial control simulation shows a residual drift of $0.00091\frac{^\circ C}{\textbf{Year}}$ obtained from linear regression. b) Both simulations have been corrected by subtracting the residual drift. The resulting simulated global warming over the period 1850 to 2014 is $1.4^\circ C$. In comparison to observational estimates from HadCRUT5 (Morice et al., 2021) warming is overestimated by 0.4 K, likely due to fixed aerosols in the AWI-CM3 prototype.

In Figure 3.11b we have corrected both runs by deducting the linear trend. The resulting temperature change represents a global warming over the period 1850 to 2014 of 1.4°C, most of which comes in a steep rise between 1960 and 2000. Comparison with observational values from HadCRUT5 (Morice et al., 2021) shows that AWI-CM3 gets the timing of historical warming spikes right, however the strength is overestimated by 40% ($1.0^\circ C$ vs. $1.4^\circ C$).

The main reason for the stronger than observed historical warming is that the increase in global aerosol emissions, which partially masks the warming induced by well mixed greenhouse gases, is not incorporated in the version of OpenIFS (CY43R3) used here. The integration of the tropospheric aerosol component M7 into OpenIFS CY43R3 is still ongoing within the EC-Earth consortium (private communication with the EC-Earth aerosol working group). The sixth IPCC report (Masson-Delmotte et al., 2021) concludes that the anthropogenic aerosols direct and indirect contributions to the effective radiative forcing amount to about $-0.5W/m^2$. Comparing to the total anthropogenic forcing of $+1.5W/m^2$, we foresee that, once transient aerosols will have been included in OpenIFS CY43R3, AWI-CM3 historical global warming will be much closer to the observed value.

The map of temperature changes in Figure 3.12a shows that under historic well-mixed greenhouse gas and solar forcing AWI-CM3 simulates a temperature increase of approximately 1-2$^\circ C$ in the Tropics, Antarctic and large parts of Eurasia. Mid-latitude oceans in both hemispheres see a weaker warming of 0.6-1$^\circ C$.

Larger warming of 2-3°C can be found in the Middle East, North America, the Caucasus, Australia and South Africa. Sea ice covered regions in the Arctic experience the strongest air temperature increases, with the Arctic (65-90°N) warming by 3-8°C. Defining an Arctic Amplification Index (AAI) as the ratio of warming north of 65°N to whole northern hemisphere warming (Davy et al., 2018; Johannessen et al., 2016), the resulting AAI is 2.87. Note that, in contrast to observations as well as full-forcing CMIP simulations, there is no trace of a warming hole in the North Atlantic south of Greenland. Whether this might be due to the missing transient aerosol forcing in our simulation is unclear. Earlier studies have linked the warming hole rather to a weakening of the AMOC (Keil et al., 2020), but although our historic simulation does exhibit such an AMOC weakening (see Figure 3.13), no warming hole forms.

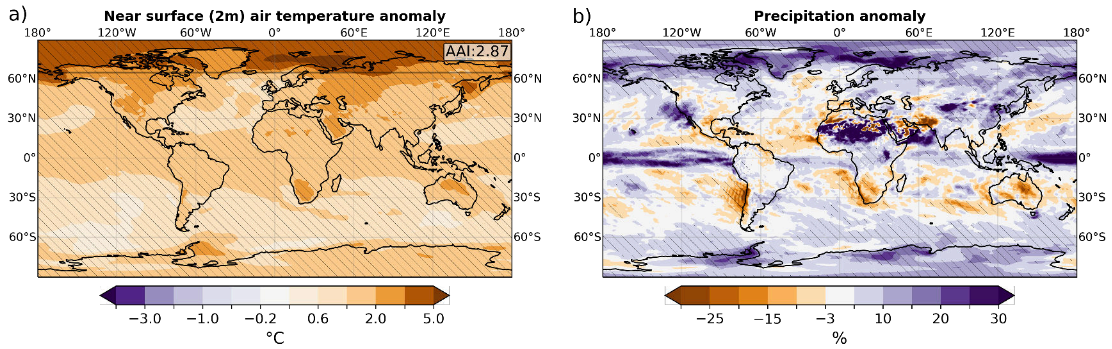

Figure 3.12: a) Temperature anomaly between last 25 years of the historic simulations and the equivalent period of the pre-industrial control run. The Arctic Amplification index, defined as the ratio of warming north of 65°N expressed as a fraction of global warming, is 2.87. Significant temperature anomalies are hatched and the 95% significance is obtained via bootstrap test. b) Same as a) but for relative precipitation changes.

Precipitation Figure 3.12b shows the simulated changes in the precipitation pattern resulting from historic well-mixed greenhouse gas and solar forcing. The most important features are: the high latitudes nearly uniformly receive more precipitation; the monsoonal precipitation in North Africa and China intensifies; the ITCZ is enhanced in the western Pacific and more focused on the equator in the eastern Pacific and in the Atlantic; considerable parts of the subtropics tend to receive less precipitation. These patterns are largely consistent with precipitation changes simulated in CMIP6 models where transient aerosols are included, although precipitation increases over the Indian Ocean and Northern Central Africa are not as pronounced as in the CMIP6 model mean and more pronounced over the Indonesian warm pool (compare with Figure SPM.5c in Masson-Delmotte et al. (2021)).

Ocean circulation The AWI-CM3 simulations reasonably reproduce the canonical pattern of the AMOC streamfunction, with an upper cell consisting of northward surface flow as well as southward return flow of North Atlantic Deep Water, and a lower cell representing the northward flow of AABW (Figures 3.13 a,b). During the spinup simulation the maximum of the northward transport between 30-45°N in AWI-CM3 fluctuates at around 20 Sv (see Figure 3.13c.). Initially the AMOC gradually slowed down to 18 Sv while the upper ocean was spuriously warming, as described in Section 3.4.1. After applying the total mass fixer starting after 500 years into the SPIN experiment the AMOC is recovered to 20 Sv along with the cooling of the upper ocean (Figure 3.3b).

Figure 3.13d shows a rather strong decline of the AMOC strength over the last 70 years of the HIST simulation, while the multi decadal natural variability of the AMOC is still high. As we do not have additional ensemble members, we do not make strong statements about the impact of historic forcing on the AMOC. However, we can conclude that our simulated AMOC response to historical forcing is consistent with recent synthesis based on observations (Caesar et al., 2022), and the ability for rapid AMOC state changes, as described in Ollinaho et al. (2017), does seem to exist in AWI-CM3, since our low resolution is indeed higher than their high resolution case. While the upper cell diminishes considerably under historic forcing, the lower one is mostly unaffected.

AMOC variability across all latitudes is well correlated, pointing to the same (northern) origin of the signal. In the HIST run the decrease of AMOC is found across all latitudes. The correlation is high but not perfect (see years between 1920 and 1930, for instance). This indicates that the recirculating cell, associated with physical and numerical mixing in the model caused by the advection operator, changes in strength (Sidorenko et al., 2021). Further conclusions would require extra analysis in the density space and the isopycnal framework (as in Sidorenko et al. (2021)) which we didn't activate in this run. However, this extra analysis was done by Sidorenko et al. (2021) and they concluded that the NAO was the main driver of AMOC variability.

Simulated volume transport fluxes were computed across several major ocean straits (Table 3.4). Historical values averaged over 1985-2014 match well the observation-based estimates for most straits. Two exceptions are the Nares and Davis Straits where the simulated transport is lower than in the observational estimates. Indeed, these very narrow straits are likely not well resolved on the CORE2 mesh. In the Arctic, the poleward inflow through the Barents Sea Opening and Bering Strait is somewhat overestimated, and counterbalanced by a southward transport at Fram Strait larger than in the observational estimates (yet all remain within the uncertainty range). The simulated Antarctic Circumpolar Current (ACC) transport through the Drake Passage is within the range of observations. While being lower than the most recent measurements by Donohue et al. (2016), our AWI-CM3 estimate is comparable to the CMIP5 multi-model mean (MMM) and larger than the CMIP6 MMM (Beadling et al., 2020).

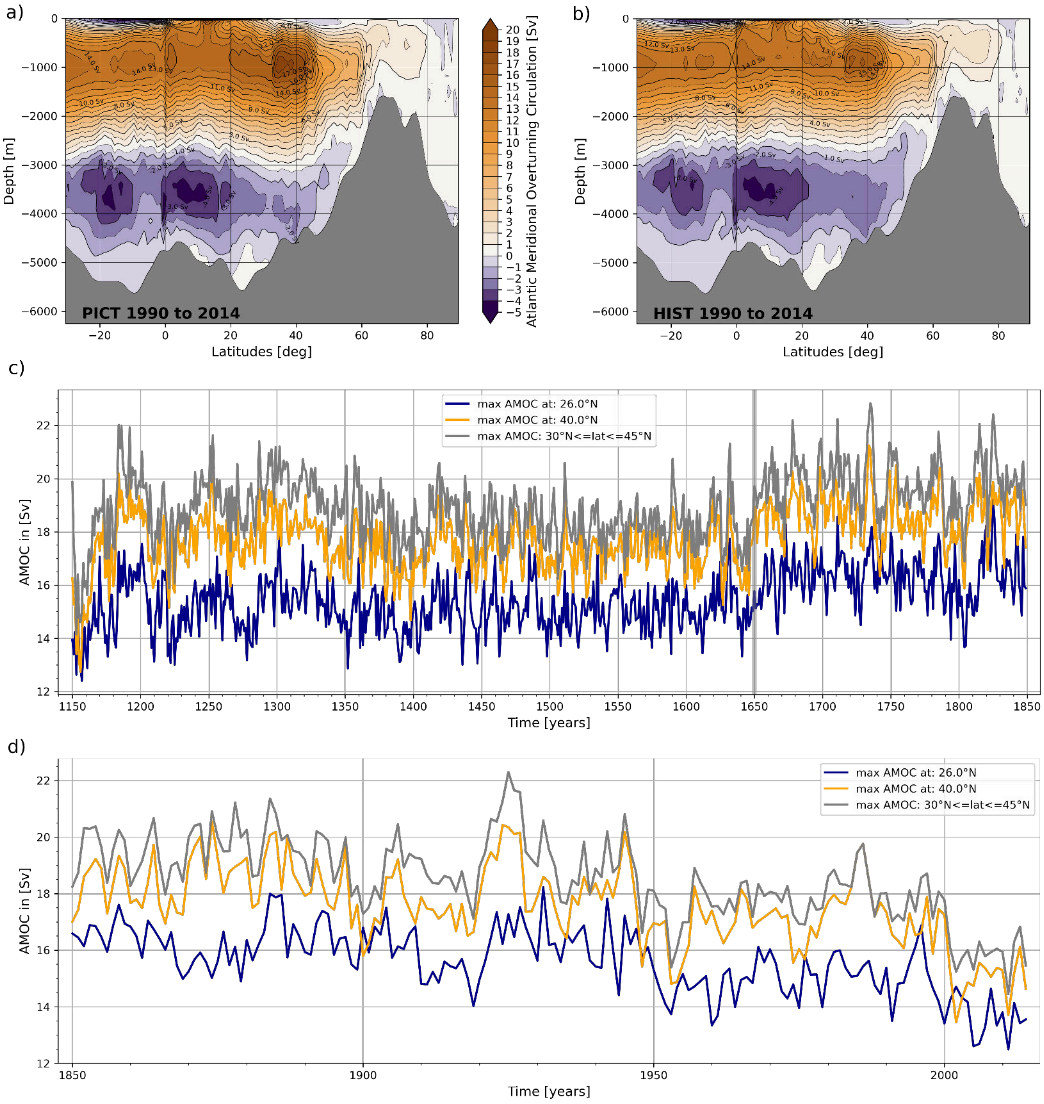

Figure 3.13: a) Atlantic Meridional Overturning Circulation (AMOC) streamfunction averaged over the last 25 years in the pre-industrial control (PICT) simulation. b) as a) but for the historic (HIST) simulation. c) Evolution of the AMOC maximum at different latitudes throughout the spinup simulation (SPIN) that precedes both PICT and HIST. d) Evolution of the AMOC during HIST.

Historical transports through major straits are thus satisfactorily reproduced in the present AWI-CM3 configuration. Future configurations with an increased resolution, eddy-resolving ocean are expected to provide even more accurate results within narrow straits and in eddy-rich areas such as the Southern Ocean, where mesoscale activity is key in accurately depicting the ACC behavior (e.g., Rackow et al., 2022).

3.4.5 Climate Sensitivity Experiments

Equilibrium Climate Sensitivity (ECS) To investigate the ability of AWI-CM3 to simulate warmer climate states, we conducted the 4xCO_2 experiment which prescribes a sudden permanent increase of the CO2 concentrations to 4 times (1137.27 ppm) the base value (284.32 ppm) from 1850. It can be used to analyze the model's inherent climate sensitivity. As shown by Gregory et al. (2004) the relationship between the change in net downward radiative flux and the change in near surface (2m) air temperature can be described by a linear regression model. The Gregory plot in Figure 3.14 a) was computed from the 4xCO_2 experiment in comparison to the pre-industrial control simulation. The first axis intersection point determines the instantaneous radiative forcing $F = 7.06\,\frac{W}{m^2}$ resulting from the quadrupling of CO2. The linear regression line intersects the second axis at an Equilibrium Temperature difference $\Delta T = 6.49\,°C$, resulting in a climate response parameter of AWI-CM3 of $\alpha = \frac{\Delta T}{F} = 0.92\,\frac{K}{Wm^2}$. Equilibrium Climate Sensitivity (ECS) is given by doubling rather than quadrupling CO2 concentrations, and is thus ECS$= \frac{\Delta T}{2} = 3.2\,°C$. With this ECS value the AWI-CM3 prototype finds itself near the center of the range predicted by CMIP6 models ($1.8 - 5.6\,°C$) (Meehl et al., 2020; Scafetta, 2021), and the same as AWI-CM1, which had a value of 3.2°C as well.

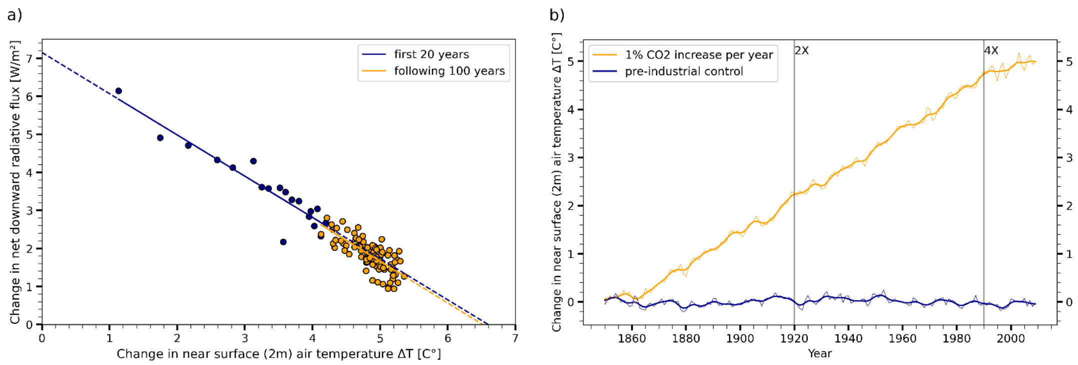

Figure 3.14: a) Gregory regression plot from the abrupt 4xCO_2 experiment in comparison to the pre-industrial control. We construct the linear regression of near surface (2m) air temperature (ΔT) change against the downward net radiative flux change (ΔF). From its axis intersection points we obtain the radiative forcing $\Delta F = 7.06\,\frac{W}{m^2}$, and the Equilibrium temperature difference $\Delta T = 6.49\,°C$. The climate response parameter of AWI-CM3 is then $\alpha = \frac{\Delta T}{\Delta F} = 0.92\,\frac{K}{W}$ and the Equilibrium Climate Sensitivity ECS$= \frac{\Delta T}{2} = 3.24\,°C$. The first 20 years already result in a linear regression almost identical to the following 100 years. b) As Figure 3.11 b), but for the experiment with 1% increase of CO_2 per year. Vertical lines indicate doubling and quadrupling of CO_2 concentrations. The estimated Transient Climate Response is 2.1°C.

Transient Climate Response (TCR) We obtain the transient climate response of AWI-CM3 TCo159L91-CORE2 from an experiment that features increased CO_2 forcing by 1% per year, starting from the 1850 value of 285 ppm. Radiative forcing thus applied results in a near surface (2m) air temperature increase of 2.1°C after 70 years, when CO_2 concentrations have doubled, as shown in Figure 3.14b. As with the ECS, the TCR of AWI-CM3 is also near the center of the CMIP6 model distribution of $1.8 - 5.6\,°C$ (Scafetta, 2021). Compared to the predecessor model AWI-CM1, the TCR did not change. Interestingly, a further doubling to a total of four times the 1850 CO_2 concentrations until the year 1990 results in another 2.6°C increase, and thus a larger global mean near surface (2m) air temperature rise than during the first period.

3.5 Computational Performance

The computational performance of a climate model can be measured according to a variety of criteria. Balaji et al. (2017) provide a good overview of what can be considered the computational performance, but in our analysis we will focus on just two aspects, the Simulated Years Per Day (SYPD) and the computational cost measured in Core Hours per Simulated Year (CHSY). Systematic and rigorous experiment design would require that we identify all the degrees of freedom and vary them in all combinations. Unfortunately the number of degrees of freedom is large, including atmosphere and ocean vertical and horizontal resolution, atmospheric spectral and grid point resolution, number of cores allocated for MPI and/or OpenMP parallelization for FESOM2, OpenIFS43 and XIOS, as well as the amount of model output for each of the main components etc. Testing all combinations is impractical. Instead we present results for setups that have been optimized empirically, involving not only the use of analytical tools such as Dr.Hook (Saarinen et al., 2005), LUCIA (Maisonnave et al., 2020) and the XIOS internal statistics, but also educated guesswork. It may well be that better configurations exist, but AWI-CM3 can at a minimum perform to the level presented here.

Tables 3.1 and 3.2 list the SYPD and CHSY values we achieved when optimization is done for speed and cost, respectively. Note, that the scaling limit of TCo319L137-DART has not been reached and simulations with upwards of 10 SYPD are likely feasible.

3.5.1 High Resolution Outlook

While we document mainly the first CMIP-prototype simulations of AWI-CM3 and its strengths and weaknesses at low resolution, we also tested higher resolution configurations. In the table of figure 3.15 we show the performance of a 31km atmosphere with 137 vertical layers, coupled to a high-resolution ocean with a mesh that features 3.1 million surface nodes and 80 layers. This configuration with the name TCo319L137-DART has been run for 50 years under constant 1990

Atmosphere grid	Ocean mesh	IO scheme	Cores	SYPD	CHSY
TCo95L91	CORE2L47	Sequential	2593	124.05	501
TCo95L91	CORE2L47	XIOS parallel	2689	134.24	480
TCo159L91	CORE2L47	Sequential	2593	60.74	1024
TCo159L91	CORE2L47	XIOS parallel	2833	68.7	988
TCo319L137	DARTL80	XIOS parallel	15680	7.90	47528

Table 3.1: Computational performance optimized for integration speed. Simulated Years Per Day (SYPD), and core hours per simulated year (CHSY) of AWI-CM3 for three atmospheric grids, two ocean meshes and two IO schemes are shown. Values were measured on HPC system juwels@fz-juelich.de with Intel Xeon Platinum 8168 CPU, 2× 24 cores, 2.7 GHz processors, accepting sub-linear strong scaling. The atmospheric grids TCo95L91, TCo159L91 and TCo319L137 have a grid point resolution of 100, 61 and 31 km and 91, 91 and 137 vertical layers, respectively. The CORE2 mesh (Figure 3.2a) has 47 vertical layers, 127k surface nodes, a peak resolution of 20km in Northern mid to high latitudes and up to 125km in Subtropical Gyres. The horizontal resolution of the DART mesh follows the local Rossby radius, peaks at a highest resolution of 5km and has a maximum spacing of 27km, with ∼3.1 million surface nodes and 80 vertical layers.

Atmosphere grid	Ocean mesh	IO scheme	Cores	SYPD	CHSY
TCo95L91	CORE2L47	XIOS parallel	721	52.34	330
TCo159L91	CORE2L47	XIOS parallel	1297	42.71	736
TCo319L137	DARTL80	XIOS parallel	6769	4.61	35220

Table 3.2: As table 3.1 but optimized for computational cost instead of integration speed by limiting total core numbers within the limit of linear strong scaling.

forcing, with some of the insights gained while performing the set of experiments at low resolution already taken into account.

Key improvements of the TCo319L137-DART setup compared to TCo159L91-CORE2 are the eddy resolving ocean in the western boundary currents, with eddy permittance in the ACC region, as well as better representation of orography and related effects in the atmospheric model. In lower latitude regions the atmosphere has sufficient resolution to resolve and react to ocean eddies. Both atmosphere and ocean feature more vertical layers, allowing for better representation of vertical processes.

The ability of the TCo319L137-DART simulation to reproduce a climate as observed during the years 1990 to 2014 is better than that of the TCo159-CORE2 runs we analyzed so far. The improvement is almost universal with only the sea ice concentrations and mixed layer depths still showing below-average performance compared to CMIP6 models. A TCo159-CORE2 simulation of the same length and with the same forcing (not shown) showed performance almost identical to the last 25 years of the HIST experiment discussed above. We conclude that the

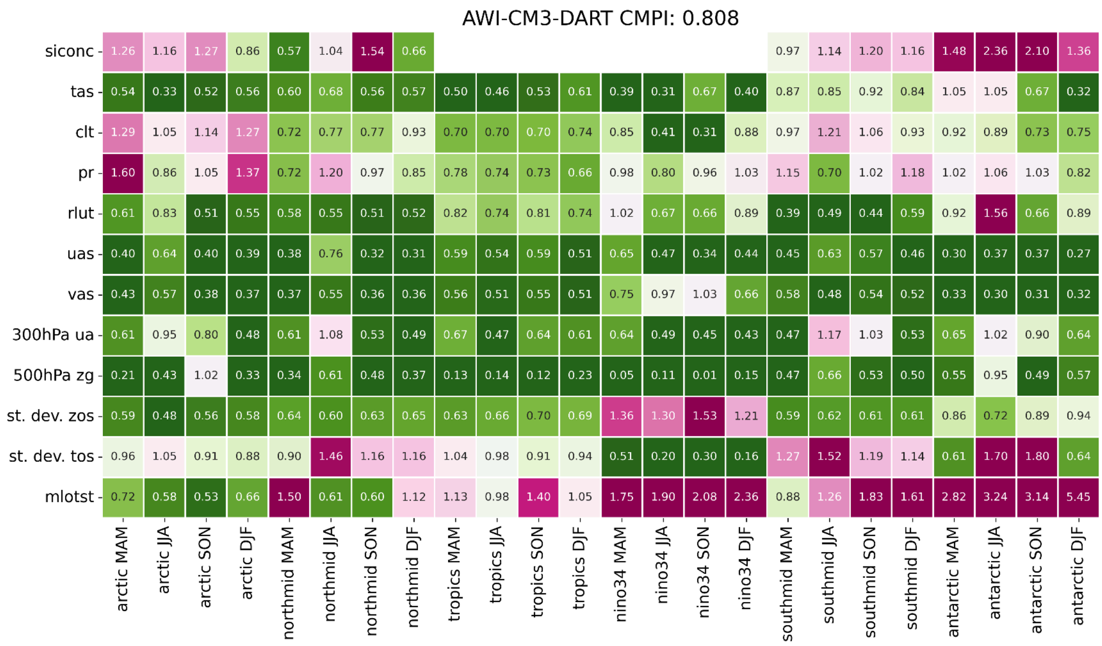

Figure 3.15: Same as Table 3.4 but for the last 10 years of a 50-year-long TCo319L137-DART simulation under constant 1990 forcing. Biases to observations are not only smaller than in our TCo159L91-CORE2 simulations, but also smaller than those of all but two (HadGEM3MM & NOAA-GFDL) of the CMIP6 models listed in 3.7 (Performance indices for CMIP6 models not shown).

improvement is related to the model resolution and continued model development, rather than the shorter run length or different forcing.

Obviously, the improved climatological performance comes at a cost, as detailed in Section 3.5. Every simulated year with TCo319L137-DART costs 35 times the CHSY and is performed at 15 times lower SYPD. More detailed exploration of the higher resolution capabilities of AWI-CM3 will be subject of future work.

3.6 Conclusions

We developed a new coupled climate model AWI-CM3, by coupling the AWI ocean model FESOM2, the ECMWF NWP atmosphere model OpenIFS CY43R3, a small runoff-mapper model, and the XIOS parallel IO library. The coupling exchange is achieved via the OASIS3-MCT 4.0 library.

We ran a set of experiments closely resembling the Coupled Model Intercomparison Project phase 6 (CMIP6) Diagnostic, Evaluation and Characterization of Klima (DECK) simulations to evaluate the representation of the climatological state and the computational performance of the new model. From the experiments we found that, when activating the humidity mass fixer for OpenIFS, the model was able to reach a near equilibrium under constant 1850 well-mixed greenhouse gas and solar forcing. After 700 years of spinup we branched off four experiments, a historic simulation (165y), a pre-industrial control run (165y), and two idealized experiments, one with a sudden increase to 4xCO_2 (120y) and the other with 1% CO_2 (150y) increase per year.

Climate sensitivity experiments with AWI-CM3 obtained an Equilibrium Climate Sensitivity and Transient Climate Response of 3.2°C and 2.1°C, respectively, both of which are near the center of the CMIP6 spreads.

Using the last 25 years of the historical simulation we established that a low resolution version of AWI-CM3 provides above CMIP6-average performance for representing the climatological state of precipitation, wind speeds, cloud fraction, 500 hPa geopotential height and air temperature north of 30°S. We found that the Southern Ocean sea ice concentration and thickness were severely underestimated, leading to large positive near-surface air temperature biases in this region, and traced the sea ice biases to spuriously large mixed layer depth, a positive ice albedo feedback and biases in shortwave downward radiation associated with cloud fraction between 45-60°S.

AWI-CM3 is capable of realistically simulating the Atlantic meridional overturning circulation (AMOC) in terms of both the shape and strength of the streamfunction, as well as reproducing a decreasing trend in the historical period consistent with observations. While the model produces an El Niño-Southern Oscillation (ENSO) at realistic frequencies, the amplitude of ENSO is currently underestimated.

Our recommendations for resolving the Southern Ocean sea ice concentration and thickness biases in future versions of AWI-CM3 include re-tuning of the vertical mixing scheme, and the inclusion of coupling minor fluxes that are at least one magnitude smaller than the ones exchanged so far. We have identified the coupling of ocean surface currents, rain temperature, enthalpy of snow falling into the ocean, enthalpy of melting icebergs and basal melt flux as promising candidates to reduce model biases. Based on literature we suggest porting and activating the Stochastically Perturbed Parametrisations scheme as a potential way to improve ENSO amplitude.

The advanced computational efficiency and scalability of AWI-CM3, combined with a very solid model and coupling physics implementation, will eventually enable us to perform full DECK and scenario simulations at resolutions of 5-25km, that were previously reserved for the high end of the HighResMIP protocol. We provide a preview with a shorter high-resolution simulation, indicating that most AWI-CM3 climatological biases at future operational resolution will be about half those of the average CMIP6 model.

The ocean model FESOM2 source code is available on Zenodo at `https://doi.org/10.5281/zenodo.6335383` and at `https://github.com/FESOM/fesom2/releases/tag/AWI-CM3_v3.0`. OpenIFS is not publicly available but rather subject to licensing by ECMWF. However, licenses are readily given free of charge to any academic or research institute. All modifications required to enable AWI-CM3 simulations with OpenIFS CY43R3V1 as provided by ECMWF can be obtained on Zenodo at: `https://doi.org/10.5281/zenodo.6335498`. The OASIS coupler is available upon registration at: `https://oasis.cerfacs.fr/en/downloads/`. The XIOS source code is available on Zenodo (`https://doi.org/10.5281/zenodo.4905653` Meurdesoif, 2017) and on the official repository (`http://forge.ipsl.jussieu.fr/ioserver`, last access: 4 March 2022). The runoff mapper scheme is available on Zenodo at `https://doi.org/10.5281/zenodo.6335474`. The compile and runtime engine esm-tools is available on Zenodo at: `https://doi.org/10.5281/zenodo.6335309`. All data required to reproduce the plots shown here can be found at: `https://doi.org/10.5281/zenodo.6337593`, `https://doi.org/10.5281/zenodo.6337571`, and `https://doi.org/10.5281/zenodo.6337627`. The processing and plotting scripts for the reproduction of the shown analysis can be found at: `https://doi.org/10.5281/zenodo.6653826`. Documentation of AWI-CM3 and a user guide can be found at: `https://awi-cm3-documentation.readthedocs.io`.

3.7 List of CMIP6 Models for CMPI Calculation

ACCESS-CM2, AWI-CM-1-1-MR, BCC-CSM2-MR, CAMS-CSM1-0, CAS-ESM2-0, CanESM5, CIESM, CESM2, CMCC-CM2-SR5, CNRM-CM6-1-HR, FGOALS-f3-L, FIO-ESM-2-0, E3SM-1-1, EC-Earth3, GFDL-CM4, GISS-E2-1-G, HadGEM3-GC31-MM, ICON-ESM-LR, IITM-ESM, INM-CM5-0, IPSL-CM6A-LR, KIOST-ESM, NESM3, NorESM2-MM, MCM-UA-1-0, MIROC6, MPI-ESM1-2-LR, MRI-ESM2-0, SAM0-UNICON, TaiESM1

Appendix A

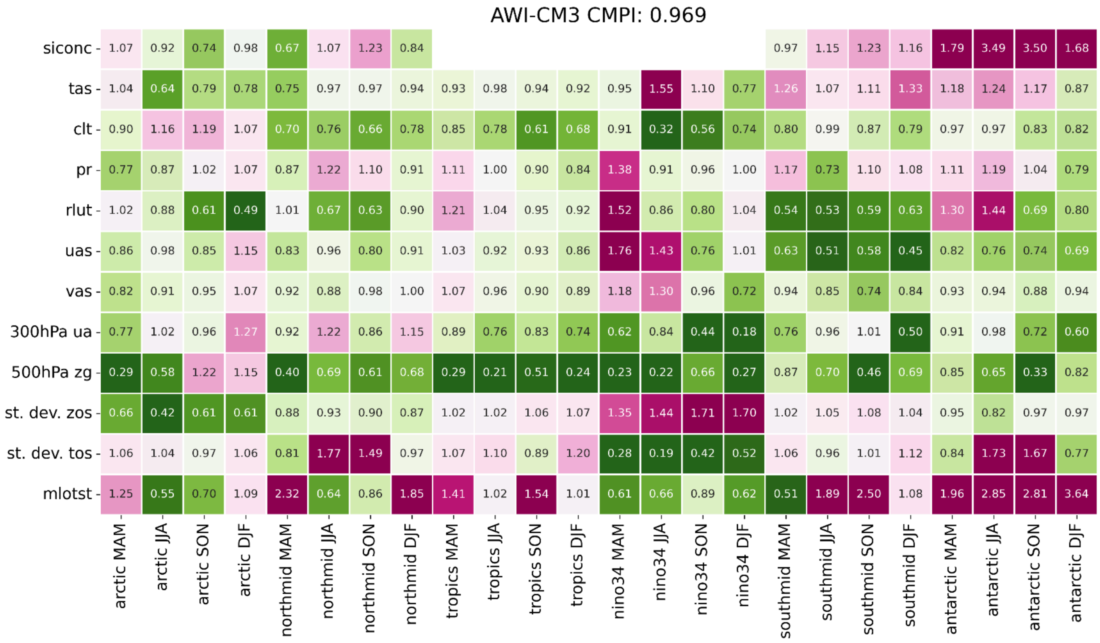

Figure 3.16: HIST biases as the table in Figure 3.4 , but using NCEP-DOE2 re-analysis by Kistler et al. (2001) instead of ERA5 for near-surface air temperature (tas), eastward near-surface wind (uas), northward near-surface wind (vas), 300 hPa eastward wind (ua), 500 hPa geopotential height. Note that ERA5 was created using IFS CY41R2, a model closely related to the OpenIFS CY43R3 atmosphere employed in AWI-CM3.

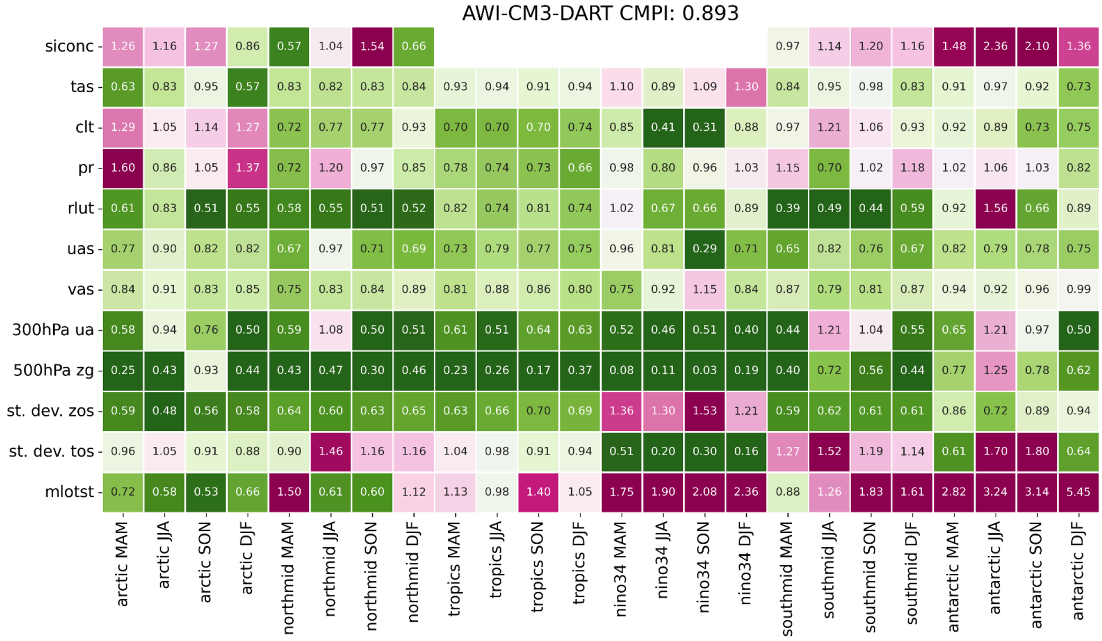

Figure 3.17: **TCo319L137-DART biases as the table in Figure 3.15, but using NCEP-DOE2 re-analysis by Kistler et al. (2001) instead of ERA5 for near-surface air temperature (tas), eastward near-surface wind (uas), northward near-surface wind (vas), 300 hPa eastward wind (ua), 500 hPa geopotential height. Note that ERA5 was created using IFS CY41R2, a model closely related to the OpenIFS CY43R3 atmosphere employed in AWI-CM3.**

Table of Observational Datasets for Climate Model Performance Index Calculation

Variable	Longname	Dataset	Time range
tas	Near surface (2m) air temperature	ERA5 Reanalysis	1989/11/01 to 2014/11/30
uas	Near surface (10m) zonal wind speed	ERA5 Reanalysis	1989/11/01 to 2014/11/30
vas	Near surface (10m) meridional wind speed	ERA5 Reanalysis	1989/11/01 to 2014/11/30
300 hPa ua	300 hPa zonal wind speed	ERA5 Reanalysis	1989/11/01 to 2014/11/30
300 hPa zg	500 hPa geopotential height	ERA5 Reanalysis	1989/11/01 to 2014/11/30
pr	Precipitation flux	GPCP v2.3	1989/11/01 to 2014/11/30
siconc	Sea ice area fraction	OSISAF OSI-450	1989/11/01 to 2014/11/30
rlut	TOA outgoing longwave flux	CERES-EBAF	2000/03/15 to 2014/06/30
clt	Cloud area fraction	MODIS Atmosphere L2	2000/03/15 to 2014/11/30
Std Dev tos	Std Dev of ocean surface temperature	HadISST	1989/11/01 to 2014/11/30
Std Dev zos	Std Dev of sea surface height	JASON-1, JASON-2, CryoSat	2002/01/01 to 2014/11/30
mlotst	Mixed layer depth	C-GLORSv7 Reanalysis	1989/11/01 to 2014/11/30

Table 3.3: Table of observational datasets for climate model performance index calculation

Ocean current flow rates

Transport (Sv)	AWI-CM3 HIST	Observations	References of observations
Fram Strait	-2.96	-2.0 ± 2.7	Schauer et al. (2008)
Davis Strait	-0.42	-1.6 ± 0.5	Curry et al. (2014)
Bering Strait	1.19	0.83 ± 0.66, 1.0 ± 0.05	Roach et al. (1995), Woodgate (2018)
Nares Strait	-0.31	-0.57 ± 0.09, -0.8 ± 0.3	Münchow and Melling (2008), Münchow et al. (2006)
Barents Sea Opening	2.46	2.0	Smedsrud et al. (2010)
Drake Passage	148.63	136.7 ± 6.9, 173.3 ± 10.7	Meredith et al. (2011), Donohue et al. (2016)
Mozambique Channel	-19.59	-16 ± 8.9	Ridderinkhof et al. (2010)

Table 3.4: Transport fluxes [Sv] through a number of straits and channels as simulated by AWI-CM3 in comparison to observational estimates. Analysis period for was 1990-2014 of the historic simulation.

Chapter 4

Evaluation Tools

"The best investment is in the tools of one's own trade."
-Benjamin Franklin

4.1 Degrees of Freedom and Information Content

Climate models ostensibly carry a very large amount of information. The CMIP6 family of model intercomparison studies features a total of 1212 variables over all Earth System Model domains. Many fields will be written monthly, some daily, others even hourly. While some interesting variables are interface and therefore single layer variables, others are defined and written on multiple model layers. The overall quantity of data produced is astounding, especially when multi-model ensembles are considered. Estimates for the total data volume produced by CMIP6 and available for dissemination exceed 20 PB.

Earth System modelling is far from the first sector confronted with big data analysis issues (Tsai et al., 2015). We are however in the fortunate situation that we define clearly what content we store, which enables the construction of simple yet powerful algorithms for discovery. The remainder of this chapter consists of the description and evaluation of one such method, which has been submitted by Streffing and Semmler to the Journal of Open Research Software.

4.2 Introduction

Climate Model Performance Indices (CMPI) after Reichler and Kim (2008) have been used by many researches as a convenient first glance to identify strengths and weaknesses of their own and other climate models (Baker and Taylor, 2016). These indices thus help to direct the focus of research and model development. With cmpitool, a climate model's ability to reproduce the observed conditions and reanalysis data for 14 key climate variables is put in relation to the abilities of either 30 widely used Coupled Model Intercomparison Project Phase 6 (CMIP6) models or to any climate model previously evaluated with cmpitool. The former can help gauge performance in comparison to the wider community, while the latter enables feature by feature based continuous evaluation during development. In particular, the latter feature is not present in previous implementations of CMPI tools. The practice of using scorecards has been long established in the Numerical Weather Prediction (NWP) community (Haiden et al., 2018, 2022), but seldom used for climate models thus far.

The toolbox is written as a number of flexible python3 functions using an object-oriented approach. It has been used in its current form by Streffing et al. (2022), and in a shell, FORTRAN90, GRADS and CDO based predecessor version by Semmler et al. (2020); Rackow and Juricke (2020). A small subset of the functionality of cmpitool is already in widespread use as an ncl recipe script inside ESMValTool (Eyring et al., 2020), based on Gleckler et al. (2008) and Righi et al. (2015). In particular, the evaluation of atmospheric climate performance compared to a fixed set of older Coupled Model Intercomparison Project Phase

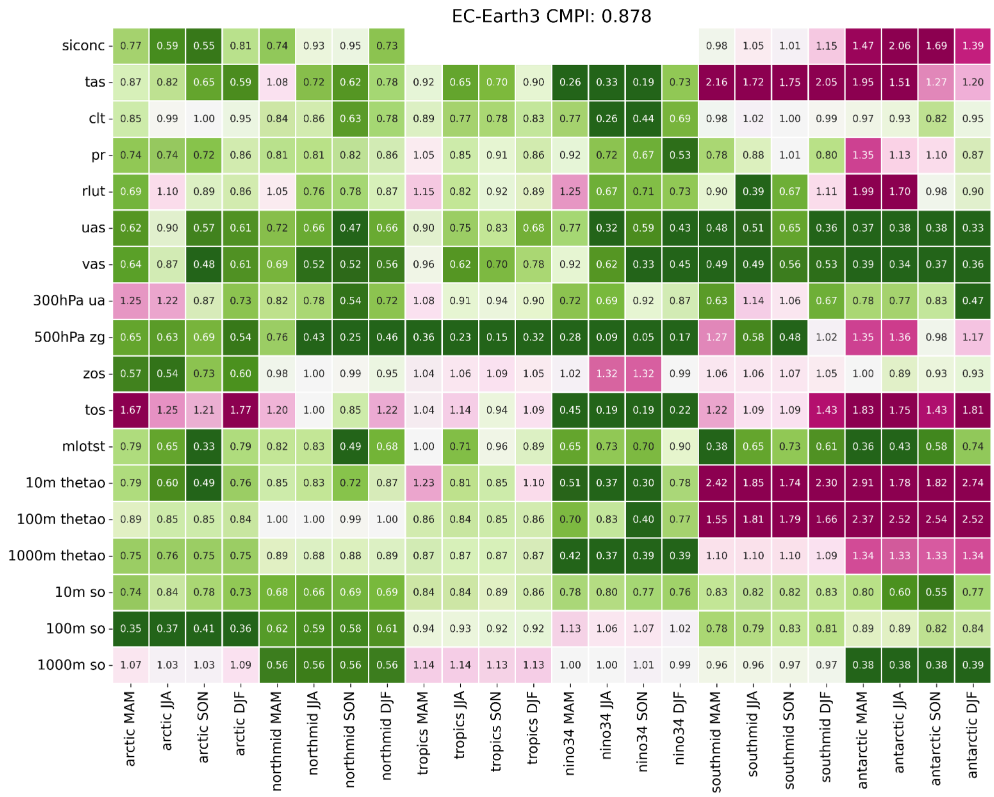

Figure 4.1: Using cmpitool to compare the simulated climate skill of one the CMIP6 models, EC-Earth3, relative to observational estimates with the average skill of 30 CMIP6 models. Values < 1 (> 1) indicate improved (degraded) agreement with observational or reanalysis data. EC-Earth shows performance almost universally above community average performance, with the exception of the Southern Ocean and Antarctica, in good agreement with the known model biases from in depth analysis Döscher et al. (2022).

5 (CMIP5) models, for 3 regions (global, northern hemisphere, southern hemisphere), and two seasons (boreal winter and summer) is available in ESMValTool (Eyring et al., 2020). In addition to these options, cmpitool allows for evaluation of both atmosphere and ocean, including some surface variances, for arbitrary regions, with up to four seasons and in comparison to either the more recent CMIP6 models or previously analysed runs. The evaluation results in an easy to interpret table, as shown in Figure 4.1.

Furthermore cmpitool is not fixed in the selection of reference models. Any run(s) once evaluated with the tool can subsequently be used as reference for further simulations. This opens up the possibility to use cmpitool during model development and tuning (parameter space estimation for observationally poorly constrained parameters (Hourdin et al., 2017)), by setting e.g. the previous, frozen version of a model as the performance baseline, and observing the changes with each newly incorporated model development or tuning setting. One example of such a model change and it's complex impact on the simulated climate in reference

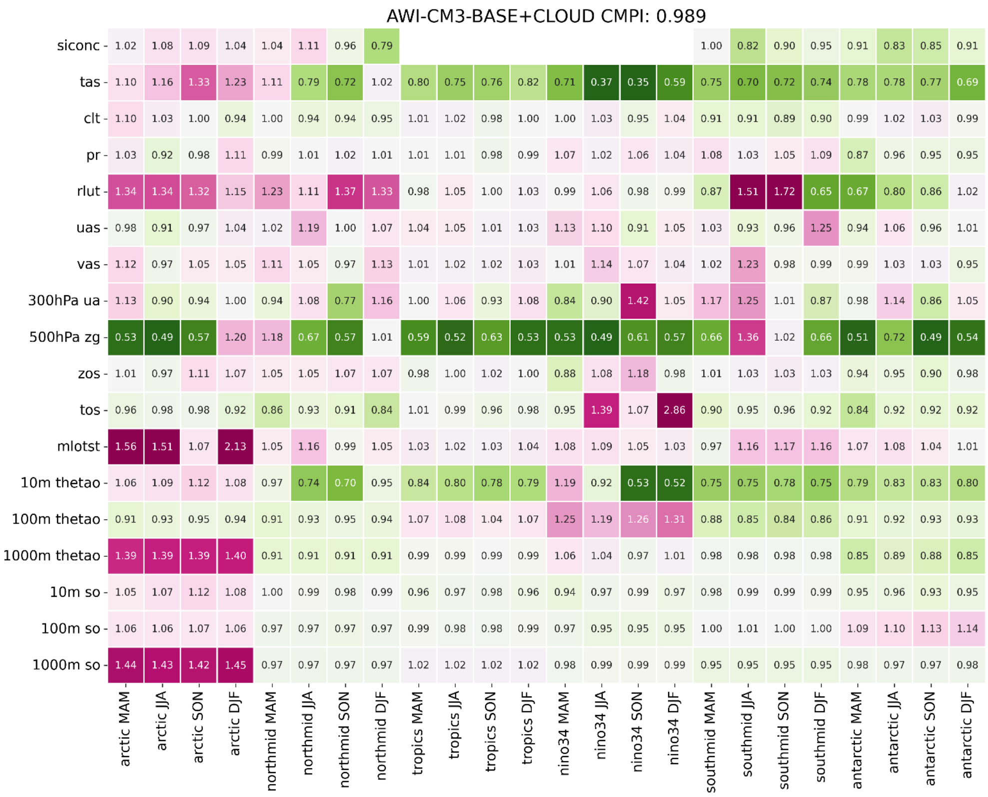

Figure 4.2: Usage of cmpitool for the generation of scorecards on an AWI-CM3 development version in order to provide an overview of the impact of model changes made between model versions. The example illustrates the impact of improving the lack of supercooled liquid water in the modelling of convective cold-air outbreaks in storm tracks (Forbes et al., 2016) on features as far removed as Arctic deep ocean salinity. Values < 1 (> 1) indicate improved (degraded) agreement with observational or reanalysis data relative to a reference version of the model. The utilised reference was the model version immediately preceding the introduction of the model improvement.

to the immediately preceding model version is shown in Figure 4.2. In this mode the tool functions in a similar fashion to the scorecard system employed by the European Centre for Medium-Range Weather Forecasts (ECMWF) to characterize the performance of each new version of their operational numerical weather prediction system (Haiden et al., 2022; Buizza et al., 2018).

Climate model tuning is the process by which individually developed and improved sections of the model are tuned towards a sensible overall simulated climate, analog to the tuning of instruments in an orchestra. Here, cmpitool can guard against a common pitfall of model tuning, whereby an intended improvement in one climate variable can, through nonlinearities and a complex causal web of effects, lead to unintended and overlooked degradation elsewhere. Because model tuning is typically a manual or at best semi-automatic process, the quality of the final result depends in large part on the breadth and depth of knowledge of the scientist doing the tuning. Tool assistance, such a provided by cmiptool and its scorecards can help guide and streamline the process.

The second major upgrade compared to previous algorithms is the inclusion of up to date observational estimates. The tool itself ships with observational estimates for 14 key climate variables listed with sources and licences in table 4.1. Wherever possible, the observational estimates cover the period from December 1989 till November 2014, constituting the last 25 years of full seasons covered by CMIP6. Provided sufficiently reliable observational estimates are available, the toolbox could also be applied to evaluation of past climate states.

Variable	Shorthandle	Unit	Type	Source
Sea Ice Concentration	siconc	%	Satellite	OSISAF
Total Cloud Cover Percentage	clt	%	Satellite	MODIS
Precipitation	pr	$\frac{kg}{m^2 s}$	Satellite	GPCP
TOA Outgoing Longwave Radiation	rlut	$\frac{W}{m^2}$	Satellite+	CERES-EBAF
Near-Surface (2m) Air Temperature	tas	°C	Reanalysis	ERA5
Eastward Near-Surface (10m) Wind	uas	$\frac{m}{s}$	Reanalysis	ERA5
Northward Near-Surface (10m) Wind	vas	$\frac{m}{s}$	Reanalysis	ERA5
Eastward 300hPa Wind	300hPa ua	$\frac{m}{s}$	Reanalysis	ERA5
500hPa Pressure Level Height	500hPa zg	m	Reanalysis	ERA5
SD of Sea Level Anomalies	zos	m	Satellite	NOAA-LSA
SD of Sea Surface Temperature	tos	C°	Satellite	HadISST2
Mixed Layer Thickness Defined by Sigma T	mlotst	m	Reanalysis	C-GLORSv7
Ocean Temperature at 10m, 100m, 1000m	thetao	K	In-Situ+	EN4
Salinity at 10m, 100m, 1000m	so	PSU	In-Situ+	EN4

Table 4.1: Table of key climate variables that cmpitool evaluates climate models for. Types with the + indicator denote, that in addition to the instrument measurements some degree of modelling took place to arrive at the observational estimate. Not all observational analysis and reanalysis data is equally reliable. For example the Mixed Layer Thickness reanalysis depends on the vertical mixing parameterization choices made in the ocean model used for the reanalysis. The evaluation datasets are a constrained estimate of the truth, not necessarily the truth itself.

4.3 Implementation and Architecture

The implementation we present here is done solely through python, with a minimal number of dependencies. Climate model raw output has to be pre-processed to fit the Climate Model Output Rewriter (CMOR) (Nadeau et al., 2018) naming and unit convention. Via separation of concerns, the pre-processing is done outside of cmpitool, and we deliver the tool with example scripts for both CMORized and not CMORized model data. Integration of cmpitool into existing toolboxes, which could for example provide raw data pre-processing capabilities and replace the example scripts, should therefore be relatively straightforward. Care was taken to ensure that the redistribution of the included subsets of satellite observation and reanalysis data is either covered by an open licence for the original dataset

(OSI SAF, ERA5, EN4, GPCP, HadISST2), or explicitly permitted by the authors of the datasets (CERES-EBAF, C-GLORSv7, NOAA-LSA, MODIS).

4.4 Quality Control

Cmpitool has been unit tested at function level and functionally tested with 30 CMIP6 models. For models with which the authors are familiar, such as EC-Earth3 (Döscher et al., 2022), AWI-CM3 (Streffing et al., 2022) and AWI-CM1 (Semmler et al., 2020), functional tests showed that cmpitool can detect the mean model biases that are known for these model versions. A load test places a full model bias analysis with cmpitool at a reasonable 40 seconds. Documentation is built via Sphinx and provided with the tool as pdf, as well as via readthedocs at: `https://cmpitool.readthedocs.io/`.

4.5 Availability

Operating system

Cmpitool can be used on any system capable of running python ≥3.6.0

Programming language

The python version required for running cmpitool is ≥3.6.0

Additional system requirements

-

4.6 Dependencies

Cmpitool depends on the python libraries geopandas, matplotlib, numpy, pandas ≥1.0.0, pooch, regionmask, seaborn, tqdm and xarray. In order to limit dependencies on observational estimates from third parties, the relevant subsets are shipped with cmpitool. The list of data sources and permissions to do so are listed in table 4.2.

Dataset	Citation	License for redistribution of subset of data
CERES-EBAF	NASA/LARC/SD/ASDC (2019)	Permission granted
C-GLORSv7	Storto et al. (2016a)	Permission granted
EN4	Good et al. (2013)	https://www.nationalarchives.gov.uk/doc/non-commercial-government-licence/version/2/
ERA5	Hersbach et al. (2020b)	https://cds.climate.copernicus.eu/api/v2/terms/static/licence-to-use-copernicus-products.pdf
GPCP	Adler et al. (2018a)	https://cds.climate.copernicus.eu/api/v2/terms/static/global-precipitation-climatology-project.pdf
HadISST2	Titchner and Rayner (2014b)	https://www.nationalarchives.gov.uk/doc/non-commercial-government-licence/version/2/
MODIS	Platnick (2017)	Permission granted
NOAA-LSA	only acknowledgement	Permission granted
OSISAF	OSISAF (2017)	https://osisaf-hl.met.no/sites/osisaf-hl.met.no/files/user_manuals/osisaf_cdop3_ss2_pum_ice-conc_v1p6.pdf

Table 4.2: Table of observational and reanalysis estimates for which the subsets relevant for cmpitool are shipped together with the toolbox. For a number of these datasets the license agreements explicitly allow republishing in this context. For those without obvious license statement permission was obtained.

4.7 Reuse Potential

Tuning and development of climate models is an ongoing process undertaken on several dozen global models, at hundreds of research institutes and universities, involving thousands of researches. Tools that aid our community on making informed decisions on where to focus our efforts, where each individual model has its strengths and weaknesses will find ample use. The two main use cases will be the CMIP6 intercomparison mode and the scorecard mode. In the former mode, researchers will use cmpitool for a broad comparison with the wider climate modelling community and the identification of model weaknesses. In the latter mode, researchers will use cmpitool to reveal complex and sometimes unexpected impacts of incremental changes made during model development, allowing more responsive model development cycles.

Extension of the tool comes in three complexity steps. For the scorecard mode, researchers will easily be able to add their new variables and define any interest region they wish to focus on. For the CMIP6 mode such extensions are also possible, but require more work, as the new variable or region has to be added for each model. Finally, users can add a completely new evaluation dataset, for example HighResMIP (Haarsma et al., 2016) or the upcomping CMIP7. The integration of cmpitool into existing evaluation libraries will also be possible, as the tool is using a widely used data analysis language and provides a clear interface.

Chapter 5

Coupling Improvements and Applications

"Since all models are wrong the scientist must be alert to what is importantly wrong. It is inappropriate to be concerned about mice when there are tigers abroad."

-George E. P. Box

In the previous four chapters I laid out the foundations for this main part of my work. I gave my motivation for working on coupled climate models and in particular at the interface, where knowledge from multiple domains is needed. I touched on some of the fundamentals of coupled climate modelling, and then described and evaluated my own model AWI-CM3. With CMIP-Tool I then introduced a tool which can be used to quickly asses the first order impact of coupled climate model changes.

With a baseline AWI-CM3 version 3.0 coupled, described, and evaluated in chapter 3, as well as armed with knowledge of how to break down the climate model output into readily comparable metrics from chapter 4, I now focus on the coupling interface improvement of AWI-CM3. A number of the collected improvements are of my own design, others were synergy effects due to co-developments and early applications of the model. Yet more represent the adaptations progress made in the wider community, which I incorporated into AWI-CM3.

5.1 Data Assimilation and New Sea Ice Surface Thermodynamics

This section contains results first presented in a peer-reviewed paper by Mu et al. (2022) which implemented ensemble Kalman filter data assimilation into AWI-CM3. My own share of this work was to infer some of the early issues with AWI-CM3 coupling from the direction that the data assimilation algorithm had to pull the model fields into. As such, the work presented in Mu et al. (2022) directly led me to transfer the sea ice surface thermodynamics from OpenIFS into FESOM2. Since FESOM2 did not yet have sea ice surface thermodynamics for the coupled model code, I adapted a simple scheme from ECHAM6 that had been successfully used by AWI-CM1 and AWI-CM2. The source code that I implemented into FESOM2 can be found in appendix C.3.

Sea ice thickness in AWI-CPS The first major application of AWI-CM3 was through the AWI Coupled Prediction System (AWI-CPS). The data assimilation in AWI-CPS targets the ocean and sea ice, constraining sea-ice concentration, sea-ice thickness, sea-ice velocity (u-component and v-component), 3D temperature, 3D salinity, and sea-surface height. The methodology employed is the Local Error Subspace Transform Kalman Filter (LESTKF) by Nerger et al. (2012). For the technical realization AWI-CPS implements AWI-CM3 into the Parallel Data Assimilation Framework (PDAF) (Nerger and Hiller (2013), http://pdaf.awi.de) with online-coupled data assimilation (Nerger et al., 2020), providing high efficiency and full parallelization of the daily analysis and forecast steps (Mu et al., 2022). Figure 5.1 provides an overview of the layout of the ensemble of AWI-CM3 simulations orchestrated via PDAF.

The ultimate application of AWI-CPS is to provide sea ice forecasts for research

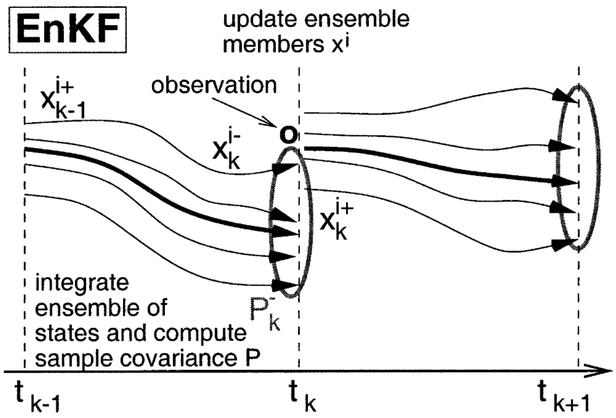

Figure 5.1: Schematic of the Ensemble Kalman Filter (EnKF) AWI Coupled Prediction System. The ensemble has 30 AWI-CM3 members orchestrated by the Parallel Data Assimilation Framework. Within the continuous spinup run, the filtering is applied daily. After every 3 spinup months a one year long free running prediction experiment is branched off. Graphic taken from Reichle et al. (2002). Further details on AWI-CPS can be found in Mu et al. (2022).

and commercial applications, for example helping light ships travelling within the sea ice marginal zones avoiding thicker ice, or guiding research vessels like Polarstern to suitable ice floes for scientific exploration. In the meantime, however, the co-development of AWI-CPS and the underlying AWI-CM3 provides opportunities to learn about the model errors of the latter. The integration of AWI-CM3 into PDAF and thus the creation of AWI-CPS started before model version 3.0 was finalized. The results presented in this section did in fact find their way into the first released version v3.0.

The state of sea ice thickness in a free run without data assimilation can be seen in the top row of figure 5.2. The Antarctic sea ice was almost non existent, while Arctic sea ice had more reasonable values but lacked the strong thickness gradient from Greenland to Siberia found in GIOMAS reanalysis data (bottom row of figure 5.2).

Evaluation of correctional terms generated by PDAF in order to bring the model closer to observational estimates showed that early versions of AWI-CPS were also systematically pulling AWI-CM3 towards larger sea ice thicknesses in the Southern Hemisphere. At the same time, AWI-CPS showed reasonably small sea ice velocity correctional terms, leading me to the conclusion that the existing sea ice thickness trends and biases in the free running model were the result of limitations in the thermodynamics rather than the dynamics of sea ice.

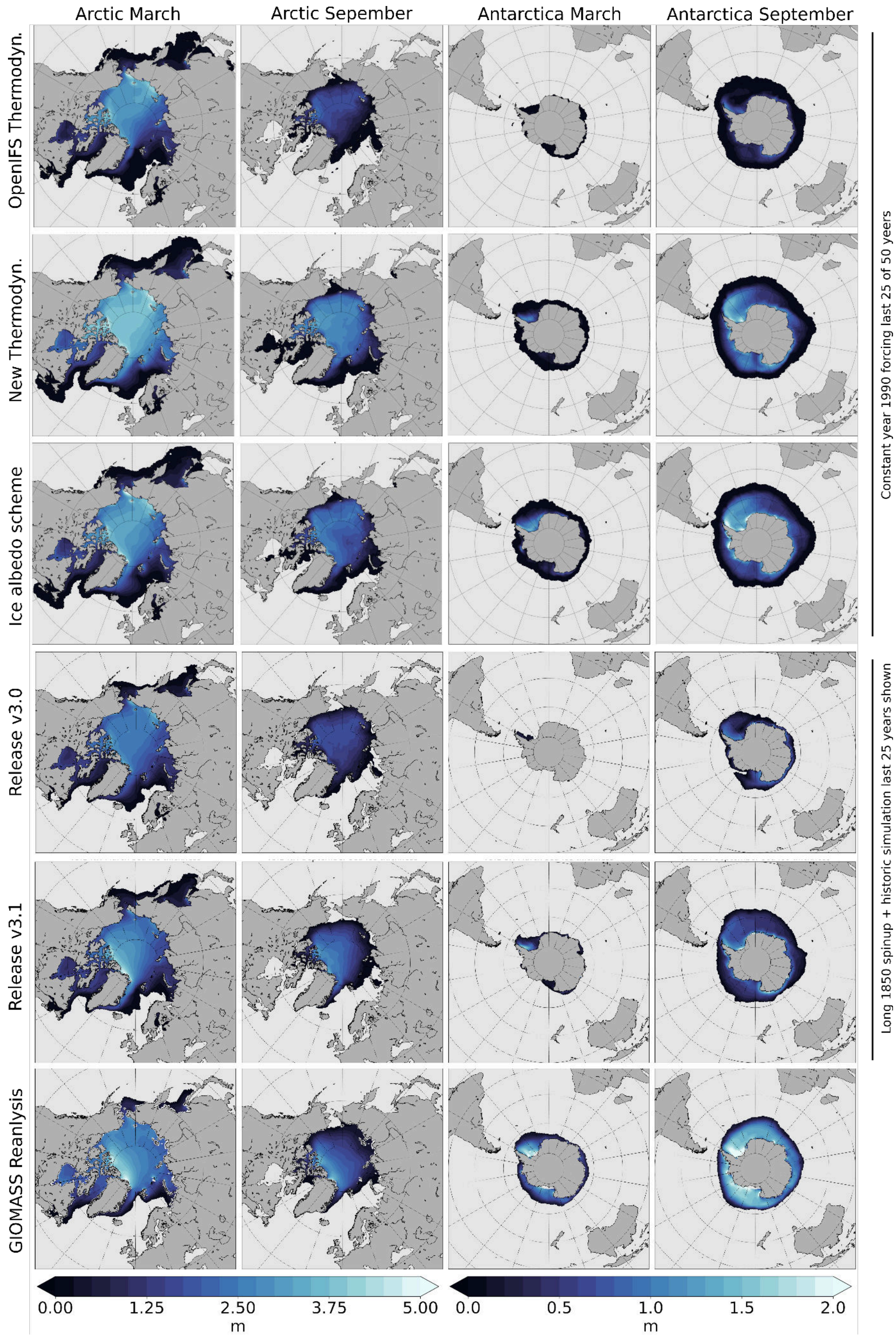

Figure 5.2: Evolution of sea ice thickness representation in AWI-CM3 free runs. 1^{st} row: Original OpenIFS ice thermodynamics with fixed thickness. Last 25 years of 50 year constant 1990 forcing run. second row: Large jump in thicknesses after switching to newly implemented sea ice surface temperature in FESOM2. 3^{rd} row: Slight reduction in Arctic after inclusion of simple melt pond parameterization. 4^{th} row: First release v3.0 shows little sea ice in last 25 years of historic period (HIST) after 700 year spinup. 5^{th} row: as 4^{th} row but for second release v3.1 after 500 year spinup and containing the improvements described in this manuscript. Arctic sea ice distribution is well captured, Antarctic better than in v3.0. 6^{th} row: GIOMASS reanalysis product for comparison (Zhang and Rothrock, 2003).

New sea ice surface thermodynamics In building a coupling interface for AWI-CM3 based on the coupling interface of AWI-CM1&2 (Sidorenko et al., 2015, 2019), I first used the sea ice physics implemented in OpenIFS. Prompted by the AWI-CPS insights I investigated these sea ice surface thermodynamics further and found that despite coupling the FESOM2 sea ice thickness to OpenIFS, the actual thickness used for the calculation of the sea ice surface temperature and the resulting sensible heat flux through the sea ice layer was always 1.5m. Coupling of a somewhat realistic sea ice model was not foreseen when this part of OpenIFS was built. This brazen simplification represents a year round underestimation (overestimation) of Arctic (Antarctic) sea ice thicknesses compared to present day observational estimates. For the developers of OpenIFS, who are mainly interested in NWP, the resulting errors are acceptable for their simulation lengths, which are typically two weeks or less. For longer climate timescale applications over years to millennia, the resulting sensible heat fluxes were too large (small) and led to too much (little) sea ice formation.

Rather than to try and patch up the basic OpenIFS sea ice surface thermodynamics, I decided to transfer the calculations from OpenIFS to FESOM2. The main motivators were that in most configurations FESOM2 has a higher horizontal resolution in high latitudes than OpenIFS, and furthermore is in the process of receiving upgrades to the sea ice thermodynamics (Zampieri et al., 2021b). As the Icepack coupling was not complete yet, I implemented a simpler scheme based on what was used for AWI-CM1&2 in the atmospheric model ECHAM6 (Stevens et al., 2013). This realization of the sea ice surface thermodynamics relies on atmosphere to sea ice surface heat fluxes calculated in OpenIFS. It takes into account the sea ice thickness as well as the thickness of the snow cover on sea ice. Based on these, the heat flux from the ocean to the atmosphere through the sea ice as well as sea ice growth / melting are computed. The implemented routine can be found in appendix C.3.

In the following, I will present the calculations of the new AWI-CM3 sea ice surface temperature, as adopted from ECHAM6. The central equation 5.1 relates change of thermal energy in the surface thin layer with height $h_0 = 0.1$m on the left to the sum of atmospheric fluxes Q_{atm} and the conductive heat flux through the thicker ice below Q_{cice}. Here $C_{v,sn+ice}$ is the time discrete heat capacity (in $\frac{J}{m^2K}$) of the thin surface layer which can change temperature. This thin layer is needed as the main ice mass is approximated without internal temperature distribution following the ideas of Hibler (1979). Meanwhile, ΔT_{si} is the change in skin temperature and Δt is the model time step.

$$C_{v,sn+ice}\frac{\Delta T_{si}}{\Delta t} = Q_{atm} + Q_{cice} \quad (5.1)$$

On the right hand side the total heat flux from atmosphere Q_{atm}, is the sum of shortwave Q_{sw}, longwave Q_{lw}, sensible Q_{se} and latent Q_{lat} fluxes over ice.

$$Q_{atm} = Q_{sw} + Q_{lw} + Q_{se} + Q_{lat} \quad (5.2)$$

Conductive heat flux Q_{cice} through sea ice and snow is computed from the thermal conductivity of ice $a_{ice} = 2.1656\frac{W}{mK}$, the temperature T_0 at which sea-ice starts freezing/melting, and the effective snow plus ice thickness z_{sn+ice}.

$$Q_{cice} = a_{ice}\frac{T_{si,t} - T_0}{z_{ice+sn}} \tag{5.3}$$

The phase transition temperature T_0 was computed from local ocean surface salinity using an empirical freezing-point depression formula (not shown). The effective snow plus ice thickness z_{sn+ice} is computed from the ice thickness h_{ice}, the snow depth on sea-ice h_{sn}, and the unitless conductivity equivalence fraction thickness of ice/snow $C_{v,sn+ice}h_{sn}$, while safeguarding against division through small numbers with a minimum ice thickness $d_{ice} = 0.05$.

$$z_{sn+ice} = MAX(h_{ice}, d_{ice}) + C_{v,sn+ice}h_{sn} \tag{5.4}$$

In eq. 5.1, expand ΔT_{si} to current ($T_{si,t}$) minus previous temperature ($T_{si,t-1}$) and insert eq. 5.2 and eq. 5.3. Equation 5.1 can thus be rewritten to:

$$C_{v,sn+ice}\frac{T_{si,t} - T_{si,t-1}}{\Delta t} = Q_{atm} + a_{ice}\frac{T_{si,t} - T_0}{z_{ice+sn}} \tag{5.5}$$

In this form we can solve for the new surface temperature $T_{si,t}$:

$$T_{si,t} = \frac{Q_{atm} + \frac{C_{v,sn+ice}}{\Delta t}T_{si,t-1} - \frac{a_{ice}}{z_{ice+sn}}T_0}{\frac{C_{v,sn+ice}}{\Delta t} - \frac{a_{ice}}{z_{ice+sn}}} \tag{5.6}$$

For the implemented algorithm shown in appendix C.3, we simplify the notation somewhat by precalculating some of the terms of equation 5.6. In particular, we calculate the energy E_{ice+sn} required to change the snow temperature by 1K

$$\frac{C_{v,sn+ice}}{\Delta t} = E_{ice+sn} = e_{ice}d_{ice} + e_{sn}h_{sn} \tag{5.7}$$

for which I scale the specific energy that would be required for a 1m thick ice (snow) layer e_{ice} (e_{sn}) by the thin ice layer thickness d_{ice} (snow thickness h_{sn}). e_{ice} in turn is computed from the ice density ρ_{ice}, the specific heat capacity of ice $C_{p,ice}$, and the time step Δt.

$$e_{ice} = \frac{\rho_{ice}C_{p,ice}}{\Delta t} \tag{5.8}$$

In the same manner I can compute the energy e_{sn} required to change the temperature of 1m of snow from the snow density ρ_{sn}, the specific heat capacity of snow $C_{p,sn}$, and the time step Δt.

$$e_{sn} = \frac{\rho_{sn}C_{p,sn}}{\Delta t} \tag{5.9}$$

Using the knowledge that equation 5.6 is solved for $T_{si,t}$, we can compute a Q_{cice^*}, which depends only on T_0:

$$Q_{cice^*} = \frac{a_{ice}}{z_{ice+sn}} T_0 \tag{5.10}$$

The simplified notation of eq. 5.6 is

$$T_{si,t} = \frac{Q_{atm} + E_{ice+sn} T_{si,t-1} - Q_{cice^*}}{E_{ice+sn} - \frac{a_{ice}}{z_{ice+sn}}} \tag{5.11}$$

and can be found in the implemented algorithm appendix C.3.

Evaluation To test the new sea ice performance, I ran a set of standardized 50 year long TCo95L91-CORE2 constant year 1990 greenhouse gases tests, which I generally use for most model development and tuning evaluation. With the new sea ice surface thermodynamics, the central Arctic (Beaufourt Gyre) March sea ice thickness bias against GIOMAS reanalysis degraded from about +0.5m to + 1m. The same bias was improved for the month of September from around -1m to -0.5m, as shown in the second row of figure 5.2. In line with expectations, improvements were larger around Antarctica, where the assumptions of constant 1.5m thick sea ice in the OpenIFS sea ice surface thermodynamics where furthest from reality. Here, the mean September sea ice thickness bias in the Weddell Sea shrank from -1.5 to -0.5m, while the March bias went from -1.5 to -1m. Besides the better representation of mean sea ice conditions, AWI-CM3 also gained the ability to react to Climate Change and Arctic Amplification, as the ice thickness now actually feeds back onto the heat flux through the sea ice. Clearly some issues remain around Antarctica at this point, where sea ice is still too thin. The problem of the missing cross Arctic thickness gradient did not improve either with this set of changes. Both will be addressed in the following sections.

Meltpond parameterization Since sea ice surface temperature is now calculated in FESOM2, the opportunity presented itself to refine the sea ice albedo parameterization for AWI-CM3. In the previously used OpenIFS scheme, a climatological monthly sea ice albedo was used. In other words, the sea ice albedo was unable to react to changes in the sea ice surface conditions with regard to temperature and snow cover. In my new simple sea ice albedo parameterization in FESOM2 the presence of snow cover or bare ice, and whether the sea ice or snow-on-sea ice surface temperature is close to the melting point is used to select one of four albedo values. Within the range of observational estimates I chose a relatively low albedo value of $\alpha_{bi} = 0.43$ for bare ice close to the melting point, to parameterize the presence of meltponds.

As can be learned from ERA5 reanalysis data (not shown) present day conditions of the Southern Hemisphere sea ice favors a more consistent snow cover, while much of the Arctic sea ice becomes snow free in summer. There are a number of contributing factors at play here, including the milder Arctic summer temperatures, and more dust sources from nearby land resulting in reduced snow albedo and leading to faster snow melting. Without a snow cover at the height of summer, the new sea ice albedo scheme simulates a thinning of sea ice in the Arctic, while leaving the Antarctic sea ice virtually untouched. Arctic September sea ice thickness bias is reduced back down from about +1m to +0.5m, while the trans Arctic gradient from thicker ice off of Greenland to thinner ice off of Siberia is still not captured. The reduced September minimum sea ice thickness bias shows persistence throughout the winter and results in similar improvements as the March sea ice maximum.

This is the state of the scheme that was tuned for version v3.0. As seen in the fourth row of figure 5.2, after 700 years of pre-industrial (year 1850 GHG) spinup, the results were severely degraded compared to the 50 year long previous tests. Antarctic sea ice has a strong negative bias of about -1.5m in September, while it is virtually none-existent in March. Investigations into such model drift on longer timescales, the underlying coupling issues, and their solutions are found in the following section 5.2.

5.2 Coupling of Second Order Terms

Starting out from the state of v3.0, I reevaluated the validity of simplifications made during the development of the original AWI-CM1&2 coupling scheme, which were thus far employed for AWI-CM3 as well. The work falls into two categories. Firstly, a reevaluation of the deterministic coupling flux fields in subsection 5.2; secondly, the selection of near surface parameterizations in subsection 5.3. In sections 5.4 and 5.5 I characterize the improvements made as well as remaining issues. The introduction of stochastic coupling is reserved for section 5.6.

Enthalpy of snow falling into open ocean One of the flux components I found missing when reevaluating the coupling interface is the heat flux resulting from the enthalpy of fusion of snow falling into the ocean. The phase change of water from solid to liquid absorbs the enthalpy of fusion $H_{H_2O} = 333.55\frac{J}{g}$, which will be provided by the liquid water into which the snow or hail falls. Together with the snow mass flux μ_{sn}, I can write the equation for the heat flux caused by the enthalpy of snow falling into open ocean $Q_{H,sn}$.

$$Q_{H,sn} = \mu_{sn} H_{H_2O} \tag{5.12}$$

The implementation in the source code can be found in section C.1. Figure 5.3 depicts up to -6 $\frac{W}{m^2}$ annual mean heat flux from this effect. Instantaneous values in the midst of a strong snow shower can reach as high as 100 $\frac{W}{m^2}$ (not shown). In comparison, longwave upward radiation in this region has an annual mean value of about $265\frac{W}{m^2}$, and anthropogenic greenhouse gas increase results in $+1\frac{W}{m^2}$ globally.

The cooling resulting from the implementation leads to a reduction of the SO warm bias by about 1°C, with significant reduction of the temperatures of

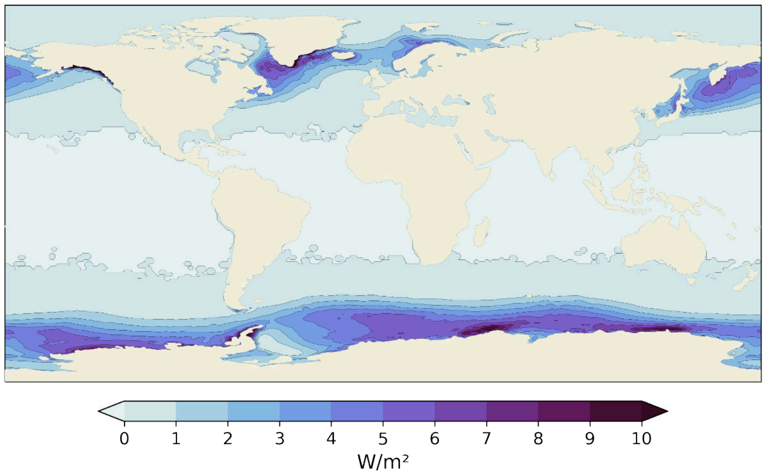

Figure 5.3: 25 year mean heat flux resulting from the melting of snow falling into the open ocean and undergoing phase change from solid to liquid.

water entrained into the Antarctic Intermediate Waters. In the Arctic, existing cold biases got exacerbated. The resulting changes in ocean surface temperature and impact on the CMPI-tool metrics across a number of variables are shown in appendix B.1.

Heat flux from precipitation temperature In a very similar manner, a heat flux $Q_{H,prec}$ can result not only from the phase change of precipitation but also from a difference of precipitation temperature compared to ocean surface temperature. The rain and snow temperatures are not directly available in OpenIFS, so instead I approximated them with the near surface (2m) air temperature T_a. I assume a fast adjustment of the precipitation temperature and the surrounding air temperature. The formula for the resulting heat flux is then given by

$$Q_{H,prec} = Q_{H,rain} + Q_{H,snow_{pos}} + Q_{H,snow_{n}eg} \tag{5.13}$$

where the snow precipitation warming/cooling has been split into one part below and one part above the 0°C. The reason for this is the different mass specific heat capacity of snow and liquid water. The individual parts can be computed as

$$Q_{H,rain} = \big((T_a - T_o)\mu_{rn}h_{rn}\big) \tag{5.14}$$

$$Q_{H,snow_+} = \big((T_a - T_o)_+\mu_{rn}h_{sn}\big) \tag{5.15}$$

$$Q_{H,snow_-} = \big((T_a - T_o)_-\mu_{sn}h_{sn}\big) \tag{5.16}$$

where T_o is the ocean surface temperature, μ_{rn} and μ_{sn} are the rain and snow mass fluxes, and $h_{rn} = 4.186\frac{J}{kgK}$ and $h_{sn} = 2.108\frac{J}{kgK}$ are the specific heat capacities for liquid and solid water. Note, that first the entire heat flux is treated as if the mass flux was in liquid phase, using (h_{rn}) and afterwards the part of the heat flux for which the mass flux was in solid state $((h_{rn} - h_{sn})$ is subtracted.

During the daytime, short wave radiation penetrates through the atmosphere and warms the coupled system from the top of the ocean where the shortwave radiation is absorbed. At night, a gradient of ocean surface temperature to near surface (2m) air temperature is reversed, however, as convective precipitation tends to be skewed to the afternoon and evening, so the resulting heat flux is mostly negative. Only in select regions, where ocean currents transport cold waters equatorwards at the surface, like in the Falkland Current, does the heat flux become slightly positive in the long term mean.

Unless there is a rare temperature inversion, the rain warms up while it falls, due to the tropospheric lapse rate. Thus, using the near surface (2m) air temperature as substitute for the rain temperature is a conservative choice, which will on average underestimate the negative heat flux. Notably, our ocean model is missing near surface diurnal warm layers, due to thick vertical layers in the model implementation, which could result in a further underestimation of the effect.

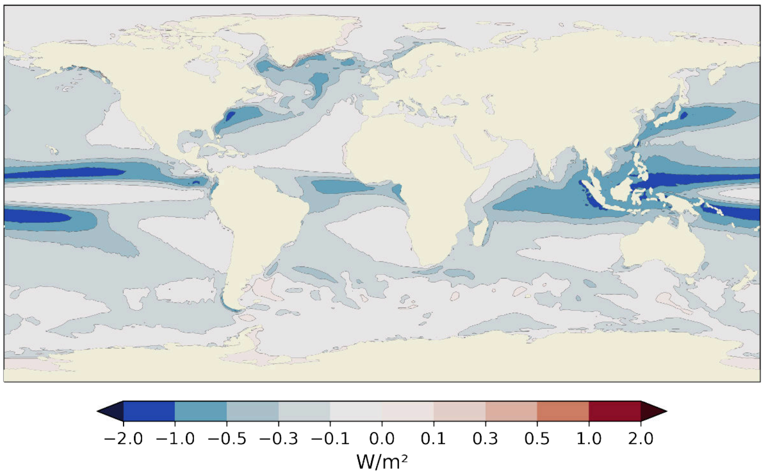

Figure 5.4: Heat flux resulting from rain falling into the ocean with a temperature differing from the ocean surface temperature. Rain temperature is approximated by near surface (2m) air temperature.

The resulting heat flux, shown in figure 5.4, is no larger than -2$\frac{W}{m^2}$ in the ITCZ, with lower values elsewhere. As the tropical ocean emits around 460$\frac{W}{m^2}$ of long wave radiation in the annual mean, the relative effect of this additional heat flux is much smaller than that of the enthalpy of fusion presented above. The largest relative impact can be found in western boundary currents, where the rainfall temperature induced heat fluxes also reach -1 to -2$\frac{W}{m^2}$, but outgoing longwave heat fluxes are only around 300-350$\frac{W}{m^2}$. As shown in appendix B.2, the impact of this new coupling heat flux is very minor.

Heat flux from quasi-icebergs I introduced a new water mass flux of snow that falls onto glaciers. In the real world, snow falling on perennial ice stays frozen until it is transported through ice dynamics to a region of lower altitude, where it returns back into liquid form in one of three ways. If summer surface temperatures are sufficiently warm at the new lower altitude the glacial ice can melt from the top. In this case the snowfall is belatedly added to river runoff. Alternatively, the ice flow can reach the ocean where either basal melt or iceberg calving and subsequent iceberg drift and melting return the snow water mass to the ocean.

In the case of AWI-CM3, no land ice dynamics are simulated. As such, I have to assume that the ice sheets are in equilibrium and the snowfall onto glaciers is balanced with the sum of surface melt, basal melt, and iceberg melt. A future more comprehensive AWI-ESM, including a dynamic land ice model will be able to simulate these fluxes in a transient ice sheet.

For now though, water and heat flux conservation suggest that the perennial snowfall shall be treated in a simplified manner. For v3.1, I re-use the runoff-mapper, which normally treats liquid runoff. To the regular river runoff I add all snowfall that would increase the snow depth to above 10m water mass equivalent. In contrast to the normal water mass, I calculate a negative heat flux based on the mass flux and the enthalpy of fusion of $333.55\frac{J}{g}$. The equation 5.17 for this effect is similar to the equation for the heat flux resulting from snow falling directly into the open ocean (equation 5.14):

$$Q_{H,imf} = \mu_{sn}\frac{A_{ib}}{A_{sn}}H_{H_2O} \tag{5.17}$$

The main difference is that the snow mass flux μ_{sn} has to be scaled by the ratio of the iceberg melt area A_{ib} to the snow fall area on the glacier A_{sn}. The solution implemented in the runoff mapper is a temporary one, which will be replaced by an actual Lagrangian iceberg drift and melting model coupled to FESOM2, likely as early as AWI-CM3 v3.2. Because of the temporary nature of the parameterization I chose the area that the heat flux is applied to in a very simplistic fashion as three boxes in the SO. The boxes implemented can be seen in the arrival point mask of the runoff-mapper in figure 5.5. The resulting heat flux applied over the area shown in figure 5.5a) is about -0,6$\frac{W}{m^2}$. As there is no melting temperature component in the implementation, the heat flux is parameterized to be uniform. Note that there is no heat flux applied near the Antarctic coastline, as air and ocean temperatures here prohibit iceberg melting throughout much of the year. Given the limited impact area and the relatively small heat flux, the resulting changes in a 50-year test simulation were not significant (not shown).

Ocean current feedback Another effect neglected in v3.0 is that of the ocean surface velocities on atmospheric fluxes. This effect is called ocean current feedback and it has gained renewed attention in recent years. Research on ocean current feedback goes back several decades, with early contributions by Bye (1985) recognizing the two-way coupled nature of the air sea momentum flux exchange. Meanwhile, Kelly et al. (2001) point out that in select regions like the South Equatorial Current the impact on momentum flux can be as large as -20%. More

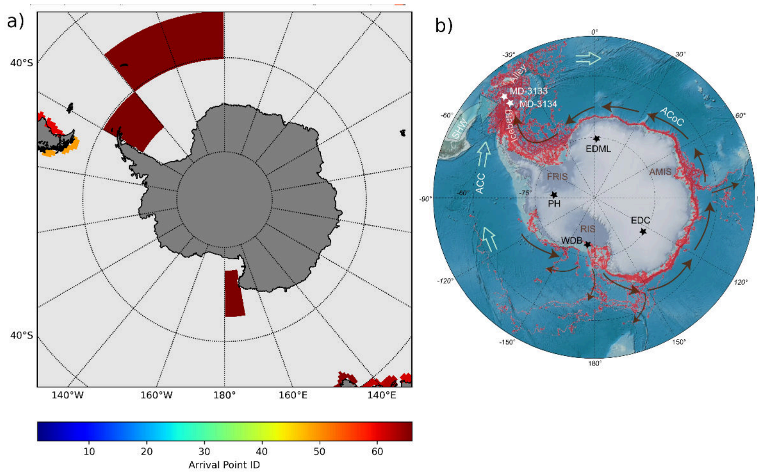

Figure 5.5: a) Drainage basins around the Southern Ocean, including three rectangular areas (A_{ib}) selected for parameterized iceberg melting related heat and freshwater fluxes. b) Observed iceberg drift trajectories by Weber et al. (2021).

recently, the works of Renault et al. (2016b, 2019) provided a great summary of the implementation and led to improved understanding of the importance of ocean current feedback for the representation of EKE pathways in the coupled system.

Fortunately, a lot of work had already been done on the OpenIFS side to prepare the atmospheric model for using ocean current velocities as described by Renault et al. (2016b). A good overview of what is available inside OpenIFS can be found in the technical report by Hersbach et al. (2008). The first modification is to replace the absolute winds with relative ones in the surface stress computation, as shown in equation 5.18, resulting in changes to the wind stress norm. Here the new surface wind stress $\boldsymbol{\tau}_{t+1}$ is computed with the air density ρ_a, the drag coefficient C_D, the atmospheric surface (height=0) wind $\mathbf{u}_a^0$, and the ocean surface current averaged over the coupling period $\left(\tilde{\mathbf{u}}_o^0\right)_{t-1}$.

$$\boldsymbol{\tau}_{t+1} = \rho_a C_D \left|\left|(\mathbf{u}_a^0)_t - \left(\tilde{\mathbf{u}}_o^0\right)_{t-1}\right|\right| \left(\left(\mathbf{u}_a^0\right)_t - \left(\tilde{\mathbf{u}}_o^0\right)_{t-1}\right) \tag{5.18}$$

Besides the obvious use of relative winds in the surface stress computation, the ocean current information, and therefore relative wind velocities had already been implemented into the solver for the tridiagonal system of equations for vertical diffusion. This results in the correct alterations of the wind stress orientation in the boundary layer. A detailed description of this effect and the implemented formula can be found in the technical report by Lemarié (2015).

Besides these two main mechanisms, the ocean current information is also used to account for the effects of current-induced wave propagation inside the IFS wave submodule WAM (ECMWF, 2017c). Furthermore, the information about surface currents is used to generate new waves and changes in the wave spectrum resulting from wave refraction, wave breaking, and other nonlinear effects.

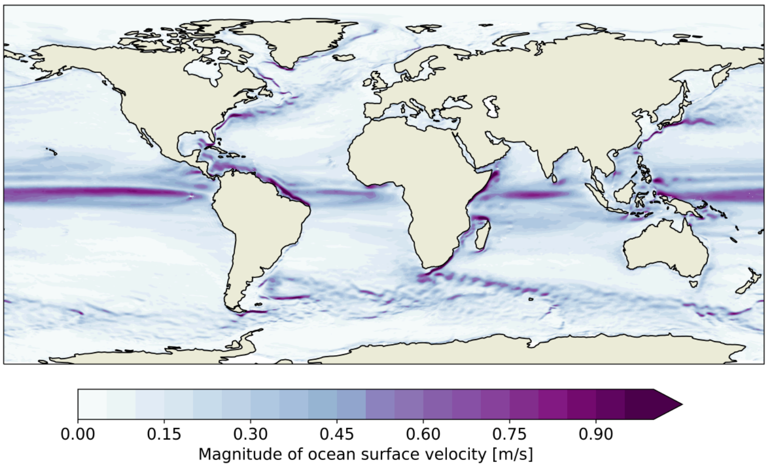

Figure 5.6: Magnitude of surface ocean velocity in low resolution TCo319L137-DART simulation. Shown is the mean over the first 10 years of a spinup simulation.

Ocean currents can be a significant fraction of the relative velocities in the tropics and in western boundary currents, as seen by comparing figure 5.6 to the mean wind velocities in the range of 1 to 10 $\frac{m}{s}$. As the technical foundations were available in OpenIFS, the implementation of ocean current feedback for AWI-CM3 was as simple as finding the right surface velocity field in FESOM2, finding a sufficiently smooth interpolation method (bicubic) to preserve curl and gradients, and integrating the coupled velocity components into OpenIFS.

Evaluation of the current feedback at low resolution (TCo95L91-CORE2) via CMPI-Tool showed mostly minor changes, depicted in appendix B.3. This is expected, as ocean eddies are largely unresolved at this resolution and just have their effect on the mean flow parameterized by Gent-McWilliams (Gent and Mcwilliams, 1990). At higher resolution (TCo319L137-DART), where ocean eddies are largely resolved in FESOM2 and start to be resolved in OpenIFS (31km horizontal resolution), ocean current feedback provides the well known pathway for EKE between ocean and atmosphere (not shown). This eddy killing effect has previously been documented in studies implementing ocean current feedback, and helps to control ocean currents such that they better match observational estimates (Eden and Dietze, 2009; Renault et al., 2016a; Shan et al., 2020). An evaluation at a model resolution that has the atmosphere fully resolve ocean eddies in most ocean regions (e.g. TCo1279L137-DART) has not yet been performed.

5.3 Physics Parameterization Selection and Tuning

Aside from new implementations and couplings, I also had a fresh look at parameterizations that act at or close to the air-sea interface. While I found many options to be already well chosen, two major changes were in order.

Salt plume parameterization Based on figure 3.6c), I knew that the salinity profile in the Weddell sea underestimates the observed salinity gradient. I thus looked for already implemented but currently either tuned down or deactivated parameterizations that could help alleviate the issue. One such case is the salt plume parameterization, which was first tested for AWI-CM1 by Sidorenko et al. (2018) but is not turned on by default.

When new sea ice forms, part of the sea water freezes into an ice crystal lattice, leaving the salt, mostly Chloride and Sodium, behind as the molecules are too large to fit into the crystal lattice. The salt forms small pockets of hyper saline water in a process called brine rejection (Cox and Weeks, 1974). The cryogenic brine has a lower freezing temperature and higher density the larger the salt concentration is. This eventually leads to the brine sinking through the sea ice and entering the liquid water underneath. Because of its much higher density, brine entering into the ocean falls in convective plumes (Nguyen et al., 2009). The convective plumes then sink as far as the halocline, where they spread out sideways.

Since convective brine plumes have a horizontal extend in the meter scale they are too small to be explicitly resolved by our global sea ice model. However, their effect of delivering brine not just to the ocean surface but down to the halocline can be parameterized.

Following the approach of Nguyen et al. (2009), Sidorenko et al. (2018) implemented a split, by which 30% of rejected brine remain at the surface, while the other 70% are distributed down into the ocean. One way to solve the question of what depth D_s the salt plumes reach to, is to equate D_s to the neutral buoyancy depth z_n, which can be derived from laboratory experiments by BUSH and WOODS (1999) as

$$D_s = z_n \in \left(3.0 - 1.0\frac{B_0^{\frac{1}{3}}}{N}, 3.0 + 1.0\frac{B_0^{\frac{1}{3}}}{N}\right) \tag{5.19}$$

where N is the Brunt-Väisälä frequency:

$$N = \sqrt{-\frac{g}{p}\frac{dp}{dz}} \tag{5.20}$$

with the pressure p, the gravitational constant g and depth z. B_0 is plume buoyancy flux per unit length:

$$B_0 = V_0 g \frac{\rho_0 - \rho_{sw}}{\rho_{sw}} \tag{5.21}$$

which depends on the plume volume flux per unit length V_0 ($\frac{m^2}{s}$), the initial density of the salt plume ρ_0, and the density of the surrounding sea water ρ_{sw}. Other options to find D_s exist, and involve for example hooking directly into a vertical mixing parameterization, such as the KPP scheme to obtain the MLD. The flux of plume transported salt $s(z)$ within the depth range from surface to D_s follows a power law:

$$s(z) = \begin{cases} Az^n, |z| \geq |D_s| \\ 0 \quad , |z| < |D_s| \end{cases} \tag{5.22}$$

The cumulative salt $S(z)$ as a function of depth z is then given by:

$$S(z) = \int_0^z s(z')dz' \tag{5.23}$$

Note that most of the plume transported salt ends up nearer to D_s than the surface, as this is where the plumes come to rest and disperse horizontally. The improvements in surface to deep ocean salinity gradient seen in figure 5.9b) can be partially attributed to activation of the salt plume paramterization in AWI-CM3 v3.1.

Monin Obukhov Mixing In order to further reduce the erroneously large MLD in the Weddell Sea, I turned off the Monin-Obukhov mixing (MOMIX). MOMIX serves as a parameterisation of the wind-driven mixing in the SO and is especially effective in the melting season. In standalone FESOM2, it helped to reduce winter deep convection in the Weddell Sea (Scholz et al., 2022). The implementation of MOMIX in FESOM2 follows the approach of Timmermann and Beckmann (2004b).

For reasons not yet fully explored, the effects of MOMIX are reversed in the coupled AWI-CM3 as compared to the standalone model. The working hypothesis is that the heat flux, freshwater flux, wind stress, sea ice concentration, and sea ice velocity on which the calculation of the Monin Obukhov length is based differ substantially in the coupled model. I concluded that applying the enhanced vertical diffusivity at depth given by the Monin Obukhov length in the coupled model results in the discrepancy. Direct comparison with observational estimates is difficult, as the MLD is not directly observable. Evidence pointing in this direction can be found in the Weddell Sea salinity and pycnocline evaluation for v3.1 in section 5.4. While the salinity and pycnocline can serve as a proxy for MLD, further investigation of the question why turning off MOMIX resulted in the changes seen is warranted.

5.4 General Evaluation of Version v3.1

The evaluation of the new AWI-CM3 model version is done with the same set of python scripts and tools and against the same observational and reanalysis datasets as were used for the peer-reviewed first release v3.0 in Streffing et al. (2022). Here, I directly contrast results that have seen major changes between versions v3.0 and v3.1. The full set of evaluation diagnostics can be found in the release section of the AWI-CM3 documentation website at: `https://awi-cm3-documentation.rtfd.io`.

The first set of plots in figure 5.7 highlights the improvements I was able to achieve in the radiation budget and subsequently in the ocean heat uptake. As I analyzed in section 3.4.1, for the first 500 years for the spinup simulation, v3.0 ran mass conservation only for the dry mass, experiencing a strong model drift. The last 200 years of the spinup of version v3.0 fixed this drift, yet still suffered from two distinct but connected issues. Firstly, this version showed a spurious source of energy of about $0,7\frac{W}{m^2}$ (grey curve in 5.7a)). Secondly, this energy was being exported into ocean (blue curve in 5.7a)), rather than radiating at the top of the atmosphere (yellow curve in 5.7a) is close to 0 $\frac{W}{m^2}$).

Version v3.1 addressed both issues, as the spurious energy source (grey curve in 5.7b)) became a smaller sink of $-0.18\frac{W}{m^2}$, and the extra energy is not exported into the ocean anymore (blue curve in 5.7b) is close to 0 $\frac{W}{m^2}$).

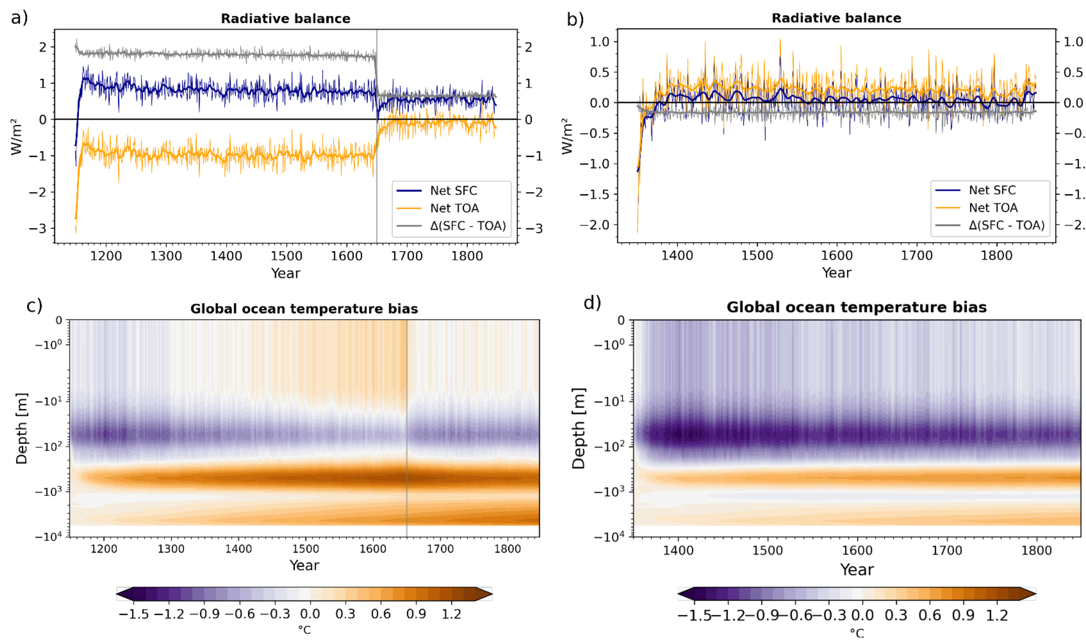

Figure 5.7: Radiation budget of net surface (SFC) and net top of atmosphere (TOA) for the full duration of the spinup simulation for a) v3.0 before and b) v3.1 after second order coupling and retuning. Note that b) uses a smaller range for the vertical axis than a). For the same time frame the semi-logarithmic Hovmöller diagram of ocean temperature over depth shows the evolution of temperature biases against PHC3 for c) v3.0 and d) v3.1. Note: The first 500 years of v3.0 ran without mass conservation fixer.

As a result, I was able to reduce the spurious ocean heat uptake, shown in the second row of figure 5.7. While the top 10 meters now show a slight cold bias, and a layer between 50 and 100 meters features an increased cold bias, the previously strong mid and deep ocean warm biases have reduced substantially. Note the semi-logarithmic nature of the Hovmöller diagrams. The total ocean heat uptake bias is strongly reduced by the large volume between 100 and 1000 meters depth that is better represented in v3.1.

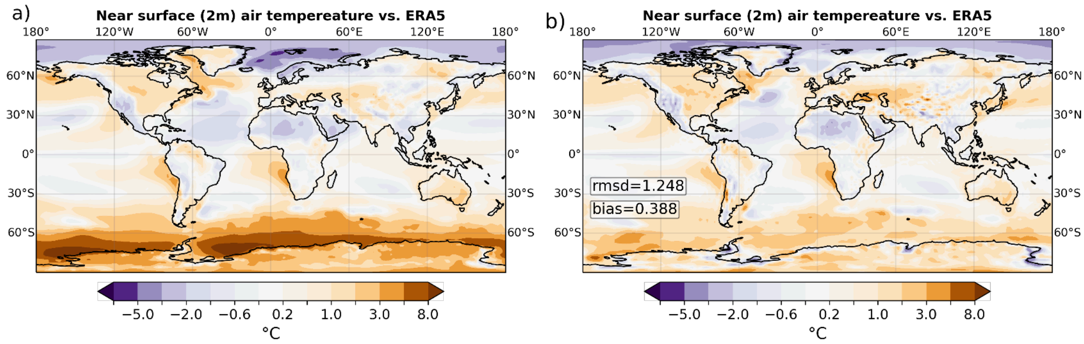

Figure 5.8: Mean near surface (2m) air temperature bias against ERA5 over last 25 years of historic simulation (HIST) in version a) v3.0 before b) v3.1 after second order coupling and retuning.

As expected the near surface (2m) air temperature biases (figure 5.8) over the oceans have also improved as a result of the improved surface heat budget. Especially the SO was improved where the additional negative heat fluxes (section 5.2) have resulted in less heat uptake at the surface in summer.

Furthermore the same region also benefited from the change of vertical mixing parameterization outlined in section 5.3. The parameterized vertical salinity transport to down to 100 meters depth leads to a drastically different salinity profile in the Weddell Sea in winter, as shown in figure 5.9. Version v3.0 features a high salinity bias in the top 100 meters, over a low salinity bias at depths greater than 100 meters.

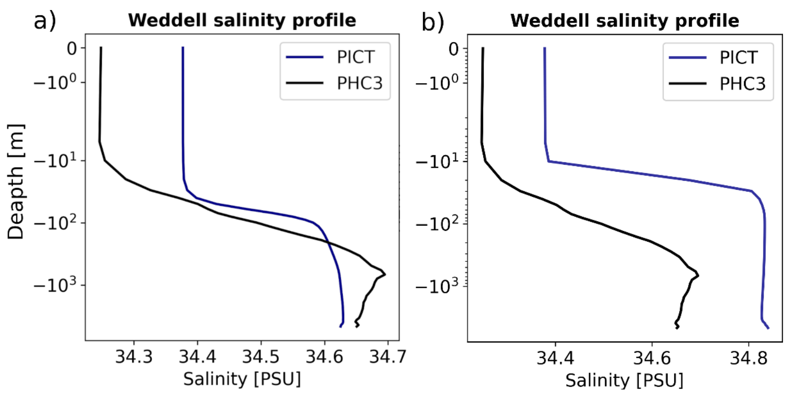

Figure 5.9: Mean salinity profile over last 25 years of historic simulation (HIST) in a) v3.0 before, and b) v3.1 after second order coupling and retuning. In black the observational data from PHC3.

Meanwhile, in version v3.1 the bias is positive at all depths so that the improvements are not immediately obvious at first glance. However, the main effect of salinity is in the density gradients. And while the absolute errors are as large as before, the difference between top and bottom layer and the stability this gives to the fresh water lense capping of the ocean in this region is more accurately captured in the new version. The resulting reduction in austral winter MLD limits the ocean vertical heat transport in winter and leads to more realistic sea ice formation, which in turn provides a sea ice albedo feedback that leads to relative cooling of the ocean in summer.

As seen in Figure 5.10, this resulted in a reduction of not only the SO warm bias at the surface but also the deep ocean warm biases at 4000m meters in every ocean basin. This is chiefly the result of now colder surface water masses in the Antarctic polar front zone getting entrained into AAIW. From there the now less warm biased water masses are transported into all ocean basins via the ACC.

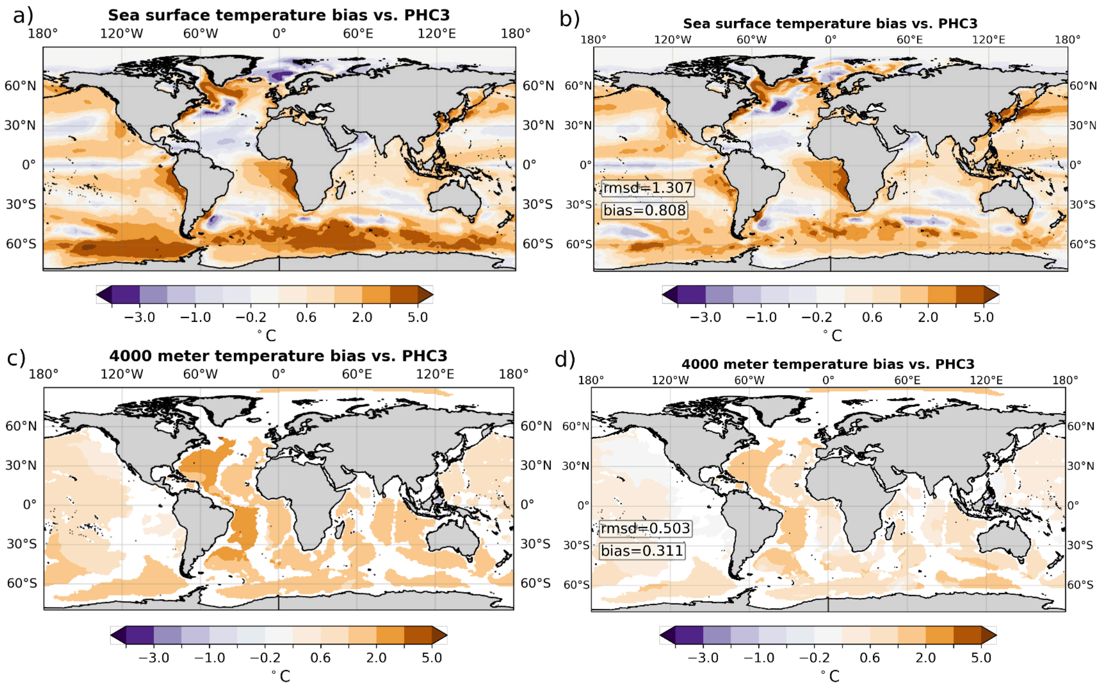

Figure 5.10: Mean water temperature bias against PHC3 over last 25 years of historic simulation (HIST) in version in a) v3.0 at surface before and b) v3.1 at surface after second order coupling and retuning. Same for c) v3.0 at 4000m depth before and d) v3.1 at 4000m depth after second order coupling and retuning.

Somewhat unexpectedly the new model version v3.1 performs worse in the transient historical (HIST) simulation (figure 5.11) regarding the reproduction of observed global warming. As the new model version now features sea ice in the SO, it becomes prone to an issue that afflicts many climate models of the CMIP6 generation, in that the SO reacts with Antarctic Amplification towards global warming. This manifests as $2 - 3K$ warming over the SO sea ice area. Observational estimates until today do not show a strong reduction in SO sea ice area, nor an increase of ocean surface temperature. A study conducted with the predecessor model AWI-CM1 has recently shown that the SO warm bias and too early sea ice decline may be model resolution dependent (Rackow et al., 2022). Preliminary AWI-CM3 results at TCo319-DART show that this model too, may be colder in the SO at higher resolution.

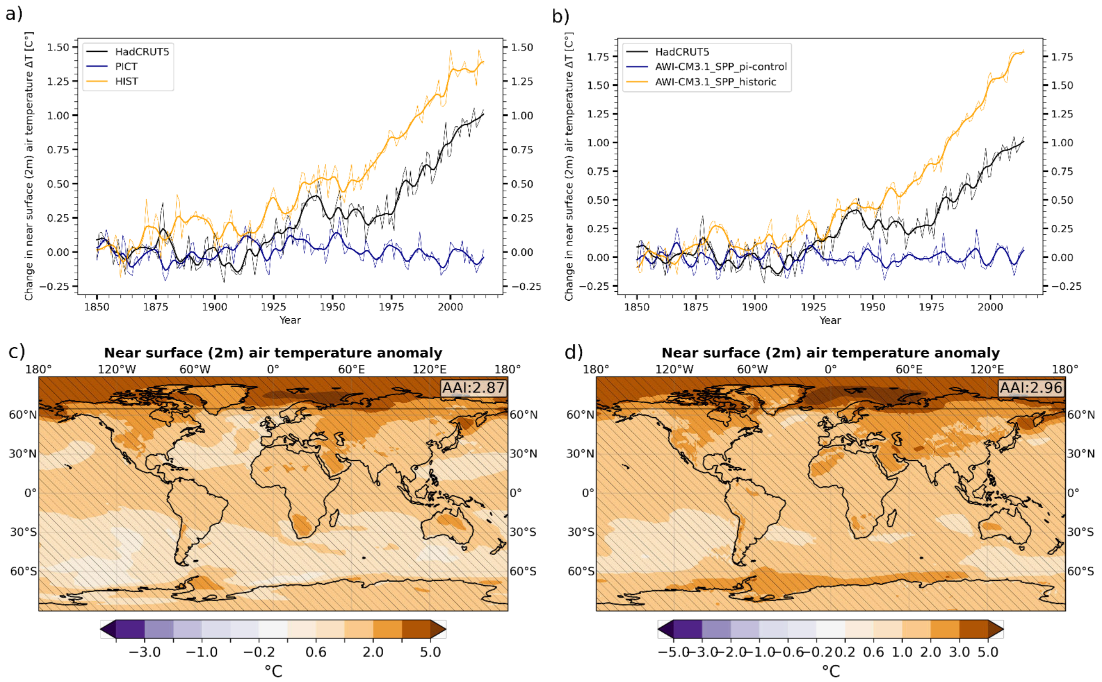

Figure 5.11: AWI-CM3 model response to historic (HIST) greenhouse gas changes in yellow for a) version v3.0, and b) version v3.1. Note that both versions miss the $-0.5\frac{W}{m^2}$ from anthropogenic aerosol emissions, and thus can be expected to overestimate global warming. c) Spatial distribution of historic (HIST) warming for version v3.0 and d) the same for v3.1. The Antarctic Amplification Index (AAI) is slightly higher in v3.1. The pre-industrial control and observed temperatures changes are shown in the blue and black curves.

As shown in figure 5.11c-d), v3.0 largely did not see warming in the regions of SO sea ice cover. Meanwhile, v3.1 does show 2-3K warming, exhibiting even some polar amplification between 65° and 70° South. The new model version is thus prone to misrepresentation of the Antarctic sea ice paradox, in a way the first version was not. Closer inspection however reveals that v3.0 got the warming signal right for the wrong reasons. While observational records such as ERA5 (not shown) feature an Antarctic sea ice region that has stayed cold and ice covered until now, in v3.0 this region was already 5K too warm and spuriously ice free in the pre-industrial control simulation.

In version v3.1, the Antarctic sea ice cover is present in the pre-industrial control simulation. However, the reduced but still existing SO warm bias of about +1-2K, seen in figure 5.10 a&b), has primed sea ice to react to historic warming of the period 1850 to 2014 in a way that the real SO sea ice is expected to react in a 2-3K warmer than pre-industrial world.

In summary, v3.1 addresses some of the largest sources of model mean bias that were present in the peer-reviewed v3.0. The implementation of second order importance fluxes and changes in the near surface parameterizations brought the model closer to modelling present day conditions. Some issues remain in the transient model behavior, which shows too strong global warming over the period 1850 to 2014. This will have be targeted in future releases, for example through the implementation of anthropogenic aerosol forcing. Overall AWI-CM3 has taken a good step forward to being a useful climate research tool. The first scientific application of v3.1, and what I was able to learn from it for further model development, will be presented in the next section 5.5.

5.5 Comparison with in situ observational estimates through nudging

The OpenIFS spectral nudging method for AWI-CM3 was first used by Athanase et al. (2022), and the results I show here are published in Pithan et al. (2023). My own contribution to this work is improvement of snow and sea ice surface temperature and sensible heat flux calculation in AWI-CM3, based on the results of the nudged experiments.

Assessing and enhancing the quality of models requires a comparison between the output of general circulation models and observational estimates. A key restriction is the comparability of observational estimates with model output. Observational estimates that are available over large scales and with frequent time coverage, such as satellite products, are well suited. Even better coverage can be obtained from reanalysis products, which assimilate all manner of observational estimates to more or less tightly constrain a climate model and thus produce model output close to observational estimates (Hersbach et al., 2020b). Reanalysis systems still have their own biases, which sometimes can be quite major, as shown by Batrak and Müller (2019b). Satellite based data products come with a different set of limitations, as they require a multi-step algorithm to obtain the physical quantity from the raw instrument output. The obtained observational estimates of Level 3 or 4 satellite products, such as CERES-EBAF are thus limited by these retrieval algorithms (Zabolotskikh, 2019). Note, that Level 3 satellite products algorithmically derive geophysical parameters from raw data, while Level 4 products further refine and integrate multiple datasets to provide advanced analyzes. Depending on instrument type, coverage can be limited by cloud cover or daylight availability.

In light of the limitations of model evaluation against observational datasets with good spatial and temporal coverage, the direct comparison with in situ data is attractive. In situ data are usually more precise than satellite data and often used for satellite data evaluation. However, in situ data is sparse, and a freely evolving climate model is expected to match it only as a temporal mean and variance over temporal scales of decades. Either the in situ data has to cover a long enough time series to allow for effective comparison of mean and variance, or the climate model has to be constrained in some manner. Long stationary in situ measuring campaigns are expensive and technically challenging. More frequently in situ data is available for a year or less. In the following I will present a basic method of constraining a climate model, called Newtonian relaxation or nudging (Jeuken et al., 1996), through which direct comparisons become possible. A second more advanced method, ensemble Kalman filter data assimilation, more akin to what reanalysis products use was already presented in section 5.1. While AWI-CPS works with ocean observational estimates constraining FESOM2, the nudging presented here incorporates atmospheric observational estimates into OpenIFS.

Spectral nudging There exist two distinct nudging methods for OpenIFS, one in spectral and the other in grid point space. Spectral nudging involves modifying the model's governing equations pulling the low frequency components to an observed large scale state. This is done by adding a term to the vorticity equations in spectral space. Spectral nudging is typically used to improve the simulation of large-scale phenomena, such as the position and intensity of storms, by preventing small-scale disturbances from growing through pulling the large scales towards reanalysis. Nudging in grid point space involves modifying the model's initial or boundary conditions to force the model solution towards the observed state, and is typically used to improve the simulation of small-scale phenomena, such as the timing and location of individual convective cells. Of the two, spectral nudging was used as it is more appropriate for the tests at hand, and it leaves the model to freely calculate boundary layer physics, while ensuring that large scale weather matches the weather during the short observational period.

For the nudged experiment setup, a suitable time period for which one can compare to observational estimates needs to be selected. In this case, the observational estimates are made in the context of the MOSAiC (Multidisciplinary drifting Observatory for the Study of Arctic Climate) expedition Rabe et al. (2022). The MOSAiC expedition was a large-scale research project focused on studying the Arctic climate system, wherein the research ice breaker Polarstern was moored to an ice floe in the Arctic for a year. Observational estimates were taken from instrumentation installed on board and deployed on the sea ice nearby. While surface conditions in the Arctic tend to be fairly stable in winter and summer, where the sensitive heat flux uniformly goes into the atmosphere and ocean, respectively, the transitional periods are of particular interest, and hard to capture in model parametrizations. Thus, the month of April 2020 is chosen as the observational period to compare the model against. Figure 5.12 shows the track of the generally southward drifting Polarstern during this period, as well as nearby atmospheric grid points. The original study was a multi-model intercomparison. Beside AWI-CM3, it also featured the predecessor model AWI-CM1, and the Com-

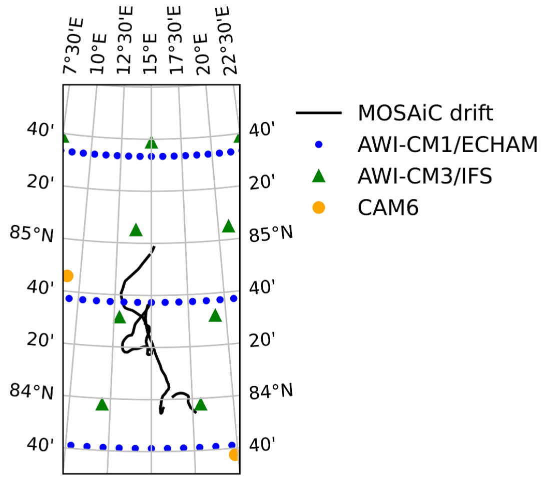

Figure 5.12: Drift of the MOSAiC central observatory during April 2020 and model grid points covering the area. The observatory is drifting southward. Graphic from Pithan et al. (2023). The original study was a multi-model intercomparison. Beside AWI-CM3, it also featured the predecessor model AWI-CM1, and the Community Atmosphere Model CAM6 (Danabasoglu et al., 2020).

munity Atmosphere Model CAM6 (Danabasoglu et al., 2020). For the analysis, the grid point closest to the ship track for each observation time step is chosen.

During the observational period, multiple strong warm air intrusions occurred which, thanks to nudging, also appear in the corresponding AWI-CM3 simulation. Thus, the nudged model can match observed near surface (2m) air temperature to a reasonable degree, as shown in figure 5.13. Besides a number of interesting conclusions regarding cloud microphysics found in our original paper (Pithan et al., 2023), the main finding of interest here was that the sensible heat flux over sea ice for AWI-CM3 was not behaving as expected from theoretical considerations. Qualitatively, the sign of the flux should change according to the sign of T_{sn}-T_a. The magnitude of the heat flux should scale with the temperature difference, as well as the wind speed. The surface roughness is nearly constant for the duration of the experiment, as it depends on the sea ice cover fraction, which remains above 95% (not shown).

Correction of sensible heat flux over snow covered sea ice Figure B.11b) depicts that while the sensible heat flux measured during MOSAiC follows the qualitative understanding, the AWI-CM3 heat flux did not. Instead, it was found in quadrant 1, meaning sensible heat flowed against the temperature gradient. Generally wind seemed to have little impact but most worryingly the model frequently computed heat fluxes that went against the temperature gradient. A deep dive into the new sea ice surface thermodynamics developed as written in section 5.1 showed that two assumptions made during the implementations were not met.

The first contributing factor results from the changes I made in chapter 5.1. In this implementation, the new sea ice surface temperature scheme I build into

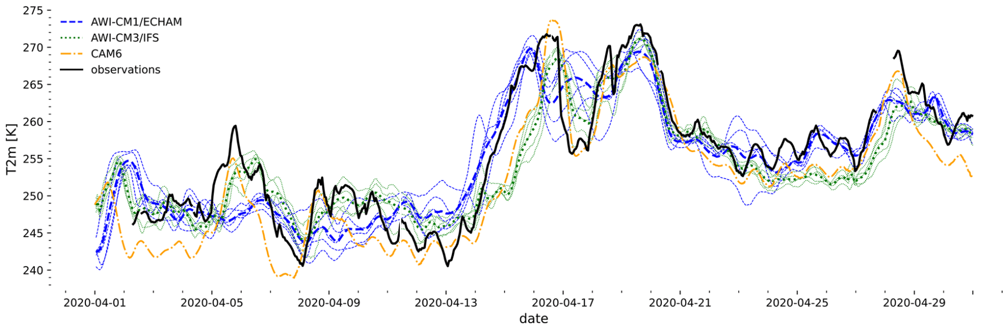

Figure 5.13: Observed and nearest neighbor of the modelled hourly 2m temperatures during April 2020 at the MOSAiC site. Thin dashed and dotted lines show individual ensemble members, and the thicker lines show the ensemble mean for each AWI model. Throughout the paper, full black lines represent the observational estimates, blue dashed lines AWI-CM1/ECHAM, green dotted lines AWI-CM3/IFS and orange dash-dotted lines CAM6. From Pithan et al. (2023).

FESOM2 is modelled after the one used in our predecessor coupled models AWI-CM1 & 2. However, in AWI-CM1&2 both the sea ice and snow surface temperature calculation are done in the atmospheric component ECHAM6, accepting the coarser horizontal resolution grid. A benefit of this choice is that the sea ice surface temperature and sensible heat flux calculation are coupled sequentially (see section 2.2.3) at level four (see section 2.2.1) with an atmospheric model time step of no more than 15 minutes at the coarsest resolution. The coupling is thus very tight. For AWI-CM3 on the other hand, sea ice surface temperature and sensible heat flux calculation are coupled in parallel at level 2, with a coupling time step of up to 2 hours. The coupling is comparatively loose.

The second contributing factor is that the sea ice in FESOM1 and FESOM2 does not have a heat capacity, since their sea ice thermodynamics use a zero layer model. Consequently, any input or extraction of thermal energy results in the freezing or melting of sea ice, rather than temperature changes. The sea ice surface temperature is a necessary extension placed on top to provide a surface temperature in a zero layer thermodynamics model, which otherwise would not have any temperatures for sea ice. This extension is needed because I have moved the system interface from in between ocean and sea ice to in between sea ice and atmosphere. In order to be able to compute a surface temperature at all, the thickness of a thin layer of sea ice that can respond to the sensible heat flux within one ice temperature-to-heat flux coupling cycle has to be chosen. The actual value of this layer thickness is somewhat arbitrary and represents a tuning parameter. If the layer thickness is too large, the surface temperature reacts sluggishly to heat flux changes. If the layer is too thin, the sea ice surface temperature can become unstable and fluctuate.

In the original ECHAM6 scheme this is solved by defining the surface layer as the top 5 cm of ice plus the entire snow depth, regardless of snow depth. For AWI-CM3 we mirrored this conservative choice for snow thickness, as we considered sluggish behavior less concerning than the risk of unstable fluctuations. Although somewhat reduced, a lot of fluctuations still remained at this point.

The makeshift solution of the problem was the realization that OpenIFS has its own snow and sea ice surface layer "thickness", defined as a fixed heat conductivity C_{surf} of the surface layer. If C_{surf} is selected to be a small value, e.g. $7\frac{W}{mK}$, a temperature profile will develop in the atmospheric sea ice representation where the surface adjusts to a new temperature $T_{si,t}$, while areas lower within the surface layer are closer to the old temperature $T_{si,t-1}$. The larger the heat conductivity, the more the lower areas within the surface layer will adjust towards the new temperature. The heat storage capacity of the surface layer grows until in the limit of large numbers of heat conductivity the surface layer acts like a bulk slab, completely adjusting to the new temperature.

By default the low value of $7\frac{W}{mK}$ was hard coded in OpenIFS. I provide an effectively thicker surface layer by changing the conductivity to $50\frac{W}{mK}$, as the higher conductivity leads to a larger thermal mass reacting to the sensible heat flux. The spurious quadrant in the sensible heat flux calculation was resolved with this modification, as I show in the bottom B.11.

While the makeshift solution saw substantial improvements to the sensible heat flux dynamic behavior, a better implementation could be made. As I outline in chapter 6.2, it would be beneficial to join the sea ice surface heat flux and sea ice surface temperature calculation back into a single model sphere again, while keeping the improved physics implemented in chapter 5.1. This way we could couple fluxes and the surface temperature in series using level three or four coupling (see chapters 2.2.1 and 2.2.1).

5.6 Stochastic Coupling

As already eluded to at the end of chapter 2.1, I investigated not just the physics of the model coupling interface, but also their numerics. This work is build on previous work by Rackow and Juricke (2020). Under the headline of stochastic coupling, I present my suggested additions to ongoing attempts by the climate modelling community to retain as much information as possible in the process of coupling atmosphere and ocean models. In particular, it presents a set of modifications to the sparse matrix multiplication that seeks to transfer information that cannot be communicated in the spatial domain into the temporal domain instead.

5.6.1 Theory

One of the fundamental challenges of separating the concerns of ocean and atmosphere modelling, is that the respective research groups typically choose a model grid that is particularly suited to their respective model domain. For the ocean this results in a number of ocean model grids that find smart ways to circumvent the grid singularity problem at the North and South pole. Examples include a stretched pole like the NEMO triangular ORCA grid family (Madec et al., 2017), or the displaced grids of the POP ocean model (McInnes et al., 2006).

Additionally, the ocean has a distinctly anisotropic structure due to the uneven distribution of land masses, the hard constriction on both its top and bottom boundary, and the incompressibility of the fluid. In the mid latitudes, the wind stress imparted by Westerly winds is balanced by a meridional North to South water transport (Sverdrup, 1947). As first described by Stommel (1948) in a rotating frame of reference, the latitude dependent Coriolis parameter causes the South to North counter-flow to be focused along a narrow area near the Western edge of the ocean basins. As a result, ocean current velocities and eddy activity are increased in these regions. Last but not least, the world ocean has a single landmass free band between 55 and 61°S in the SO, which has no equivalent on the Northern Hemisphere and allows for a strong interplanetary circulation pattern, the ACC (Nowlin Jr and Klinck, 1986). Peak surface ocean current velocities and sea surface height variability are one to two orders of magnitude higher in these regions than elsewhere in the ocean.

With respect to peak fluid dynamic velocities the atmosphere is comparatively isotropic. Since planet Earth does not feature orography higher than the troposphere, there are no coastlines in atmospheric dynamics models. As the models must cover the whole globe it is not possible to circumvent the pole problem, which instead has to be solved by taking the pole into account during dynamical core formulation. One solution is to use the approximately spherical shape of the atmosphere to formulate part of the dynamical core in spectral space using spherical harmonics.

Unless the separation of concerns was not fully applied during model development and atmosphere and ocean model were conceptualized as one, these factors will in sum likely result in the selection of different grid types for the ocean and the atmosphere model. AWI-CM3's constituent models OpenIFS and FESOM2 are prime examples for differing meshes fully optimized for their respective task.

Gauss weighted remapping For the first functional version v3.0 the coupling has been done without taking into account the specific setup. For the so far realized coupling, every grid point on the target mesh is associated with its N_N nearest neighbors on the source grid. Because of limitations to the interpolation library SCRIP (A spherical Coordinate Remapping and Interpolation Package; Jones et al. (1998)) included in OASIS, the number of neighbors N_N is a global variable manually selected during model setup. For each of the source-to-target cell connection, the distance between the center of the target grid-cell and the center source grid-cell is computed, as shown in figure 5.14. The resulting distances are multiplied with a Gaussian distribution of globally tunable kurtosis. Finally, the weights are normalized such that the sum of the N_N weights connecting source to target grid-cell centers is equal to one.

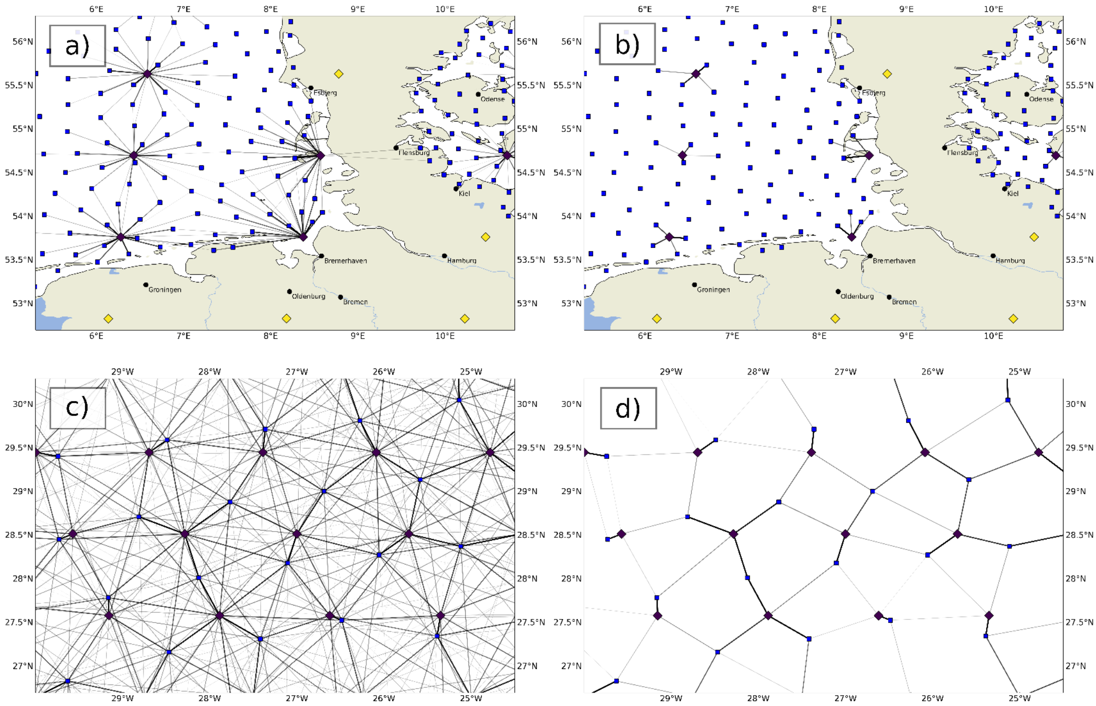

Figure 5.14: Coupling of ocean surface values to the bottom of the atmospheric cells in AWI-CM is done via Gauss weighted remapping. Here atmospheric cells over water receive ocean model surface values from the N_N nearest ocean neighbor cells. The importance of the contribution of each of the ocean surface values is weighted by the distance between atmosphere and ocean cell centers, weighted by a Gaussian curve. The number of neighbors is a global variable. a) In areas where the ratio of ocean to atmospheric resolution G_{oa} is large, such as the North Sea, a large number of neighbors, e.g. $N_N = 25$, may be appropriate. b) Failure mode A: Using a smaller number, e.g. $N_N = 4$, ignores many ocean surface points for the calculation of fluxes in the atmosphere. c) Failure mode B: In regions like the Atlantic subtropical gyre, where G_{oa} is small, a large number of neighbors ($N_N = 25$) leads to far flung influences and numerical smoothing. d) A small number of neighbors ($N_N = 4$) is more appropriate here. Gauss weighted remapping via SCRIP, cannot ensure that $G_{oa} \approx N_N$.

While this approach is in widespread use, there are considerable downsides that come with it. There is no mechanism in place to ensure that every ocean surface value can have an impact on the atmosphere. As such, the flux calculation, which for AWI-CM3 and many other coupled climate models takes place in the atmosphere, can be blind to ocean surface processes that exist in a region that is not coupled. For AWI-CM3 this problem is exacerbated by the strong regional differences in FESOM2 horizontal resolution. I call this behavior failure mode A, and it can be seen in figure 5.14b).

While under sampling the ocean is of concern where the ratio of ocean to atmospheric resolution cell area G_{oa} (in $\frac{(km)^2}{(km)^2}$) is larger than N_N, on the opposite end, where $G_{oa} << N_N$, the use of many neighbors exposes a particular atmospheric cell to ocean surface values from needlessly far away locations. This failure mode B can be seen in the example of the open Atlantic in figure 5.14c), where the maximum distance of ocean cell influence to an atmospheric cell is $273\,km$, and thus much larger than the atmospheric grid spacing of $100\,km$. This numerical smoothing introduced through the coupling algorithm is not desirable, as it inhibits the atmosphere from reacting to resolved ocean processes.

Conservative remapping In addition to a fixed number of the nearest neighbors Gauss weighted option, SCRIP also offers 1st order conservative remapping, through which the coupled quantity is conserved, but the spatial gradients or higher-order moments may not be. For this method the number of source cells that are connected to a target cell is variable, and the weights depend not on distance between cell centers, but on the fraction of the target cell area that overlaps with the source cell area. The polygons outlining the grid cell control volumes of FESOM2 and OpenIFS are shown in figure 5.15. Details on the implementation and required changes to work with SCRIP 1st order conservative remapping are given in section 5.6.2

While 1st order conservative remapping by itself can stop failure mode B, i.e. the spurious smoothing over Gauss weighted remapping in areas where $G_{oa} << N_N$, it newly introduces smoothing of spatially sharp ocean signals in key ocean areas with $G_{oa} \approx N_N$ or even $G_{oa} > N_N$. Note that for conservative remapping the number for neighbors is no longer fixed, but dependent on the source cell to target cell overlap. This new conservative remapping-based variation of failure mode A is critical, as areas where the ocean resolution is high in FESOM2, by design, are those with intense ocean dynamics and thus likely to contain processes that I would like to capture on the atmospheric side.

As we will see in the following subsection, stochastic processes placed on top of conservative remapping weights may offer a satisfactory solution for both failure modes A and B at the same time. It also increases the generally underestimated surface flux variability due to coupling and incorporates uncertainty estimates, as elaborated in Rackow and Juricke (2020).

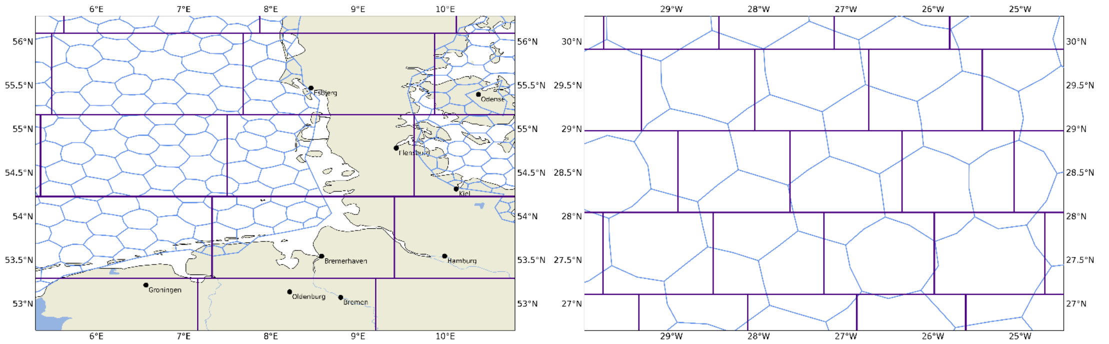

Figure 5.15: When generating coupling weights between source and target cell for 1st order conservative remapping, the number of weights is flexible. a) In areas where the ratio of ocean to atmospheric resolution G_{oa} is high, such as the North Sea, as many as 30 FESOM2 cells make up the final value of ocean surface variables for the OpenIFS cell above. b) In regions like the Atlantic subtropical gyre, where the ratio of ocean/atmosphere resolution is low, the number of contributing overlapping cells is low as well.

Simple stochastic coupling In its simplest form, the idea of stochastic coupling is implemented as a weighted random selection. For normal, deterministic conservative remapping each source cell value is multiplied by the respective cell weight. The final target value consists of the sum over the products,

$$y = \sum_{n=1}^{N_N} A_n x_n \tag{5.24}$$

as shown in equation 5.24. The value on the target grid y is determined as the sum of the products of weights A_n and source grid field values x_n. For the weighted random stochastic coupling I use the weights A_n as a selection probability instead. The selected A_i is set to 1, all others to 0, for the coupling period. Thus, only one of the source values gets through to the target grid. Reproducibility is in many cases a desirable quality of climate models. In order to retain this quality, I seed the FORTRAN RAND pseudo random number generator with the incoming source grid value in the first element of the source vector y_1. The resulting random number will differ in time and space while the simulation remains bit reproducible. An example for a likely selection pattern for this method is depicted in figure 5.16, which mirrors the behavior in the previous AWI-CM1 bespoke implementation by Rackow and Juricke (2020).

Stochastic coupling with temporal autocorrelation The weighted stochastic coupling has the potential downside of being too random. For modern climate and earth system models the coupling period is often one hour or shorter. Such frequent coupling is shorter than the characteristic timescale of boundary layer atmospheric dynamics, which can be on the order of hours to days (Krol et al., 2018).

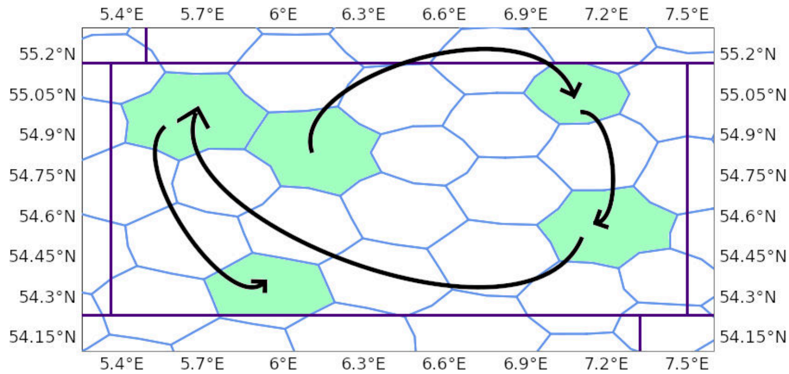

Figure 5.16: **Simple stochastic coupling bases the probability for selection of a single source cell on relative weight of each source grid cell. The target cell value is equal to the single selected source cell, rather than a weighted average of all N_N neighbors.**

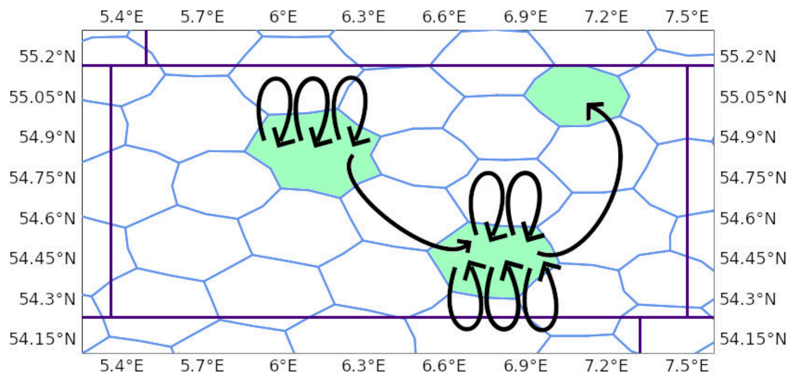

Figure 5.17: **Weighted stochastic coupling increases the probability of selecting the same source cell multiple times in a row. The goal is to match the switching frequency to the characteristic timescale of boundary layer atmospheric dynamics, which can be on the order of hours to days (Krol et al., 2018).**

A possible solution I explore here, is to dampen the frequency and spatial jump distance when a new stochastic selection is made. Dampening of the frequency can be achieved by increasing the selection probability, i.e. the base weight, of the source cell that was selected in the previous coupling step. This is realized by simply adding a fixed value to that particular weight before selecting the source cell for the current time step. Provided the remapping weight calculation worked correctly, the sum of SCRIP calculated weights for a given target cell is 1:

$$\sum_{n=1}^{N} A_n = 1 \tag{5.25}$$

Adding a source cell memory factor and normalizing the sum back to 1 I can raise the chance of selecting the same source cell as in the previous coupling time step. The mean lingering time, or number of reselections, T_l of the same source cell until a switch happens is given by the sum of a geometric series:

$$T_l = \frac{1 - x^{n+1}}{1 - x} \tag{5.26}$$

Where x is the common ratio constant factor between consecutive terms of the geometric series and n the number of selections. Given that we couple many times on many gridpoints, we can assume that the number of selections $\lim_{n\to\infty}$. With $0 < x < 1$, I can solve for the reselection chance that needs to be implemented to obtain a desired T_l:

$$x = \frac{T_l}{T_l + 1} \tag{5.27}$$

For a range of desired mean lingering time T_l, I plot the required individual reselection chance x in figure 5.18.

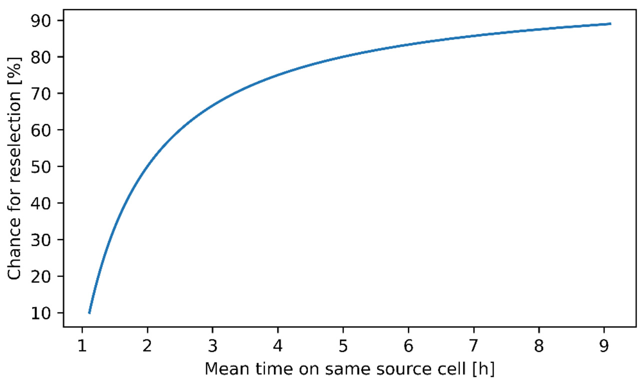

Figure 5.18: Individual chance for source cell reselection that is required to implement a desired lingering time in coupling time steps. The lingering time can be matched to the characteristic timescale of the atmospheric boundary layer.

With the assumption of a characteristic atmospheric boundary layer time of six hours, and the coupling frequency of one hour, I need to reselect the same cell on average six times. The reselection chance to obtain $T_l = 6$ is $x = 85.7\%$. If for example the coupling was only performed every two hours, T_l would reduce to 3, and the required reselections chance would come out as $x = 75\%$.

5.6.2 Implementation

While the concept of stochastic coupling is simple on paper, it requires implementation at a very particular location within the coupled climate model system. The information about source grid, target grid, and the respective remapping weights for each source-target connection all have to be available within a matching data structure.

Naturally, this leads to an implementation within the coupling API library OASIS, specifically in the MCT library for distributed memory sparse matrix multiplication. Since both the source and target models are hybrid (distributed and shared) memory parallelized, it is possible that not all elements of the source grid field required to calculate a single target grid value may be available in local memory.

Luckily, MCT already comes with a rearranger function to exchange the required values, resulting in data locality and allowing for implementation in the MCT function *sMatAvMult_DataLocal_* [sic]. In appendix C.4, I present the implementation of my stochastic coupling algorithm into a version of this function that, for simplicity, is stripped down to its used options. All unused options were removed for readability.

5.6.3 Evaluation and Outlook of Stochastic Coupling

Evaluation The first evaluation of the stochastic coupling is done at low resolution TCo95L91-CORE2, and with using Gauss weighted remapping weights instead of conservative ones as initial probability for source point selection.

I do not expect large benefits at the given model resolution, as the CORE2 ocean mesh is too coarse to resolve the sort of mesoscale ocean processes that we would like to transmit to the OpenIFS grid. This preliminary evaluation mainly serves two purposes. Firstly, to show that stochastic coupling can be realized not only with a bespoke coupling algorithm like in Rackow and Juricke (2020) for the AWI-CM1 model but also in the widely used Oasis3MCT library. And secondly, to show that the realization does not degrade the simulation quality when using grid ratios that do not play into the schemes strengths.

Figure 5.19a) provides an overview of the changes in mean model bias resulting from simple stochastic coupling between ocean and atmosphere fields. The coupling was implemented using Gauss weighted remapping with $N_N = 25$ neighbors, compared to a deterministic simulation with both spanning 50 years each. The TCo95L91-CORE2 simulations were forced with constant year 1990 conditions and the analysis focused on the last 25 years of these simulations. The evaluation was conducted using the CMPI-Tool (refer to section 4). Figure 5.19b) shows the same analysis with only one difference to 5.19a): The stochastic coupling had a time autocorrelation with $T_l = 6h$.

The introduction of simple stochastic coupling appears to be largely beneficial for the Nino34 region, an area where the previous related study by Rackow and Juricke (2020) already found benefits of the system. The first attempt at matching the characteristic atmospheric timescales does at least not make results worse, with some variables perhaps even seeing reduced biases. The reimplementation of the bespoke AWI-CM1 stochastic coupling algorithm into the more widely available OASIS3MCT is thus achieved. The resolution with which these simulations were performed, TCo95L91-CORE2, is not conducive to thorough testing of the suspected mechanisms for improvement of coupling information retention. Further investigation at higher resolution and looking into more advanced model diagnosis will be needed.

Outlook While conservative and stochastic coupling have both been developed for AWI-CM3, the combination of stochastic coupling with probabilities based on conservative weights is not yet functional. Completion of this feature is the highest priority before high resolution evaluation of the feature begins.

Once this issue has been solved, at least three standard 50 year TCo319L137-DART simulations without stochastic coupling, with simple stochastic coupling, and with stochastic coupling featuring temporal autocorrelation will be computed. These simulations will serve as the basis for evaluation of the atmospheric temporal scale matching hypothesis, meaning I will check if the temporal autocorrelation improves dynamical modes of the coupled model.

While the CMPI-Tool climate performance, as described in chapter 4, will once again serve as the starting point, the planned evaluation goes deeper into climate variability modes. Here previous research by Juricke et al. (2013); Weisheimer et al. (2014); Rackow and Juricke (2020); Strommen et al. (2019) has shown stochastic climate processes to improve simulation of long-term climate aspects (ENSO, weather regimes, monsoon, sea ice), enhance surface field variability, reduce biases (convective activity, precipitation), and increase MJO frequencies. I provide an outlook on further planning work in chapter 6.

A further potential improvement to the source point selection is to move away from jumps of random spatial length within the source grid towards a selection method for the next source grid points that favors points within the neighborhood of the previous source point. An example of the kind of random walk patterns to be expected is given in figure 5.20.

It is currently unclear what further improvements are expected by such a random walk compared to the already implemented behavior of the weighted stochastic coupling with limited memory, while technical challenges regarding location information at the MCT interface remain, leading to a lower priority for the development of this feature.

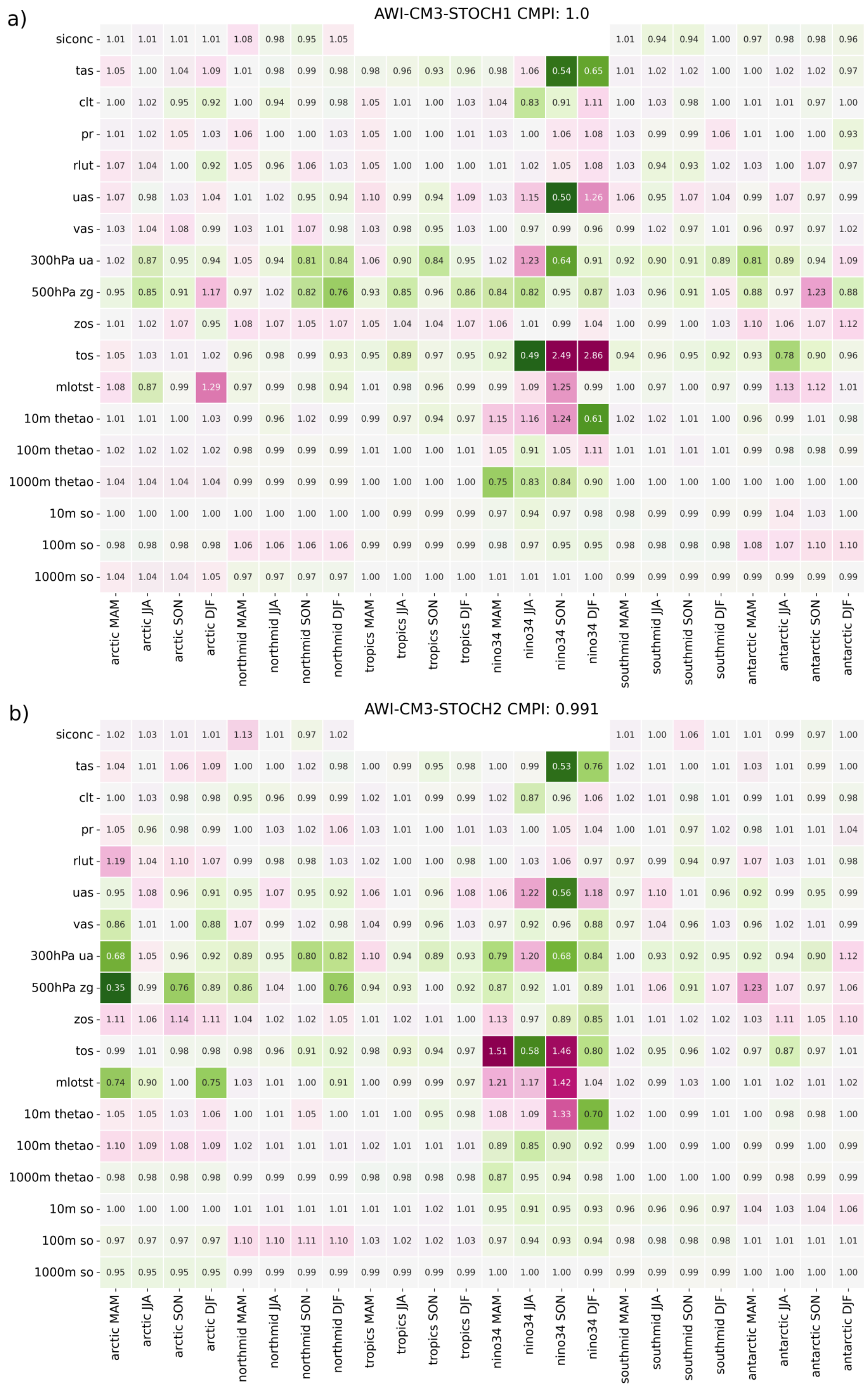

Figure 5.19: a) Changes to climate model performance according to chapter 4, resulting from simple stochastic coupling on top of Gauss weighted remappings ($N_N = 25$) without lingering time as shown in section 5.6.1. b) Changes to climate model performance, resulting from stochastic coupling on top of Gauss weighted remappings ($N_N = 25$) with 6 hour lingering time as described in section 5.6.1. For both cases the simulation was made with TCo95L91-CORE2 resolution and the last 25 out of 50 years were analyzed with the CMPI-Tool.

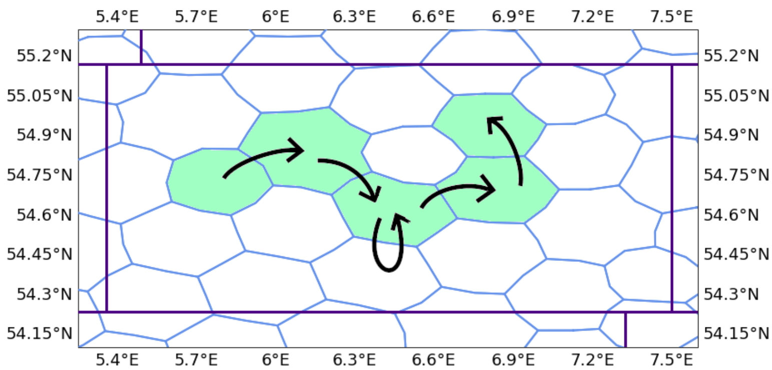

Figure 5.20: **Example for random walk stochastic coupling increases the probability of selecting the nearby source cells over far away ones. The goal is to match the switching frequency to the characteristic timescale of boundary layer atmospheric dynamics, which can be on the order of hours to days (Krol et al., 2018).**

Chapter 6

Conclusion

"One doesn't discover new lands
without loosing sight of the shore."
-Andre Gide

6.1 Summary

The summary below outlines the main sections of the research presented in this thesis.

In chapter 2 of this work, I give an overview of the separation of the geosphere in various spheres for the purpose of facilitating the development of numerical models. I outline the opportunities and challenges in connecting single sphere models into a coupled climate model. In particular, I show how limits in the research scope of any one researcher or research group lead to practical issues with source code repository management and model integration depth. At the same time, I point out how these problems are connected with model physics and related concerns about characteristic timescales of the individual spheres. In the last section of the chapter, I give a broad overview of the kind of fields exchanged at the air-sea interface in a typical state-of-the-art climate model.

I then describe and evaluate the first released version of a next generation coupled climate model, AWI-CM3 in chapter 3. I present a numerical implementation of an atmosphere-ocean coupling interface between OpenIFS43 and FESOM2 based on previous theoretical considerations and the predecessors models AWI-CM1, AWI-CM2, and EC-Earth3. The evaluation of this version of AWI-CM3 (v3.0) was done following the Coupled Model Intercomparison Project (CMIP6) DECK (Diagnostic, Evaluation and Characterization of Klima) protocol. I establish a considerable level of realism in mean present day climate, historical climate change between the years 1850 and 2014, and in future transient and equilibrium model behavior. Furthermore, I used v3.0 and the DECK simulations to identify a number of model biases and misrepresentations compared to observational estimates of the real climate. These were in turn the direct input to chapter 5, where I present my improvements to the AWI-CM3 coupling interface. In particular, my work focuses on improving Southern Ocean salinity gradients, mixed layer depth, and warm biases seen in AWI-CM3. Interestingly, other IFS based coupled models, such as EC-Earth3 or the ECMWF IFS-NEMO HighresMIP contribution had to contend with similar biases in recent years.

When working with a significant number of hypotheses for coupling improvement and interface parameterization tuning options, a quick overview of the respective effects can provide valuable insights. In chapter 4, I present my work on reducing the dimensionality of coupled climate model output. I called the tool in question the Climate Model Performance Intercomparison Tool, or short CMPI-Tool. CMPI-Tool allows for a quick first glance at a number of ocean atmosphere and sea ice mean state variables, as well as a very limited look at model variability. It serves as a sanity check on further model development and tuning, in order to ensure that improvements I may make in one location, variable, or physical process do not lead to inadvertent and overlooked degradation elsewhere in the model. CMPI-Tool is thus applied extensively in chapter 5.

6.2 Discussion and Outlook

In the one of the major parts of this thesis, in chapter 5, I introduce and assess several atmosphere-ocean and atmosphere-sea ice coupling improvements for the AWI-CM3 coupled climate model. Many of these advancements I have collected in the second release version v3.1, while others still need to undergo further testing with the aim at a release in AWI-CM3 v3.2.

I first gained insight into the nature of limitations of the original sea ice surface thermodynamics through the AWI-CM3 based ensemble Kalman filer data assimilation tool AWI-CPS. The clear indication that existing sea ice thickness biases where the result of shortcomings in the thermodynamics, and not the dynamics, of the model prompted me to transfer sea ice surface thermodynamics based on the atmospheric model ECHAM6 into FESOM2. This superseded the previously used sea ice surface thermodynamics scheme of OpenIFS. The resulting global increase in sea ice thickness reduced negative thickness biases in the Antarctic but increased positive ones in the Arctic. To further enhance the model realism I introduced another set of changes, by which I made the sea ice albedo temperature and snow cover dependent. The outcome of my subsequent tuning effort targeting the sea ice albedo scheme was that a reduction of bare ice albedo near the melting temperature could target the Arctic positive thickness bias, without affecting Antarctic sea ice. The underlying physical explanation is that meltponds lower the albedo of the warmer Arctic sea ice more frequently than the typically snow covered Southern Ocean ice.

While the new sea ice thermodynamics are superior to the OpenIFS originals, further analysis through spectral nudging revealed that the splitting of sea ice surface flux calculation (still in OpenIFS) and sea ice surface temperature (now in FESOM2) is problematic. While in ECHAM6 the temperature and flux calculation was called in series every 15 minutes, in AWI-CM3 the two happen in parallel in separate model spheres and executables. The exchange of coupling data happens at most once an hour, and in some resolutions every two hours. The surface layers which are allowed to change their temperature as a result of the sensible heat flux had to be made thicker in both spheres in order to inhibit nonphysical behavior. With the increased thicknesses, the surface layers on both the atmospheric and ocean representation of the sea ice surface layer gained in heat capacity, resulting in a degraded ability to respond to fast thermodynamic changes, like the diurnal cycle or warm air intrusions. For future developments it would be beneficial to keep the improved sea ice surface thermodynamics but to consolidate the temperature and flux calculation in the same sphere and executable with level three or four (see chapters 2.2.1 and 2.2.1) serial coupling.

Another major set of changes was the deactivation of the Monin Obukhov scheme for vertical mixing (MOMIX) and activation of the Salt Plume Parameterization (SPP). In their combined effect these changes where highly effective in increasing the diapycnal vertical gradient in the Weddell Sea from low to high salinity in the top 100 meters. This resulted in a larger surface to deep ocean density gradient, which stabilized the freshwater lens in the region, and led to much decreased and more realistic mixed layer depth in the region. While the mechanism of action of SPP in AWI-CM3 is consistent with previous work on this parameterization, the effect of MOMIX is different in AWI-CM3 than in standalone FESOM2. Full understanding of why the MOMIX behavior diverges and why turning it off helped reduce the mixed layer depths is still forthcoming. This open issue may be subject of future work.

A third and ongoing body of work is the inclusion of stochastic coupling processes into the sparse matrix multiplication in the model coupling library OASIS3MCT. Previous work has shown that when introduced as bespoke paramterization in the predecessor model AWI-CM1, stochastic coupling helped to better represent key coupled dynamic model physics, such as ENSO phase locking. First results with my OASIS3MCT based implementation indicate that the method does not negatively effect a low resolution simulation. In a bid to match the stochastic switching frequency to the characteristic timescales of the atmospheric boundary layer, I developed an extension to the method by which the source grid points selected in the previous coupled timestep have a higher chance to get selected again. Tentative evaluation at low resolution indicated that the extension of the method may have a positive impact an the simulated mean climate and climate variability. One prospective further extension of the stochastic coupling method is the inclusion of a random walk scheme. This particular feature requires the geographic location of each source grid cell to be available and associated with the respective coupling weight at the location of sparse matrix multiplication. The technical challenges for random walk stochastic coupling are as of yet unsolved. My entire body of work on stochastic coupling will require further evaluation at an appropriate high resolution of 5-30km in both atmosphere and ocean. Finally, peer review and publication of the work done on stochastic coupling is planned. Another goal is to merge the stochastic coupling developments back into the OASIS3MCT main branch, such that the feature is made available to the wider coupled climate modeling community.

One byproduct of the stochastic coupling work is that I made AWI-CM3 capable of using 1st order locally conservative remapping. I conducted short tests, which established the technical capability to send atmosphere to ocean fluxes using locally conservative instead of Gauss weighted remapping. However, there is still a need for longer simulations to thoroughly examine the effects of employing these remappings. Additionally, I am interested in exploring whether the utilization of 1st order conservative remapping is suitable for all heat and mass fluxes or only a subset, while also integrating stochastic ocean surface fields with locally conservative flux coupling. Technical tests with all fluxes produced numerically stable simulations but the physical results have not yet been evaluated.

On the way to being able to run the upcoming Climate Model Intercomparison Project (CMIP7) simulations, and as one contribution to reduce the spuriously large historical warming found in v3.1, a version of AWI-CM3 was developed which can read in historical anthropogenic tropospheric aerosol forcings. In fact, two different realizations exist, a simple scaling approach developed by Tido Semmler (Met Éireann), and a more complex scheme based on MACv2-SP by Joakim Kjellsson (GEOMAR). I want to test both, study the impact of historical climate change, and decide which one to use going forward.

The river routing component currently used in AWI-CM3, the runoff-mapper, is highly simplistic, contains no water storage capabilities, basin orography, or flood dynamics. These shortcomings will be addressed by the implementation of the Catchment-based Macro-scale Floodplain (CaMa-Flood) global river hydrodynamics model into ECLand. ECLand in turn will be available for AWI-CM3 once the OpenIFS model is upgraded to cycle 48r1, which is planned for Q3 or Q4 2023. Given extensive developments at ECMWF between the current cycle 43r3 and 48r1, the inclusion of the new OpenIFS version has the potential to improve AWI-CM3s' physical and computational performance in numerous ways, including but not limited to: Peak cyclone wind velocities, moist physics, single precision, convection scheme, 3D rather than 2D aerosol climatology.

While the upgrade to the next OpenIFS cycle may promise model improvements, it also generates a significant amount of work, as implementations made for 43r3 have to be transferred and adapted to the 48r1 OpenIFS source code.

Multiple exciting developments are currently taking place on the road towards improved cryosphere capabilities of AWI-CM3. Pengyang Song (AWI) has included ice cavities, which provide basal melt fluxes for FESOM2 in AWI-ESM2. I am planning to integrate this feature into AWI-CM3/ESM3 as a partial replacement of the excess snow to iceberg melt flux developments I presented in section 5.2. A further step towards upgrading the cryosphere treatment will be taken by the adaptation of the Lagrangian ICEBERG drift model by Lars Ackermann (AWI) from AWI-ESM2 to AWI-CM3/ESM3. Preliminary results indicate that this step may reduce the remaining Antarctic sea ice thickness low bias, which may in turn reduce and improve the simulated historic global warming. On a somewhat longer timescale two more major upgrades to the cryosphere are planned, which will start to truly transform AWI-CM3 into AWI-ESM3. Firstly, a level one coupling between AWI-CM3 and the PISM Parallel IceSheet Model; and secondly, the inclusion of a permafrost model in the OpenIFS land surface scheme HTESSEL/ECLand. Another comparatively minor change would be the planned inclusion of the feedback of cloud cover on ice albedo. The cloud cover would be used to modify the spectrum of incoming shortwave radiation. As the sea ice albedo differs depending on wavelength, the broad band albedo is impacted. Finally there are tentative plans to use ICEPACK, a multi layer sea ice thermodynamics scheme recently implemented into FESOM2, instead of the currently employed zero layer thermodynamics.

A vital step on the way to transforming AWI-CM3 into AWI-ESM3 will be the coupling of a dynamic vegetation model LPJ-GUESS 4.1, which is currently under-way at the University Lund. I will likely contribute by integrating LPJ-GUESS into the AWI runscript environment esm-tools and assessing the (paleo)climate performance of the dynamic vegetation enabled AWI-ESM3.

Further work towards AWI-ESM3 is going to be made by the development of a coupled carbon cycle in atmosphere, land surface, and ocean. To this purpose OpenIFS will be connected to the already existing FESOM2-RECOM setup. The Regulated ECOsystem and biogeochemistry Model (RECOM) is an ocean biogeochemistry model developed in the biology department of AWI. For a coupled carbon cycle setup of AWI-ESM3, the first order terms will be surface pressure and CO_2 flux coupling. Continuative work may include the coupling of fluvial dissolved organic carbon.

Besides AWI-CM3/ESM3 the second major branch of work influenced by the coupling improvements I present here is the Destination Earth (DestinE) program where climate models are developed which are supposed to resemble the real world to the point of being called digital twins (DT). One of the DTs under development is IFS cy48r1 FESOM2 level three / single executable coupling. The technical infrastructure of the DT differs substantially from AWI-CM3/ESM3 to accommodate the exceptionally high horizontal resolutions of the DT (up to 2.5km). However, the physical flux improvements and the inclusion of second order effects have already found their way into the IFS-FESOM2 DT, and resulted in substantial improvements of its mean climate. Once the DestinE project is further advanced and AWI-CM3/ESM3 switches to OpenIFS cy48r1, some transfer of scalability improvements from the DT to AWI-CM3/ESM3 may be accomplished. Both model systems will continue to be co-developed, with the respective foci on extreme resolution and full ESM feedbacks. Depending on future open source policies of the various actors involved with DestinE, a convergence of AWI-ESM3 and the IFS-FESOM DT appears plausible in the long term.

Appendix A

Glossary

"For every minute spent in organizing,
an hour is earned."
-Benjamin Franklin

A.1 Constants

Table A.1: Constant descriptions

Variable	Long name	Value
a_{ice}	Thermal conductivity of ice	$2.1656\frac{W}{mK}$
d_{ice}	Minimum sea ice thickness for numerical stability	$0.05m$
H_{H_2O}	Enthalpy of fusion for water	$333.55\frac{J}{g}$
R	Earth radius	$6.371\,km$
S	Solar constant	$1361\,\frac{W}{m^2}$
σ	Stefan-Boltzmann constant	$5.67 \times 10^8\,\frac{W}{m^2K^4}$
Ω	Rotation rate of the Earth,	$7.2921 \times 10^{-5}\frac{rad}{s}$

A.2 Variables

Table A.2: Variable Definitions

Variable	Long name	Unit
a	Rossby radius of deformation	m
clt	Cloud cover	$\%$
e_{ice}	Specific energy to warm 1m thick ice by 1K	$\frac{J}{m}$
e_{sn}	Specific energy to warm 1m thick snow by 1K	$\frac{J}{m}$
g	Gravitational force (often constant Earth surface)	$\frac{m}{s^2}$
h_{rn}	Specific heat capacity of rain	$\frac{J}{kgK}$
h_{sn}	Specific heat capacity of snow	$\frac{J}{kgK}$
$mlotst$	Mixed layer depth	m
n	Number of simulation timestep	-
p	Fluid pressure	$\frac{kgm}{s^2}$
pr	Total precipitation	$\frac{mm}{day}$
$rlut$	Top of atmosphere outgoing longwave radiation	$\frac{W}{m^2}$
s	Plume transported salt	PSU
$siconc$	Sea ice concentration	$\%$
so	3D ocean salinity	PSU
t	Simulation timestep	-
$tas\ \ T_a$	Near surface (2m) air temperature	$°C$
$thetao$	3D ocean temperature	$°C$
$tos\ \ T_o$	Ocean surface temperature	K
u	Zonal fluid velocity	$\frac{m}{s}$
uas	Zonal surface wind velocity	$\frac{m}{s}$
v	Meridional fluid velocity	$\frac{m}{s}$
vas	Meridional surface wind velocity	$\frac{m}{s}$

Continued on the next page

Table A.2: Variable Definitions (continued)

Variable	Long name	Unit
w	Vertical fluid velocity	$\frac{m}{s}$
z_{ice+sn}	Effective thickness of sea ice plus snow	m
z_g	Geopotential height	m
z_n	Neutral buoyancy depth	m
zos	Sea surface height	m
$C_{v,sn+ice}$	Heat capacity for snow and top sea ice layer	$\frac{J}{K}$
F_r	3D friction force	$\frac{kgm}{s^2}$
A_{ib}	iceberg melt area	m^2
A_{sn}	Snow accumulation area on glacier	m^2
B_0	Salt plume buoyancy flux per unit length	$\frac{m^4}{s^2}$
C_D	Drag coefficient	-
F_{rx}	Zonal friction force	$\frac{kgm}{s^2}$
F_{ry}	Meridional friction force	$\frac{kgm}{s^2}$
F_{rz}	Vertical friction force	$\frac{kgm}{s^2}$
E_{ice+sn}	Energy required to change the snow temperature by 1K	J
G_{oa}	Ratio of ocean to atmospheric resolution cell area	-
K_d	Thermal diffusivity of the climate system	$\frac{m^2}{s}$
M_x	Zonal momentum flux component	$\frac{kg}{ms^2}$
M_y	Meridional momentum flux component	$\frac{kg}{ms^2}$
N	Brunt–Väisälä frequency	$\frac{rad}{s}$
N_N	Number of neighbours for remapping weights	-
Q_d	Diffusive flux $\frac{W}{m^2}$	
Q_{atm}	Total air-sea heat flux	$\frac{W}{m^2}$
Q_{cice}	Conductive heat flux through sea ice	$\frac{W}{m^2}$
Q_{cice*}	Preliminary heat flux through sea ice	$\frac{W}{m^2}$
$Q_{H,sn}$	Enthalpy of snow falling into open ocean	$\frac{W}{m^2}$
Q_{lat}	Latent heat flux	$\frac{W}{m^2}$
Q_{lw}	(Net) longwave heat flux	$\frac{W}{m^2}$
Q_{lwo}	Outgoing longwave radiation	$\frac{W}{m^2}$
Q_{ns}	Non-solar heat flux	$\frac{W}{m^2}$
Q_{se}	Sensible heat flux	$\frac{W}{m^2}$
Q_{sw}	(Net) shortwave heat flux	$\frac{W}{m^2}$
Q_{swi}	Unidirectional incoming shortwave radiation	$\frac{W}{m^2}$
Q_{swr}	Reflected shortwave radiation	$\frac{W}{m^2}$
S	Cumulative salt over plume	PSU
T_0	Salinity dependent freezing temperature of water	K
T_s	Surface temperature	K
T_{si}	Sea ice surface temperature	K
V_0	Salt plume volume flux per unit length	$\frac{m^2}{s}$

Continued on the next page

Table A.2: Variable Definitions (continued)

Variable	Long name	Unit
$\mathbf{U}$	Fluid velocity vector	$\frac{m}{s}$
α	Albedo	-
ϵ	Emissivity	-
μ_{rn}	Rain mass flux	$\frac{kg}{m^2 s}$
μ_{sn}	Snow mass flux	$\frac{kg}{m^2 s}$
ρ	Fluid density	$\frac{kg}{m^3}$
τ	Surface wind stress tensor	Pa
ϕ	Latitude angle	rad
ω	Vertical velocity	$\frac{Pa}{s}$

Appendix B

Additional plots

"Perhaps too much of everything is as bad as too little."

-Edna Ferber

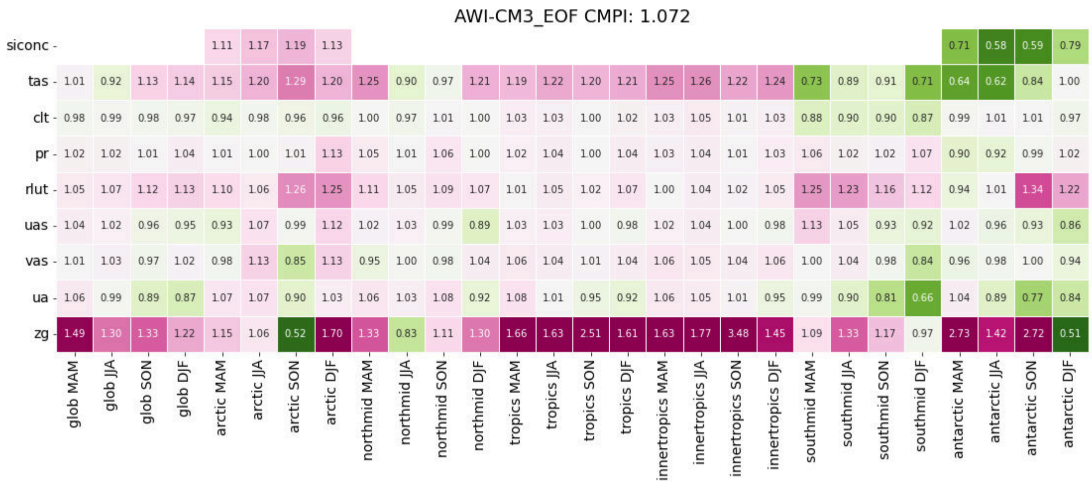

Figure B.1: **Impact of coupling enthalphy of fusion of snow falling into open ocean. Last 25 years of 50 years constant 1990 forcing.**

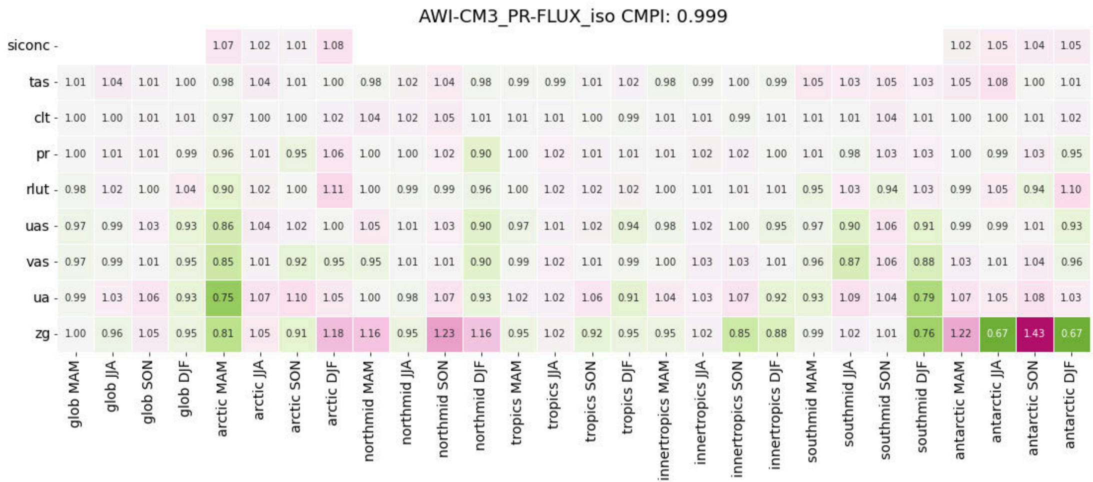

Figure B.2: **Impact of coupling heat flux from divergence of SKT and T2M. Last 25 years of 50 years constant 1990 forcing.**

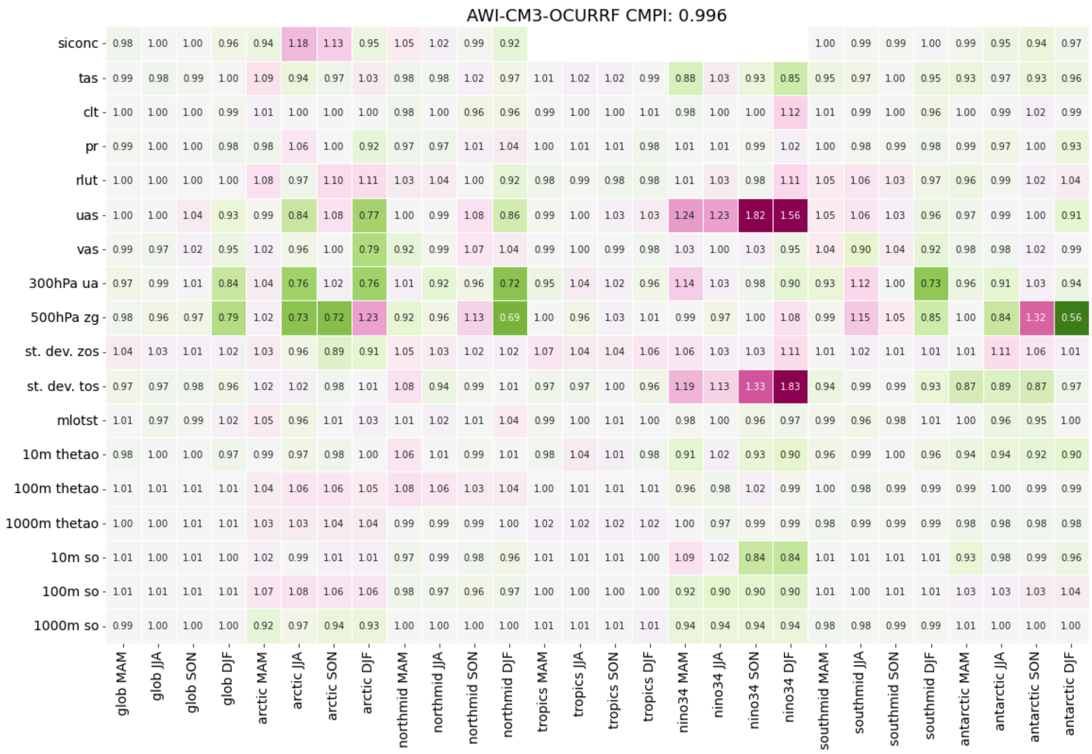

Figure B.3: Impact of coupling current feedback. Last 25 years of 50 years constant 1990 forcing.

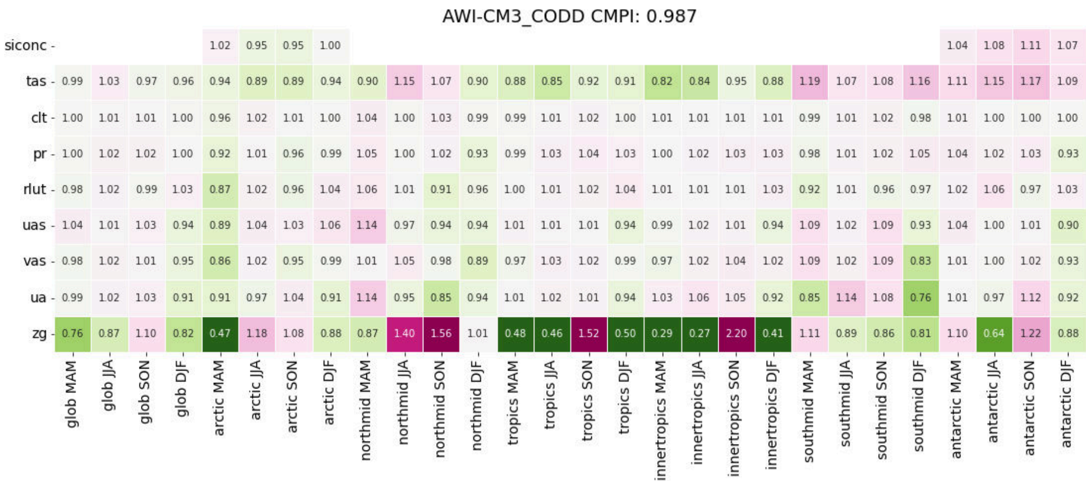

Figure B.4: **Impact of switching from total solar insolation to spectral solar insolation with OpenIFS cy43r3v2. Last 25 years of 50 years constant 1990 forcing.**

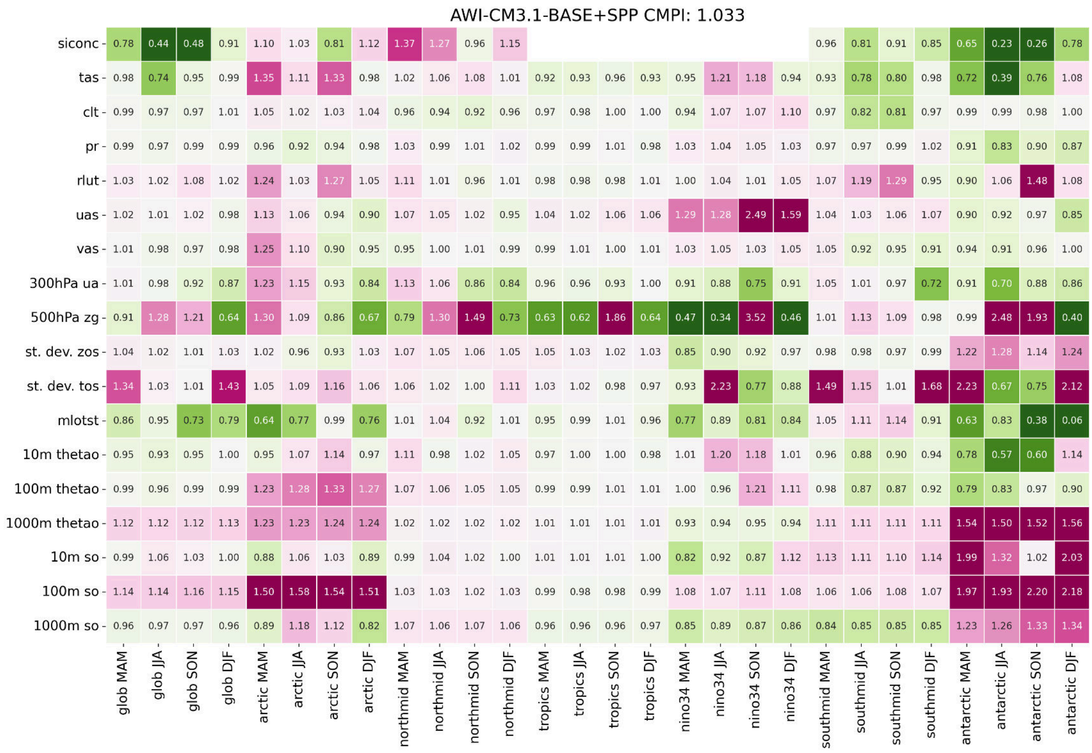

Figure B.5: Impact of switching from Monin Obukov mixing to Salt Splume Parameterization. Last 25 years of 50 years constant 1990 forcing.

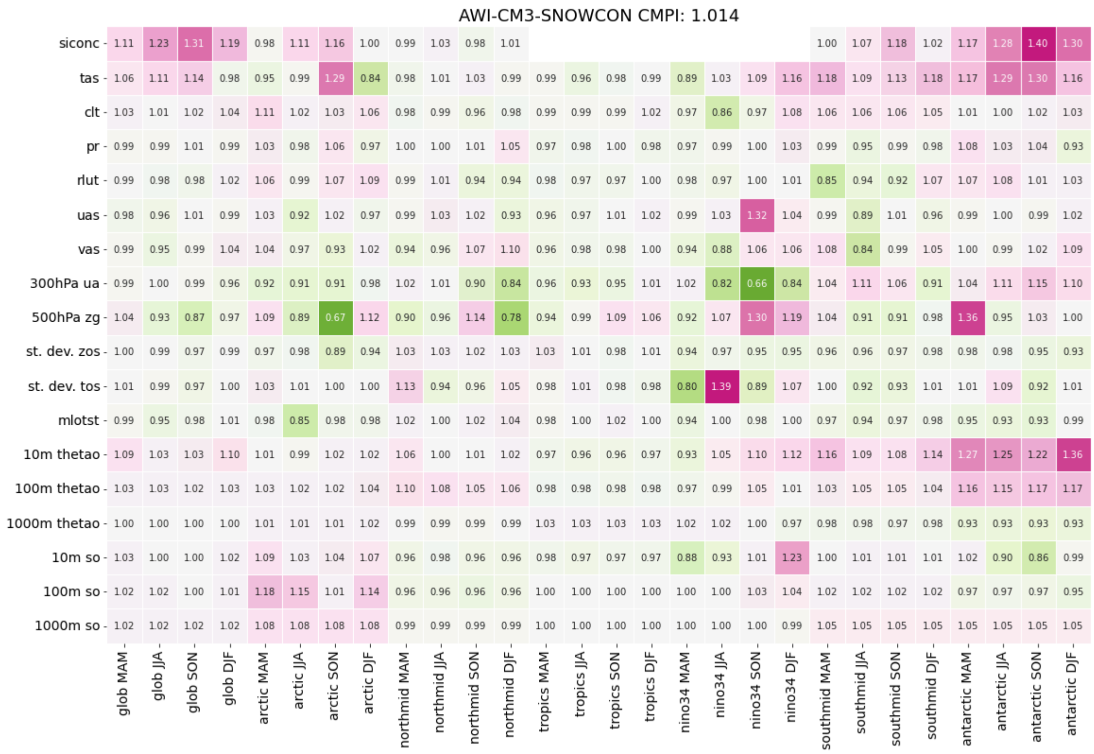

Figure B.6: **Impact of correcting sensible heat flux into snow covered sea ice. Last 25 years of 50 years constant 1990 forcing.**

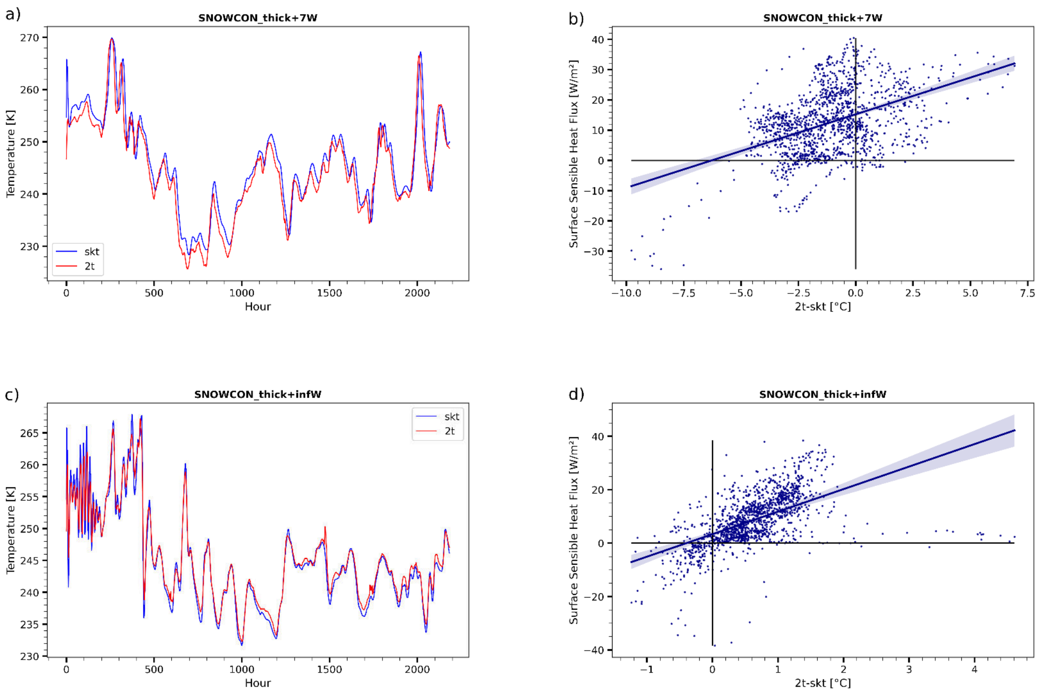

Figure B.11: **Top row: Before increasing the thermal thickness of OpenIFS snow surface layer. Bottom row: After increases of the thermal conductivity from 7 to 50 $\frac{W}{mK}$. Left: Correspondance of sea ice surface temperature to near surface (2m) air temperature. Right: Spatial correlation of surface sensible heat flux with air-sea ice temperature difference. Note the shift from the nonphysical 1. Quadrant to the 2 Quadrand. Shown are the first 2500 hours of short test simulations.**

Appendix C

Source code

*"Computers are like old testament gods.
Lots of rules, and no mercy"*

-Joseph Campbell

C.1 Atmosphere to ocean fluxes

```
!! Uwe Fladrich, SMHI           2017-Aug        Original
!! Jan Streffing, AWI           2017-Nov        Adapted for coupling with FESOM2


SUBROUTINE FESOM_SET_OCEAN_FLUXES(YDGEOMETRY,YDSURF,KDIM,SURFL,PSURF,FLUX,PAUX)

    USE GEOMETRY_MOD,       ONLY: GEOMETRY

    USE PARKIND1,           ONLY : JPRB, JPIM
    USE YOMHOOK,            ONLY : LHOOK, DR_HOOK
    USE YOMPHYDER,          ONLY : DIMENSION_TYPE, SURF_AND_MORE_LOCAL_TYPE, &
      & SURF_AND_MORE_TYPE, FLUX_TYPE, AUX_TYPE
    USE SURFACE_FIELDS_MIX, ONLY : TSURF
    USE YOMCST,             ONLY : RLVTT, RLSTT, RSIGMA, RCPD
    USE CPLNG
    USE YOETHF,             ONLY : RHOH2O
    USE YOMRIP,             ONLY : YRRIP
    USE YOS_SOIL,           ONLY : TSOIL

    IMPLICIT NONE

    ! Arguments
    TYPE(GEOMETRY),                 INTENT(IN) :: YDGEOMETRY
    TYPE(TSURF),                    INTENT(INOUT) :: YDSURF
    TYPE(DIMENSION_TYPE),           INTENT(IN) :: KDIM
    TYPE(SURF_AND_MORE_LOCAL_TYPE),INTENT(IN) :: SURFL
    TYPE(SURF_AND_MORE_TYPE),       INTENT(INOUT) :: PSURF
    TYPE(FLUX_TYPE),                INTENT(IN) :: FLUX
    TYPE(AUX_TYPE),                 INTENT(IN) :: PAUX

    ! Locals
    REAL(KIND=JPRB)     :: ZHOOK_HANDLE
    INTEGER(KIND=JPIM) :: IL,IE,IG,I
    REAL(KIND=JPRB)     :: ZMASK(KDIM%KLON)
    REAL(KIND=JPIM)     :: POSMASK(KDIM%KLON)
    REAL(KIND=JPRB)     :: ZEXSNOW(KDIM%KLON)
    REAL(KIND=JPRB)     :: HEATPREC(KDIM%KLON)
    REAL(KIND=JPRB)     :: HEATRAIN(KDIM%KLON)
    REAL(KIND=JPRB)     :: HEATSNOW_POS(KDIM%KLON)
    REAL(KIND=JPRB)     :: HEATSNOW_NEG(KDIM%KLON)
    REAL(KIND=JPRB)     :: SST(KDIM%KLON)
    REAL(KIND=JPRB)     :: T2M(KDIM%KLON)
    REAL(KIND=JPRB)     :: NEGATIVE_PART(KDIM%KLON)
    REAL(KIND=JPRB)     :: POSITIVE_PART(KDIM%KLON)
    REAL(KIND=JPRB)     :: RAIN(KDIM%KLON)
    REAL(KIND=JPRB)     :: SNOW(KDIM%KLON)

    ASSOCIATE(YSD_VD=>YDSURF%YSD_VD, TSTEP=>YRRIP%TSTEP, PGELAT=>PAUX%PGELAT, &
            & YSP_SG=>YDSURF%YSP_SG, YSD_VF=>YDSURF%YSD_VF)

    IF (LHOOK) CALL DR_HOOK('FESOM_SET_OCEAN_FLUXES',0,ZHOOK_HANDLE)

    ! ======================================================================
    ! *** Pre-compute indices
    ! ======================================================================

    IL = KDIM%KIDIA                                                          ! Start of horizontal loop
    IE = KDIM%KFDIA - KDIM%KIDIA                                             ! End of horizontal oop
    IG = KDIM%KSTGLO - 1 + KDIM%KIDIA                                        ! Start adress of
         computation in NGPTOT-sized arrays

    ! ======================================================================
    ! *** Momentum fluxes (stresses)
    ! ======================================================================
    CPLNG_FLD(CPLNG_IDX('A_TauX_oce'))%D(IG:IG+IE,1,1) = PSURF%PUSTRTI(IL:IL+IE,1)
    CPLNG_FLD(CPLNG_IDX('A_TauY_oce'))%D(IG:IG+IE,1,1) = PSURF%PVSTRTI(IL:IL+IE,1)
    CPLNG_FLD(CPLNG_IDX('A_TauX_ice'))%D(IG:IG+IE,1,1) = PSURF%PUSTRTI(IL:IL+IE,2)
    CPLNG_FLD(CPLNG_IDX('A_TauY_ice'))%D(IG:IG+IE,1,1) = PSURF%PVSTRTI(IL:IL+IE,2)

    ! ======================================================================
    ! *** Heat fluxes (radiative and latent)
    ! ======================================================================
    SST(IL:IL+IE) = PSURF%PSD_VF(IL:IL+IE,YSD_VF%YSST%MP)
    T2M(IL:IL+IE) = PSURF%PSD_VD(IL:IL+IE,YSD_VD%Y2T%MP)
    RAIN(IL:IL+IE) = FLUX%PFPLCL(IL:IL+IE,KDIM%KLEV) / RHOH2O + FLUX%PFPLSL(IL:IL+IE,KDIM%KLEV) / RHOH2O
    SNOW(IL:IL+IE) = FLUX%PFPLCN(IL:IL+IE,KDIM%KLEV) / RHOH2O + FLUX%PFPLSN(IL:IL+IE,KDIM%KLEV) / RHOH2O
    HEATRAIN = ((T2M-SST)*RAIN*4.186_JPRB)*1000000_JPRB
    ! Split snow temperature change into part above and below 0C, because of different heat mass specific
         capacity
    DO I = IL, IL + IE
        ! Find the absolute difference
        POSITIVE_PART(I) = ABS(T2M(I) - SST(I))

        ! Determine the sign of the original difference
        IF (T2M(I) - SST(I) >= 0) THEN
```

```
            POSITIVE_PART(I) = ABS(T2M(I) - SST(I))
            NEGATIVE_PART(I) = 0.0
        ELSE
            POSITIVE_PART(I) = 0.0
            NEGATIVE_PART(I) = ABS(T2M(I) - SST(I))
        END IF

        ! In case of snow cooling, negative sign
        IF (T2M(I) >= SST(I)) THEN
            POSITIVE_PART(I) = -POSITIVE_PART(I)
            NEGATIVE_PART(I) = -NEGATIVE_PART(I)
        END IF
    END DO
    HEATSNOW_POS = (POSITIVE_PART*SNOW*4.186_JPRB)*1000000_JPRB
    HEATSNOW_NEG = (NEGATIVE_PART*SNOW*2.108_JPRB)*1000000_JPRB
    HEATPREC = HEATRAIN + HEATSNOW_POS + HEATSNOW_NEG
    CPLNG_FLD(CPLNG_IDX('A_Qns_oce'))%D(IG:IG+IE,1,1) = &                      ! Heat over ocean =
       PSURF%PEVAPTI(IL:IL+IE,1) * RLVTT + &                                    ! Latent from evap +
       PSURF%PAHFSTI(IL:IL+IE,1) + &                                            ! Sensible at surface +
       SURFL%ZAHFTRTI(IL:IL+IE,1) - &                                           ! Net lw rad at surface
       (FLUX%PFPLCN(IL:IL+IE,KDIM%KLEV) + &                                     ! (Enthalpy of fusion of
           snow with
       FLUX%PFPLSN(IL:IL+IE,KDIM%KLEV)) * 333.5_JPRB * 1000.0_JPRB + &          ! conversion from m depth
           to gramm)
       HEATPREC(IL:IL+IE)                                                       ! Heatflux from
           precipitation temperature

    ZMASK(IL:IL+IE) = 0                                                         ! Initialze Binary sea ice
         mask
    WHERE(SURFL%ZFRTI(IL:IL+IE,2) .NE. 0.0) ZMASK(IL:IL+IE) = 1                ! where more than 0 sea
        ice -> mask = 1

    CPLNG_FLD(CPLNG_IDX('A_Q_ice'))%D(IG:IG+IE,1,1) = &                        ! Heat over ice =
       (PSURF%PEVAPTI(IL:IL+IE,2) * RLSTT + &                                   ! Latent from subl +
       PSURF%PAHFSTI(IL:IL+IE,2) + &                                            ! Sensible at surface +
       SURFL%ZAHFTRTI(IL:IL+IE,2) + &                                           ! Net lw rad at surface
       SURFL%ZFRSOTI(IL:IL+IE,2)) * &                                           ! Net sw rad at surface
       ZMASK(IL:IL+IE)                                                          ! Send only where there is
            any sea ice

    CPLNG_FLD(CPLNG_IDX('A_Qs_all'))%D(IG:IG+IE,1,1) = &                       ! Separatly send SW down
        ocean for SW-penetration
       SURFL%ZFRSOTI(IL:IL+IE,1)

    ! ======================================================================
    ! *** Mass fluxes (runoff+calving, precipitation, evaporation)
    ! ======================================================================
    ZEXSNOW(IL:IL+IE) = MAX(PSURF%PSP_SG(IL:IL+IE,YSP_SG%YF%MP9)+&            ! Snow water mass [kg/m
        **2]
                            PSURF%PSNSE1(IL:IL+IE)*TSTEP-10000.0_JPRB,0.)      ! Snow mass tendency [kg/
                                sm**2] - perannial snow hight [kg/m**2]

    PSURF%PSNSE1(IL:IL+IE) = PSURF%PSNSE1(IL:IL+IE)-&
                             ZEXSNOW(IL:IL+IE)/TSTEP

    CPLNG_FLD(CPLNG_IDX('A_Calving'))%D(IG:IG+IE,1,1) = &
       (ZEXSNOW(IL:IL+IE)/TSTEP)/1000

    CPLNG_FLD(CPLNG_IDX('A_Runoff'))%D(IG:IG+IE,1,1) = &
       (FLUX%PFWRO1(IL:IL+IE) + FLUX%PFWROD(IL:IL+IE))/1000

    CPLNG_FLD(CPLNG_IDX('A_Precip_liquid'))%D(IG:IG+IE,1,1) = &
       FLUX%PFPLCL(IL:IL+IE,KDIM%KLEV) / RHOH2O + &
       FLUX%PFPLSL(IL:IL+IE,KDIM%KLEV) / RHOH2O

    CPLNG_FLD(CPLNG_IDX('A_Precip_solid'))%D(IG:IG+IE,1,1) = &
       FLUX%PFPLCN(IL:IL+IE,KDIM%KLEV) / RHOH2O + &
       FLUX%PFPLSN(IL:IL+IE,KDIM%KLEV) / RHOH2O

    CPLNG_FLD(CPLNG_IDX('A_Evap'))%D(IG:IG+IE,1,1) = &
       PSURF%PEVAPTI(IL:IL+IE,1) / RHOH2O

    CPLNG_FLD(CPLNG_IDX('A_Subl'))%D(IG:IG+IE,1,1) = &
       (PSURF%PEVAPTI(IL:IL+IE,2) / RHOH2O)

    IF (LHOOK) CALL DR_HOOK('FESOM_SET_OCEAN_FLUXES',1,ZHOOK_HANDLE)

    END ASSOCIATE

END SUBROUTINE FESOM_SET_OCEAN_FLUXES
```

C.2 Integration of ocean surface values

```
SUBROUTINE FESOM_UPDCLIE(YDGEOMETRY,YDSURF,PTSTEP)

USE GEOMETRY_MOD , ONLY : GEOMETRY
USE SURFACE_FIELDS_MIX , ONLY : TSURF
USE PARKIND1 , ONLY : JPRD, JPIM, JPRB, JPIB
USE YOMHOOK , ONLY : LHOOK, DR_HOOK
USE YOERAD , ONLY : YRERAD
USE YOEPHY , ONLY : YREPHY
USE YOMCST , ONLY : RDAY, RTT, RPI
USE YOMCT0 , ONLY : CNMEXP, LTWOTL
USE YOMCT3 , ONLY : NSTEP
USE YOMLUN , ONLY : NULOUT, NULCO, NULERR
USE YOMMCC , ONLY : YRMCC
USE YOMCOU , ONLY : YRCOU
USE YOMMP0 , ONLY : MYPROC
USE YOMMSC , ONLY : NINTLEN, NREALEN
USE YOMRIP0 , ONLY : NINDAT
USE YOMRIP , ONLY : YRRIP
USE YOM_YGFL , ONLY : YGFL
USE MPL_MODULE, ONLY : MPL_BROADCAST, MPL_BARRIER
USE DISGRID_MOD, ONLY : DISGRID_SEND, DISGRID_RECV
USE GRIB_API_INTERFACE, ONLY : IGRIB_OPEN_FILE, IGRIB_NEW_FROM_FILE,&
 & JPGRIB_END_OF_FILE, JPGRIB_SUCCESS, IGRIB_GET_VALUE, IGRIB_RELEASE,&
 & IGRIB_CLOSE_FILE, IGRIB_SET_VALUE
    USE FESOM
    USE CPLNG

    IMPLICIT NONE

#include "surf_inq.h"
#include "surfpp.h"

    ! Arguments
    REAL(KIND=JPRB)   ,INTENT(IN)    :: PTSTEP ! Time step
    TYPE(GEOMETRY)    ,INTENT(IN)    :: YDGEOMETRY
    TYPE(TSURF)       ,INTENT(INOUT) :: YDSURF


    ! Locals
    REAL(KIND=JPRB) :: ZHOOK_HANDLE
INTEGER(KIND=JPIM) :: IA, IA0, IADD, IAE, IAN, ICCYY0, ICCYYE,&
 & ICLIM, ICOU, ID, IDIF, IDIFD, IDUMY, IEND,&
 & IEXTRA, IFIRST, IGRIB, IDGNH, IFIRST1, IGRIB1,&
 & IIM1, IIM2, IJ0, IJDCR, IJE, IJOUR,&
 & IJT1, IJT2, IJUL, IJUL0, IJUL1, IJUL2, IJULE, IJULBC,&
 & IM, IM0, IME, IMM0, IMME, IMOIS, IMT1,&
 & IPAR31, IPAR139, IPAR174, IPARAM, IPARAM1, IPARAM2,&
 & IPARAM3, IPARAM4, IPAR131, IPAR132, JGRIBC, IPARMAL,&
 & IBL, IRET, IST, ISTADDE,&
 & ITAG, ITIM, ITIME,&
 & IYYM0, IYYMD, J, JCL, JCL1,  JF, JGL, JBC,&
 & JM, JROF, JSTGLO, JTIM, JY, II, ISST1, ISST2, ICSTEP, ISTEP, JL, ISECND,&
 & ICLIMT

    REAL(KIND=JPRB),POINTER :: CPL_FLD_SST(:)
    REAL(KIND=JPRB),POINTER :: CPL_FLD_ICE_FRAC(:)
    REAL(KIND=JPRB),POINTER :: CPL_FLD_ICE_TEMP(:)
    REAL(KIND=JPRB),POINTER :: CPL_FLD_ICE_ALB(:)
    REAL(KIND=JPRB),POINTER :: CPL_FLD_OUCURR(:)
    REAL(KIND=JPRB),POINTER :: CPL_FLD_OVCURR(:)

    REAL(KIND=JPRB) ::ZRTFREEZSICE, ZRCIMIN, ZTS, ZCI, ZTI, ZSSTCI, ZDSST0, ZR2D
    LOGICAL :: LLICE0(0:YDGEOMETRY%YRGEM%NGPTOT),LLICEN(0:YDGEOMETRY%YRGEM%NGPTOT),LLAKE(0:YDGEOMETRY%YRGEM%
        NGPTOT)
    LOGICAL :: LLMISS

ASSOCIATE(YDDIM=>YDGEOMETRY%YRDIM,YDDIMV=>YDGEOMETRY%YRDIMV, &
  & YDGEM=>YDGEOMETRY%YRGEM, YDMP=>YDGEOMETRY%YRMP, YDGSGEOM_NB=>YDGEOMETRY%YRGSGEOM_NB)
ASSOCIATE(NACTAERO=>YGFL%NACTAERO, &
 & NDGLG=>YDDIM%NDGLG, NDGNH=>YDDIM%NDGNH, NDLON=>YDDIM%NDLON, &
 & NPROMA=>YDDIM%NPROMA, &
 & INVML=>YREPHY%INVML, LE4ALB=>YREPHY%LE4ALB, LECURR=>YREPHY%LECURR, &
 & LEFLAKE=>YREPHY%LEFLAKE, LEOBC=>YREPHY%LEOBC, LEOBCICE=>YREPHY%LEOBCICE, &
 & LEOCCO=>YREPHY%LEOCCO, LEOCLAKE=>YREPHY%LEOCLAKE, LEOCML=>YREPHY%LEOCML, &
 & LEOCWA=>YREPHY%LEOCWA, LEOLAKESST=>YREPHY%LEOLAKESST, &
 & REASTML=>YREPHY%REASTML, RNORTHML=>YREPHY%RNORTHML, &
 & RSOUTHML=>YREPHY%RSOUTHML, RWESTML=>YREPHY%RWESTML, YSURF=>YREPHY%YSURF, &
 & LPERPET=>YRERAD%LPERPET, &
 & NGPTOT=>YDGEM%NGPTOT, NGPTOTG=>YDGEM%NGPTOTG, NHTYP=>YDGEM%NHTYP, &
 & NLOENG=>YDGEM%NLOENG, &
 & CLIMR=>YRMCC%CLIMR, LMCC04=>YRMCC%LMCC04, LMCCICEIC=>YRMCC%LMCCICEIC, &
 & LMCCIEC=>YRMCC%LMCCIEC, LNEMOCOUP=>YRMCC%LNEMOCOUP, NCLIGC=>YRMCC%NCLIGC, &
 & LNEMO1WAY=>YRMCC%LNEMO1WAY, &
 & NCLIMR=>YRMCC%NCLIMR, NDIFC=>YRMCC%NDIFC, NJDCR=>YRMCC%NJDCR, &
 & NJDCR1=>YRMCC%NJDCR1, NOACOMM=>YRMCC%NOACOMM, NP1=>YRMCC%NP1, NP2=>YRMCC%NP2,&
```

```
 & NUNITC=>YRMCC%NUNITC, OCEANBC=>YRMCC%OCEANBC, ZLAKE=>YRMCC%ZLAKE, &
 & NSSTICEOP=>YRMCC%NSSTICEOP, &
 & NSTADD=>YRRIP%NSTADD, NSTOP=>YRRIP%NSTOP, &
 & SD_VF=>YDSURF%SD_VF, SP_OM=>YDSURF%SP_OM, SP_RR=>YDSURF%SP_RR, &
 & SP_SB=>YDSURF%SP_SB, SP_SL=>YDSURF%SP_SL, YSD_VF=>YDSURF%YSD_VF, &
 & YSP_OM=>YDSURF%YSP_OM, YSP_RR=>YDSURF%YSP_RR, YSP_SB=>YDSURF%YSP_SB, &
 & YSP_SL=>YDSURF%YSP_SL)


    IF (LHOOK) CALL DR_HOOK('FESOM_UPDCLIE',0,ZHOOK_HANDLE)

    ! ======================================================================
    ! *** 0. Initialisation
    ! ======================================================================

    CALL SURF_INQ(YREPHY%YSURF,PRTFREEZSICE=ZRTFREEZSICE,PRCIMIN=ZRCIMIN)

    ! ======================================================================
    ! *** 1. Update coupling fields (from CPLNG coupler)
    ! ======================================================================

    CALL CPLNG_EXCHANGE(KSTAGE=FESOM_CPL_STAGE_OCE_RCV)
    CPL_FLD_SST      => CPLNG_FLD(CPLNG_IDX('A_SST'))%D(:,1,1)
    CPL_FLD_ICE_FRAC => CPLNG_FLD(CPLNG_IDX('A_Ice_frac'))%D(:,1,1)
    CPL_FLD_ICE_TEMP => CPLNG_FLD(CPLNG_IDX('A_Ice_temp'))%D(:,1,1)
    CPL_FLD_ICE_ALB  => CPLNG_FLD(CPLNG_IDX('A_Ice_albedo'))%D(:,1,1)
    CPL_FLD_OUCURR  => CPLNG_FLD(CPLNG_IDX('A_CurX'))%D(:,1,1)
    CPL_FLD_OVCURR  => CPLNG_FLD(CPLNG_IDX('A_CurY'))%D(:,1,1)

    ! ======================================================================
    ! *** 2. Update IFS variables from coupling
    ! ======================================================================
    IF(LMCC04) THEN
      ICLIM=NCLIMR+2
      IF (LECURR) THEN
        ICLIM=NCLIMR+4
      ENDIF
    ELSE
      ICLIM=NCLIMR
    ENDIF

    DO JSTGLO=1,NGPTOT,NPROMA

      IEND = MIN(NPROMA,NGPTOT-JSTGLO+1)
      IBL = (JSTGLO-1)/NPROMA+1
! Fill arrays, ensuring compatibility of ice T, ice cover, SST and
!    surface T
    DO JCL=1,ICLIM
      IF (NCLIGC(JCL) == 139) EXIT
    ENDDO
    IPAR139=JCL
    DO JCL=1,ICLIM
      IF (NCLIGC(JCL) == 31) EXIT
    ENDDO
    IPAR31=JCL
    ZR2D = 180.0_JPRB / RPI

    DO JROF =1,IEND
      IF (LECURR) THEN
        SD_VF(JROF,YSD_VF%YUCUR%MP,IBL) = CPL_FLD_OUCURR(JSTGLO+JROF-1)
        SD_VF(JROF,YSD_VF%YVCUR%MP,IBL) = CPL_FLD_OVCURR(JSTGLO+JROF-1)
      ENDIF

      IF(SD_VF(JROF,YSD_VF%YLSM%MP,IBL) <= 0.5_JPRB)THEN
!  No monthly interpolation of SST possible from OASIS
        ZTS = CPL_FLD_SST(JSTGLO+JROF-1)
        ZCI = CPL_FLD_ICE_FRAC(JSTGLO+JROF-1)
        ZTI = CPL_FLD_ICE_TEMP(JSTGLO+JROF-1)
!    DEFINE LOGICALS FOR RESOLVED LAKES
        LLAKE(JROF)=(SD_VF(JROF,YSD_VF%YCLK%MP,IBL) > 0.5_JPRB)
!    DEFINE LOGICALS FOR OLD AND NEW SEA-ICE
        LLICEO(JROF)=SD_VF(JROF,YSD_VF%YCI%MP,IBL) > ZRCIMIN
        LLICEN(JROF)=ZCI > ZRCIMIN

        IF (LLICEN(JROF)) THEN
          SD_VF(JROF,YSD_VF%YCI%MP,IBL) = ZCI
          SP_SB(JROF,1,YSP_SB%YTL%MP,IBL) = ZTI
        ELSE
          SD_VF(JROF,YSD_VF%YCI%MP,IBL)=0.
            SP_SB(JROF,1,YSP_SB%YTL%MP,IBL) = ZRTFREEZSICE
            SP_SB(JROF,2,YSP_SB%YTL%MP,IBL) = ZRTFREEZSICE
            SP_SB(JROF,3,YSP_SB%YTL%MP,IBL) = ZRTFREEZSICE
            SP_SB(JROF,4,YSP_SB%YTL%MP,IBL) = ZRTFREEZSICE
        ENDIF
!TEST FOR MISSING DATA IN SST
        LLMISS=(ZTS == 19591204.0_JPRB)
!UPDATE ICE and OCEAN TEMPERATURES
        IF (LLICEN(JROF).AND.LLICEO(JROF)) THEN
! SEA-ICE TO SEA-ICE
```

```
          IF (.NOT.LLAKE(JROF)) THEN
            IF (LLMISS) THEN
              ZTS=SP_RR(JROF,YSP_RR%YT%MP,IBL)
            ENDIF

            SELECT CASE (NSSTICEOP) ! INTEGER NUMBER CORRESPONDING TO SSTICEOPT CHOICE IN SSA
            CASE (9) ! SST already corrected in the analysis - trust SST field
              ZSSTCI = MAX(ZTS,ZRTFREEZSICE)
            CASE (1) !'T0220' - use weighted average of sst and ZRTFREEZSICE weight=(tanh((icecover-0.2)*20)+1)/2
              ZSSTCI = ZRTFREEZSICE*0.5_JPRB*(TANH((SD_VF(JROF,YSD_VF%YCI%MP,IBL)-0.2_JPRB)*20.0_JPRB)+1.0_JPRB)+ &
               & MAX(ZTS,ZRTFREEZSICE)*(1.0_JPRB-0.5_JPRB*(TANH((SD_VF(JROF,YSD_VF%YCI%MP,IBL)-0.2_JPRB)*20.0_JPRB)+1.0_JPRB))
            CASE (0) !'orig' - SST is freezing temperature of ice if any ice present
              IF (LLICEN(JROF)) THEN
                ZSSTCI = ZRTFREEZSICE
              ELSE
                ZSSTCI = ZTS
              ENDIF
            CASE (2) !'T0310' use weighted average of sst and ZRTFREEZSICE weight=(tanh((icecover-0.3)*10)+1)/2
              ZSSTCI = ZRTFREEZSICE*0.5_JPRB*(TANH((SD_VF(JROF,YSD_VF%YCI%MP,IBL)-0.3_JPRB)*10.0_JPRB)+1.0_JPRB)+ &
               & MAX(ZTS,ZRTFREEZSICE)*(1.0_JPRB-0.5_JPRB*(TANH((SD_VF(JROF,YSD_VF%YCI%MP,IBL)-0.3_JPRB)*10.0_JPRB)+1.0_JPRB))
            CASE (3) !'L20' for ice concentration greater than 20% reset to -1.8C else linear weight sst/ZRTFREEZSICE
              IF (SD_VF(JROF,YSD_VF%YCI%MP,IBL) > 0.2_JPRB) THEN
                ZSSTCI = ZRTFREEZSICE
              ENDIF
              IF (SD_VF(JROF,YSD_VF%YCI%MP,IBL) <= 0.2_JPRB) THEN
                ZSSTCI = ZRTFREEZSICE*SD_VF(JROF,YSD_VF%YCI%MP,IBL)+ &
                 & MAX(ZTS,ZRTFREEZSICE)*(1_JPRB-SD_VF(JROF,YSD_VF%YCI%MP,IBL))
              ENDIF
            CASE (4) !'L50' for ice concentration greater than 50% reset to -1.8C else linear weight sst/ZRTFREEZSICE
               IF (SD_VF(JROF,YSD_VF%YCI%MP,IBL) > 0.5_JPRB) THEN
                ZSSTCI = ZRTFREEZSICE
              ENDIF
              IF (SD_VF(JROF,YSD_VF%YCI%MP,IBL) <= 0.5_JPRB) THEN
                ZSSTCI = ZRTFREEZSICE*SD_VF(JROF,YSD_VF%YCI%MP,IBL)+ &
                 &  MAX(ZTS,ZRTFREEZSICE)*(1_JPRB-SD_VF(JROF,YSD_VF%YCI%MP,IBL))
              ENDIF
            CASE DEFAULT
              CALL ABOR1('UPDCLIE:␣UNKNOWN␣NSSTICEOP')
            END SELECT

            IF (LEOCWA .OR. LEOCCO) THEN
              ZDSST0=ZSSTCI-SD_VF(JROF,YSD_VF%YSST%MP,IBL)
            ELSE
              ZDSST0=0.
            ENDIF

            IF (LLMISS) THEN
              ZDSST0=0.
            ENDIF

            SD_VF(JROF,YSD_VF%YSST%MP,IBL)     =ZSSTCI

          ELSE
!         if sea ice present but a lake point then:
             SD_VF(JROF,YSD_VF%YSST%MP,IBL)     =ZRTFREEZSICE
          ENDIF

          SP_SB(JROF,1,YSP_SB%YT%MP,IBL)=SD_VF(JROF,YSD_VF%YCI%MP,IBL)*SP_SB(JROF,1,YSP_SB%YTL%MP,IBL)+&
           & (1.-SD_VF(JROF,YSD_VF%YCI%MP,IBL))*SD_VF(JROF,YSD_VF%YSST%MP,IBL)
          SP_SB(JROF,2,YSP_SB%YT%MP,IBL)=SD_VF(JROF,YSD_VF%YCI%MP,IBL)*SP_SB(JROF,2,YSP_SB%YTL%MP,IBL)+&
           & (1.-SD_VF(JROF,YSD_VF%YCI%MP,IBL))*SD_VF(JROF,YSD_VF%YSST%MP,IBL)
          SP_SB(JROF,3,YSP_SB%YT%MP,IBL)=SD_VF(JROF,YSD_VF%YCI%MP,IBL)*SP_SB(JROF,3,YSP_SB%YTL%MP,IBL)+&
           & (1.-SD_VF(JROF,YSD_VF%YCI%MP,IBL))*SD_VF(JROF,YSD_VF%YSST%MP,IBL)
          SP_SB(JROF,4,YSP_SB%YT%MP,IBL)=SD_VF(JROF,YSD_VF%YCI%MP,IBL)*SP_SB(JROF,4,YSP_SB%YTL%MP,IBL)+&
           & (1.-SD_VF(JROF,YSD_VF%YCI%MP,IBL))*SD_VF(JROF,YSD_VF%YSST%MP,IBL)
! RESTORE SKIN TEMPERATURE ONLY ON OCEAN IF FLAKE IS ACTIVE
          IF (LEFLAKE) THEN
            IF (.NOT.LLAKE(JROF)) THEN
              SP_RR(JROF,YSP_RR%YT%MP,IBL)    =SP_SB(JROF,1,YSP_SB%YT%MP,IBL)
            ENDIF
          ELSE
            SP_RR(JROF,YSP_RR%YT%MP,IBL)    =SP_SB(JROF,1,YSP_SB%YT%MP,IBL)
          ENDIF
        ELSEIF (LLICEN(JROF).AND..NOT.LLICEO(JROF)) THEN
! SEA TO SEA-ICE
          IF (.NOT.LLAKE(JROF)) THEN
            IF (LLMISS) THEN
              ZTS=SP_RR(JROF,YSP_RR%YT%MP,IBL)
            ENDIF

            SELECT CASE (NSSTICEOP) ! INTEGER NUMBER CORRESPONDING TO SSTICEOPT CHOICE IN SSA
```

```
          CASE (9) ! SST already corrected in the analysis - trust SST field
            ZSSTCI = MAX(ZTS,ZRTFREEZSICE)
          CASE (1) !'T0220' - use weighted average of sst and ZRTFREEZSICE weight=(tanh((icecover-0.2)*20)+1)/2
            ZSSTCI = ZRTFREEZSICE*0.5_JPRB*(TANH((SD_VF(JROF,YSD_VF%YCI%MP,IBL)-0.2_JPRB)*20.0_JPRB)+1.0_JPRB)+ &
             & MAX(ZTS,ZRTFREEZSICE)*(1.0_JPRB-0.5_JPRB*(TANH((SD_VF(JROF,YSD_VF%YCI%MP,IBL)-0.2_JPRB)*20.0_JPRB)+1.0_JPRB))
          CASE (0) !'orig' - SST is freezing temperature of ice if any ice present
            IF (LLICEN(JROF)) THEN
              ZSSTCI = ZRTFREEZSICE
            ELSE
              ZSSTCI = ZTS
            ENDIF
          CASE (2) !'T0310' use weighted average of sst and ZRTFREEZSICE weight=(tanh((icecover-0.3)*10)+1)/2
            ZSSTCI = ZRTFREEZSICE*0.5_JPRB*(TANH((SD_VF(JROF,YSD_VF%YCI%MP,IBL)-0.3_JPRB)*10.0_JPRB)+1.0_JPRB)+ &
             & MAX(ZTS,ZRTFREEZSICE)*(1.0_JPRB-0.5_JPRB*(TANH((SD_VF(JROF,YSD_VF%YCI%MP,IBL)-0.3_JPRB)*10.0_JPRB)+1.0_JPRB))
          CASE (3) !'L20' for ice concentration greater than 20% reset to -1.8C else linear weight sst/ZRTFREEZSICE
            IF (SD_VF(JROF,YSD_VF%YCI%MP,IBL) > 0.2_JPRB) THEN
              ZSSTCI = ZRTFREEZSICE
            ENDIF
            IF (SD_VF(JROF,YSD_VF%YCI%MP,IBL) <= 0.2_JPRB) THEN
              ZSSTCI = ZRTFREEZSICE*SD_VF(JROF,YSD_VF%YCI%MP,IBL)+ &
               & MAX(ZTS,ZRTFREEZSICE)*(1_JPRB-SD_VF(JROF,YSD_VF%YCI%MP,IBL))
            ENDIF
          CASE (4) !'L50' for ice concentration greater than 50% reset to -1.8C else linear weight sst/ZRTFREEZSICE
            IF (SD_VF(JROF,YSD_VF%YCI%MP,IBL) > 0.5_JPRB) THEN
              ZSSTCI = ZRTFREEZSICE
            ENDIF
            IF (SD_VF(JROF,YSD_VF%YCI%MP,IBL) <= 0.5_JPRB) THEN
              ZSSTCI = ZRTFREEZSICE*SD_VF(JROF,YSD_VF%YCI%MP,IBL)+ &
               &  MAX(ZTS,ZRTFREEZSICE)*(1_JPRB-SD_VF(JROF,YSD_VF%YCI%MP,IBL))
            ENDIF
          CASE DEFAULT
            CALL ABOR1('UPDCLIE: UNKNOWN NSSTICEOP')
          END SELECT

          IF (LEOCWA .OR. LEOCCO) THEN
            ZDSST0=ZSSTCI-SD_VF(JROF,YSD_VF%YSST%MP,IBL)
          ELSE
            ZDSST0=0.
          ENDIF

          IF (LLMISS) THEN
            ZDSST0=0.
          ENDIF

          SD_VF(JROF,YSD_VF%YSST%MP,IBL)      =ZSSTCI
        ELSE
          SD_VF(JROF,YSD_VF%YSST%MP,IBL)      =ZRTFREEZSICE
        ENDIF

        SP_SB(JROF,1,YSP_SB%YTL%MP,IBL)=ZRTFREEZSICE
        SP_SB(JROF,2,YSP_SB%YTL%MP,IBL)=ZRTFREEZSICE
        SP_SB(JROF,3,YSP_SB%YTL%MP,IBL)=ZRTFREEZSICE
        SP_SB(JROF,4,YSP_SB%YTL%MP,IBL)=ZRTFREEZSICE
        SP_SB(JROF,1,YSP_SB%YT%MP,IBL)=SD_VF(JROF,YSD_VF%YCI%MP,IBL)*SP_SB(JROF,1,YSP_SB%YTL%MP,IBL)+&
         & (1.-SD_VF(JROF,YSD_VF%YCI%MP,IBL))*SD_VF(JROF,YSD_VF%YSST%MP,IBL)
        SP_SB(JROF,2,YSP_SB%YT%MP,IBL)=SD_VF(JROF,YSD_VF%YCI%MP,IBL)*SP_SB(JROF,2,YSP_SB%YTL%MP,IBL)+&
         & (1.-SD_VF(JROF,YSD_VF%YCI%MP,IBL))*SD_VF(JROF,YSD_VF%YSST%MP,IBL)
        SP_SB(JROF,3,YSP_SB%YT%MP,IBL)=SD_VF(JROF,YSD_VF%YCI%MP,IBL)*SP_SB(JROF,3,YSP_SB%YTL%MP,IBL)+&
         & (1.-SD_VF(JROF,YSD_VF%YCI%MP,IBL))*SD_VF(JROF,YSD_VF%YSST%MP,IBL)
        SP_SB(JROF,4,YSP_SB%YT%MP,IBL)=SD_VF(JROF,YSD_VF%YCI%MP,IBL)*SP_SB(JROF,4,YSP_SB%YTL%MP,IBL)+&
         & (1.-SD_VF(JROF,YSD_VF%YCI%MP,IBL))*SD_VF(JROF,YSD_VF%YSST%MP,IBL)
! RESTORE SKIN TEMPERATURE ONLY ON OCEAN IF FLAKE IS ACTIVE
        IF (LEFLAKE) THEN
           IF (.NOT.LLAKE(JROF)) THEN
             SP_RR(JROF,YSP_RR%YT%MP,IBL)     =SP_SB(JROF,1,YSP_SB%YT%MP,IBL)
           ENDIF
        ELSE
          SP_RR(JROF,YSP_RR%YT%MP,IBL)     =SP_SB(JROF,1,YSP_SB%YT%MP,IBL)
        ENDIF
      ELSE
!    SEA TO SEA OR SEA-ICE TO SEA
!       calculate SKIN TEMPERATURE INCREMENT TO BE OF THE SAME AMOUNT AS SST (on ocean)
        IF (LEOCWA .OR. LEOCCO) THEN
          ZDSST0=ZTS-SD_VF(JROF,YSD_VF%YSST%MP,IBL)
        ELSE
          ZDSST0=0.
        ENDIF
        IF (LLMISS)THEN
          ZDSST0=0.
          ZTS=SP_RR(JROF,YSP_RR%YT%MP,IBL)
        ENDIF
```

```
          SD_VF(JROF,YSD_VF%YSST%MP,IBL)      =ZTS
! RESTORE SKIN TEMPERATURE ONLY ON OCEAN IF FLAKE IS ACTIVE
          IF (LEFLAKE) THEN
             IF (.NOT.LLAKE(JROF)) THEN
               SP_RR(JROF,YSP_RR%YT%MP,IBL)     =SP_RR(JROF,YSP_RR%YT%MP,IBL)+ZDSST0
             ENDIF
          ELSE
            SP_RR(JROF,YSP_RR%YT%MP,IBL)     =SP_RR(JROF,YSP_RR%YT%MP,IBL)+ZDSST0
          ENDIF
          SP_SB(JROF,1,YSP_SB%YT%MP,IBL)=ZTS
          SP_SB(JROF,2,YSP_SB%YT%MP,IBL)=ZTS
          SP_SB(JROF,3,YSP_SB%YT%MP,IBL)=ZTS
          SP_SB(JROF,4,YSP_SB%YT%MP,IBL)=ZTS
          SP_SB(JROF,1,YSP_SB%YTL%MP,IBL)=ZRTFREEZSICE
          SP_SB(JROF,2,YSP_SB%YTL%MP,IBL)=ZRTFREEZSICE
          SP_SB(JROF,3,YSP_SB%YTL%MP,IBL)=ZRTFREEZSICE
          SP_SB(JROF,4,YSP_SB%YTL%MP,IBL)=ZRTFREEZSICE
        ENDIF

          SD_VF(JROF,YSD_VF%YALBF%MP,IBL) = CPL_FLD_ICE_ALB(JSTGLO+JROF-1)


        ENDIF ! LSM <= 0.5_JPRB
      ENDDO ! JROF = 1,IEND
    ENDDO ! JSTGLO=1,NGPTOT,NPROMA

    IF (LHOOK) CALL DR_HOOK('FESOM_UPDCLIE',1,ZHOOK_HANDLE)

    END ASSOCIATE
    END ASSOCIATE

END SUBROUTINE FESOM_UPDCLIE
```

C.3 Sea ice surface temperature calculation in FESOM2

```
 subroutine ice_surftemp(ithermp, h,hsn,a2ihf,t)
  ! INPUT:
  ! a2ihf - Total atmo heat flux to ice
  ! A  - Ice fraction
  ! h  - Ice thickness
  ! hsn   - Snow thickness
  !
  ! INPUT/OUTPUT:
  ! t     - Ice surface temperature

  implicit none
  type(t_ice_thermo), intent(in), target :: ithermp
  !---- atmospheric heat net flux into to ice (provided by OpenIFS)
  real(kind=WP)  a2ihf
  !---- ocean variables (provided by FESOM)
  real(kind=WP)  h
  real(kind=WP)  hsn
  real(kind=WP)  t
  !---- local variables
  real(kind=WP)  snicecond
  real(kind=WP)  zsniced
  real(kind=WP)  zicefl
  real(kind=WP)  hcapice
  real(kind=WP)  zcpdt
  real(kind=WP)  zcpdte
  real(kind=WP)  zcprosn
  !---- local parameters
  real(kind=WP), parameter :: dice  = 0.10_WP                        ! Thickness for top ice "layer"
  !---- freezing temperature of sea-water [K]
  real(kind=WP)  :: TFrezs

  real(kind=WP), pointer :: con, consn, cpsno, rhoice, rhosno
  con    => ice%thermo%con
  consn  => ice%thermo%consn
  cpsno  => ice%thermo%cpsno
  rhoice => ice%thermo%rhoice
  rhosno => ice%thermo%rhosno

  !---- compute freezing temperature of sea-water from salinity
  TFrezs = -0.0575_WP*S_oc + 1.7105e-3_WP*sqrt(S_oc**3) - 2.155e-4_WP*(S_oc**2)+273.15

  snicecond = con/consn                 ! equivalence fraction thickness of ice/snow
  zsniced=h+snicecond*hsn               ! Ice + Snow-Ice-equivalent thickness [m]
  zicefl=con*TFrezs/zsniced             ! Conductive heat flux through sea ice [W/m^2]
  hcapice=rhoice*cpice*dice             ! heat capacity of upper 0.05 cm sea ice layer [J/(m^2K)]
```

```
  zcpdt=hcapice/dt                      ! Energy required to change temperature of top ice "layer" [J/(sm^2K)]
  zcprosn=rhosno*cpsno/dt               ! Specific Energy required to change temperature of 1m snow on ice [J/(sm^3K)]
  zcpdte=zcpdt+zcprosn*hsn              ! Combined Energy required to change temperature of snow + 0.05m of upper ice
  t=(zcpdte*t+a2ihf+zicefl)/(zcpdte+con/zsniced) ! New sea ice surf temp [K]
  t=min(273.15_WP,t)
end subroutine ice_surftemp
```

C.4 Implementation of stochastic coupling in OASIS3MCT

```

 subroutine sMatAvMult_DataLocal_(xAV, sMat, yAV, Vector, rList, TrList, Stoch, StochNumber, StochIndex)
!
! !USES:
!
      use m_realkinds, only : FP
      use m_stdio,     only : stderr
      use m_die,       only : MP_perr_die, die, warn

      use m_List, only : List_identical => identical
      use m_List, only : List_nitem => nitem
      use m_List, only : GetIndices => get_indices

      use m_AttrVect, only : AttrVect
      use m_AttrVect, only : AttrVect_lsize => lsize
      use m_AttrVect, only : AttrVect_zero => zero
      use m_AttrVect, only : AttrVect_indexRA => indexRA
      use m_AttrVect, only : SharedAttrIndexList

      use m_SparseMatrix, only : SparseMatrix
      use m_SparseMatrix, only : SparseMatrix_lsize => lsize
      use m_SparseMatrix, only : SparseMatrix_indexIA => indexIA
      use m_SparseMatrix, only : SparseMatrix_indexRA => indexRA
      use m_SparseMatrix, only : SparseMatrix_vecinit => vecinit

      implicit none

! !INPUT PARAMETERS:

      type(AttrVect),     intent(in)    :: xAV
      logical,optional,   intent(in)    :: Vector, Stoch
      integer,optional,   intent(in)    :: StochNumber, StochIndex
      character(len=*),optional, intent(in)    :: rList
      character(len=*),optional, intent(in)    :: TrList


! !INPUT/OUTPUT PARAMETERS:

      type(SparseMatrix), intent(inout)    :: sMat
      type(AttrVect),     intent(inout) :: yAV

! !REVISION HISTORY:
! 15Jan01 - J.W. Larson <larson@mcs.anl.gov> - API specification.
! 10Feb01 - J.W. Larson <larson@mcs.anl.gov> - Prototype code.
! 24Apr01 - J.W. Larson <larson@mcs.anl.gov> - Modified to accomodate
!           changes to the SparseMatrix datatype.
! 25Apr01 - J.W. Larson <larson@mcs.anl.gov> - Reversed loop order
!           for cache-friendliness
! 17May01 - R. Jacob <jacob@mcs.anl.gov> - Zero the output
!           attribute vector
! 10Oct01 - J. Larson <larson@mcs.anl.gov> - Added optional LOGICAL
!           input argument InterpInts to make application of the
!           multiply to INTEGER attributes optional
! 15Oct01 - J. Larson <larson@mcs.anl.gov> - Added feature to
!           detect when attribute lists are identical, and cross-
!           indexing of attributes is not needed.
! 29Nov01 - E.T. Ong <eong@mcs.anl.gov> - Removed MP_PERR_DIE if
!           there are zero elements in sMat. This allows for
!           decompositions where a process may own zero points.
! 29Oct03 - R. Jacob <jacob@mcs.anl.gov> - add Vector argument to
!           optionally use the vector-friendly version provided by
!           Fujitsu
! 21Nov06 - R. Jacob <jacob@mcs.anl.gov> - Allow attributes to be
!           to be multiplied to be specified with rList and TrList.
!EOP ___________________________________________________________________

  character(len=*),parameter :: myname_=myname//'::sMatAvMult_DataLocal_'

! Matrix element count:
  integer :: num_elements

! Matrix row, column, and weight indices:
  integer :: icol, irow, iwgt

! Overlapping attribute index number
  integer :: num_indices

! Overlapping attribute index storage arrays:
  integer, dimension(:), pointer :: xAVindices, yAVindices

! Temporary variables for multiply do-loop
  integer :: row, col, row_old, row_max, row_num, index, seed(1)
  real(FP) :: wgt, rand_num
```

```
  real(FP),dimension(:,:),allocatable :: wgt_mat, wgt_mat_stoch
  real(FP),dimension(:,:,:),allocatable,save :: wgt_mat_stoch_previous
  real(FP),dimension(:),allocatable :: wgt_vect

! Error flag and loop indices
  integer :: ierr, i, m, n, x, l,ier
  integer :: inxmin,outxmin
  integer :: ysize, numav,j

! Character variable used as a data type flag:
  character*7 :: data_flag

! logical flag
  logical :: DoStoch,usevector,TrListIsPresent,rListIsPresent
  logical :: init_rnd_walk=.false.
  logical :: contiguous,ycontiguous


  DoStoch = .false.
  if(present(Stoch)) then
    if(Stoch) DoStoch = .true.
  end if

       ! Retrieve the number of elements in sMat:

  num_elements = SparseMatrix_lsize(sMat)

       ! Indexing the sparse matrix sMat:

  irow = SparseMatrix_indexIA(sMat,'lrow')    ! local row index
  icol = SparseMatrix_indexIA(sMat,'lcol')    ! local column index
  iwgt = SparseMatrix_indexRA(sMat,'weight')  ! weight index

       ! Multiplication sMat by REAL attributes in xAV:
       ! zero the output AttributeVector
     call AttrVect_zero(yAV, zeroInts=.FALSE.)

     num_indices = List_nitem(xAV%rList)


       if (DoStoch) then
         ! Logic to find largest number of wgt
         ! associated with one target point
         row_old = 1
         row_max = 1
         row_num = 0
         do n=1,num_elements
           row = sMat%data%iAttr(irow,n)
           if (row == row_old) then
             row_num = row_num +1
             if (row_num > row_max) then; row_max = row_num; end if
           else
             row_num = 1
           end if
           row_old = row
         end do

         ! Allocate the weight matrix with the maximum
         ! number of weights per row in local memory
         allocate(wgt_mat(sMat%data%iAttr(irow,num_elements),row_max),stat=ier)
         allocate(wgt_mat_stoch(sMat%data%iAttr(irow,num_elements),row_max),stat=ier)
         allocate(wgt_vect(num_elements),stat=ier)
         if (.not. allocated(wgt_mat_stoch_previous)) then
           allocate(wgt_mat_stoch_previous(sMat%data%iAttr(irow,num_elements),row_max,StochNumber),stat=ier)
           wgt_mat_stoch_previous=0
           init_rnd_walk=.true.
         end if

         do n=1,num_elements
           row = sMat%data%iAttr(irow,n)
           wgt = sMat%data%rAttr(iwgt,n)

           if (row == row_old) then
             row_num = row_num +1
           else
             row_num = 1
           end if
           wgt_mat(row, row_num) = wgt
           row_old = row
         end do

         ! Stochastically select a weight for each row
         ! First we initialize the random number generator from the source data
         ! This way we should stay bit reproducible
         seed(1) = int(xAV%rAttr(1,1)*1e8)
         call random_seed(put=seed)

         ! For every row we pick rand_num and find first index larger than it.
         n = 1
```

```
          do x = 1, size(wgt_mat , 1)
            call random_number(rand_num)
            do i = 1, size(wgt_mat , 2)
              if (rand_num <= sum(wgt_mat(x,1:i))) then
                index = i
                exit
              end if
            end do
            ! wgt of matching index=1
            wgt_mat_stoch(x,:)=0
            wgt_mat_stoch(x,index)=1
            ! linearize back to original format
            do i = 1, size(wgt_mat , 2)
               if (wgt_mat(x,i)>0) then
                 wgt_vect(n) = wgt_mat_stoch(x,i)
                 n=n+1
               end if
            end do
          end do
          wgt_mat_stoch_previous(:,:,StochIndex)=wgt_mat_stoch
          deallocate(wgt_mat)
          deallocate(wgt_mat_stoch)
        end if !DoStoch




        do n=1,num_elements
         row = sMat%data%iAttr(irow,n)
         col = sMat%data%iAttr(icol,n)
         if (DoStoch) then
           wgt = wgt_vect(n)
         else
           wgt = sMat%data%rAttr(iwgt,n)
         end if

          ! loop over attributes being regridded.
!DIR$ IVDEP
         do m=1,num_indices
           yAV%rAttr(m,row) = yAV%rAttr(m,row) + wgt * xAV%rAttr(m,col)
         end do ! m=1,num_indices
       end do ! n=1,num_elements

! lists are not identical or only want to do part.
  if (DoStoch) then
    deallocate(wgt_vect)
  end if

 end subroutine sMatAvMult_DataLocal_
```

C.5 Defining FESOM mesh corners for conservative remapping

```fortran


  subroutine cpl_oasis3mct_define_unstr(partit, mesh)

#ifdef __oifs
    use mod_oasis_auxiliary_routines, ONLY:     oasis_get_debug, oasis_set_debug
#else
    use mod_oasis_method, ONLY: oasis_get_debug, oasis_set_debug
#endif
    use mod_mesh
    USE MOD_PARTIT
    USE MOD_PARSUP
    use g_rotate_grid
    use mod_oasis, only: oasis_write_area, oasis_write_mask
    implicit none
    save
    type(t_mesh),   intent(in),    target :: mesh
    type(t_partit), intent(inout), target :: partit
    !-------------------------------------------------------------------
    ! Definition of grid and field information for ocean
    ! exchange between FESOM, ECHAM6 and OASIS3-MCT.
    !--------------------------------------------------------------------
    ! Arguments
    !
    ! Local declarations

    integer, parameter          :: nbr_grids   = 1
    integer, parameter          :: nbr_parts   = 1
    integer, parameter          :: nbr_masks   = 1
    integer, parameter          :: nbr_methods = 1

    integer                     :: grid_id(nbr_grids)    ! ids returned by oasis_def_grid
    integer                     :: part_id(nbr_parts)    ! ids returned by oasis_def_grid

    integer                     :: point_id(nbr_methods) ! ids returned by oasis_set_points

    integer                     :: mask_id(nbr_masks)    ! ids returned by oasis_set_mask

    integer                     :: shape(2,3)     ! shape of arrays passed to OASIS4
    integer                     :: total_shape(4) ! shape of arrays passed to OASIS3MCT
    integer                     :: nodim(2)
    integer                     :: data_type      ! data type of transients

    integer                     :: ig_paral(3)

    integer                     :: il_flag
    logical                     :: new_points

    integer                     :: i, j, k           ! local loop indicees
    integer                     :: l,m,n, done       ! local loop indicees

    character(len=32)           :: point_name     ! name of the grid points

    integer                     :: my_number_of_points
    integer                     :: number_of_all_points
    integer                     :: counts_from_all_pes(partit%npes)
    integer                     :: displs_from_all_pes(partit%npes)
    integer                     :: my_displacement
    integer                     :: my_max_elem(partit%npes)
    integer                     :: my_max_edge(partit%npes)
    integer                     :: all_max_elem, all_max_edge, n_neg, n_pos
    integer                     :: el(2), enodes(2), edge

    integer,allocatable         :: unstr_mask(:,:), coastal_edge_list(:,:)
    real(kind=WP)               :: max_x          ! max longitude on corners of control volume
    real(kind=WP)               :: min_x          ! min longitude on corners of control volume
    real(kind=WP)               :: temp                  ! temp storage for corner sorting
    real(kind=WP)               :: this_x_coord          ! longitude coordinates
    real(kind=WP)               :: this_y_coord          ! latitude coordinates
    real(kind=WP)               :: this_x_corners        ! longitude node corners
    real(kind=WP)               :: this_y_corners        ! latitude node corners
    !
    ! Corner data structure for a OASIS3-MCT Reglonlatvrt grid
    !
    real(kind=WP), allocatable :: pos_x(:)       ! longitude to the right of dateline
    real(kind=WP), allocatable :: pos_y(:)       ! latitude to the right of dateline
    real(kind=WP), allocatable :: neg_x(:)       ! longitude to the left of dateline
    real(kind=WP), allocatable :: neg_y(:)       ! latitude to the left of dateline
    real(kind=WP), allocatable :: temp_x_coord(:)    ! longitude coordinates
    real(kind=WP), allocatable :: temp_y_coord(:)    ! longitude coordinates
    real(kind=WP), allocatable :: my_x_coords(:)     ! longitude coordinates
    real(kind=WP), allocatable :: my_y_coords(:)     ! latitude  coordinates
```

```
    real(kind=WP), allocatable :: angle(:,:)         ! array for holding corner angle for sorting
    real(kind=WP), allocatable :: my_x_corners(:,:)     ! longitude node corners
    real(kind=WP), allocatable :: my_y_corners(:,:)     ! latitude node corners
    real(kind=WP), allocatable :: coord_e_edge_center(:,:,:)   ! edge center coords
    real(kind=WP), allocatable :: all_x_coords(:, :)      ! longitude coordinates
    real(kind=WP), allocatable :: all_y_coords(:, :)      ! latitude  coordinates
    real(kind=WP), allocatable :: all_x_corners(:,:,:)     ! longitude node corners
    real(kind=WP), allocatable :: all_y_corners(:,:,:)     ! latitude node corners
    real(kind=WP), allocatable :: all_area(:,:)
    logical, allocatable       :: coastal_nodes(:)


#include "associate_part_def.h"
#include "associate_mesh_def.h"
#include "associate_part_ass.h"
#include "associate_mesh_ass.h"


#ifdef VERBOSE
      print *, '================================================================'
      print *, 'cpl_oasis3mct_define_unstr␣:␣coupler␣definition␣for␣OASIS3-MCT'
      print *, '****************************************************************'
      call fesom_flush
#endif /* VERBOSE */

    ! -----------------------------------------------------------------
    ! ... Some initialisation
    ! -----------------------------------------------------------------

    send_id = 0
    recv_id = 0

    ! -----------------------------------------------------------------
    ! ... Some MPI stuff relevant for optional exchange via root only
    ! -----------------------------------------------------------------

    localRank = mype
    localSize = npes

#ifdef VERBOSE
    print *, 'This␣is␣FESOM␣local␣rank␣', localRank, commRank
#endif /* VERBOSE */

! Note: We assume here that each process sends its local field.
! -----------------------------------------------------------------
! ... Define the partition
! -----------------------------------------------------------------

    my_number_of_points = myDim_nod2d
    number_of_all_points = nod2d
    if (mype .eq. 0) then
      print *, 'FESOM␣Before␣ALLGATHERV'
    endif
    CALL MPI_ALLGATHER(my_number_of_points, 1, MPI_INTEGER, &
                       counts_from_all_pes, 1, MPI_INTEGER, MPI_COMM_FESOM, ierror)
    if (mype .eq. 0) then
      print *, 'FESOM␣after␣ALLGATHERV'
    endif

    if (mype .eq. 0) then
      my_displacement = 0
    else
      my_displacement = SUM(counts_from_all_pes(1:mype))
    endif

    CALL MPI_BARRIER(MPI_COMM_FESOM, ierror)

    my_max_elem=0
    my_max_elem = maxval(nod_in_elem2D_num(1:myDim_nod2D))
    all_max_elem = 0
    call MPI_Allreduce(my_max_elem, all_max_elem, &
          1, MPI_INTEGER, MPI_MAX, &
          MPI_COMM_FESOM, MPIerr)

    my_max_edge=0
    my_max_edge=maxval(nn_num)
    all_max_edge=0
    call MPI_AllREDUCE( my_max_edge, all_max_edge, &
          1, MPI_INTEGER,MPI_MAX, &
          MPI_COMM_FESOM, MPIerr)

    CALL MPI_BARRIER(MPI_COMM_FESOM, ierror)

    if (mype .eq. 0) then
      print *, 'Max␣elements␣per␣node:', all_max_elem, 'Max␣edges␣per␣node:', all_max_edge
      print *, 'FESOM␣before␣def␣partition'
    endif

    ig_paral(1) = 1                       ! Apple Partition
```

```
ig_paral(2) = my_displacement         ! Global Offset
ig_paral(3) = my_number_of_points     ! Local Extent

! For MPI_GATHERV we need the location of the local segment in the global vector
displs_from_all_pes(1) = 0
do i = 2, npes
  displs_from_all_pes(i) = SUM(counts_from_all_pes(1:(i-1)))
enddo

CALL oasis_def_partition( part_id(1), ig_paral, ierror )
if (mype .eq. 0) then
  print *, 'FESOM␣after␣def␣partition'
endif
if ( ierror /= 0 ) then
   print *, 'FESOM␣commRank␣def_partition␣failed'
   call oasis_abort(comp_id, 'cpl_oasis3mct_define_unstr', 'def_partition␣failed')
endif

ALLOCATE(coastal_nodes(number_of_all_points))
ALLOCATE(angle(my_number_of_points,all_max_elem+all_max_edge))
ALLOCATE(my_x_corners(my_number_of_points,all_max_elem+all_max_edge))
ALLOCATE(my_y_corners(my_number_of_points,all_max_elem+all_max_edge))
ALLOCATE(coord_e_edge_center(2,my_number_of_points, all_max_edge))

! We need to know for every node if any of it's edges are coastal, because
! in case they are the center point will be a corner of the nodal area
coastal_nodes=.False.
allocate (coastal_edge_list(my_number_of_points*2,my_number_of_points*2))
do edge=1, myDim_edge2D
  ! local indice of nodes that span up edge
  enodes=edges(:,edge)
  ! local index of element that contribute to edge
  el=edge_tri(:,edge)
  if(el(2)>0) then
    ! Inner edge
    continue
  else
    ! Boundary/coastal edge
    coastal_nodes(enodes(1))=.True.
    coastal_nodes(enodes(2))=.True.
    coastal_edge_list(enodes(1),enodes(2))=edge
    coastal_edge_list(enodes(2),enodes(1))=edge
  end if
end do


! For every node, loop over neighbours, calculate edge center as mean of node center and neighbour node center.
coord_e_edge_center=0
do i = 1, my_number_of_points
  ! if we are on coastal node, include node center n=1 as corner
  if (coastal_nodes(i)==.True.) then
    do n = 1, nn_num(i)
      call edge_center(i, nn_pos(n,i), this_x_coord, this_y_coord, mesh)
      call r2g(coord_e_edge_center(1,i,n), coord_e_edge_center(2,i,n), this_x_coord, this_y_coord)
    end do
  ! else we skip n=1 and use only the edge centers n=2:nn_num(i)
  else
    do n = 2, nn_num(i)
      call edge_center(i, nn_pos(n,i), this_x_coord, this_y_coord, mesh)
      call r2g(coord_e_edge_center(1,i,n-1), coord_e_edge_center(2,i,n-1), this_x_coord, this_y_coord)
    end do
  end if
end do

ALLOCATE(my_x_coords(my_number_of_points))
ALLOCATE(my_y_coords(my_number_of_points))

! Obtain center coordinates as node center on open ocean and as mean of corners at coastline
do i = 1, my_number_of_points
  ! Center coord as mean of corner coordiantes along coastline
  if (coastal_nodes(i)==.True.) then
    ! So we define temp_corner coordiantes
    allocate(temp_x_coord(nod_in_elem2D_num(i)+nn_num(i)))
    allocate(temp_y_coord(nod_in_elem2D_num(i)+nn_num(i)))
    temp_x_coord=0
    temp_y_coord=0
    do j = 1, nod_in_elem2D_num(i)
      temp_x_coord(j) = x_corners(i,j)*rad
      temp_y_coord(j) = y_corners(i,j)*rad
    end do
    ! Loop over edges
    do j = 1, nn_num(i)
      ! We skip coastal edge center points for the new center point calculation
      ! such that 1 element islands have the node center at the right angle
      ! We only do so if n elements is > 2, to avoid having only 3 corners
      if ((j>1) .and. (nod_in_elem2D_num(i) > 2)) then
        edge = coastal_edge_list(i,nn_pos(j,i))
        ! if edge is coastal, we leave it out of the mean equation, replaced by the node center
```

```fortran
            if (edge>0) then
              this_x_coord = coord_nod2D(1, i)
              this_y_coord = coord_nod2D(2, i)
              ! unrotate grid
              call r2g(my_x_coords(i), my_y_coords(i), this_x_coord, this_y_coord)
              temp_x_coord(j+nod_in_elem2D_num(i))=my_x_coords(i)
              temp_y_coord(j+nod_in_elem2D_num(i))=my_y_coords(i)
            ! case for only two elements, we need the real edge centers to ensure center coord
            ! is inside polygon
            else
              temp_x_coord(j+nod_in_elem2D_num(i)) = coord_e_edge_center(1,i,j)
              temp_y_coord(j+nod_in_elem2D_num(i)) = coord_e_edge_center(2,i,j)
            end if
          ! Open ocean case, we just use the corner coords
          else
            temp_x_coord(j+nod_in_elem2D_num(i)) = coord_e_edge_center(1,i,j)
            temp_y_coord(j+nod_in_elem2D_num(i)) = coord_e_edge_center(2,i,j)
          end if
        end do
        min_x = minval(temp_x_coord)
        max_x = maxval(temp_x_coord)
        ! if we are at dateline (fesom cell larger than pi)
        if (max_x-min_x > pi) then

          ! set up separate data structures for the two hemispheres
          n_pos=count(temp_x_coord>=0)
          n_neg=count(temp_x_coord<0)
          allocate(pos_x(n_pos))
          allocate(pos_y(n_pos))
          allocate(neg_x(n_neg))
          allocate(neg_y(n_neg))
          pos_x = 0
          pos_y = 0
          neg_x = 0
          neg_x = 0
          n=1
          do j = 1, size(temp_x_coord)
            ! build separate corner vectors for the hemispheres
            if (temp_x_coord(j) >= 0) then
              pos_x(n) = temp_x_coord(j)
              pos_y(n) = temp_y_coord(j)
              n=n+1
            end if
          end do
          n=1
          do j = 1, size(temp_x_coord)
            if (temp_x_coord(j) < 0) then
              neg_x(n) = temp_x_coord(j)
              neg_y(n) = temp_y_coord(j)
              n=n+1
            end if
          end do
          ! if sum on right side of dateline are further from the dateline we shift the negative sum over to the right
          if (-sum(pos_x)+pi*n_pos >= sum(neg_x)+pi*n_neg) then
            this_x_coord = (sum(pos_x) + sum(neg_x) + 2*pi*n_neg) / (n_pos + n_neg)
            this_y_coord = (sum(pos_y) + sum(neg_y)) / (n_pos + n_neg)
          ! else we shift the positive sum over to the left side
          else
            this_x_coord = (sum(pos_x) - 2*pi*n_pos + sum(neg_x)) / (n_pos + n_neg)
            this_y_coord = (sum(pos_y) + sum(neg_y)) / (n_pos + n_neg)
          end if
          deallocate(pos_x,pos_y,neg_x,neg_y)
        ! max_x-min_x > pi -> we are not at dateline, just a normal mean is enough
        else
          this_x_coord = sum(temp_x_coord)/(size(temp_x_coord))
          this_y_coord = sum(temp_y_coord)/(size(temp_y_coord))
        end if
        my_x_coords(i)=this_x_coord
        my_y_coords(i)=this_y_coord
        deallocate(temp_x_coord, temp_y_coord)
      ! coastal_nodes(i)==.True. -> Node center on open ocean, we can use node center
      else
        this_x_coord = coord_nod2D(1, i)
        this_y_coord = coord_nod2D(2, i)
        ! unrotate grid
        call r2g(my_x_coords(i), my_y_coords(i), this_x_coord, this_y_coord)
      end if
    end do

    ! Add the different corner types to single array in preparation for angle calculation
    do i = 1, my_number_of_points
      ! First for element center based corners
      do j = 1, nod_in_elem2D_num(i)
        my_x_corners(i,j) = x_corners(i,j)*rad ! atan2 takes radian and elem corners come in grad
        my_y_corners(i,j) = y_corners(i,j)*rad
      end do
      ! Then we repeat for edge center coordinate
      ! The coast j=1 is the node center
```

```
      if (coastal_nodes(i)==.True.) then
        do j = 1, nn_num(i)
          my_x_corners(i,j+nod_in_elem2D_num(i)) = coord_e_edge_center(1,i,j)
          my_y_corners(i,j+nod_in_elem2D_num(i)) = coord_e_edge_center(2,i,j)
        end do
      ! On open ocean we dont use the node center as corner, and thus have one less corner
      else
        do j = 1, nn_num(i)-1
          my_x_corners(i,j+nod_in_elem2D_num(i)) = coord_e_edge_center(1,i,j)
          my_y_corners(i,j+nod_in_elem2D_num(i)) = coord_e_edge_center(2,i,j)
        end do
      end if
    end do

    ! calculate angle between corners and center
    do i = 1, my_number_of_points
      if (coastal_nodes(i)==.True.) then
        n=0
      else
        n=1
      end if
      do j = 1, nod_in_elem2D_num(i)+nn_num(i)-n
        ! If they have different sign we are near the dateline and need to bring the corner onto
        ! the same hemisphere as the center (only for angle calc, the coord for oasis remains as before)
        ! Default: same sign -> normal atan2
        if (my_x_coords(i) <=0 .and. my_x_corners(i,j) <=0 .or. my_x_coords(i) >0 .and. my_x_corners(i,j) >0)
             then
          angle(i,j) = atan2(my_x_corners(i,j) - my_x_coords(i), my_y_corners(i,j) - my_y_coords(i))
        else
          ! at dateline center is on the right side
          if (my_x_coords(i) >=pi/2) then
            angle(i,j) = atan2(my_x_corners(i,j) + 2*pi - my_x_coords(i), my_y_corners(i,j) - my_y_coords(i))
          ! at dateline center is on the left side
          else if (my_x_coords(i) <=-pi/2) then
            angle(i,j) = atan2(my_x_corners(i,j) - 2*pi - my_x_coords(i), my_y_corners(i,j) - my_y_coords(i))
          ! at prime meridan -> also default
          else
            angle(i,j) = atan2(my_x_corners(i,j) - my_x_coords(i), my_y_corners(i,j) - my_y_coords(i))
          end if
        end if
      end do
    end do

    ! Oasis requires corners sorted counterclockwise, so we sort by angle
    do i = 1, my_number_of_points
      if (coastal_nodes(i)==.True.) then
        n=0
      else
        n=1
      end if
      do l = 1, nod_in_elem2D_num(i)+nn_num(i)-1-n
        do m = l+1, nod_in_elem2D_num(i)+nn_num(i)-n
          if (angle(i,l) < angle(i,m)) then
            ! Swap angle
            temp = angle(i,m)
            angle(i,m) = angle(i,l)
            angle(i,l) = temp
            ! Swap lon
            temp = my_x_corners(i,m)
            my_x_corners(i,m) = my_x_corners(i,l)
            my_x_corners(i,l) = temp
            ! Swap lat
            temp = my_y_corners(i,m)
            my_y_corners(i,m) = my_y_corners(i,l)
            my_y_corners(i,l) = temp
          end if
        end do
      end do
    end do

    ! We can have a variable number of corner points.
    ! Luckly oasis can deal with that by just repeating the last one.
    ! Note, we are only allowed to repeat one coordinate and
    ! the last one is not an element center, but an edge center
    do i = 1, my_number_of_points
      do j = 1, all_max_elem+all_max_edge
        if (coastal_nodes(i)==.True.) then
          if (j < nod_in_elem2D_num(i)+nn_num(i)) then
            my_y_corners(i,j)=my_y_corners(i,j)
            my_x_corners(i,j)=my_x_corners(i,j)
          else
            my_y_corners(i,j)=my_y_corners(i,nod_in_elem2D_num(i)+nn_num(i))
            my_x_corners(i,j)=my_x_corners(i,nod_in_elem2D_num(i)+nn_num(i))
          end if
        else
          if (j < nod_in_elem2D_num(i)+nn_num(i)-1) then
            my_y_corners(i,j)=my_y_corners(i,j)
            my_x_corners(i,j)=my_x_corners(i,j)
          else
```

```
            my_y_corners(i,j)=my_y_corners(i,nod_in_elem2D_num(i)+nn_num(i)-1)
            my_x_corners(i,j)=my_x_corners(i,nod_in_elem2D_num(i)+nn_num(i)-1)
          end if
        end if
      end do
    end do

    ! Oasis takes grad angles
    my_x_coords=my_x_coords/rad
    my_y_coords=my_y_coords/rad
    my_x_corners=my_x_corners/rad
    my_y_corners=my_y_corners/rad


    if (mype .eq. localroot) then
      ALLOCATE(all_x_coords(number_of_all_points, 1))
      ALLOCATE(all_y_coords(number_of_all_points, 1))
      ALLOCATE(all_x_corners(number_of_all_points, 1, all_max_elem+all_max_edge))
      ALLOCATE(all_y_corners(number_of_all_points, 1, all_max_elem+all_max_edge))
      ALLOCATE(all_area(number_of_all_points, 1))
    else
      ALLOCATE(all_x_coords(1, 1))
      ALLOCATE(all_y_coords(1, 1))
      ALLOCATE(all_x_corners(1, 1, all_max_elem+all_max_edge))
      ALLOCATE(all_y_corners(1, 1, all_max_elem+all_max_edge))
      ALLOCATE(all_area(1, 1))
    endif


    if (mype .eq. 0) then
      print *, 'FESOM before 1st GatherV', displs_from_all_pes(npes), counts_from_all_pes(npes),
           number_of_all_points
    endif
    CALL MPI_GATHERV(my_x_coords, my_number_of_points, MPI_DOUBLE_PRECISION, all_x_coords,  &
                    counts_from_all_pes, displs_from_all_pes, MPI_DOUBLE_PRECISION, localroot, MPI_COMM_FESOM
                          , ierror)

    if (mype .eq. 0) then
      print *, 'FESOM before 2nd GatherV'
    endif
    CALL MPI_GATHERV(my_y_coords, my_number_of_points, MPI_DOUBLE_PRECISION, all_y_coords,  &
                    counts_from_all_pes, displs_from_all_pes, MPI_DOUBLE_PRECISION, localroot, MPI_COMM_FESOM
                          , ierror)

    if (mype .eq. 0) then
      print *, 'FESOM before 3rd GatherV', displs_from_all_pes(npes), counts_from_all_pes(npes),
           number_of_all_points
    endif

    do j = 1, all_max_elem+all_max_edge
      CALL MPI_GATHERV(my_x_corners(:,j), my_number_of_points, MPI_DOUBLE_PRECISION, all_x_corners(:,:,j),  &
                    counts_from_all_pes, displs_from_all_pes, MPI_DOUBLE_PRECISION, localroot, MPI_COMM_FESOM
                          , ierror)
      CALL MPI_GATHERV(my_y_corners(:,j), my_number_of_points, MPI_DOUBLE_PRECISION, all_y_corners(:,:,j),  &
                    counts_from_all_pes, displs_from_all_pes, MPI_DOUBLE_PRECISION, localroot, MPI_COMM_FESOM
                          , ierror)
    end do

    if (mype .eq. 0) then
      print *, 'FESOM before 4th GatherV'
    endif
    CALL MPI_GATHERV(area(1,:), my_number_of_points, MPI_DOUBLE_PRECISION, all_area,  &
                    counts_from_all_pes, displs_from_all_pes, MPI_DOUBLE_PRECISION, localroot, MPI_COMM_FESOM
                          , ierror)

    if (mype .eq. 0) then
      print *, 'FESOM after 4th GatherV'
    endif


    CALL MPI_Barrier(MPI_COMM_FESOM, ierror)
    if (mype .eq. 0) then
      print *, 'FESOM after Barrier'
    endif

    if (mype .eq. localroot) then
      print *, 'FESOM before start_grids_writing'
       CALL oasis_start_grids_writing(il_flag)
       IF (il_flag .NE. 0) THEN

          print *, 'FESOM before write grid'
          CALL oasis_write_grid (grid_name, number_of_all_points, 1, all_x_coords(:,:), all_y_coords(:,:))

          print *, 'FESOM before write corner'
          CALL oasis_write_corner (grid_name, number_of_all_points, 1, all_max_elem+all_max_edge,
               all_x_corners(:,:,:), all_y_corners(:,:,:))

          ALLOCATE(unstr_mask(number_of_all_points, 1))
          unstr_mask=0
```

```
          print *, 'FESOM before write mask'
          CALL oasis_write_mask(grid_name, number_of_all_points, 1, unstr_mask)
          DEALLOCATE(unstr_mask)

          print *, 'FESOM before write area'
          CALL oasis_write_area(grid_name, number_of_all_points, 1, all_area)

       end if
      print *, 'FESOM before terminate_grids_writing'
      call oasis_terminate_grids_writing()
      print *, 'FESOM after terminate_grids_writing'
    endif !localroot

    DEALLOCATE(all_x_coords, all_y_coords, my_x_coords, my_y_coords)
    DEALLOCATE(all_x_corners, all_y_corners, my_x_corners, my_y_corners, angle)
    DEALLOCATE(coastal_nodes, coord_e_edge_center)
!-------------------------------------------------------------------
! 3rd Declare the transient variables
!-------------------------------------------------------------------
!
!
! ... Define symbolic names for the transient fields send by the ocean
!     These must be identical to the names specified in the SMIOC file.
!
#if defined (__oifs)
    cpl_send( 1)='sst_feom' ! 1. sea surface temperature [K]       ->
    cpl_send( 2)='sie_feom' ! 2. sea ice extent [%-100]            ->
    cpl_send( 3)='snt_feom' ! 3. snow thickness [m]                ->
    cpl_send( 4)='ist_feom' ! 4. sea ice surface temperature [K]   ->
    cpl_send( 5)='sia_feom' ! 5. sea ice albedo [%-100]            ->
    cpl_send( 6)='u_feom'   ! 6. eastward  surface velocity [m/s]  ->
    cpl_send( 7)='v_feom'   ! 7. northward surface velocity [m/s]  ->
#else
    cpl_send( 1)='sst_feom' ! 1. sea surface temperature [degC]      ->
    cpl_send( 2)='sit_feom' ! 2. sea ice thickness [m]             ->
    cpl_send( 3)='sie_feom' ! 3. sea ice extent [%-100]            ->
    cpl_send( 4)='snt_feom' ! 4. snow thickness [m]                ->
#endif



!
! ...  Define symbolic names for transient fields received by the ocean.
!      These must be identical to the names specified in the SMIOC file.
!
#if defined (__oifs)
    cpl_recv(1)  = 'taux_oce'
    cpl_recv(2)  = 'tauy_oce'
    cpl_recv(3)  = 'taux_ico'
    cpl_recv(4)  = 'tauy_ico'
    cpl_recv(5)  = 'prec_oce'
    cpl_recv(6)  = 'snow_oce'
    cpl_recv(7)  = 'evap_oce'
    cpl_recv(8)  = 'subl_oce'
    cpl_recv(9)  = 'heat_oce'
    cpl_recv(10) = 'heat_ico'
    cpl_recv(11) = 'heat_swo'
    cpl_recv(12) = 'hydr_oce'
    cpl_recv(13) = 'enth_oce'
#else
    cpl_recv(1)  = 'taux_oce'
    cpl_recv(2)  = 'tauy_oce'
    cpl_recv(3)  = 'taux_ico'
    cpl_recv(4)  = 'tauy_ico'
    cpl_recv(5)  = 'prec_oce'
    cpl_recv(6)  = 'snow_oce'
    cpl_recv(7)  = 'evap_oce'
    cpl_recv(8)  = 'subl_oce'
    cpl_recv(9)  = 'heat_oce'
    cpl_recv(10) = 'heat_ico'
    cpl_recv(11) = 'heat_swo'
    cpl_recv(12) = 'hydr_oce'
#endif

    if (mype .eq. 0) then
       print *, 'FESOM after declaring the transient variables'
    endif

    data_type = oasis_DOUBLE
!     nodim(1): the overall number of dimensions of array that is going
!               to be transferred with var_id, i.e. same than grid_nodims
!               except for bundle variables for which it is one more.

    nodim(1) = 1 ! check, 3 for OASIS4
    nodim(2) = 1
!
! ... Announce send variables, all on T points.
!
    total_shape(1) = number_of_all_points
```

```
    total_shape(2) = 1

    do i = 1, nsend
       call oasis_def_var(send_id(i), cpl_send(i), part_id(1), &
            nodim, oasis_Out, total_shape, oasis_Double, ierror)
       if (ierror /= oasis_Ok) then
          print *, 'Failed␣to␣define␣transient␣', i, trim(cpl_send(i))
          call oasis_abort(comp_id, 'cpl_oasis3mct_define_unstr', 'def_var␣failed')
       endif
    enddo

    if (mype .eq. 0) then
       print *, 'FESOM␣after␣announcing␣send␣variables'
    endif

!
!
! ... Announce recv variables, all on T points
!
    do i = 1, nrecv
       call oasis_def_var(recv_id(i), cpl_recv(i), part_id(1), &
            nodim, oasis_In, total_shape, oasis_Double, ierror)
       if (ierror /= oasis_Ok) then
          print *, 'Failed␣to␣define␣transient␣', i, trim(cpl_recv(i))
          call oasis_abort(comp_id, 'cpl_oasis3mct_define_unstr', 'def_var␣failed')
       endif
    enddo

    if (mype .eq. 0) then
       print *, 'FESOM␣after␣announcing␣revieved␣variables'
    endif

!------------------------------------------------------------------
! 4th End of definition phase
!------------------------------------------------------------------

   call oasis_enddef(ierror)
   if (commRank) print *, 'fesom␣oasis_enddef:␣COMPLETED'
#ifndef __oifs
   if (commRank) print *, 'FESOM:␣calling␣exchange_roots'
   call exchange_roots(source_root, target_root, 1, partit%MPI_COMM_FESOM, MPI_COMM_WORLD)
   if (commRank) print *, 'FESOM␣source/target␣roots:␣', source_root, target_root
#endif
   if (mype .eq. 0) then
      print *, 'After␣enddef'
   endif

   ! WAS VOM FOLGENDEN BRAUCHE ICH NOCH ???

   allocate(cplsnd(nsend, myDim_nod2D+eDim_nod2D))
   allocate(exfld(myDim_nod2D))
   cplsnd=0.
   o2a_call_count=0
   if (mype .eq. 0) then
      print *, 'Before␣last␣barrier'
   endif

   CALL MPI_BARRIER(MPI_COMM_FESOM, ierror)
   if (mype .eq. 0) then
      print *, 'Survived␣cpl_oasis3mct_define'
   endif

  end subroutine cpl_oasis3mct_define_unstr
```

Bibliography

Adcroft, A. and Campin, J.-M. (2004). Rescaled height coordinates for accurate representation of free-surface flows in ocean circulation models. *Ocean Modelling*, 7(3):269–284.

Adler, R. F., Sapiano, M. R., Huffman, G. J., Wang, J.-J., Gu, G., Bolvin, D., Chiu, L., Schneider, U., Becker, A., Nelkin, E., et al. (2018a). The global precipitation climatology project (gpcp) monthly analysis (new version 2.3) and a review of 2017 global precipitation. *Atmosphere*, 9(4):138.

Adler, R. F., Sapiano, M. R. P., Huffman, G. J., Wang, J.-J., Gu, G., Bolvin, D., Chiu, L., Schneider, U., Becker, A., Nelkin, E., Xie, P., Ferraro, R., and Shin, D.-B. (2018b). The global precipitation climatology project (gpcp) monthly analysis (new version 2.3) and a review of 2017 global precipitation. *Atmosphere*, 9(4).

Ali, A., Christensen, K. H., Øyvind Breivik, Malila, M., Raj, R. P., Bertino, L., Chassignet, E. P., and Bakhoday-Paskyabi, M. (2019). A comparison of langmuir turbulence parameterizations and key wave effects in a numerical model of the north atlantic and arctic oceans. *Ocean Modelling*, 137:76–97.

Arrhenius, S. (1896). Xxxi. on the influence of carbonic acid in the air upon the temperature of the ground. *The London, Edinburgh, and Dublin Philosophical Magazine and Journal of Science*, 41(251):237–276.

Athanase, M., Schwager, M., Streffing, J., Andrés-Martínez, M., Loza, S. N., and Goessling, H. F. (2022). Impact of the atmospheric circulation on the arctic snow cover and ice thickness variability.

Auclair, F., Bordois, L., Dossmann, Y., Duhaut, T., Paci, A., Ulses, C., and Nguyen, C. (2018). A non-hydrostatic non-boussinesq algorithm for free-surface ocean modelling. *Ocean Modelling*, 132:12–29.

Baker, A. J., Schiemann, R., Hodges, K. I., Demory, M.-E., Mizielinski, M. S., Roberts, M. J., Shaffrey, L. C., Strachan, J., and Vidale, P. L. (2019). Enhanced climate change response of wintertime north atlantic circulation, cyclonic activity, and precipitation in a 25-km-resolution global atmospheric model. *Journal of Climate*, 32(22):7763–7781.

Baker, N. C. and Taylor, P. C. (2016). A framework for evaluating climate model performance metrics. *Journal of Climate*, 29(5):1773 – 1782.

Balaji, V., Maisonnave, E., Zadeh, N., Lawrence, B. N., Biercamp, J., Fladrich, U., Aloisio, G., Benson, R., Caubel, A., Durachta, J., Foujols, M.-A., Lister, G., Mocavero, S., Underwood, S., and Wright, G. (2017). Cpmip: measurements of real computational performance of earth system models in cmip6. *Geoscientific Model Development*, 10(1):19–34.

Balsamo, G., Beljaars, A., Scipal, K., Viterbo, P., van den Hurk, B., Hirschi, M., and Betts, A. K. (2009). A Revised Hydrology for the ECMWF Model: Verification from Field Site to Terrestrial Water Storage and Impact in the Integrated Forecast System. *Journal of Hydrometeorology*, 10(3):623–643.

Barbi, D., Wieters, N., Gierz, P., Andrés-Martínez, M., Ural, D., Chegini, F., Khosravi, S., and Cristini, L. (2021). Esm-tools version 5.0: a modular infrastructure for stand-alone and coupled earth system modelling (esm). *Geoscientific Model Development*, 14(6):4051–4067.

Batrak, Y. and Müller, M. (2019a). On the warm bias in atmospheric reanalyses induced by the missing snow over arctic sea-ice. *Nature Communications*, 10(1):4170.

Batrak, Y. and Müller, M. (2019b). On the warm bias in atmospheric reanalyses induced by the missing snow over arctic sea-ice. *Nature Communications*, 10(1):4170.

Beadling, R. L., Russell, J. L., Stouffer, R. J., Mazloff, M., Talley, L. D., Goodman, P. J., Sallée, J. B., Hewitt, H. T., Hyder, P., and Pandde, A. (2020). Representation of southern ocean properties across coupled model intercomparison project generations: Cmip3 to cmip6. *Journal of Climate*, 33(15):6555 – 6581.

Bock, L., Lauer, A., Schlund, M., Barreiro, M., Bellouin, N., Jones, C., Meehl, G. A., Predoi, V., Roberts, M. J., and Eyring, V. (2020). Quantifying progress across different cmip phases with the esmvaltool. *Journal of Geophysical Research: Atmospheres*, 125(21):e2019JD032321. e2019JD032321 2019JD032321.

Buizza, R., Alonso-Balmaseda, M., Brown, A., English, S., Forbes, R., Geer, A., Haiden, T., Leutbecher, M., Magnusson, L., Rodwell, M., Sleigh, M., Stockdale, T., Vitart, F., and Wedi, N. (2018). The development and evaluation process followed at ecmwf to upgrade the integrated forecasting system (ifs). *ECMWF Technical Memoranda*.

Buizza, R., Milleer, M., and Palmer, T. N. (1999). Stochastic representation of model uncertainties in the ecmwf ensemble prediction system. *Quarterly Journal of the Royal Meteorological Society*, 125(560):2887–2908.

BUSH, J. W. M. and WOODS, A. W. (1999). Vortex generation by line plumes in a rotating stratified fluid. *Journal of Fluid Mechanics*, 388:289–313.

Bye, J. A. (1985). Chapter 6 large-scale momentum exchange in the coupled atmosphere-ocean. In Nihoul, J., editor, *Coupled Ocean-Atmosphere Models*, volume 40 of *Elsevier Oceanography Series*, pages 51–61. Elsevier.

Caesar, L., McCarthy, G. D., Thornalley, D. J. R., Cahill, N., and Rahmstorf, S. (2022). Reply to: Atlantic circulation change still uncertain. *Nature Geoscience*.

Cauquoin, A., Werner, M., and Lohmann, G. (2019). Water isotopes – climate relationships for the mid-holocene and preindustrial period simulated with an isotope-enabled version of mpi-esm. *Climate of the Past*, 15(6):1913–1937.

Charney, J. G., Fjörtoft, R., and Von Neumann, J. (1950). Numerical integration of the barotropic vorticity equation. *Tellus*, 2(4):237–254.

Cohen, J., Zhang, X., Francis, J., Jung, T., Kwok, R., Overland, J., Ballinger, T. J., Bhatt, U. S., Chen, H. W., Coumou, D., Feldstein, S., Gu, H., Handorf, D., Henderson, G., Ionita, M., Kretschmer, M., Laliberte, F., Lee, S., Linderholm, H. W., Maslowski, W., Peings, Y., Pfeiffer, K., Rigor, I., Semmler, T., Stroeve, J., Taylor, P. C., Vavrus, S., Vihma, T., Wang, S., Wendisch, M., Wu, Y., and Yoon, J. (2020). Divergent consensuses on arctic amplification influence on midlatitude severe winter weather. *Nature Climate Change*, 10(1):20–29.

Cox, G. F. N. and Weeks, W. F. (1974). Salinity variations in sea ice. *Journal of Glaciology*, 13(67):109–120.

Craig, A., Valcke, S., and Coquart, L. (2017a). Development and performance of a new version of the oasis coupler, oasis3-mct_3. 0. *Geoscientific Model Development*, 10(9):3297–3308.

Craig, A., Valcke, S., and Coquart, L. (2017b). Development and performance of a new version of the oasis coupler, oasis3-mct_3.0. *Geoscientific Model Development*, 10(9):3297–3308.

Curry, B., Lee, C. M., Petrie, B., Moritz, R. E., and Kwok, R. (2014). Multiyear volume, liquid freshwater, and sea ice transports through davis strait, 2004–10. *Journal of Physical Oceanography*, 44(4):1244 – 1266.

Danabasoglu, G., Lamarque, J.-F., Bacmeister, J., Bailey, D. A., DuVivier, A. K., Edwards, J., Emmons, L. K., Fasullo, J., Garcia, R., Gettelman, A., Hannay, C., Holland, M. M., Large, W. G., Lauritzen, P. H., Lawrence, D. M., Lenaerts, J. T. M., Lindsay, K., Lipscomb, W. H., Mills, M. J., Neale, R., Oleson, K. W., Otto-Bliesner, B., Phillips, A. S., Sacks, W., Tilmes, S., van Kampenhout, L., Vertenstein, M., Bertini, A., Dennis, J., Deser, C., Fischer, C., Fox-Kemper, B., Kay, J. E., Kinnison, D., Kushner, P. J., Larson, V. E., Long, M. C., Mickelson, S., Moore, J. K., Nienhouse, E., Polvani, L., Rasch, P. J., and Strand, W. G. (2020). The community earth system model version 2 (cesm2). *Journal of Advances in Modeling Earth Systems*, 12(2):e2019MS001916. e2019MS001916 2019MS001916.

Danek, C., Shi, X., Stepanek, C., Yang, H., Barbi, D., Hegewald, J., and Lohmann, G. (2020). Awi awi-esm1.1lr model output prepared for cmip6 cmip.

Danilov, S., Sidorenko, D., Wang, Q., and Jung, T. (2017). The finite-volume sea ice–ocean model (fesom2). *Geoscientific Model Development*, 10(2):765–789.

Danilov, S., Wang, Q., Timmermann, R., Iakovlev, N., Sidorenko, D., Kimmritz, M., Jung, T., and Schröter, J. (2015). Finite-element sea ice model (fesim), version 2. *Geosci. Model Dev.*, 8:1747–1761.

Davini, P., Corti, S., D'Andrea, F., Rivière, G., and von Hardenberg, J. (2017). Improved winter european atmospheric blocking frequencies in high-resolution global climate simulations. *Journal of Advances in Modeling Earth Systems*, 9(7):2615–2634.

Davy, R., Chen, L., and Hanna, E. (2018). Arctic amplification metrics. *International Journal of Climatology*, 38(12):4384–4394.

Dawson, A. (2016). Eofs: A library for eof analysis of meteorological, oceanographic, and climate data. *Journal of Open Research Software*, 4(1).

Delworth, T. L., Broccoli, A. J., Rosati, A., Stouffer, R. J., Balaji, V., Beesley, J. A., Cooke, W. F., Dixon, K. W., Dunne, J., Dunne, K. A., Durachta, J. W., Findell, K. L., Ginoux, P., Gnanadesikan, A., Gordon, C. T., Griffies, S. M., Gudgel, R., Harrison, M. J., Held, I. M., Hemler, R. S., Horowitz, L. W., Klein, S. A., Knutson, T. R., Kushner, P. J., Langenhorst, A. R., Lee, H.-C., Lin, S.-J., Lu, J., Malyshev, S. L., Milly, P. C. D., Ramaswamy, V., Russell, J., Schwarzkopf, M. D., Shevliakova, E., Sirutis, J. J., Spelman, M. J., Stern, W. F., Winton, M., Wittenberg, A. T., Wyman, B., Zeng, F., and Zhang, R. (2006). Gfdl's cm2 global coupled climate models. part i: Formulation and simulation characteristics. *Journal of Climate*, 19(5):643–674.

Delworth, T. L., Rosati, A., Anderson, W., Adcroft, A. J., Balaji, V., Benson, R., Dixon, K., Griffies, S. M., Lee, H.-C., Pacanowski, R. C., Vecchi, G. A., Wittenberg, A. T., Zeng, F., and Zhang, R. (2012). Simulated climate and climate change in the gfdl cm2.5 high-resolution coupled climate model. *Journal of Climate*, 25(8):2755 – 2781.

Donohue, K. A., Tracey, K. L., Watts, D. R., Chidichimo, M. P., and Chereskin, T. K. (2016). Mean antarctic circumpolar current transport measured in drake passage. *Geophysical Research Letters*, 43(22):11,760–11,767.

Döscher, R., Acosta, M., Alessandri, A., Anthoni, P., Arneth, A., Arsouze, T., Bergmann, T., Bernadello, R., Bousetta, S., Caron, L.-P., Carver, G., Castrillo, M., Catalano, F., Cvijanovic, I., Davini, P., Dekker, E., Doblas-Reyes, F. J., Docquier, D., Echevarria, P., Fladrich, U., Fuentes-Franco, R., Gröger, M., v. Hardenberg, J., Hieronymus, J., Karami, M. P., Keskinen, J.-P., Koenigk, T., Makkonen, R., Massonnet, F., Ménégoz, M., Miller, P. A., Moreno-Chamarro, E., Nieradzik, L., van Noije, T., Nolan, P., O'Donnell, D., Ollinaho, P., van den Oord, G., Ortega, P., Prims, O. T., Ramos, A., Reerink, T., Rousset, C., Ruprich-Robert, Y., Le Sager, P., Schmith, T., Schrödner, R., Serva, F., Sicardi, V., Sloth Madsen, M., Smith, B., Tian, T., Tourigny, E., Uotila, P., Vancoppenolle, M., Wang, S., Wårlind, D., Willén, U., Wyser, K., Yang, S., Yepes-Arbós, X., and Zhang, Q. (2021). The ec-earth3 earth system model for the climate model intercomparison project 6. *Geoscientific Model Development Discussions*, 2021:1–90.

Döscher, R., Acosta, M., Alessandri, A., Anthoni, P., Arneth, A., Arsouze, T., Bergmann, T., Bernadello, R., Bousetta, S., Caron, L.-P., et al. (2021). The ec-earth3 earth system model for the climate model intercomparison project 6. *Geoscientific Model Development Discussions*, 1:2021.

Döscher, R., Acosta, M., Alessandri, A., Anthoni, P., Arsouze, T., Bergman, T., Bernardello, R., Boussetta, S., Caron, L.-P., Carver, G., Castrillo, M., Catalano, F., Cvijanovic, I., Davini, P., Dekker, E., Doblas-Reyes, F. J., Docquier, D., Echevarria, P., Fladrich, U., Fuentes-Franco, R., Gröger, M., v. Hardenberg, J., Hieronymus, J., Karami, M. P., Keskinen, J.-P., Koenigk, T., Makkonen, R., Massonnet, F., Ménégoz, M., Miller, P. A., Moreno-Chamarro, E., Nieradzik, L., van Noije, T., Nolan, P., O'Donnell, D., Ollinaho, P., van den Oord, G., Ortega, P., Prims, O. T., Ramos, A., Reerink, T., Rousset, C., Ruprich-Robert, Y., Le Sager, P., Schmith, T., Schrödner, R., Serva, F., Sicardi, V., Sloth Madsen, M., Smith, B., Tian, T., Tourigny, E., Uotila, P., Vancoppenolle, M., Wang, S., Wårlind, D., Willén, U., Wyser, K., Yang, S., Yepes-Arbós, X., and Zhang, Q. (2022). The ec-earth3 earth system model for the coupled model intercomparison project 6. *Geoscientific Model Development*, 15(7):2973–3020.

ECMWF (2017a). *IFS Documentation CY43R3 - Part III: Dynamics and numerical procedures*, chapter 3, pages 1–31. Number 3 in IFS Documentation. ECMWF.

ECMWF (2017b). *IFS Documentation CY43R3 - Part IV: Physical processes*, chapter 4, pages 1–221. Number 4 in IFS Documentation. ECMWF.

ECMWF (2017c). *IFS Documentation CY43R3 - Part VII: ECMWF wave model*, chapter 7, pages 1–99. Number 7 in IFS Documentation. ECMWF.

Eden, C. and Dietze, H. (2009). Effects of mesoscale eddy/wind interactions on biological new production and eddy kinetic energy. *Journal of Geophysical Research: Oceans*, 114(C5).

Exner, F. M. (1908). Uber eine erste annäherung zur vorausberechnung synoptischer wetterkarten. *Meteor. Zeit*, 25:57–67.

Eyring, V., Bock, L., Lauer, A., Righi, M., Schlund, M., Andela, B., Arnone, E., Bellprat, O., Brötz, B., Caron, L.-P., Carvalhais, N., Cionni, I., Cortesi, N., Crezee, B., Davin, E. L., Davini, P., Debeire, K., de Mora, L., Deser, C., Docquier, D., Earnshaw, P., Ehbrecht, C., Gier, B. K., Gonzalez-Reviriego, N., Goodman, P., Hagemann, S., Hardiman, S., Hassler, B., Hunter, A., Kadow, C., Kindermann, S., Koirala, S., Koldunov, N., Lejeune, Q., Lembo, V., Lovato, T., Lucarini, V., Massonnet, F., Müller, B., Pandde, A., Pérez-Zanón, N., Phillips, A., Predoi, V., Russell, J., Sellar, A., Serva, F., Stacke, T., Swaminathan, R., Torralba, V., Vegas-Regidor, J., von Hardenberg, J., Weigel, K., and Zimmermann, K. (2020). Earth system model evaluation tool (esmvaltool) v2.0 – an extended set of large-scale diagnostics for quasi-operational and comprehensive evaluation of earth system models in cmip. *Geoscientific Model Development*, 13(7):3383–3438.

Forbes, R., Geer, A., Lonitz, K., and Ahlgrimm, M. (2016). Reducing systematic errors in cold-air outbreaks. *ECMWF newsletter*, 146:17–22.

Garrison, T. S. (2012). *Oceanography: an invitation to marine science*. Cengage Learning.

Gent, P. R. and Mcwilliams, J. C. (1990). Isopycnal mixing in ocean circulation models. *Journal of Physical Oceanography*, 20(1):150–155.

Gierz, P., Ackermann, L., Rodehacke, C. B., Krebs-Kanzow, U., Stepanek, C., Barbi, D., and Lohmann, G. (2020). Simulating interactive ice sheets in the multi-resolution AWI-ESM 1.2: A case study using SCOPE 1.0. *Geoscientific Model Development*.

Gleckler, P. J., Taylor, K. E., and Doutriaux, C. (2008). Performance metrics for climate models. *Journal of Geophysical Research: Atmospheres*, 113(D6).

Good, S. A., Martin, M. J., and Rayner, N. A. (2013). En4: Quality controlled ocean temperature and salinity profiles and monthly objective analyses with uncertainty estimates. *Journal of Geophysical Research: Oceans*, 118(12):6704–6716.

Goosse, H., Brovkin, V., Fichefet, T., Haarsma, R., Huybrechts, P., Jongma, J., Mouchet, A., Selten, F., Barriat, P.-Y., Campin, J.-M., Deleersnijder, E., Driesschaert, E., Goelzer, H., Janssens, I., Loutre, M.-F., Morales Maqueda, M. A., Opsteegh, T., Mathieu, P.-P., Munhoven, G., Pettersson, E. J., Renssen, H., Roche, D. M., Schaeffer, M., Tartinville, B., Timmermann, A., and Weber, S. L. (2010). Description of the earth system model of intermediate complexity loveclim version 1.2. *Geoscientific Model Development*, 3(2):603–633.

Gough, D. (1981). Solar interior structure and luminosity variations. In *Physics of Solar Variations: Proceedings of the 14th ESLAB Symposium held in Scheveningen, The Netherlands, 16–19 September, 1980*, pages 21–34. Springer.

Gregory, J. M., Ingram, W. J., Palmer, M. A., Jones, G. S., Stott, P. A., Thorpe, R. B., Lowe, J. A., Johns, T. C., and Williams, K. D. (2004). A new method for diagnosing radiative forcing and climate sensitivity. *Geophysical Research Letters*, 31(3).

Guenther, H., Hasselmann, S., and Janssen, P. A. E. M. (1992). The wam model cycle 4. Technical report, ECMWF, Germany. DKRZ-TR–4(reved).

Haarsma, R. J., Roberts, M. J., Vidale, P. L., Senior, C. A., Bellucci, A., Bao, Q., Chang, P., Corti, S., Fučkar, N. S., Guemas, V., von Hardenberg, J., Hazeleger, W., Kodama, C., Koenigk, T., Leung, L. R., Lu, J., Luo, J.-J., Mao, J., Mizielinski, M. S., Mizuta, R., Nobre, P., Satoh, M., Scoccimarro, E., Semmler, T., Small, J., and von Storch, J.-S. (2016). High resolution model intercomparison project (highresmip v1.0) for cmip6. *Geoscientific Model Development*, 9(11):4185–4208.

Haiden, T., Janousek, M., Vitart, F., Ben-Bouallegue, Z., Ferranti, L., Prates, F., and Richardson, D. (2022). *Evaluation of ECMWF forecasts, including the 2021 upgrade*, chapter 884, pages 1–56. ECMWF.

Haiden, T., Janousek, M., Vitart, F., Bouallègue, Z. B., Ferranti, L., Prates, F., and Richardson, D. (2018). *Evaluation of ECMWF forecasts, including the 2018 upgrade*. European Centre for Medium Range Weather Forecasts Reading, UK.

Hanke, M., Redler, R., Holfeld, T., and Yastremsky, M. (2016). Yac 1.2. 0: new aspects for coupling software in earth system modelling. *Geoscientific Model Development*, 9(8):2755–2769.

Hazeleger, W., Severijns, C., Semmler, T., Ştefănescu, S., Yang, S., Wang, X., Wyser, K., Dutra, E., Baldasano, J. M., Bintanja, R., et al. (2010). Ec-earth: a seamless earth-system prediction approach in action. *Bulletin of the American Meteorological Society*, 91(10):1357–1364.

Hersbach, H., Bell, B., Berrisford, P., Hirahara, S., Horányi, A., Muñoz-Sabater, J., Nicolas, J., Peubey, C., Radu, R., Schepers, D., et al. (2020a). The era5 global reanalysis. *Quarterly Journal of the Royal Meteorological Society*, 146(730):1999–2049.

Hersbach, H., Bell, B., Berrisford, P., Hirahara, S., Horányi, A., Muñoz-Sabater, J., Nicolas, J., Peubey, C., Radu, R., Schepers, D., Simmons, A., Soci, C., Abdalla, S., Abellan, X., Balsamo, G., Bechtold, P., Biavati, G., Bidlot, J., Bonavita, M., De Chiara, G., Dahlgren, P., Dee, D., Diamantakis, M., Dragani, R., Flemming, J., Forbes, R., Fuentes, M., Geer, A., Haimberger, L., Healy, S., Hogan, R. J., Hólm, E., Janisková, M., Keeley, S., Laloyaux, P., Lopez, P., Lupu, C., Radnoti, G., de Rosnay, P., Rozum, I., Vamborg, F., Villaume, S., and Thépaut, J.-N. (2020b). The era5 global reanalysis. *Quarterly Journal of the Royal Meteorological Society*, 146(730):1999–2049.

Hersbach, H., Bidlot, J.-R., Beljaars, A., Janssen, P., Alonso-Balmaseda, M., Stockdale, T., Vitart, F., Abdalla, S., and Hamrud, M. (2008). The relevance of ocean surface current in the ecmwf analysis and forecast system.

Hertwig, E., von Storch, J.-S., Handorf, D., Dethloff, K., Fast, I., and Krismer, T. (2015). Effect of horizontal resolution on echam6-amip performance. *Climate Dynamics*, 45(1):185–211.

Hibler, W. D. (1979). A dynamic thermodynamic sea ice model. *Journal of Physical Oceanography*, 9(4):815 – 846.

Hill, C., DeLuca, C., Suarez, M., Da Silva, A., et al. (2004). The architecture of the earth system modeling framework. *Computing in Science & Engineering*, 6(1):18–28.

Holbrook, N., Scannell, H., Sen Gupta, A., Benthuysen, J., Feng, M., Oliver, E., Alexander, L., Burrows, M., Donat, M., Hobday, A., Moore, P., Perkins-Kirkpatrick, S., Smale, D., Straub, S., and Wernberg, T. (2019). A global assessment of marine heatwaves and their drivers. *Nature Communications*, 10.

Holton, J. R. (1973). An introduction to dynamic meteorology. *American Journal of Physics*, 41(5):752–754.

Hortal, M. and Simmons, A. J. (1991). Use of reduced gaussian grids in spectral models. *Monthly Weather Review*, 119(4):1057 – 1074.

Houghton, J. T., Meira Filho, L. G., Griggs, D. J., and Maskell, K. (1997). *An introduction to simple climate models used in the IPCC Second Assessment Report*, volume 410. WMO.

Hourdin, F., Mauritsen, T., Gettelman, A., Golaz, J.-C., Balaji, V., Duan, Q., Folini, D., Ji, D., Klocke, D., Qian, Y., Rauser, F., Rio, C., Tomassini, L., Watanabe, M., and Williamson, D. (2017). The art and science of climate model tuning. *Bulletin of the American Meteorological Society*, 98(3):589 – 602.

Hunke, E., Allard, R., Bailey, D. A., Blain, P., Craig, A., Dupont, F., DuVivier, A., Grumbine, R., Hebert, D., Holland, M., Jeffery, N., Lemieux, J.-F., Osinski, R., Rasmussen, T., Ribergaard, M., Roach, L., Roberts, A., Turner, M., and Winton, M. (2020). Cice-consortium/icepack: Icepack 1.2.1.

Jeuken, A. B. M., Siegmund, P. C., Heijboer, L. C., Feichter, J., and Bengtsson, L. (1996). On the potential of assimilating meteorological analyses in a global climate model for the purpose of model validation. *Journal of Geophysical Research: Atmospheres*, 101(D12):16939–16950.

Johannessen, O. M., Kuzmina, S. I., Bobylev, L. P., and Miles, M. W. (2016). Surface air temperature variability and trends in the arctic: new amplification assessment and regionalisation. *Tellus A: Dynamic Meteorology and Oceanography*, 68(1):28234.

Jones, P. W. et al. (1998). A user's guide for scrip: A spherical coordinate remapping and interpolation package. *Los Alamos National Laboratory, Los Alamos, NM*.

Jung, T., Miller, M. J., Palmer, T. N., Towers, P., Wedi, N., Achuthavarier, D., Adams, J. M., Altshuler, E. L., Cash, B. A., Kinter, J. L., Marx, L., Stan, C., and Hodges, K. I. (2012). High-resolution global climate simulations with the ecmwf model in project athena: Experimental design, model climate, and seasonal forecast skill. *Journal of Climate*, 25(9):3155 – 3172.

Jungclaus, J. H., Fischer, N., Haak, H., Lohmann, K., Marotzke, J., Matei, D., Mikolajewicz, U., Notz, D., and von Storch, J. S. (2013). Characteristics of the ocean simulations in the max planck institute ocean model (mpiom) the ocean component of the mpi-earth system model. *Journal of Advances in Modeling Earth Systems*, 5(2):422–446.

Juricke, S., Danilov, S., Koldunov, N., Oliver, M., Sein, D. V., Sidorenko, D., and Wang, Q. (2020). A kinematic kinetic energy backscatter parametrization: From implementation to global ocean simulations. *Journal of Advances in Modeling Earth Systems*, 12:e2020MS002175.

Juricke, S., Lemke, P., Timmermann, R., and Rackow, T. (2013). Effects of stochastic ice strength perturbation on arctic finite element sea ice modeling. *Journal of Climate*, 26(11):3785 – 3802.

Keil, P., Mauritsen, T., Jungclaus, J., Hedemann, C., Olonscheck, D., and Ghosh, R. (2020). Multiple drivers of the north atlantic warming hole. *Nature Climate Change*, 10(7):667–671.

Kelly, K. A., Dickinson, S., McPhaden, M. J., and Johnson, G. C. (2001). Ocean currents evident in satellite wind data. *Geophysical Research Letters*, 28(12):2469–2472.

Kimmritz, M., Danilov, S., and Losch, M. (2016). The adaptive evp method for solving the sea ice momentum equation. *Ocean Modelling*, 101:59–67.

Kistler, R., Kalnay, E., Collins, W., Saha, S., White, G., Woollen, J., Chelliah, M., Ebisuzaki, W., Kanamitsu, M., Kousky, V., van den Dool, H., Jenne, R., and Fiorino, M. (2001). The ncep–ncar 50-year reanalysis: Monthly means cd-rom and documentation. *Bulletin of the American Meteorological Society*, 82(2):247 – 268.

Kjellsson, J., Streffing, J., Carver, G., and Köhler, M. (2020). From weather forecasting to climate modelling using openifs. *ECMWF Newsletter*, 164:38–41.

Koldunov, N. V., Aizinger, V., Rakowsky, N., Scholz, P., Sidorenko, D., Danilov, S., and Jung, T. (2019a). Scalability and some optimization of the finite-volume sea ice–ocean model, version 2.0 (fesom2). *Geoscientific Model Development*, 12(9):3991–4012.

Koldunov, N. V., Danilov, S., Sidorenko, D., Hutter, N., Losch, M., Goessling, H., Rakowsky, N., Scholz, P., Sein, D., Wang, Q., and Jung, T. (2019b). Fast evp solutions in a high-resolution sea ice model. *Journal of Advances in Modeling Earth Systems*, 11(5):1269–1284.

Komen, G., Cavaleri, L., Donelan, M., Hasselmann, K., Hasselmann, S., and Janssen, P. (1996). Dynamics and modelling of ocean waves. *Cambridge University Press, UK*, 554:1271–1285.

Krol, M., De Bruine, M., Killaars, L., Ouwersloot, H., Pozzer, A., Yin, Y., Chevallier, F., Bousquet, P., Patra, P., Belikov, D., et al. (2018). Age of air as a diagnostic for transport timescales in global models. *Geoscientific Model Development*, 11(8):3109–3130.

Large, W. G., McWilliams, J. C., and Doney, S. C. (1994). Oceanic vertical mixing: A review and a model with a nonlocal boundary layer parameterization. *Reviews of Geophysics*, 32(4):363–403.

Lavergne, T., Sørensen, A. M., Kern, S., Tonboe, R., Notz, D., Aaboe, S., Bell, L., Dybkjær, G., Eastwood, S., Gabarro, C., et al. (2019). Version 2 of the eumetsat osi saf and esa cci sea-ice concentration climate data records. *The Cryosphere*, 13(1):49–78.

Lemarié, F. (2015). Numerical modification of atmospheric models to include the feedback of oceanic currents on air-sea fluxes in ocean-atmosphere coupled models. Technical Report RT-0464, INRIA Grenoble - Rhône-Alpes ; Laboratoire Jean Kuntzmann ; Universite de Grenoble I - Joseph Fourier ; INRIA.

Lemarié, F., Blayo, E., and Debreu, L. (2015). Analysis of ocean-atmosphere coupling algorithms: Consistency and stability. *Procedia Computer Science*, 51:2066–2075. International Conference On Computational Science, ICCS 2015.

Lemke, P. (1987). A coupled one-dimensional sea ice-ocean model. *Journal of Geophysical Research: Oceans*, 92(C12):13164–13172.

Lemke, P., Ren, J., Alley, R. B., Allison, I., Carrasco, J., Flato, G., Fujii, Y., Kaser, G., Mote, P., Thomas, R. H., et al. (2007). Observations. changes in snow, ice and frozen ground. chapter 4. *ICCP AR4*.

Light, B., Smith, M. M., Perovich, D. K., Webster, M. A., Holland, M. M., Linhardt, F., Raphael, I. A., Clemens-Sewall, D., Macfarlane, A. R., Anhaus, P., and Bailey, D. A. (2022). Arctic sea ice albedo: Spectral composition, spatial heterogeneity, and temporal evolution observed during the MOSAiC drift. *Elementa: Science of the Anthropocene*, 10(1). 000103.

Lohmann, G. (2020). Temperatures from energy balance models: The effective heat capacity matters. *Earth System Dynamics*, 11(4):1195–1208.

Lynas, M., Houlton, B. Z., and Perry, S. (2021). Greater than 99% consensus on human caused climate change in the peer-reviewed scientific literature. *Environmental Research Letters*, 16(11):114005.

Ma, X., Jing, Z., Chang, P., Liu, X., Montuoro, R., Small, R. J., Bryan, F. O., Greatbatch, R. J., Brandt, P., Wu, D., Lin, X., and Wu, L. (2016). Western boundary currents regulated by interaction between ocean eddies and the atmosphere. *Nature*, 535(7613):533–537.

Madec, G., Bourdallé-Badie, R., Bouttier, P.-A., Bricaud, C., Bruciaferri, D., Calvert, D., Chanut, J., Clementi, E., Coward, A., Delrosso, D., et al. (2017). *NEMO ocean engine*, chapter 3.6, page 1. NEMO consortium.

Maisonnave, E., Coquart, L., and Piacentini, A. (2020). A better diagnostic of the load imbalance in oasis based coupled systems. Technical report, Technical Report, TR/CMGC/20/176, CECI, UMR CERFACS/CNRS No5318, France.

Malardel, S., Diamantakis, M., Agusti-Panareda, A., and Flemming, J. (2019). *Dry mass versus total mass conservation in the IFS*. ECMWF.

Malardel, S., Wedi, N., Deconinck, W., Diamantakis, M., Kühnlein, C., Mozdzynski, G., Hamrud, M., and Smolarkiewicz, P. (2016). A new grid for the ifs. *ECMWF newsletter*, 146(23-28):321.

Marti, O., Nguyen, S., Braconnot, P., Valcke, S., Lemarié, F., and Blayo, E. (2021). A schwarz iterative method to evaluate ocean–atmosphere coupling schemes: implementation and diagnostics in ipsl-cm6-sw-vlr. *Geoscientific Model Development*, 14(5):2959–2975.

Masson-Delmotte, V., Zhai, P., Pirani, A., Connors, S., Péan, C., Berger, S., Caud, N., Chen, Y., Goldfarb, L., Gomis, M., Huang, M., Leitzell, K., Lonnoy, E., Matthews, J., Maycock, T., Waterfield, T., Yelekçi, O., Yu, R., , and (eds.), B. Z. (2021). Summary for policymakers. in: Climate change 2021: The physical science basis. contribution of working group i to the sixth assessment report of the intergovernmental panel on climate change. Technical report, Intergovernmental Panel on Climate Change.

McGregor, J. L. (2005). *C-CAM: Geometric aspects and dynamical formulation.* CSIRO Atmospheric Research Dickson ACT.

McInnes, L., Allan, B., Armstrong, R., Benson, S., Bernholdt, D., Dahlgren, T., Diachin, L., Krishnan, M., Kohl, J., Larson, J., Lefantzi, S., Nieplocha, J., Norris, B., Parker, S., Ray, J., and Zhou, S. (2006). *Parallel PDE-Based Simulations Using the Common Component Architecture*, volume 51, pages 327–381. Springer.

Meehl, G. A., Richter, J. H., Teng, H., Capotondi, A., Cobb, K., Doblas-Reyes, F., Donat, M. G., England, M. H., Fyfe, J. C., Han, W., Kim, H., Kirtman, B. P., Kushnir, Y., Lovenduski, N. S., Mann, M. E., Merryfield, W. J., Nieves, V., Pegion, K., Rosenbloom, N., Sanchez, S. C., Scaife, A. A., Smith, D., Subramanian, A. C., Sun, L., Thompson, D., Ummenhofer, C. C., and Xie, S.-P. (2021). Initialized earth system prediction from subseasonal to decadal timescales. *Nature Reviews Earth & Environment*, 2(5):340–357.

Meehl, G. A., Senior, C. A., Eyring, V., Flato, G., Lamarque, J.-F., Stouffer, R. J., Taylor, K. E., and Schlund, M. (2020). Context for interpreting equilibrium climate sensitivity and transient climate response from the cmip6 earth system models. *Science Advances*, 6(26):eaba1981.

Meredith, M. P., Woodworth, P. L., Chereskin, T. K., Marshall, D. P., Allison, L. C., Bigg, G. R., Donohue, K., Heywood, K. J., Hughes, C. W., Hibbert, A., Hogg, A. M., Johnson, H. L., Jullion, L., King, B. A., Leach, H., Lenn, Y.-D., Morales Maqueda, M. A., Munday, D. R., Naveira Garabato, A. C., Provost, C., Sallée, J.-B., and Sprintall, J. (2011). Sustained monitoring of the southern ocean at drake passage: Past achievements and future priorities. *Reviews of Geophysics*, 49(4).

Monin, A. S. and Obukhov, A. M. (1954). Basic laws of turbulent mixing in the surface layer of the atmosphere. *Contributions to Atmospheric Physics*, 27(4):675–678.

Monterey, G. and Levitus, S. (1997). Climatological cycle of mixed layer depth in the world ocean. *US government printing office, NOAA NESDIS, Washington, DC*, 5.

Morice, C. P., Kennedy, J. J., Rayner, N. A., Winn, J. P., Hogan, E., Killick, R. E., Dunn, R. J. H., Osborn, T. J., Jones, P. D., and Simpson, I. R. (2021). An updated assessment of near-surface temperature change from 1850: The hadcrut5 data set. *Journal of Geophysical Research: Atmospheres*, 126(3):e2019JD032361. e2019JD032361 2019JD032361.

Mu, L., Nerger, L., Streffing, J., Tang, Q., Niraula, B., Zampieri, L., Loza, S. N., and Goessling, H. F. (2022). Sea-ice forecasts with an upgraded awi coupled prediction system. *Journal of Advances in Modeling Earth Systems*, 14(12):e2022MS003176. e2022MS003176 2022MS003176.

Münchow, A. and Melling, H. (2008). Ocean current observations from nares strait to the west of greenland: Interannual to tidal variability and forcing. *Journal of Marine Research*, 66(6):801–833.

Münchow, A., Melling, H., and Falkner, K. K. (2006). An observational estimate of volume and freshwater flux leaving the arctic ocean through nares strait. *Journal of Physical Oceanography*, 36(11):2025 – 2041.

Nadeau, D., Doutriaux, C., and Taylor, K. (2018). Climate model output rewriter (cmor version 3.3). Technical report, Tech. rep., Lawrence Livermore National Laboratory, available at: https ....

NASA/LARC/SD/ASDC (2019). Ceres energy balanced and filled (ebaf) toa monthly means data in netcdf edition4.1.

Nerger, L. and Hiller, W. (2013). Software for ensemble-based data assimilation systems—implementation strategies and scalability. *Computers & Geosciences*, 55:110–118. Ensemble Kalman filter for data assimilation.

Nerger, L., Janjić, T., Schröter, J., and Hiller, W. (2012). A unification of ensemble square root kalman filters. *Monthly Weather Review*, 140(7):2335 – 2345.

Nerger, L., Tang, Q., and Mu, L. (2020). Efficient ensemble data assimilation for coupled models with the parallel data assimilation framework: example of awi-cm (awi-cm-pdaf 1.0). *Geoscientific Model Development*, 13(9):4305–4321.

Nguyen, A. T., Menemenlis, D., and Kwok, R. (2009). Improved modeling of the arctic halocline with a subgrid-scale brine rejection parameterization. *Journal of Geophysical Research: Oceans*, 114(C11).

Nowlin Jr, W. D. and Klinck, J. M. (1986). The physics of the antarctic circumpolar current. *Reviews of geophysics*, 24(3):469–491.

Ollinaho, P., Lock, S.-J., Leutbecher, M., Bechtold, P., Beljaars, A., Bozzo, A., Forbes, R. M., Haiden, T., Hogan, R. J., and Sandu, I. (2017). Towards process-level representation of model uncertainties: stochastically perturbed parametrizations in the ecmwf ensemble. *Quarterly Journal of the Royal Meteorological Society*, 143(702):408–422.

OSISAF (2017). Global sea ice concentration [interim] climate data record 1979-2015 (v2.0, 2017) [2016-2022].

Parkinson, C. L. and Washington, W. M. (1979). A large-scale numerical model of sea ice. *Journal of Geophysical Research: Oceans*, 84(C1):311–337.

Perovich, D. K., Grenfell, T. C., Light, B., and Hobbs, P. V. (2002). Seasonal evolution of the albedo of multiyear arctic sea ice. *Journal of Geophysical Research: Oceans*, 107(C10):SHE 20–1–SHE 20–13.

Petersen, M. R., Jacobsen, D. W., Ringler, T. D., Hecht, M. W., and Maltrud, M. E. (2015). Evaluation of the arbitrary lagrangian–eulerian vertical coordinate method in the mpas-ocean model. *Ocean Modelling*, 86:93–113.

Pithan, F., Athanase, M., Dahlke, S., Sánchez-Benítez, A., Shupe, M. D., Sledd, A., Streffing, J., Svensson, G., and Jung, T. (2023). Nudging allows direct evaluation of coupled climate models with in situ observations: a case study from the mosaic expedition. *Geoscientific Model Development*, 16(7):1857–1873.

Pithan, F., Shepherd, T. G., Zappa, G., and Sandu, I. (2016). Climate model biases in jet streams, blocking and storm tracks resulting from missing orographic drag. *Geophysical Research Letters*, 43(13):7231–7240.

Platnick, S., e. a. (2017). Modis atmosphere l3 daily product. nasa modis adaptive processing system.

Platnick, S., Ackerman, S., King, M., Meyer, K., Menzel, W., Holz, R., Baum, B., and Yang, P. (2015). Modis atmosphere l2 cloud product (06_l2), nasa modis adaptive processing system, goddard space flight center.

Pörtner, H.-O., Roberts, D. C., Adams, H., Adler, C., Aldunce, P., Ali, E., Begum, R. A., Betts, R., Kerr, R. B., Biesbroek, R., et al. (2022). *Climate change 2022: Impacts, adaptation and vulnerability.* IPCC Geneva, Switzerland:.

Prša, A., Harmanec, P., Torres, G., Mamajek, E., Asplund, M., Capitaine, N., Christensen-Dalsgaard, J., Depagne, É., Haberreiter, M., Hekker, S., et al. (2016). Nominal values for selected solar and planetary quantities: Iau 2015 resolution b3. *The Astronomical Journal*, 152(2):41.

Rabe, B., Heuzé, C., Regnery, J., Aksenov, Y., Allerholt, J., Athanase, M., Bai, Y., Basque, C., Bauch, D., Baumann, T. M., Chen, D., Cole, S. T., Craw, L., Davies, A., Damm, E., Dethloff, K., Divine, D. V., Doglioni, F., Ebert, F., Fang, Y.-C., Fer, I., Fong, A. A., Gradinger, R., Granskog, M. A., Graupner, R., Haas, C., He, H., He, Y., Hoppmann, M., Janout, M., Kadko, D., Kanzow, T., Karam, S., Kawaguchi, Y., Koenig, Z., Kong, B., Krishfield, R. A., Krumpen, T., Kuhlmey, D., Kuznetsov, I., Lan, M., Laukert, G., Lei, R., Li, T., Torres-Valdés, S., Lin, L., Lin, L., Liu, H., Liu, N., Loose, B., Ma, X., McKay, R., Mallet, M., Mallett, R. D. C., Maslowski, W., Mertens, C., Mohrholz, V., Muilwijk, M., Nicolaus, M., O'Brien, J. K., Perovich, D., Ren, J., Rex, M., Ribeiro, N., Rinke, A., Schaffer, J., Schuffenhauer, I., Schulz, K., Shupe, M. D., Shaw, W., Sokolov, V., Sommerfeld, A., Spreen, G., Stanton, T., Stephens, M., Su, J., Sukhikh, N., Sundfjord, A., Thomisch, K., Tippenhauer, S., Toole, J. M., Vredenborg, M., Walter, M., Wang, H., Wang, L., Wang, Y., Wendisch, M., Zhao, J., Zhou, M., and Zhu, J. (2022). Overview of the MOSAiC expedition: Physical oceanography. *Elementa: Science of the Anthropocene*, 10(1).

Rackow, T., Danilov, S., Goessling, H. F., Hellmer, H. H., Sein, D. V., Semmler, T., Sidorenko, D., and Jung, T. (2022). Delayed antarctic sea-ice decline in high-resolution climate change simulations. *Nature Communications*, 13(1):637.

Rackow, T., Goessling, H. F., Jung, T., Sidorenko, D., Semmler, T., Barbi, D., and Handorf, D. (2018). Towards multi-resolution global climate modeling with echam6-fesom. part ii: climate variability. *Climate Dynamics*, 50(7):2369–2394.

Rackow, T. and Juricke, S. (2020). Flow-dependent stochastic coupling for climate models with high ocean-to-atmosphere resolution ratio. *Quarterly Journal of the Royal Meteorological Society*, 146(726):284–300.

Reichle, R. H., Walker, J. P., Koster, R. D., and Houser, P. R. (2002). Extended versus ensemble kalman filtering for land data assimilation. *Journal of Hydrometeorology*, 3(6):728 – 740.

Reichler, T. and Kim, J. (2008). How well do coupled models simulate today's climate? *Bulletin of the American Meteorological Society*, 89(3):303 – 312.

Renault, L., Lemarié, F., and Arsouze, T. (2019). On the implementation and consequences of the oceanic currents feedback in ocean–atmosphere coupled models. *Ocean Modelling*, 141:101423.

Renault, L., Molemaker, M. J., Gula, J., Masson, S., and McWilliams, J. C. (2016a). Control and stabilization of the gulf stream by oceanic current interaction with the atmosphere. *Journal of Physical Oceanography*, 46(11):3439 – 3453.

Renault, L., Molemaker, M. J., McWilliams, J. C., Shchepetkin, A. F., Lemarié, F., Chelton, D., Illig, S., and Hall, A. (2016b). Modulation of wind work by oceanic current interaction with the atmosphere. *Journal of Physical Oceanography*, 46(6):1685 – 1704.

Ridderinkhof, H., van der Werf, P. M., Ullgren, J. E., van Aken, H. M., van Leeuwen, P. J., and de Ruijter, W. P. M. (2010). Seasonal and interannual variability in the mozambique channel from moored current observations. *Journal of Geophysical Research: Oceans*, 115(C6).

Righi, M., Eyring, V., Gottschaldt, K.-D., Klinger, C., Frank, F., Jöckel, P., and Cionni, I. (2015). Quantitative evaluation of ozone and selected climate parameters in a set of emac simulations. *Geoscientific Model Development*, 8(3):733–768.

Ritchie, H. (1987). Semi-Lagrangian Advection on a Gaussian Grid. *Monthly Weather Review*, 115(2):608–619.

Ritchie, H., Temperton, C., Simmons, A., Hortal, M., Davies, T., Dent, D., and Hamrud, M. (1995). Implementation of the Semi-Lagrangian Method in a High-Resolution Version of the ECMWF Forecast Model. *Monthly Weather Review*, 123(2):489–514.

Roach, A. T., Aagaard, K., Pease, C. H., Salo, S. A., Weingartner, T., Pavlov, V., and Kulakov, M. (1995). Direct measurements of transport and water properties through the bering strait. *Journal of Geophysical Research: Oceans*, 100(C9):18443–18457.

Roach, L. A., Bitz, C. M., Horvat, C., and Dean, S. M. (2019). Advances in modeling interactions between sea ice and ocean surface waves. *Journal of Advances in Modeling Earth Systems*, 11(12):4167–4181.

Robert, A., Henderson, J., and Turnbull, C. (1972). An implicit time integration scheme for baroclinic models of the atmosphere. *Monthly Weather Review*, 100(5):329 – 335.

Roberts, C. D., Senan, R., Molteni, F., Boussetta, S., Mayer, M., and Keeley, S. P. (2018). Climate model configurations of the ecmwf integrated forecasting system (ecmwf-ifs cycle 43r1) for highresmip. *Geoscientific model development*, 11(9):3681–3712.

Roser, M. and Ortiz-Ospina, E. (2016). Literacy. *Our World in Data*. https://ourworldindata.org/literacy.

Roser, M., Ritchie, H., Ortiz-Ospina, E., and Rodés-Guirao, L. (2013). World population growth. *Our World in Data*. https://ourworldindata.org/world-population-growth.

Ross, C. (2011). " trying all things": romantic polymaths, social factors, and the legacies of a rhetorical education. *Texas Studies in Literature and Language*, 53(4):401–430.

Ruddiman, W. (2008). *Earth's Climate: Past and Future*. W. H. Freeman.

Saarinen, S., Hamrud, M., Salmond, D., and Hague, J. (2005). Dr. hook instrumentation tool. Technical report, European Centre for Medium-Range Weather Forecasts.

Samaniego, L., Kumar, R., and Attinger, S. (2010). Multiscale parameter regionalization of a grid-based hydrologic model at the mesoscale. *Water Resources Research*, 46(5).

Satoh, M., Stevens, B., Judt, F., Khairoutdinov, M., Lin, S.-J., Putman, W. M., and Düben, P. (2019). Global cloud-resolving models. *Current Climate Change Reports*, 5(3):172–184.

Scafetta, N. (2021). Testing the cmip6 gcm simulations versus surface temperature records from 1980–1990 to 2011–2021: High ecs is not supported. *Climate*, 9(11).

Schauer, U., Beszczynska-Möller, A., Walczowski, W., Fahrbach, E., Piechura, J., and Hansen, E. (2008). *Variation of Measured Heat Flow Through the Fram Strait Between 1997 and 2006*, pages 65–85. Springer Netherlands, Dordrecht.

Schiemann, R., Demory, M.-E., Shaffrey, L. C., Strachan, J., Vidale, P. L., Mizielinski, M. S., Roberts, M. J., Matsueda, M., Wehner, M. F., and Jung, T. (2017). The resolution sensitivity of northern hemisphere blocking in four 25-km atmospheric global circulation models. *Journal of Climate*, 30(1):337–358.

Scholz, P., Sidorenko, D., Danilov, S., Wang, Q., Koldunov, N., Sein, D., and Jung, T. (2022). Assessment of the finite-volume sea ice–ocean model (fesom2.0) – part 2: Partial bottom cells, embedded sea ice and vertical mixing library cvmix. *Geoscientific Model Development*, 15(2):335–363.

Scholz, P., Sidorenko, D., Gurses, O., Danilov, S., Koldunov, N., Wang, Q., Sein, D., Smolentseva, M., Rakowsky, N., and Jung, T. (2019). Assessment of the finite-volume sea ice-ocean model (fesom2.0) – part 1: Description of selected key model elements and comparison to its predecessor version. *Geoscientific Model Development*, 12(11):4875–4899.

SCImago, n. S. (2022). Journal & country rank.

Sein, D. V., Koldunov, N. V., Danilov, S., Wang, Q., Sidorenko, D., Fast, I., Rackow, T., Cabos, W., and Jung, T. (2017). Ocean modeling on a mesh with resolution following the local rossby radius. *Journal of Advances in Modeling Earth Systems*, 9(7):2601–2614.

Semmler, T., Danilov, S., Gierz, P., Goessling, H. F., Hegewald, J., Hinrichs, C., Koldunov, N., Khosravi, N., Mu, L., Rackow, T., Sein, D. V., Sidorenko, D., Wang, Q., and Jung, T. (2020). Simulations for cmip6 with the awi climate model awi-cm-1-1. *Journal of Advances in Modeling Earth Systems*, 12(9):e2019MS002009. e2019MS002009 2019MS002009.

Shan, X., Jing, Z., Sun, B., and Wu, L. (2020). Impacts of ocean current–atmosphere interactions on mesoscale eddy energetics in the kuroshio extension region. *Geoscience Letters*, 7(1):3.

Sidorenko, D., Danilov, S., Streffing, J., Fofonova, V., Goessling, H. F., Scholz, P., Wang, Q., Androsov, A., Cabos, W., Juricke, S., Koldunov, N., Rackow, T., Sein, D. V., and Jung, T. (2021). Amoc variability and watermass transformations in the awi climate model. *Journal of Advances in Modeling Earth Systems*, 13(10):e2021MS002582. e2021MS002582 2021MS002582.

Sidorenko, D., Goessling, H., Koldunov, N., Scholz, P., Danilov, S., Barbi, D., Cabos, W., Gurses, O., Harig, S., Hinrichs, C., Juricke, S., Lohmann, G., Losch, M., Mu, L., Rackow, T., Rakowsky, N., Sein, D., Semmler, T., Shi, X., Stepanek, C., Streffing, J., Wang, Q., Wekerle, C., Yang, H., and Jung, T. (2019). Evaluation of fesom2.0 coupled to echam6.3: Preindustrial and highresmip simulations. *Journal of Advances in Modeling Earth Systems*, 11(11):3794–3815.

Sidorenko, D., Koldunov, N. V., Wang, Q., Danilov, S., Goessling, H. F., Gurses, O., Scholz, P., Sein, D. V., Volodin, E., Wekerle, C., and Jung, T. (2018). Influence of a salt plume parameterization in a coupled climate model. *Journal of Advances in Modeling Earth Systems*, 10(9):2357–2373.

Sidorenko, D., Rackow, T., Jung, T., Semmler, T., Barbi, D., Danilov, S., Dethloff, K., Dorn, W., Fieg, K., Goessling, H. F., Handorf, D., Harig, S., Hiller, W., Juricke, S., Losch, M., Schröter, J., Sein, D. V., and Wang, Q. (2015). Towards multi-resolution global climate modeling with echam6–fesom. part i: model formulation and mean climate. *Climate Dynamics*, 44(3):757–780.

Silberberg, M. S. (2006). *Chemistry: The molecular nature of matter and change*. McGraw-Hill ScienceEngineering.

Smedsrud, L. H., Ingvaldsen, R., Nilsen, J. E. Ø., and Skagseth, Ø. (2010). Heat in the barents sea: transport, storage, and surface fluxes. *Ocean Science*, 6(1):219–234.

Steele, M., Morley, R., and Ermold, W. (2001). Phc: A global ocean hydrography with a high-quality arctic ocean. *Journal of Climate*, 14(9):2079–2087.

Stephens, G. L., O'Brien, D., Webster, P. J., Pilewski, P., Kato, S., and Li, J.-l. (2015). The albedo of earth. *Reviews of Geophysics*, 53(1):141–163.

Sterl, A., Bintanja, R., Brodeau, L., Gleeson, E., Koenigk, T., Schmith, T., Semmler, T., Severijns, C., Wyser, K., and Yang, S. (2012). A look at the ocean in the ec-earth climate model. *Climate Dynamics*, 39(11):2631–2657.

Stevens, B., Giorgetta, M., Esch, M., Mauritsen, T., Crueger, T., Rast, S., Salzmann, M., Schmidt, H., Bader, J., Block, K., Brokopf, R., Fast, I., Kinne, S., Kornblueh, L., Lohmann, U., Pincus, R., Reichler, T., and Roeckner, E. (2013). Atmospheric component of the mpi-m earth system model: Echam6. *Journal of Advances in Modeling Earth Systems*, 5(2):146–172.

Stommel, H. (1948). The westward intensification of wind-driven ocean currents. *Eos, Transactions American Geophysical Union*, 29(2):202–206.

Storto, A., Masina, S., and Navarra, A. (2016a). Evaluation of the cmcc eddy-permitting global ocean physical reanalysis system (c-glors, 1982–2012) and its assimilation components. *Quarterly Journal of the Royal Meteorological Society*, 142(695):738–758.

Storto, A., Masina, S., and Navarra, A. (2016b). Evaluation of the cmcc eddy-permitting global ocean physical reanalysis system (c-glors, 1982–2012) and its assimilation components. *Quarterly Journal of the Royal Meteorological Society*, 142(695):738–758.

Streffing, J., Sidorenko, D., Semmler, T., Zampieri, L., Scholz, P., Andrés-Martínez, M., Koldunov, N., Rackow, T., Kjellsson, J., Goessling, H., Athanase, M., Wang, Q., Hegewald, J., Sein, D. V., Mu, L., Fladrich, U., Barbi, D., Gierz, P., Danilov, S., Juricke, S., Lohmann, G., and Jung, T. (2022). Awi-cm3 coupled climate model: description and evaluation experiments for a prototype post-cmip6 model. *Geoscientific Model Development*, 15(16):6399–6427.

Strommen, K., Christensen, H. M., MacLeod, D., Juricke, S., and Palmer, T. N. (2019). Progress towards a probabilistic earth system model: examining the impact of stochasticity in the atmosphere and land component of ec-earth v3.2. *Geoscientific Model Development*, 12(7):3099–3118.

Sverdrup, H. U. (1947). Wind-driven currents in a baroclinic ocean; with application to the equatorial currents of the eastern pacific. *Proceedings of the National Academy of Sciences*, 33(11):318–326.

Timmermann, R. and Beckmann, A. (2004a). Parameterization of vertical mixing in the weddell sea. *Ocean modelling*, 6(1):83–100.

Timmermann, R. and Beckmann, A. (2004b). Parameterization of vertical mixing in the weddell sea. *Ocean Modelling*, 6(1):83–100.

Timmermann, R., Danilov, S., Schröter, J., Böning, C., Sidorenko, D., and Rollenhagen, K. (2009). Ocean circulation and sea ice distribution in a finite element global sea ice–ocean model. *Ocean modelling*, 27(3-4):114–129.

Titchner, H. A. and Rayner, N. A. (2014a). The met office hadley centre sea ice and sea surface temperature data set, version 2: 1. sea ice concentrations. *Journal of Geophysical Research: Atmospheres*, 119(6):2864–2889.

Titchner, H. A. and Rayner, N. A. (2014b). The met office hadley centre sea ice and sea surface temperature data set, version 2: 1. sea ice concentrations. *Journal of Geophysical Research: Atmospheres*, 119(6):2864–2889.

Tsai, C.-W., Lai, C.-F., Chao, H.-C., and Vasilakos, A. V. (2015). Big data analytics: a survey. *Journal of Big Data*, 2(1):21.

van Haren, R., Haarsma, R. J., Van Oldenborgh, G. J., and Hazeleger, W. (2015). Resolution dependence of european precipitation in a state-of-the-art atmospheric general circulation model. *Journal of Climate*, 28(13):5134–5149.

Vignati, E., Wilson, J., and Stier, P. (2004). M7: An efficient size-resolved aerosol microphysics module for large-scale aerosol transport models. *Journal of Geophysical Research: Atmospheres*, 109(D22).

Voldoire, A., Saint-Martin, D., Sénési, S., Decharme, B., Alias, A., Chevallier, M., Colin, J., Guérémy, J.-F., Michou, M., Moine, M.-P., Nabat, P., Roehrig, R., Salas y Mélia, D., Séférian, R., Valcke, S., Beau, I., Belamari, S., Berthet, S., Cassou, C., Cattiaux, J., Deshayes, J., Douville, H., Ethé, C., Franchistéguy, L., Geoffroy, O., Lévy, C., Madec, G., Meurdesoif, Y., Msadek, R., Ribes, A., Sanchez-Gomez, E., Terray, L., and Waldman, R. (2019). Evaluation of cmip6 deck experiments with cnrm-cm6-1. *Journal of Advances in Modeling Earth Systems*, 11(7):2177–2213.

Walker, D. W. and Dongarra, J. J. (1996). Mpi: a standard message passing interface. *Supercomputer*, 12:56–68.

Wallace, J. M. and Hobbs, P. V. (2006). *Atmospheric science: an introductory survey*, volume 92. Elsevier.

Walsh, J., Chapman, W., Fetterer, F., and Stewart, J. (2019). Gridded monthly sea ice extent and concentration, 1850 onward, version 2. *Boulder, Colorado USA. NSIDC: National Snow and Ice Data Center.*

Wang, S., Wang, Q., Shu, Q., Scholz, P., Lohmann, G., and Qiao, F. (2019). Improving the upper-ocean temperature in an ocean climate model (fesom 1.4): Shortwave penetration versus mixing induced by nonbreaking surface waves. *Journal of Advances in Modeling Earth Systems*, 11(2):545–557.

Watts, M., Maslowski, W., Lee, Y. J., Kinney, J. C., and Osinski, R. (2021). A spatial evaluation of arctic sea ice and regional limitations in cmip6 historical simulations. *Journal of Climate*, 34(15):6399 – 6420.

Weber, M. E., Golledge, N. R., Fogwill, C. J., Turney, C. S. M., and Thomas, Z. A. (2021). Decadal-scale onset and termination of antarctic ice-mass loss during the last deglaciation. *Nature Communications*, 12(1):6683.

Weisheimer, A., Corti, S., Palmer, T., and Vitart, F. (2014). Addressing model error through atmospheric stochastic physical parametrizations: impact on the coupled ECMWF seasonal forecasting system. *Philos Trans A Math Phys Eng Sci*, 372(2018):20130290.

Wielicki, B. A., Barkstrom, B. R., Harrison, E. F., Lee, R. B., Smith, G. L., and Cooper, J. E. (1996). Clouds and the earth's radiant energy system (ceres): An earth observing system experiment. *Bulletin of the American Meteorological Society*, 77(5):853 – 868.

Wild, M. (2020). The global energy balance as represented in cmip6 climate models. *Climate Dynamics*, 55:553–577.

Willison, J., Robinson, W. A., and Lackmann, G. M. (2015). North atlantic storm-track sensitivity to warming increases with model resolution. *Journal of Climate*, 28(11):4513–4524.

Woodgate, R. A. (2018). Increases in the pacific inflow to the arctic from 1990 to 2015, and insights into seasonal trends and driving mechanisms from year-round bering strait mooring data. *Progress in Oceanography*, 160:124–154.

Yamazaki, D., Kanae, S., Kim, H., and Oki, T. (2011). A physically based description of floodplain inundation dynamics in a global river routing model. *Water Resources Research*, 47(4).

Yang, C., Christensen, H. M., Corti, S., von Hardenberg, J., and Davini, P. (2019). The impact of stochastic physics on the el niño southern oscillation in the ec-earth coupled model. *Climate Dynamics*, 53(5):2843–2859.

Yepes-Arbós, X., van den Oord, G., Acosta, M. C., and Carver, G. D. (2021). Evaluation and optimisation of the i/o scalability for the next generation of earth system models: Ifs cy43r3 and xios 2.0 integration as a case study. *Geoscientific Model Development Discussions*, pages 1–23.

Zabolotskikh, E. V. (2019). Review of methods to retrieve sea-ice parameters from satellite microwave radiometer data. *Izvestiya, Atmospheric and Oceanic Physics*, 55(1):110–128.

Zampieri, L., Kauker, F., Fröhle, J., Sumata, H., Hunke, E. C., and Goessling, H. F. (2021a). Impact of sea-ice model complexity on the performance of an unstructured-mesh sea-ice/ocean model under different atmospheric forcings. *Journal of Advances in Modeling Earth Systems*, 13(5):e2020MS002438.

Zampieri, L., Kauker, F., Fröhle, J., Sumata, H., Hunke, E. C., and Goessling, H. F. (2021b). Impact of sea-ice model complexity on the performance of an unstructured-mesh sea-ice/ocean model under different atmospheric forcings. *Journal of Advances in Modeling Earth Systems*, 13(5):e2020MS002438. e2020MS002438 2020MS002438.

Zeman, C., Wedi, N., Dueben, P., Ban, N., and Schaer, C. (2021). Model intercomparison of cosmo 5.0 and ifs 45r1 at kilometer-scale grid spacing. *Geoscientific Model Development*, 14:4617–4639.

Zhang, J. and Rothrock, D. A. (2003). Modeling global sea ice with a thickness and enthalpy distribution model in generalized curvilinear coordinates. *Monthly Weather Review*, 131(5):845 – 861.